UNIVERSITY OF SOUTHAMPTON

FACULTY OF ENGINEERING AND THE ENVIRONMENT

The robust design of ultrasonic devices for use in oceanographic environments.

by

Michael Gedge

Thesis for the degree of Doctor of Philosophy

June 2015

Supervised by Prof. Martyn Hill

Abstract

The Earth's oceans host an enormous range of natural resources, over 90 billion kg of fish and shell fish are caught each year (WorldOceanReview, 2011). The oceans play an overriding role in climate regulation, removing vast quantities of carbon from the atmosphere. It is believed phytoplankton could account for more than half the earth's oxygen production (ConsciousAlliance, 2011). Monitoring these biological and chemical characteristics offers an invaluable insight into the way our oceans work, which can then be used to generate and verify reliable models of the global ecosystem. *In-situ* sensors have been identified as the way forward, due to the ever changing properties of the world's oceans in terms of chemistry and biology. The sensors will have to overcome harsh working conditions and process large quantities of data, whilst using as little power as possible.

The work undertaken for this thesis aims to develop ultrasonic standing wave particle manipulation techniques for use in an oceanographic environment. Ultrasonic particle manipulation techniques are generally confined to ceramic devices, which are incompatible with oceanographic sensing on a large scale deployment. This work has bridged that gap and developed fresh approaches to ultrasonic techniques in polymer devices. In addition to this, novel manufacturing methods have been developed to improve the robustness of the devices or to make the technology more compatible with cheaper, quicker and easier manufacturing techniques. A specific problem in oceanographic sensing is biofouling – the build up of microorganisms in and around the sensor. This project has investigated the feasibility of using ultrasonic techniques to reduce this build up, in particular, the formation of biofilms within sensors. The use of ultrasonics to reduce biofouling has been investigated by others, but it generally focuses on acoustic streaming techniques which induces mixing and has high power requirements incompatible with remote sensing (Sankaranarayanan et al., 2008).

This work was carried out in conjunction with the Centre for Marine Microsystems in Southampton. The centre is developing robust high performance metrology systems for use in oceanographic science. Four distinct class of sensors will all be looked at, Chemical, Physical, Nucleic acid sensors and a µ-flow cytometer (UniversityOfSouthampton, 2011).

To assist in the development of oceanographic ultrasonic sensing platforms, one dimensional and two dimensional modelling was carried out in Matlab (R2014b) and ANSYS (12.0). The models were used to design new devices as well verify experimental results. In particular, ANSYS was used to investigate the

mechanism behind standing wave particle manipulation devices. The modelling investigated the robustness of such a device and their suitability for scaling up and integration into an oceanographic sensor. Once the computational modelling had been carried out, devices were built using a variety of manufacturing techniques. As required, the techniques were adapted and optimised for the production of ultrasonic oceanographic sensors. The work went on to qualitatively and quantitatively analyse the affects of ultrasonic techniques in an oceanographic sensor. In particular, the formation of biofilm within a polymer sensor was analysed. Image processing software was optimised for the experiments then used to identify the effects of ultrasonic standing wave techniques.

The work shows that it is possible to reduce the build up of biofilms within polymer devices over substantial time periods using ultrasonic standing wave techniques. The devices used differ from conventional ceramic devices in that less than an exact half wave was set up across the fluid channel. This means there are non zero forces acting at the polymer/fluid boundary which is beneficial for the reduction of biofilm formation. The work also identifies a mechanism for the alignment of particles within a microfluidic device through the use of surface acoustic waves, though it was not possible to verify the computational results experimentally. A novel manufacturing technique using spin coating was developed that would allow easier construction of surface wave devices. In addition to this, a new type of device was developed utilising the transparent properties of lithium niobate in a bulk acoustic wave configuration. In the process of carrying out this work an experimental method has been developed allowing the depth of particles within devices to be ascertained through long exposure images. The length of the particle streak allows the position of the particle relative to a solid/fluid boundary to be inferred, and the data can be presented in such a way to build up a picture of the device characteristics.

Contents

List of Figures

List of Tables

DECLARATION OF AUTHORSHIP

I, Michael Gedge

declare that the thesis entitled

The robust design of ultrasonic devices for use in oceanographic environments.

and the work presented in the thesis are both my own, and have been generated by me as the result of my own original research. I confirm that:

this work was done wholly or mainly while in candidature for a research degree at this University;
where any part of this thesis has previously been submitted for a degree or any other qualification at this University or any other institution, this has been clearly stated;
where I have consulted the published work of others, this is always clearly attributed;
where I have quoted from the work of others, the source is always given. With the exception of such quotations, this thesis is entirely my own work;
I have acknowledged all main sources of help;
where the thesis is based on work done by myself jointly with others, I have made clear exactly what was done by others and what I have contributed myself;
parts of this work have been published as:

Minimizing biofouling in microfluidic devices through the use of continuous ultrasonic standing waves, Journal of Ocean Technology, Volume 9, Number 4, 69-89, (Gedge, Stoodley and Hill).

Theory of Surface Acoustic Wave Devices for Particle Manipulation, Microscale Acoustofluidics, T. Laurell and A. Lenshof, Eds., ed: The Royal Society of Chemistry, 2015, pp. 337-353, (Gedge and Hill).

Acoustofluidics 17: Theory and applications of surface acoustic wave devices for particle manipulation, Lab on a Chip, Volume 12, Issue 17, 2998-3007, (Gedge and Hill, 2012).

The use of ultrasonic waves to minimise biofouling in oceanographic microsensors, AIP Conference Proceedings, Volume 1433, Issue 1, 765-768, (Gedge et al., 2012).

Signed:

Date: 1st June 2015

Acknowledgements

This work was funded by EPSRC grant EP/EO16774/1 titled “Ruggedised Micro System Technology for Marine Measurement” and I express my thanks to them. I would like to express my gratitude to my supervisor Professor Martyn Hill for all the advice, feedback and technical discussions. I would like to thank Dr. Pete Glynne-Jones for all the help and guidance with my experiments and computational modelling. The work on biofouling would not have been possible without the help and advice of Dr. Dyan Ankrett and for that I am grateful. I am indebted to Dr. Nefeli Tsaloglou for her advice on cell staining. I would also like to show my appreciation to Katie Chamberlain and Dr. Anne Bernassau for their time spent manufacturing surface acoustic wave devices for me. I have also had advice and feedback along the way from Dr. Matt Mowlem and Dr. Rosie Boltryk for which I am grateful. I would also like to thank Dr. Dave Walker for preparing the *Vibrio natriegens* which were used in Chapter 4.

I would like to thank my mother for her encouragement and support. I would also like to thank my excellent friends for their support; in particular Jay, Alex and Marcus, for the motivation and stimulating conversations they provided. Finally I would like to thank my partner Rachel for her proof reading skills, encouragement and above all, her patience.

Definitions and Abbreviations

COC - Cyclic Olefin Copolymer

CTC - 5-Cyano-2,3-ditolyl Tetrazolium Chloride

DAPI - 4',6-Diamidino-2-Phenylindole

DEP - Dielectrophoresis

DNA - Deoxyribonucleic Acid

DRIE – Deep Reactive Ion Etching

E-beam – Electron Beam Evaporation

EPS - Extracellular Polymeric Substance

FACS – Fluorescence Activated Cell Sorting

FEA – Finite Element Analysis

FITC – Fluoroscein Isothiocyanate

GDP – Gross Domestic Product

HCl – Hydrochloric Acid

IDT – Interdigitated Electrode

ITO – Indium Tin Oxide

MEMS – Micro Electro-Mechanical System

mRNA – Messenger Ribonucleic acid

NDE – Non Destructive Evaluation

OH - Hydroxyl

PDMS – Polydimethylsiloxane

PEDOT:PSS – Poly(3,4-ethylendioxythiophene):Poly(styrenesulphonic acid)

PMMA – Polymethylmethacrylate

ppt – Parts Per Thousand

PZT - Lead zirconium titanate

RBC – Red Blood Cell

RMST - Ruggedised MicroSystem Technology

SAW – Surface Acoustic Wave

SOP – Solid Object Printing

UV – Ultraviolet

3MN – Minimal Marine Media with Nutrients

Nomenclature

A, B, A', B' – Constants

A_H – Hamaker Constant (J)

A_{Re} – Area (m^2)

C_A – Dilational Wave Speed ($m\ s^{-1}$)

C_B – Distortional Wave Speed ($m\ s^{-1}$)

$C_{F,R,W}$ – Wave Speed $_{\text{Fluid, Rayleigh and Wedge Respectively}}$ ($m\ s^{-1}$)

C_{hyd} – Hydraulic Capacitance ($m^3\ Pa^{-1}$)

$C_{\mathrm{L1,L2}}$ – Longitudinal Wave Speed $_{\text{Material 1 and Material 2 Respectively}}$ ($m\ s^{-1}$)

$C_{\mathrm{T1,T2}}$ – Transverse Wave Speed $_{\text{Material 1 and Material 2 Respectively}}$ ($m\ s^{-1}$)

C_{nn} – Material Constants $_{\text{Matirx Numbering}}$

D_0 – Equilibrium Distance (m)

E – Young's Modulus (Pa)

E_{AC} – Time Averaged Energy (J)

E_C – Energy Required to Overcome Capillarity (J)

E_K – Kinetic Energy (J)

E_P – Potential Energy (J)

F_g – Gravitational Force (N)

$I_{I,TR,R}$ – Acoustic Intensity Coefficients $_{\text{Incoming, Transmission and Reflection Respectively}}$

K – Bulk Modulus (Pa)

$K_{Fluid,\ Material}$ – Compressibility $_{\text{Fluid and Material Respectively}}$ (Pa^{-1})

$P_{d,1}$ – Pressure $_{\text{At Drop Voltage and At Higher Voltage Respectively}}$ (Pa)

$P_{I,R,TR}$ – Pressure $_{\text{Incoming, Refelcted and Transmitted Respectively}}$ (Pa)

P_{Re} – Perimeter (m)

Q – Flow Rate ($m^3\ s^{-1}$)

Re – Reynolds Number

$R_{1hyd,2hyd}$ – Hydrodynamic Resistance $_{\text{Channel 1 and Channel 2 Respectively}}$ ($Pa\ s\ m^{-3}$)

U – Mean Fluid Velocity ($m\ s^{-1}$)

V_B – Bead Volume (m^3)

Z_n – Acoustic Impedance $_{\text{Material Number}}$ ($kg\ m^{-2}\ s^{-1}$)

$c_{B,F}$ – Speed of Sound $_{\text{Bead and Fluid Respectively}}$ ($m\ s^{-1}$)

h - Layer Thickness (m)

h_c – Height $_{\text{Channel}}$ (m)

k – Wave Number (m^{-1})

k_L – Longitudinal Wave Number (m^{-1})

k_T – Transverse Wave Number (m^{-1})

l – Length (m)

r – radius (m)

s - $\frac{k_t}{k}$

s_C – Spreading Coefficient (J)

t – Time (s)

u_R – Rayleigh Displacement in x direction (m)

$u_{\check{\mathrm{R}}}$ – Rayleigh Displacement in x direction as a function of depth

u, v, w – Displacements (Cartesian Coordinates)

v_x – Fluid Speed $_{\text{Direction}}$ ($m\ s^{-1}$)

w_c – Width $_{\text{Channel}}$ (m)

w_R – Rayleigh Displacement in z direction (m)

$w_{\check{\mathrm{R}}}$ – Rayleigh Displacement in z direction as a function of depth

x, y, z – Cartesian Coordinates

Δ – Volume Strain/Dilation

Δp – Hydraulic Pressure (Pa)

$\Delta\rho$ – Density Difference ($kg\ m^{-3}$)

Φ – Potential Function

Ψ – Displacement Parameter

ζ – Kinematic Viscosity ($m^2\ s^{-1}$)

Ω – Electrical Impedance - Ohms

∇^2 – Laplace Operator

$\alpha_{\mathrm{L,S}}$ – Attenuation $_{\text{Longitudinal, Frictional}}$ (m^{-1})

α_R – Coefficient of Reflected Pressure

α_{TR} – Coefficient of Transmitted Pressure

α_1 – Function of Poisson's Ratio

$\beta_{B,F,P}$ – Compressibility $_{\text{Bead, Fluid and Particle Respectively}}$ ($m^2\ N^{-1}$)

$\gamma_{LG,SG,SL}$ – Surface Energy $_{\text{Liquid/Gas, Solid/Gas and Solid/Liquid Combinations Respectively}}$ (J)

γ_{L}^2 – Longitudinal Rayleigh Combination (m^{-2})

γ_{T}^2 – Transverse Rayleigh Combination (m^{-2})

ϵ – Energy density ($J\ m^{-3}$)

ϵ_{xx} – Strain $_{\text{direction and plane upon which it is acting}}$

η – Dynamic Viscosity (Pa s)

θ - Angle

ϑ_x – Rotation about the axis

λ – Wavelength (m)

λ_L – Lamé's First Constant (Pa)

λ_R – Wavelength Rayleigh (m)

μ – Shear Modulus (Pa)

ν – Poisson's Ratio

$\rho_{B,F,P,R}$ – Density Bead, Fluid, Particle and Rayleigh Half Space Respectively (kg m^{-3})

σ_{xx} – Stress direction and plane upon which it is acting (Pa)

φ – Scalar Function

ϕ – Acoustic Contrast Factor

ψ – Scalar Function

ω – Angular Frequency (s^{-1})

Chapter 1 Introduction

The Earth's oceans host an enormous range of natural resources, over 90 billion kg of fish and shell fish are caught each year (WorldOceanReview, 2011). They are a crucial element of our transport and energy infrastructures and they play an overriding role in climate regulation, removing vast quantities of carbon from the atmosphere. It is believed phytoplankton could account for more than half the earth's oxygen production (ConsciousAlliance, 2011). Monitoring these biological and chemical characteristics offers an invaluable insight into the way our oceans work, which can then be used to generate and verify reliable models of the global ecosystem. Existing methods for carrying out such monitoring are expensive, coarse in terms of spatial and temporal sampling and involve risk of sample contamination and degradation, (UniversityOfSouthampton, 2011). Remote *in-situ* microfluidic sensors are being developed to fulfill this need for data, these sensors must be small, robust, reliable and power efficient.

The oceans are a vast resource and it has been estimated that the biogeochemical cycles that take place in the oceans are worth US$22 trillion a year in "eco-system services", this is comparable to global gross domestic product (GDP) (Costanza et al., 1998). It is therefore perhaps surprising that they remain so under sampled. Whilst satellite monitoring is able to provide significant quantities of data on oceans, they are opaque to electromagnetic radiation which limits data collection to the surface.

Existing methods for carrying out detailed monitoring typically rely on the acquisition of water samples for subsequent laboratory analysis. This approach requires a well-resourced research ship complete with well trained personnel. As a result, the cost of such a method is estimated at more than £15k per day. Despite this expense, sampling is still incredibly sparse with readings likely to be taken annually at approximately 1 km intervals, (UniversityOfSouthampton, 2011). When one considers that some of the key biogeochemical reactions that take place in the ocean exhibit variations of two orders of magnitude on hourly and metre scales (UniversityOfSouthampton, 2011), the quantity of data currently being collected is a long way off what is required.

In recent years, this lack of data on such an important resource has been identified and steps have been taken to generate data *in-situ*. Autonomous underwater vehicles, gliders and Apex floats have all been deployed in recent years to better understand the biological and chemical reactions that occur in the behemoth

(1.3×10^9 km^3) (Des Marais, 2013) that is the world's oceans. Despite these improvements, there is still a significant shortfall in terms of the quantity of data being generated that requires an order of magnitude improvement in size, power consumption, reliability and robustness. The work in this thesis is part of the ruggedised microsystem technology for marine measurement project to address this technological gap.

Continuous and distributed monitoring of the oceanic environment requires biochemical sensor platforms that are small, robust, reliable, and power efficient. Ultrasonic technologies have the potential to offer a low power route to address a number of issues in a remote marine measurement system, including barrier-free pre-filtration, sample concentration, biofouling reduction and sample focusing.

Designing a sensor that uses acoustic radiation forces for use in oceanographic environments poses many challenges, not least because variations in salinity and temperature significantly affect the acoustic behavior. The harsh environments and high pressures play a part in material selection and acoustic design.

1.1 Ruggedised MicroSystem Technology for Marine Measurement

The work in this thesis forms part of a larger project titled "Ruggedised MicroSystem Technology (RMST) for marine measurement". The aim of the project was to produce the next generation of chemical and biological sensors to monitor the world's oceans. The sensing platforms will be based around microfluidic techniques to give the order of magnitude improvement required to fulfil the data shortage discussed. The project aimed to develop a µ-flow cytometer capable of speciating phytoplankton through the measurement of fluorescence and size, all within a microfluidic device.

Current sensor systems for oceanic metrology are large and expensive which inhibits the mass production and deployment of such systems. The aim of the RMST project is to develop miniaturised multi parameter biogeochemical sensors for mass deployment in the world's oceans.

1.1.1 Chemical Sensors

The project aimed to produce a suite of sensors to remotely measure *in-situ* the following chemicals and levels;

- Nitrate/Nitrite
- Ammonia

- Methane
- Alkalinity
- Phosphate
- Dissolved Oxygen
- pH
- Iron/Manganese

Current commercially available sensors for these tasks tend to be expensive, bulky, power hungry or a combination of these characteristics. These chemicals and associated readings play an important role in aquatic biological activity and so being able to accurately measure them is important to develop a better understanding of the complex interactions that occur in the ocean. For example, methane is approximately twenty times more effective as a greenhouse gas than CO_2 so being able to monitor it in an oceanographic environment is important. Alkalinity and pH sensors will give an insight into how increasing levels of CO_2 are potentially increasing ocean acidity. Current systems are not yet suitable for on ship use so there is significant work required before it can be measured *in-situ* remotely. Phosphate and dissolved oxygen are both important for all living organisms in the ocean, therefore understanding the distribution and concentration both spatially and temporally is important.

All of these sensing platforms will come up against many challenges and will require several microfluidic operations such as transportation, mixing, heating and pumping. These devices will also require readings to be taken, often electrical or optical. One of the main problems these sensing platforms will face is biofouling. When a device is placed in a marine environment, biofilms start to form, it has been shown that these films can have disruptive effects on sensors within a week (Lehaitre et al., 2008). The film is detrimental to marine sensors in more than one way. Clogging of micro channels can occur due to the excessive build up of micro organisms. Of greater effect, the localised environment will be affected by the organisms, either by uptake of chemicals and nutrients or the release of compounds or waste products. This could completely change the composition of the sample you are trying to measure. For optical and electrical sensors, the formation of a biofilm will have severe impacts, either by blocking the light path or by background radiation from fluorescent organisms.

Ultrasonic techniques have been identified as a potential method to assist with two of the challenges faced by the development of chemical sensors. Acoustic radiation forces are not suitable for the direct manipulation of chemicals; however, acoustic streaming is capable of inducing mixing. Mixing is often a problem in

microfluidic devices due to the highly laminar flow, meaning that mixing is predominantly diffusion based. Long fluid channels help resolve this problem so acoustic streaming methods for mixing were not covered in this thesis. Ultrasonic streaming also tends to have high power requirements.

The other use of ultrasonic techniques identified was as a method for reducing biofouling within microfluidic devices. This would be a novel use of the technology and would require improvements in reliability, robustness and repeatability. The acoustic radiation forces generated in a microfluidic device should be well suited to the reduction of biofouling. This is on the assumption that bacteria cells involved in biofouling are of the order of microns in terms of size and have differing properties in terms of density and compressibility compared to their surrounding medium.

1.1.2 µ-Flow Cytometer

It has been estimated that phytoplankton account for over half the world's annual oxygen production. Oxygen is essential to life on earth and so understanding its source and the variables that affect it is vital. To assist with this, the RMST project aims to develop a µ-flow cytometer capable of analysing up to 1000 cells per second. The device will accomplish this through the use of electrical impedance to measure cell size and membrane properties. The device will also use light scattering techniques to speciate the phytoplankton passing through it. This is possible because phytoplankton contain fluorescent pigments in different quantities and types depending on the species.

For a µ-flow cytometer to work there is a requirement for the phytoplankton to be aligned into a beam as they travel through the fluid channel. This allows them to be analysed in a sequential manner through the optical and electrical sensing components. There may also be a need to filter larger particulates from the sample before processing through the µ-flow cytometer. Another useful step in the process could be the concentration of phytoplankton before measurement; if the sample concentration is too low, power will be wasted on the detection equipment that will be underutilised. Further, if sheath flows are required to align the phytoplankton the concentration will be lowered which exasperates the problem. Using sheath flows will also require reservoirs of clean fluid or extra processes to produce clean fluid.

Ultrasonic manipulation techniques should be well suited to the operations required by a µ-flow cytometer for remote *in-situ* oceanographic sensing. Phytoplanktons are expected to be of a size suitable for ultrasonic standing wave techniques and it should be possible to manipulate them using relatively little power.

Even if it is not possible to manipulate phytoplankton using ultrasonic standing wave techniques, filtration operations should still be possible, as other particulates not intended for the µ-flow cytometer would experience the acoustic radiation force.

If phytoplanktons are affected by the acoustic radiation force the number of operations which could be performed for the benefit of a µ-flow cytometer is significant. Firstly, a concentration device could be created that utilises the ultrasonic standing wave technology to move particles towards a surface within a microfluidic device and removes the excess medium. This is a fairly standard use of the technology but has never been achieved outside of a laboratory environment and would be a significant step for the technology. The device would also be required to be built with polymeric materials, as ceramic devices would be too expensive to deploy on the large scale required to fill the gap in data. Ultrasonic standing wave devices have generally been limited to ceramics and transferring the technology to polymers will generate several challenges, in particular the expected lower efficiency in terms of energy propagation through the device.

Perhaps the most useful operation that could be fulfilled by ultrasonic technologies is the alignment of particles within the fluid channel prior to detection. If this could be achieved using ultrasonic techniques this would negate the need for sheath flows. Focussing phytoplankton in one dimension should be achievable in a traditional ceramic style device, but the technology would need to be adapted to achieve this in a polymer device. Two dimensional focussing of particles within a microfluidic channel is possible, but is confined to laboratory environments using ceramic devices. This work will attempt to develop a bulk acoustic wave device in polymers capable to manipulating particles in two-dimensions.

Recent developments in ultrasonic standing wave techniques have utilised surface acoustic waves (SAWs) to manipulate particles in two dimensions into a tight beam along the length of the fluid channel, (Shi et al., 2008). If this technology could be adapted to be used outside of the laboratory in a remote *in-situ* sensor it would be ideal for a µ-flow cytometer. One of the main challenges with this would be the robustness of the device in a varied oceanographic environment. Currently the technology has only been proven using a Polydimethylsiloxane (PDMS) micro channel. For a µ-flow cytometer the technology would be required to work in a more structurally rigid polymer. This will require an in depth understanding of the mechanism involved and the affects the variables would have on the performance of the device. Currently there is no convincing literature on the mechanism involved in the two dimensional manipulation of particles within a surface acoustic wave device.

1.1.3 Research Outputs

The work in this thesis investigates ultrasonic manipulation techniques for remote *in-situ* oceanographic sensing. In particular it develops bulk acoustic wave technology in polymer devices and puts forward a novel method of applying standing waves across a fluid channel that doesn't require an exact half wave within a fluid channel. The work also identifies new manufacturing techniques that are significantly more repeatable and robust than traditional methods. Attempts are made to develop a device capable of focussing particles into a beam within a fluid channel; this was achieved but had a high power requirement. Modelling confirms that this was because of the weak coupling of acoustic energy into the channel parallel to the surface of the transducer.

Further work goes on to use these novel techniques to minimise the formation of biofilms within polymer microfluidic channels. By using a robust image analysis technique it is shown that continuous ultrasonic excitation can reduce the formation of biofilms on surfaces parallel to the transducer. The work also shows a small reduction in the percentage of cells actively respiring in the biofilm present on the surface of polymer devices. The timescales over which these experiments were run is a significant step towards the remote application of the technology. Coupled with the repeatability of the devices and excitation methods, this is a significant improvement on current lab based ultrasonic devices.

The work in this thesis also models a SAW device to better understand the mechanism behind such a device and how it will be affected by changes to the size, materials and fluid. Attempts are made to produce a SAW device to match the modelling with experimental data. It was hoped this would lead to a device capable of working as an oceanographic remote *in-situ* sensor. Unfortunately it was not possible to produce a working device; part of this was due to the design of the device being decided before the project began. The work does identify a mechanism for the two dimensional manipulation of particles within a microfluidic channel due to the application of standing SAWs. This is a novel addition to the understanding of two dimensional particle manipulation in SAW devices.

1.1.4 Conclusions

In this thesis, ultrasonic standing wave techniques have been adapted for use in a marine environment and more specifically have been targeted towards anti-biofilm strategies and to particle focusing for a µ-flow cytometer. The work in this thesis successfully shows that ultrasonic particle manipulation techniques are well suited to

the reduction of biofouling in microfluidic devices. This is a novel use of ultrasonic particle manipulation and it pushes the capabilities of the field in terms of robustness, reliability and repeatability. The polymer devices used differ from the more conventional ceramic half wave type devices. Modelling and experiments have identified some benefits in using polymers such as the ability to fit any fraction of a wavelength into the fluid chamber. This gives non zero forces at the fluid/solid boundary, which is ideal for reducing biofilm formation. The devices are also less sensitive to changes in the properties of the fluid or small changes in the dimensions of the layers.

This thesis also describes a novel manufacturing technique for a bulk acoustic wave device utilising a transparent lithium niobate transducer coupled with transparent indium tin oxide electrodes. Whilst not of direct relevance to an oceanographic sensor, it has the potential to increase the number of operations ultrasonic standing wave techniques could be used for in a laboratory environment. Current devices tend to use opaque lead zirconate titanate which limits the type of microscopy that can be used or requires dyes to be added to samples to enable imaging. A transparent device allows transmission microscopy to be used.

The work on SAWs identifies a potential mechanism for the two dimensional manipulation of particles within a fluid channel. It was not possible to verify this work experimentally however it has given insight into how such a device could be scaled up and adapted for an oceanographic environment. A novel manufacturing technique is showcased that could reduce the time and costs involved with producing large quantities of devices for oceanographic sensing.

Chapter 2 Ultrasonics and Microfluidics

In this thesis, ultrasonic particle manipulation is combined with microfluidic devices with the aim of producing sensors for remote *in-situ* oceanographic sensing. In this chapter the theory detailing the propagation of waves in solids is presented. The equations are derived for bulk acoustic waves and surface acoustic waves. Key information regarding Rayleigh like waves is given and methods for inducing waves are shown. The work goes on to describe the acoustic radiation force. Microfluidic theory is presented and a series of current ultrasonic particle manipulation devices are shown.

2.1 Ultrasonics

Ultrasonics is a wide and varied field covering a whole host of applications from medical diagnostics to non-destructive evaluation (NDE) (Rose, 1999). The following section describes how acoustic waves can propagate through a medium and covers bulk waves, surface waves and interface waves. The equations of motion will be derived for the different wave types and any effects on practical applications will be covered.

2.1.1 Bulk Acoustic Waves

The theory that describes the propagation of waves through a medium is called theory of elasticity. This allows for deformations within the medium unlike rigid body dynamics which would result in a linear acceleration and rotation of the medium. The following section will describe how equations describing the progression of waves through a medium can be obtained and is based on the approach by Kolsky (Kolsky, 1953).

In an unbound isotropic elastic medium only two types of wave can propagate; dilatational and distortional. Particle motion is along the direction of propagation for dilatational waves and is perpendicular to the direction of propagation for distortional waves. These waves are more commonly known as longitudinal and transverse waves respectively (Cheeke, 2002). The stresses acting on the surface of an element of a solid do not necessarily just act normal to the surface, there are likely to be tangential components.

Imagine a set of three dimensional axes, each perpendicular to one another with directions x, y and z, and with normal and tangential stresses acting on each surface of a cube positioned according to these axes. This will lead to 9 possible stress components, of which 6 will be unique; $\sigma_{xx}, \sigma_{yy}, \sigma_{zz}, \sigma_{xy}, \sigma_{xz}$ and σ_{yz} where the first letter denotes the direction of the stress and the second letter the plane upon which it acts.

A point within this cube will be displaced by these stresses and if its original position is x, y, z, then its new position becomes $x + u, y + v, z + w$. Consider a 2nd point close to the 1st point with co-ordinates $x + \delta x, y + \delta y, z + \delta z$ before displacement, and then let the displacement it undergoes be defined as such; $u + \delta u, v + \delta v, w + \delta w$. This allows the following equations to be defined,

$$\delta u = \frac{\partial u}{\partial x}\delta x + \frac{\partial u}{\partial y}\delta y + \frac{\partial u}{\partial z}\delta z,$$
$$\delta v = \frac{\partial v}{\partial x}\delta x + \frac{\partial v}{\partial y}\delta y + \frac{\partial v}{\partial z}\delta z,$$
$$\delta w = \frac{\partial w}{\partial x}\delta x + \frac{\partial w}{\partial y}\delta y + \frac{\partial w}{\partial z}\delta z.$$

Equation 2-1 (a), (b) and (c)

If the following 9 quantities are known the displacement of any point can be found,

$$\frac{\partial u}{\partial x}, \frac{\partial u}{\partial y}, \frac{\partial u}{\partial z}, \frac{\partial v}{\partial x}, \frac{\partial v}{\partial y}, \frac{\partial v}{\partial z}, \frac{\partial w}{\partial x}, \frac{\partial w}{\partial y}, and \frac{\partial w}{\partial z}.$$

Equation 2-2 (a) – (i)

These quantities can be regrouped in the following manner for convenience,

$$\epsilon_{xx} = \frac{\partial u}{\partial x}, \quad \epsilon_{yy} = \frac{\partial v}{\partial y}, \quad \epsilon_{zz} = \frac{\partial w}{\partial z},$$
$$\epsilon_{yz} = \frac{\partial w}{\partial y} + \frac{\partial v}{\partial z}, \quad \epsilon_{zx} = \frac{\partial u}{\partial z} + \frac{\partial w}{\partial x}, \quad \epsilon_{xy} = \frac{\partial v}{\partial x} + \frac{\partial u}{\partial y},$$
$$2\vartheta_x = \frac{\partial w}{\partial y} - \frac{\partial v}{\partial z}, \quad 2\vartheta_y = \frac{\partial u}{\partial z} - \frac{\partial w}{\partial x}, \quad 2\vartheta_z = \frac{\partial v}{\partial x} - \frac{\partial u}{\partial y}.$$

Equation 2-3 (a) – (i)

The first three equations describe small contractions or expansions within the medium. The second three relate to shear strains within medium, continuing the suffix notation mentioned before. The final three correspond not to a deformation but to a rotation.

Of these nine quantities the first are the components of strain. If the last three quantities are zero the deformation is irrotational and is therefore in a pure strain condition. It is possible to write the components of strain in a matrix where the elastic constants of the material become the coefficients

$$\begin{bmatrix}\sigma_{xx}\\ \sigma_{yy}\\ \sigma_{zz}\\ \sigma_{yz}\\ \sigma_{zx}\\ \sigma_{xy}\end{bmatrix} = \begin{bmatrix}c_{11} & c_{12} & c_{13} & c_{14} & c_{15} & c_{16}\\ c_{21} & c_{22} & c_{23} & c_{24} & c_{25} & c_{26}\\ c_{31} & c_{32} & c_{33} & c_{34} & c_{35} & c_{36}\\ c_{41} & c_{42} & c_{43} & c_{44} & c_{45} & c_{46}\\ c_{51} & c_{52} & c_{53} & c_{54} & c_{55} & c_{56}\\ c_{61} & c_{62} & c_{63} & c_{64} & c_{65} & c_{66}\end{bmatrix}\begin{bmatrix}\epsilon_{xx}\\ \epsilon_{yy}\\ \epsilon_{zz}\\ \epsilon_{yz}\\ \epsilon_{zx}\\ \epsilon_{zy}\end{bmatrix}.$$

Equation 2-4

This gives 36 constants for any material; however, it can be shown that c_{ab} is identical to c_{ba}, which leaves 21 constants. For a completely aeolotropic material all 21 of these constants need to be known to define the elastic properties of the material. Many materials have some symmetry and in an isotropic solid only two independent constants remain, which are known as *Lamé's* constants,

$$\begin{bmatrix}\sigma_{xx}\\ \sigma_{yy}\\ \sigma_{zz}\\ \sigma_{yz}\\ \sigma_{zx}\\ \sigma_{xy}\end{bmatrix} = \begin{bmatrix}c_{11} & c_{12} & c_{13} & 0 & 0 & 0\\ c_{21} & c_{22} & c_{23} & 0 & 0 & 0\\ c_{31} & c_{32} & c_{33} & 0 & 0 & 0\\ 0 & 0 & 0 & c_{44} & 0 & 0\\ 0 & 0 & 0 & 0 & c_{55} & 0\\ 0 & 0 & 0 & 0 & 0 & c_{66}\end{bmatrix}\begin{bmatrix}\epsilon_{xx}\\ \epsilon_{yy}\\ \epsilon_{zz}\\ \epsilon_{yz}\\ \epsilon_{zx}\\ \epsilon_{zy}\end{bmatrix}.$$

Equation 2-5

Where the constants are defined by the following;

$$c_{12} = c_{13} = c_{21} = c_{23} = c_{31} = c_{32} = \lambda_L,$$
$$c_{44} = c_{55} = c_{66} = \mu,$$
$$c_{11} = c_{22} = c_{33} = \lambda_L + 2\mu,$$

Equation 2-6 (a), (b) and (c)

which leads to the following equations describing stress in the medium,

$$\sigma_{xx} = \lambda_L \Delta + 2\mu\epsilon_{xx},$$
$$\sigma_{yy} = \lambda_L \Delta + 2\mu\epsilon_{yy},$$
$$\sigma_{zz} = \lambda_L \Delta + 2\mu\epsilon_{zz},$$
$$\sigma_{yz} = \mu\epsilon_{yz},$$
$$\sigma_{zx} = \mu\epsilon_{zx},$$
$$\sigma_{xy} = \mu\epsilon_{xy},$$

Equation 2-7 (a) – (f)

where $\Delta = \epsilon_{xx} + \epsilon_{yy} + \epsilon_{zz}$. This is called the volume strain or dilation.

For ease, another three terms, Young's modulus, E, Poisson's ratio ν and Bulk modulus K, will be introduced, each of which can be described in terms of λ_L and μ. Firstly, imagine a 1 dimensional stress is applied parallel to the x axis, the first three equations become

$$\sigma_{xx} = (\lambda_L + 2\mu)\epsilon_{xx} + \lambda_L(\epsilon_{yy} + \epsilon_{zz}),$$
$$0 = (\lambda_L + 2\mu)\epsilon_{yy} + \lambda_L(\epsilon_{xx} + \epsilon_{zz}),$$
$$0 = (\lambda_L + 2\mu)\epsilon_{zz} + \lambda_L(\epsilon_{xx} + \epsilon_{yy}).$$

Equation 2-8 (a), (b) and (c)

These can be solved to show that

$$\epsilon_{xx} = \frac{\lambda_L + \mu}{\mu(3\lambda_L + 2\mu)}\sigma_{xx}, \qquad \epsilon_{yy} = \epsilon_{zz} = -\frac{\lambda_L}{2\mu(3\lambda_L + 2\mu)}\sigma_{xx}.$$

Equation 2-9

Young's modulus is a measure of a material's stiffness and is defined as

$$E = \frac{\sigma_{xx}}{\epsilon_{xx}} = \frac{\mu(3\lambda_L + 2\mu)}{\lambda_L + \mu}.$$

Equation 2-10

Poisson's ratio is a measure of the contraction of a specimen in one direction compared to its expansion in another direction,

$$\nu = -\frac{\epsilon_{yy}}{\epsilon_{xx}} = \frac{\lambda_L}{2(\lambda_L + \mu)}.$$

Equation 2-11

Bulk modulus is a measure of the fractional change in volume should a uniform hydrostatic pressure be applied, therefore $\sigma_{xx} = \sigma_{yy} = \sigma_{zz} = -P(say)$, and shear in the object is equal to zero. From here it can be shown that

$$\epsilon_{xx} = \epsilon_{yy} = \epsilon_{zz} = -\frac{P}{3\lambda_L + 2\mu}.$$

Equation 2-12

Knowing that volume dilation is given by $\Delta = \epsilon_{xx} + \epsilon_{yy} + \epsilon_{zz}$ the following can be deduced about K

$$K = \frac{P}{\Delta} = \frac{-(3\lambda_L + 2\mu)\epsilon_{xx}}{-3\epsilon_{xx}} = \lambda_L + \frac{2}{3}\mu.$$

Equation 2-13

Shear modulus, or μ, is the ratio between shear stress and shear strain and is given by the last equations of Equation 2-7. Now these have all been defined, it is possible to determine the equations of motion in an elastic medium. Firstly, imagine an infinitesimally small cube with sides parallel to the defined axes. Now consider the variations in stress across all 6 sides, which in the x direction will be

$$\left(\sigma_{xx} + \frac{\partial \sigma_{xx}}{\partial x}\delta x\right)\delta y\delta z - \sigma_{xx}\delta y\delta z + \left(\sigma_{xy} + \frac{\partial \sigma_{xy}}{\partial y}\delta y\right)\delta x\delta z - \sigma_{xy}\delta x\delta z$$
$$+ \left(\sigma_{xz} + \frac{\partial \sigma_{xz}}{\partial z}\delta z\right)\delta x\delta y - \sigma_{xz}\delta x\delta y,$$

Equation 2-14

this can be simplified to

$$\left(\frac{\partial \sigma_{xx}}{\partial x} + \frac{\partial \sigma_{xy}}{\partial y} + \frac{\partial \sigma_{xz}}{\partial z}\right)\delta x\delta y\delta z,$$

Equation 2-15

when coupled with Newton's second law of motion, this will be equal to

$$(\rho\delta x\delta y\delta z)\frac{\partial^2 u}{\partial t^2}.$$

Equation 2-16

Where ρ equals density and t equals time. This neglects body forces acting on the solid such as gravity. Once simplified and repeated for v and w the following is yielded

$$\rho\frac{\partial^2 u}{\partial t^2} = \frac{\partial \sigma_{xx}}{\partial x} + \frac{\partial \sigma_{xy}}{\partial y} + \frac{\partial \sigma_{xz}}{\partial z},$$
$$\rho\frac{\partial^2 v}{\partial t^2} = \frac{\partial \sigma_{yx}}{\partial x} + \frac{\partial \sigma_{yy}}{\partial y} + \frac{\partial \sigma_{yz}}{\partial z},$$
$$\rho\frac{\partial^2 w}{\partial t^2} = \frac{\partial \sigma_{zx}}{\partial x} + \frac{\partial \sigma_{zy}}{\partial y} + \frac{\partial \sigma_{zz}}{\partial z}.$$

Equation 2-17 (a), (b) and (c)

These equations can now be coupled with the isotropic elasticity constants found earlier, see Equation 2-7.

$$\rho\frac{\partial^2 u}{\partial t^2} = \frac{\partial}{\partial x}(\lambda_L \Delta + 2\mu\varepsilon_{xx}) + \frac{\partial}{\partial y}(\mu\varepsilon_{xy}) + \frac{\partial}{\partial z}(\mu\varepsilon_{xz}),$$
$$\rho\frac{\partial^2 v}{\partial t^2} = \frac{\partial}{\partial y}(\lambda_L \Delta + 2\mu\varepsilon_{yy}) + \frac{\partial}{\partial x}(\mu\varepsilon_{yx}) + \frac{\partial}{\partial z}(\mu\varepsilon_{yz}),$$
$$\rho\frac{\partial^2 w}{\partial t^2} = \frac{\partial}{\partial z}(\lambda_L \Delta + 2\mu\varepsilon_{zz}) + \frac{\partial}{\partial y}(\mu\varepsilon_{zy}) + \frac{\partial}{\partial x}(\mu\varepsilon_{zx}).$$

Equation 2-18 (a), (b) and (c)

Using Equation 2-3 (a) – (i) allows Equation 2-18 (a) to be re-written like so,

$$\rho\frac{\partial^2 u}{\partial t^2} = (\lambda_L + \mu)\frac{\partial \Delta}{\partial x} + \mu\nabla^2 u.$$

Equation 2-19 (a)

Similarly for Equation 2-18 (b) and (c),

$$\rho\frac{\partial^2 v}{\partial t^2} = (\lambda_L + \mu)\frac{\partial \Delta}{\partial y} + \mu\nabla^2 v,$$
$$\rho\frac{\partial^2 w}{\partial t^2} = (\lambda_L + \mu)\frac{\partial \Delta}{\partial z} + \mu\nabla^2 w,$$

Equation 2-19 (b) and (c)

where ∇^2 is the Laplace operator. These are the equations of motion for an isotropic solid without body forces and will be manipulated to show the two types of wave propagation possible in an unbound solid. To do this, Equation 2-19 (a) is differentiated w.r.t.x, and Equation 2-19 (b) and (c) are differentiated w.r.t.y and z respectively before adding

$$\rho \frac{\partial^2 \Delta}{\partial t^2} = (\lambda_L + 2\mu)\nabla^2 \Delta.$$

Equation 2-20

This shows that the velocity of propagation through the material is equal to

$$C_A = \left(\frac{\lambda_L + 2\mu}{\rho}\right)^{\frac{1}{2}},$$

Equation 2-21

for a dilatational wave. A similar process can be carried out whereby Equation 2.19 (b) and (c) are eliminated by differentiating w.r.t.y and z respectively and subtracting gives

$$\rho \frac{\partial^2}{\partial t^2}\left(\frac{\partial w}{\partial y} - \frac{\partial v}{\partial z}\right) = \mu\nabla^2 \left(\frac{\partial w}{\partial y} - \frac{\partial v}{\partial z}\right).$$

Equation 2-22

This reduces to the following using Equation 2-3 (g)

$$\rho \frac{\partial^2}{\partial t^2}\vartheta_x = \mu\nabla^2 \vartheta_x.$$

Equation 2-23

Similar equations can be derived for ϑ_y and ϑ_z. The velocity of propagation for a distortional wave will be equal to

$$C_B = \left(\frac{\mu}{\rho}\right)^{\frac{1}{2}}.$$

Equation 2-24

The speeds at which dilatational waves and distortional waves propagate through a medium have been shown, it will now be shown that waves can propagate through a solid with either of these velocities. If dilation is equal to zero then Equation 2-19 (a) becomes

$$\rho \frac{\partial^2 u}{\partial t^2} = \mu \nabla^2 u,$$

Equation 2-25

with similar equations for v and w. It is possible to create a set of conditions that causes rotation to vanish, using a potential function, Φ,

$$u = \frac{\partial \Phi}{\partial x}, \qquad v = \frac{\partial \Phi}{\partial y}, \qquad w = \frac{\partial \Phi}{\partial z}.$$

Equation 2-26

Which means that $\Delta = \nabla^2 \Phi$ and $\frac{\partial \Delta}{\partial x} = \nabla^2 u$. Substituting into Equation 2-19 (a) yields the following,

$$\rho \frac{\partial^2 u}{\partial t^2} = (\lambda_L + 2\mu) \nabla^2 u,$$

Equation 2-27

with similar equations for v and w. This shows that waves involving no rotation travel with velocity

$$C_A = \left(\frac{\lambda_L + 2\mu}{\rho} \right)^{\frac{1}{2}},$$

Equation 2-21 (repeat)

whilst waves propagating with no dilation travel through the medium with velocity

$$C_B = \left(\frac{\mu}{\rho} \right)^{\frac{1}{2}}.$$

Equation 2-24 (repeat)

The last thing to do is show that waves propagating through a medium must travel with one or the other of these velocities. To do this we must first consider a plane wave propagating in the x direction, since the material is isotropic this is suitable.

Assume its velocity of propagation is c then the displacements u, v and w will be functions of a single parameter $\Psi = x - ct$. This yields the following

$$\frac{\partial^2 u}{\partial t^2} = c^2 \frac{\partial^2 u}{\partial \Psi^2}, \qquad \frac{\partial^2 v}{\partial t^2} = c^2 \frac{\partial^2 v}{\partial \Psi^2}, \qquad \frac{\partial^2 w}{\partial t^2} = c^2 \frac{\partial^2 w}{\partial \Psi^2},$$
$$\frac{\partial^2 u}{\partial x^2} = \frac{\partial^2 u}{\partial \Psi^2}, \qquad \frac{\partial^2 v}{\partial x^2} = \frac{\partial^2 v}{\partial \Psi^2}, \qquad \frac{\partial^2 w}{\partial x^2} = \frac{\partial^2 w}{\partial \Psi^2}.$$

Equation 2-28 (a) – (f)

Any differential coefficients with respect to y or z will be equal to zero and these equations can be substituted into Equation 2-19 (a), (b) and (c),

$$\rho c^2 \frac{\partial^2 u}{\partial \Psi^2} = (\lambda_L + \mu) \frac{\partial^2 u}{\partial \Psi^2} + \mu \frac{\partial^2 u}{\partial \Psi^2} = (\lambda_L + 2\mu) \frac{\partial^2 u}{\partial \Psi^2},$$
$$\rho c^2 \frac{\partial^2 v}{\partial \Psi^2} = \mu \frac{\partial^2 v}{\partial \Psi^2},$$
$$\rho c^2 \frac{\partial^2 w}{\partial \Psi^2} = \mu \frac{\partial^2 w}{\partial \Psi^2}.$$

Equation 2-29

These equations can only be satisfied in two ways, either

$$c^2 = \frac{\lambda_L + 2\mu}{\rho}, \qquad \frac{\partial^2 v}{\partial \Psi^2} = \frac{\partial^2 w}{\partial \Psi^2} = 0.$$

Equation 2-30

The other possibility is

$$c^2 = \frac{\mu}{\rho}, \qquad \frac{\partial^2 u}{\partial \Psi^2} = 0.$$

Equation 2-31

The former case is classed as longitudinal waves where motion is confined to the direction of propagation and the latter is deemed transverse waves where motion is perpendicular to the direction of propagation. These wave speeds are denoted by the terms C_L and C_T respectively. As expected, transverse wave speed only depends on the shear modulus of the medium. Perhaps less intuitively, the longitudinal wave speed depends on the bulk modulus and the shear modulus of the medium. This is because

as the wave propagates there is a change in volume of the element which requires a change in the shape of the element, thus the elements resistance to shear is involved.

2.1.1.1 Waves at Boundaries

It is important to understand the interactions acoustic waves have at interfaces, whether it be *solid-solid* interfaces or *solid-fluid* interfaces. The most significant case is for plane waves approaching normal to a boundary. In such a case some of the wave will be transmitted through the boundary and some of the wave will be reflected. When an incoming wave, $_{(I)}$, reaches a boundary it will be transmitted, $_{(TR)}$, and reflected, $_{(R)}$. Acoustic impedance is commonly used for such equations and for this work it shall be denoted by Z, based on the density and the longitudinal wave speed of each medium. The subscripts $_{(1)}$ and $_{(2)}$ will be used to denote the initial medium and the second medium. To accurately describe the behaviour of waves at boundaries continuity of pressure and displacement must be assumed (Cheeke, 2002). The following equations describe the coefficient of transmitted pressure,

$$\alpha_{TR} = \frac{2Z_2}{Z_1 + Z_2} = \frac{P_{TR}}{P_I},$$

Equation 2-32

and the coefficient of reflected pressure,

$$\alpha_R = \frac{Z_2 - Z_1}{Z_1 + Z_2} = \frac{P_R}{P_I}.$$

Equation 2-33

If $Z_1 \gg Z_2$, most of the pressure will be reflected, If $Z_1 \cong Z_2$ then most of the energy will be transmitted. This is called impedance matching and corresponds to the impedance matching of electric circuits (Turner and Pretlove, 1991). Other important coefficients are the acoustic energy transmission and reflection coefficients, when the wave approaches perpendicular to the boundary these can be obtained simply from the definition of acoustic intensity,

$$I = \frac{P^2}{2Z},$$

Equation 2-34

which leads to the following for the transmission and reflection intensity coefficients,

$$\frac{I_{TR}}{I_I} = \frac{Z_1}{Z_2}|\alpha_{TR}|^2,$$

Equation 2-35

and

$$\frac{I_R}{I_I} = |\alpha_R|^2.$$

Equation 2-36

It can also be shown that energy is conserved before and after the reflection, $I_I = I_R + I_{TR}$. This theory can be extended to layers between two mediums, this is a common practice so that energy can be transferred between two mediums of differing acoustic impedance (Brekhovskikh, 1957). When a matching layer is needed it is often $\lambda/4$ thick which allows for the perfect transmission of energy from two mismatched materials. The reflected pressure is given by the following,

$$\alpha_R = \frac{Z_2^2 - Z_1 Z_3}{Z_2^2 + Z_1 Z_3}.$$

Equation 2-37

This gives the condition that $\alpha_R = 0$ when $Z_2 = \sqrt{Z_1 Z_3}$. This means that perfect transmission can be achieved by selecting a material with an acoustic impedance which when squared is equal to the product of the two surrounding mediums. This theory can be furthered to describe waves approaching a boundary at an angle, however, for the purpose of this work it is enough to consider only waves approaching normally.

2.1.1.2 Standing Waves

Much of the work in this thesis is based on standing waves rather than travelling waves. These occur when a wave interferes with a wave of the same frequency travelling in the opposite direction. For bulk acoustic waves this is usually through the reflection of a wave at a boundary, whilst for surface acoustic waves this is usually from two separate counter propagating waves. Standing waves produce static patterns of pressure nodes and antinodes which are used to manipulate particles. A pure standing wave would result in no propagation of energy (Cheeke, 2002).

Pressure and velocity are in phase quadrature for a travelling wave, so it follows that node positions for standing waves will also be in quadrature. For a rigid boundary, pressure will be at a maximum and velocity will be at a minimum. For a free boundary, pressure will be at a minimum whilst velocity will be at a maximum.

2.1.2 Surface Acoustic Waves

The theory of surface waves was first discussed by Lord Rayleigh in the late 19th century (Rayleigh, 1885). It was shown that their effect decreased rapidly with depth and that their velocity of propagation is smaller than that of body waves (Kolsky, 1953). As these waves spread in only two dimensions their amplitude decays more slowly with distance than other types of elastic waves. At the time they were of importance in seismology but have since found use at a significantly smaller scale, such as NDE and in microfluidics (Rose, 1999, Shi et al., 2008), they also have significant use in electronic filters and sensors (Oliner et al., 1978). Rayleigh waves are a combination of longitudinal motion and transverse motion confined to the surface of an elastic medium, penetrating only to about one wavelength in depth. Surface waves on a solid are similar to surface waves on a liquid, in that particle motion is elliptical; however there are differences in direction and restoring forces. In solids it is elastic forces while in liquids it is gravity and surface tension that supply that restoring force (Kolsky, 1953).

The use of surface waves in microfluidic applications has grown appreciably in the past decade and the following sections will describe the governing equations and the different types of surface waves. Lamb waves will not be considered here, as they are currently not of use in microfluidic applications; however, it can be shown that a Lamb wave transforms into a Rayleigh wave as the thickness of the substrate increases (Farnell and Adler, 1972). Other Rayleigh like waves such as leaky Rayleigh, Scholte, interface and Stoneley waves will be presented and key information regarding their use in particle manipulation techniques will be discussed.

2.1.2.1 Rayleigh Waves

In an unbounded isotropic solid only two types of elastic wave can propagate; however, surface and interface waves exist at free boundaries and interfaces respectively, allowing Rayleigh waves to be used to manipulate particles and fluids when used in a microfluidic device.

The equations of motion used to describe longitudinal and transverse waves in an isotropic unbounded medium can be manipulated to generate equations detailing the displacements of a surface wave propagating along a half space. Rotation phenomena can be decoupled from dilation phenomena and then stress free boundary

conditions can be used to solve the resulting equations. This will define the Rayleigh wave number in terms of longitudinal and transverse wave numbers.

The equation of motion for an unbound isotropic elastic solid in which body forces are absent can be written as (Kolsky, 1953):

$$\rho \frac{\partial^2 u}{\partial t^2} = (\lambda_L + \mu) \frac{\partial \Delta}{\partial x} + \mu \nabla 2u,$$

Equation 2-38

where u defines displacement in the x direction. Similarly v and w are displacements in the *y* and *z* directions respectively. ∇^2 is the Laplace operator whilst ρ, λ_L and μ define the density, Lamé's constant and shear modulus of the medium. Δ, see Equation 2-40, defines the volume strain of the medium. As an isotropic, unbounded solid is being considered, similar expressions can be written for v and w. The solutions to these equations define the longitudinal wave speed ($_L$) and transverse, or shear, wave speed ($_T$) in the x direction:

$$C_L^2 = \frac{\lambda_L + 2\mu}{\rho}, \qquad C_T^2 = \frac{\mu}{\rho}.$$

Equation 2-39

Following the approach of Kolsky (Kolsky, 1953) the same equations will be used to generate the equations of motion for a surface wave propagating in the x direction on a half space. Take z to be positive towards the interior of the half space and make the xy plane the free boundary of that half space. The wave will be polarized in the xz plane, so there are no displacements in the y direction, see Figure 2-1.

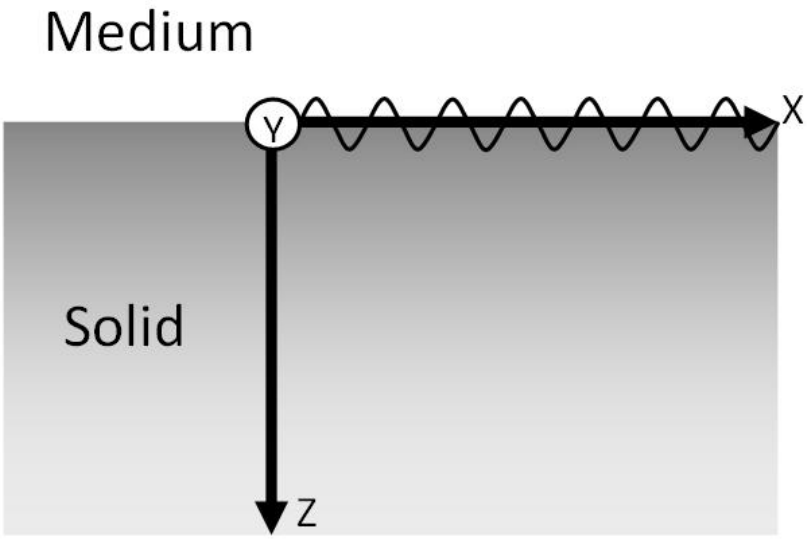

Figure 2-1 A schematic of a surface wave propagating along the xy plane of a half space. Reproduced from (Gedge and Hill, 2012) with permission from The Royal Society of Chemistry.

This leads to the following equations describing the volume strain, or dilation Δ of the medium,

$$\Delta = \frac{\partial u}{\partial x} + \frac{\partial w}{\partial z},$$

Equation 2-40

and the rotation ϑ_y in the xz plane

$$\vartheta_y = \frac{\partial u}{\partial z} - \frac{\partial w}{\partial x}.$$

Equation 2-41

From here it is possible to define two scalar functions $\boldsymbol{\varphi}$ and $\boldsymbol{\psi}$ so that dilation and rotation effects can be decoupled

$$u = \frac{\partial \varphi}{\partial x} + \frac{\partial \psi}{\partial z}, \qquad w = \frac{\partial \varphi}{\partial z} - \frac{\partial \psi}{\partial x}.$$

Equation 2-42 (a) and (b)

This allows for dilation and rotation to be defined as $\nabla^2\varphi$ and $\nabla^2\psi$ respectively. By substituting Equation 2-42 (a) and (b) into Equation 2-38 it is seen that the equations of motion for u and w are satisfied given that

$$\frac{\partial^2\varphi}{\partial t^2} = \frac{\lambda_L + 2\mu}{\rho}\nabla^2\varphi = C_{\mathrm{L}}^2\nabla^2\varphi, \qquad \frac{\partial^2\psi}{\partial t^2} = \frac{\mu}{\rho}\nabla^2\psi = C_{\mathrm{T}}^2\nabla^2\psi.$$

Equation 2-43 (a) and (b)

Now consider a sinusoidal wave of angular frequency ω and wave number k propagating in the x direction and look for solutions of φ and ψ of the form

$$\varphi = F(z)\, e^{\mathrm{i}(\omega t - kx)}, \qquad \psi = G(z) e^{\mathrm{i}(\omega t - kx)}.$$

Equation 2-44 (a) and (b)

These trial solutions can be substituted into Equation 2-43 (a) and (b) which after re-arranging give the following

$$\frac{\partial^2}{\partial z^2}F(z) - (k^2 - k_{\mathrm{L}}{}^2)F(z) = 0, \qquad \frac{\partial^2}{\partial z^2}G(z) - (k^2 - k_{\mathrm{T}}{}^2)G(z) = 0,$$

Equation 2-45 (a) and (b)

where k_{L} and k_{T} are the longitudinal and transverse wave numbers respectively. The longitudinal and transverse wave numbers can be expressed in the following format:

$$k_{\mathrm{L}} = \frac{\omega}{C_{\mathrm{L}}}, \qquad k_{\mathrm{T}} = \frac{\omega}{C_{\mathrm{T}}}.$$

Equation 2-46 (a) and (b)

Hence:

$$\frac{k_{\mathrm{L}}^2}{k_{\mathrm{T}}^2} = \frac{\mu}{\lambda_L + 2\mu} = \frac{1-2\nu}{2-2\nu} = \alpha_1{}^2,$$

Equation 2-47

where in the third expression we have introduced the Poisson's ratio given by

$$\nu = \frac{\lambda_L}{2(\lambda_L + \mu)}.$$

Equation 2-48

Hence the longitudinal wave number can be expressed as the product of the transverse wave number (k_T) and a function of Poisson's ratio (α_1)

$$k_\mathrm{L} = \alpha_1 k_\mathrm{T}\,.$$

Equation 2-49

It is known that $k_\mathrm{L}^2 < k_\mathrm{T}^2$ and it is assumed that $k_\mathrm{T}^2 < k^2$ (this will be confirmed later). To determine the dispersion relation of omega in terms of k, we seek solutions of Equation 2-45 (a) and (b) of the form

$$F(z) = A\mathrm{e}^{(-\gamma_\mathrm{L} z)} + A'\mathrm{e}^{(\gamma_\mathrm{L} z)}, \qquad G(z) = B\mathrm{e}^{(-\gamma_\mathrm{T} z)} + B'\mathrm{e}^{(\gamma_\mathrm{T} z)},$$

Equation 2-50 (a) and (b)

where $\gamma_\mathrm{L}^2 = k^2 - k_\mathrm{L}^2$ for the *longitudinal-Rayleigh* combination and $\gamma_\mathrm{L}^2 = k^2$-$k_\mathrm{T}^2$ for the *transverse-Rayleigh* combination and where A, B, A' and B' are constants. The A' and B' components of these equations are physically unrealistic as they would lead to an increase in displacement amplitude with increasing depth, z. This leads to the following equations describing φ and ψ

$$\varphi = A\mathrm{e}^{(-\gamma_\mathrm{L} z)}\mathrm{e}^{\mathrm{i}(\omega t - kx)}, \qquad \psi = B\mathrm{e}^{(-\gamma_\mathrm{T} z)}\mathrm{e}^{\mathrm{i}(\omega t - kx)}.$$

Equation 2-51 (a) and (b)

Boundary conditions can now be applied that allow the elimination of A and B, which ultimately leads to the determination of the displacements in the x and z directions. Plane stress and shear stress will be equal to zero at the free surface, i.e. when z is equal to zero. For plane stress:

$$\sigma_{zz} = \lambda_L \Delta + 2\mu \frac{\partial w}{\partial z},$$

Equation 2-52

which can be expressed in terms of φ and ψ:

$$\sigma_{zz} = (\lambda_L + 2\mu)\frac{\partial^2\varphi}{\partial z^2} + \lambda\frac{\partial^2\varphi}{\partial x^2} - 2\mu\frac{\partial^2\psi}{\partial x\partial z}.$$

Equation 2-53

Inserting the components of Equation 2-51 (a) and (b) yields for z equals zero:

$$A[(\lambda_L + 2\mu)\gamma_L + \lambda k^2] - 2\mu B i\gamma_T k = 0.$$

Equation 2-54

A similar approach is then taken for shear stress in the half space

$$\sigma_{zx} = \mu\left(\frac{\partial u}{\partial z} + \frac{\partial w}{\partial x}\right),$$

Equation 2-55

which again can be expressed in terms of φ and ψ

$$\sigma_{zx} = \mu\left(2\frac{\partial^2\varphi}{\partial x\partial z} - \frac{\partial^2\psi}{\partial x^2} + \frac{\partial^2\psi}{\partial z^2}\right).$$

Equation 2-56

Once again inserting the decaying components of Equation 2-50 (a) and (b) yields for z equals zero

$$2i\gamma_L kA + (\gamma_T{}^2 + k^2)B = 0.$$

Equation 2-57

Equation 2-54 and Equation 2-57 can be combined to eliminate A and B, yielding the following:

$$4\mu\gamma_L\gamma_T k^2 = \left[(\lambda_L + 2\mu)\gamma_L^2 - \lambda_L k^2\right]\left(\gamma_T^2 + k^2\right).$$

Equation 2-58

Squaring both sides of the equation and inserting expressions for γ_L and γ_T yields:

$$16\left(1 - \frac{k_L^2}{k^2}\right)\left(1 - \frac{k_T^2}{k^2}\right) = \left[2 - \frac{(\lambda_L + 2\mu)}{\mu}\frac{k_L^2}{k^2}\right]^2\left(2 - \frac{k_T^2}{k^2}\right)^2.$$

Equation 2-59

Using Equation 2-49 this expression can be written as

$$16\left(1-\frac{{\alpha_1}^2 k_{\mathrm{T}}^2}{k^2}\right)\left(1-\frac{k_{\mathrm{T}}^2}{k^2}\right)=\left(2-\frac{k_{\mathrm{T}}^2}{k^2}\right)^4.$$

Equation 2-60

Expanding and replacing k_{T}/k with s yields

$$s^6-8s^4+(24-16{\alpha_1}^2)s^2+16{\alpha_1}^2-16=0.$$

Equation 2-61

If the Poisson's ratio of the half space is known this can be solved numerically and used to find the Rayleigh wave speed, with the following

$$s=\frac{k_{\mathrm{T}}}{k}=\frac{\omega}{kC_{\mathrm{T}}}.$$

Equation 2-62

The Rayleigh wave speed has been defined as $C_{\mathrm{R}}=\omega/k$, meaning that $s=C_{\mathrm{R}}/C_{\mathrm{T}}$. The velocity of propagation is thus independent of the frequency and the waves are therefore non dispersive. The velocity of the wave depends solely on the elastic constants of the material. The rate at which the wave amplitude reduces with the depth z depends on the values of the factors γ_{L} and γ_{T} which are given by:

$$\frac{\gamma_{\mathrm{L}}^2}{k^2}=1-\alpha_1^2 s^2,\qquad \frac{\gamma_{\mathrm{T}}^2}{k^2}=1-s^2.$$

Equation 2-63 (a) and (b)

If $\nu > 0.263$ there are two complex conjugate roots and one real root. If $\nu \leq 0.263$ then there will be three real roots (Rose, 1999); however, only one of these roots will be realistic. The change of amplitude with depth for a Rayleigh wave can be calculated from:

$$u_{\mathrm{R}}=\frac{\partial\varphi}{\partial x}+\frac{\partial\psi}{\partial z}=-(Aike^{-\gamma_{\mathrm{L}}z}+B\gamma_{\mathrm{T}}e^{-\gamma_{\mathrm{T}}z})e^{[i(\omega t-kx)]},$$

Equation 2-64

$$w_{\mathrm{R}} = \frac{\partial \varphi}{\partial z} - \frac{\partial \psi}{\partial x} = -(A\gamma_{\mathrm{L}} e^{-\gamma_{\mathrm{L}} z} - Bike^{-\gamma_{\mathrm{T}} z}) e^{[\mathrm{i}(\omega t - kx)]}.$$

Equation 2-65

These reduce to the following if the real parts are taken and B is substituted for A:

$$u_R = Ak\left(e^{-\gamma_L z} - \frac{2\gamma_L \gamma_T}{(\gamma_T^2 + k^2)} e^{-\gamma_T z}\right) sin(\omega t - kx),$$

Equation 2-66

$$w_R = A\gamma_L\left(e^{-\gamma_L z} - \frac{2k^2}{(\gamma_T^2 + k^2)} e^{-\gamma_T z}\right) cos(\omega t - kx).$$

Equation 2-67

The rate at which the amplitude of displacement along the direction of propagation changes with depth depends on the factors:

$$u_{\check{\mathrm{R}}} = e^{-\gamma_L z} - \frac{2\gamma_L \gamma_T}{(\gamma_T^2 + k^2)} e^{-\gamma_T z},$$

Equation 2-68

$$w_{\check{\mathrm{R}}} = e^{-\gamma_{\mathrm{L}} z} - \frac{2k^2}{(\gamma_{\mathrm{T}}^2 + k^2)} e^{-\gamma_{\mathrm{TR}} z}.$$

Equation 2-69

Displacement in the x (horizontal) direction decreases rapidly as z increases; this can be seen in Figure 2-2 which shows an example of displacements as a function of depth. The functions are normalised against the amplitude of the motion perpendicular to the propagation direction at the surface. At a depth of about z/λ = 0.2 the displacement in the x direction passes through zero, and changes polarity. Movement perpendicular to the surface, i.e. in the z direction, increases slightly before reaching a maximum at a depth of about 0.076 wavelengths and then falls away but does not change polarity.

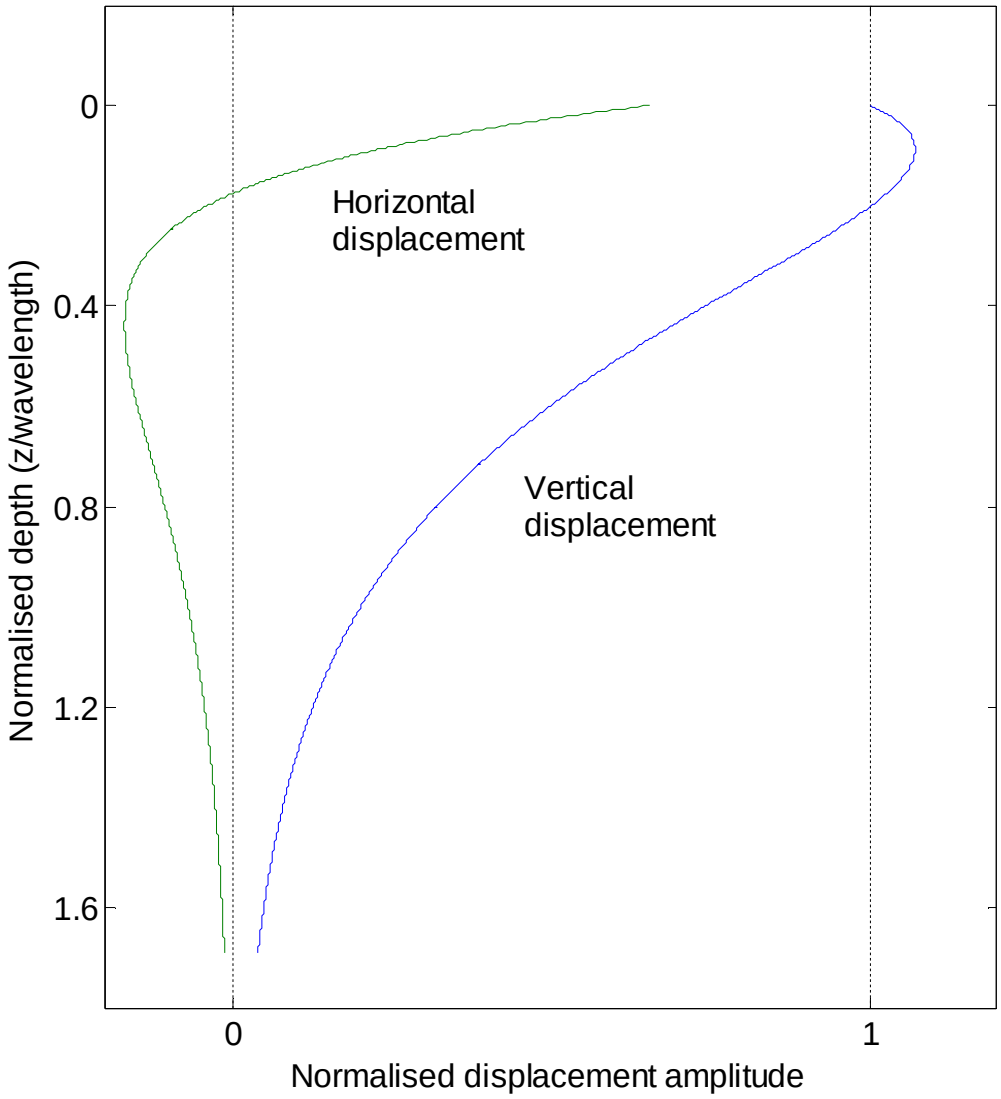

Figure 2-2 Displacement amplitudes for a Rayleigh wave as a function of depth for an example isotropic material. Green represents motion in the x or horizontal direction. Blue represents motion in the z or vertical direction. Reproduced from (Gedge and Hill, 2012) with permission from The Royal Society of Chemistry.

From Equation 2-66 and Equation 2-67, it can be seen that the displacements u and w, are functions of $sine$ and $cosine$ respectively. From this it can be deduced that the motion of particles is rotational about the y axis, rather than traversing back and forth along a curved path. This can be seen in Figure 2-3 which shows the paths of particles (arbitrary amplitude) at depths corresponding to Figure 2-2.

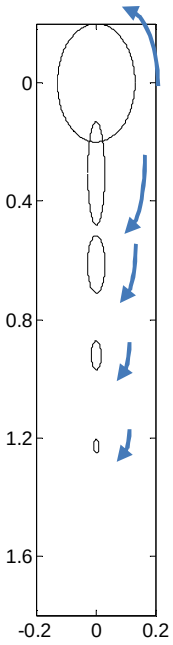

Figure 2-3 Typical elliptical particle motion for different depths. The top ellipse will rotate in the opposite direction to the lower ellipses. Reproduced from (Gedge and Hill, 2012) with permission from The Royal Society of Chemistry.

Particle motion can be thought of as planes of elliptical motion, whose shape and phase at any given time depends upon the depth. The motion is anticlockwise near the surface but reverses to a clockwise motion below the zero crossing of the *u* velocity component. An alternative, simpler approximation for the speed of Rayleigh waves (i.e. the root of Equation 2-61), which expresses s solely in terms of Poisson's ratio, is quoted by (Viktorov, 1967).

$$s = \frac{0.87 + 1.12\nu}{1 + \nu}.$$

Equation 2-70

Thus as ν varies from 0 up to 0.5, C_R varies from $0.87C_T$ to $0.96C_T$. This is shown in Figure 2-4

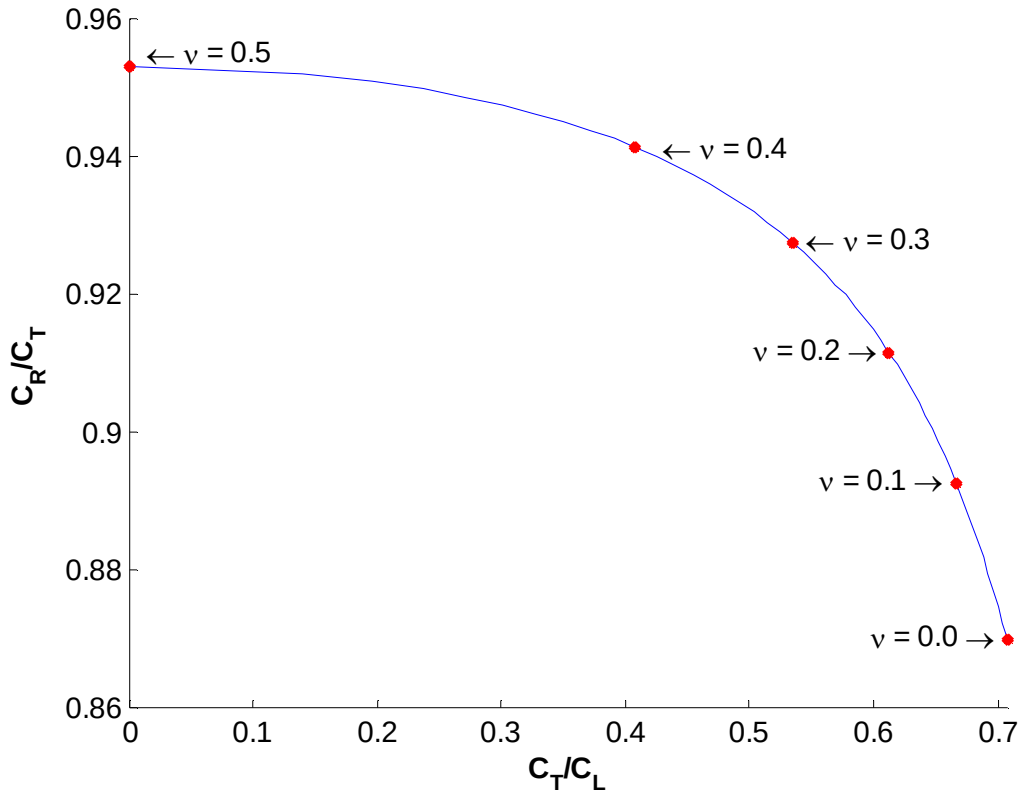

Figure 2-4 Variation in the ratio C_R/C_T as function of C_T/C_L. Values of Poisson's ratio are marked along the curve. Reproduced from (Gedge and Hill, 2012) with permission from The Royal Society of Chemistry.

As expected, displacement in the x and z direction is at a maximum when Poisson's ratio is at a maximum. The depth at which displacement changes direction happens at a lower depth as Poisson's ratio increases and the extent to which the displacement drops into the negative also increases, see Figure 2-5.

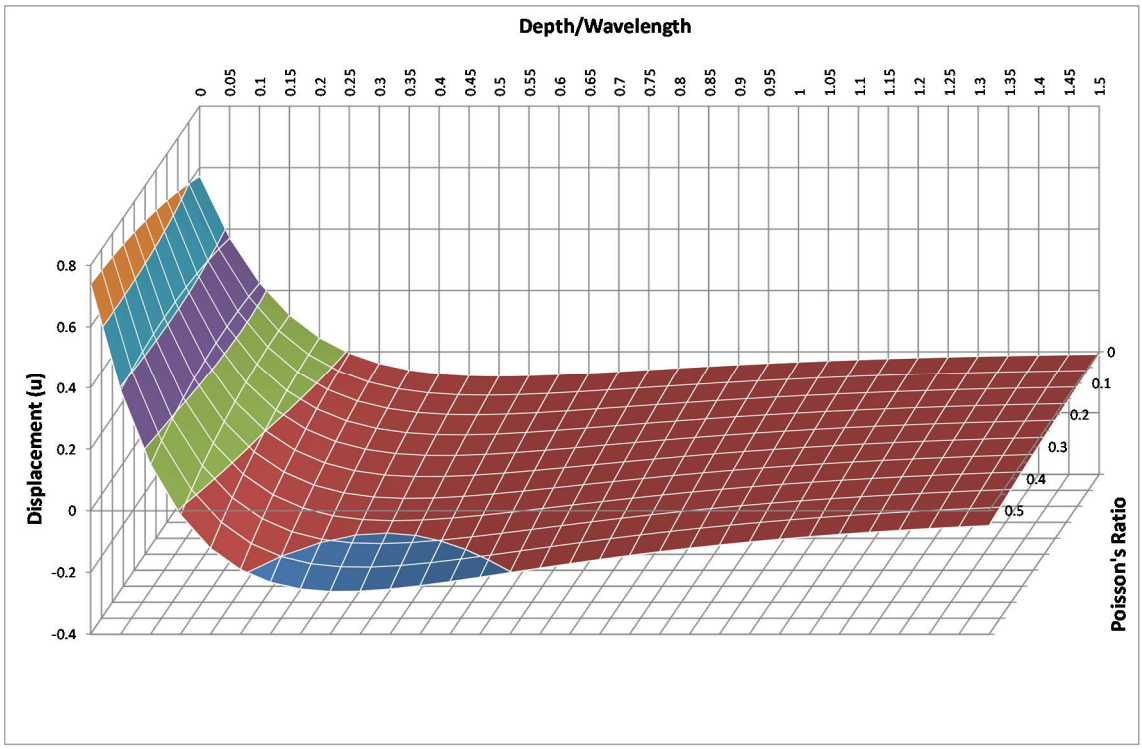

Figure 2-5 A plot showing how displacement (u) in the x direction varies with depth and Poisson's ratio. The values are normalised against displacement in the z direction when Poisson's ratio is 0 at the surface of the half space.

When Poisson's ratio is at a minimum, displacement in the z direction falls away monotonically. As Poisson's ratio increases a peak of maximum displacement forms between 0.05 and 0.15 wavelengths. As Poissons' ratio increases it takes longer for the displacement of the wave to decay, see Figure 2-6. As an example (Ristic, 1983), in a device operating at 100 MHz with 10 mW average power in a beam 1 cm wide on a substrate with SAW velocity 3 km s^{-1}, the wavelength is 30 µm and the peak vertical displacement of the order of 10^{-10} m.

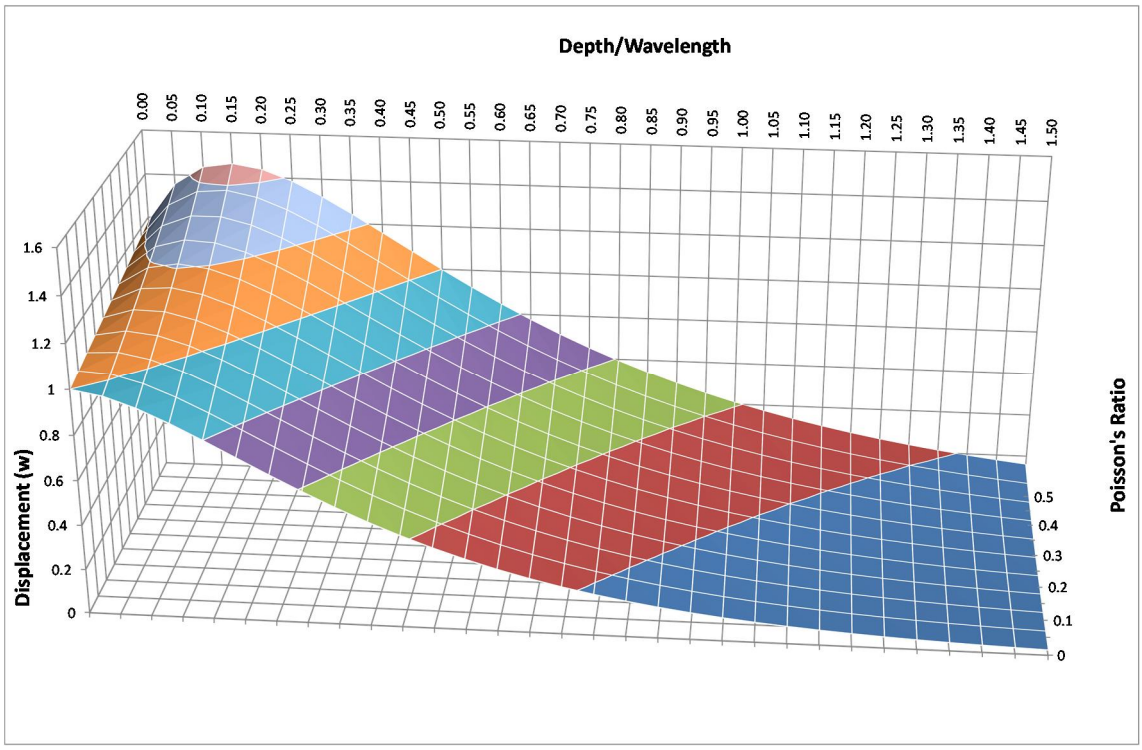

Figure 2-6 A plot showing how displacement (w) in the z direction varies with depth and Poisson's ratio. The values are normalised against displacement in the z direction when Poisson's ratio is 0 at the surface of the half space.

2.1.2.2 Leakey Rayleigh Waves

A pure Rayleigh wave (with a completely free surface) is generally of less interest in microfluidics than a surface bounded by a fluid or solid into which the surface wave will deliver energy. This will lead to an exponentially decaying wave propagating along the *fluid-solid* interface (Überall, 1973). In practice this attenuation is relatively small for *solid-gas* interfaces. In the following a fluid loaded structure is considered. The fluid is assumed to be unbound. As the impedance of the fluid rises from zero, the wave will behave less like a pure Rayleigh wave and will transform into a "leaky" Rayleigh wave. The components of a Rayleigh wave can be broken down into normal and tangential displacements and arranged into the following form (Cheeke, 2002);

$$4k^2\gamma_{\mathrm{L}}\gamma_{\mathrm{T}} - \left(k^2 + \gamma_{\mathrm{T}}^2\right)^2 = 0.$$

Equation 2-71

When the surface is loaded with a fluid, the boundary conditions change. By including the continuity of normal stress into the above equation the following equation is generated:

$$4k^2\gamma_L\gamma_T - \left(k^2 + \gamma_T^2\right)^2 = \mathrm{i}\frac{\rho_F}{\rho_R}\frac{\gamma_L k_T^4}{\sqrt{k_L^2 - k^2}},$$

Equation 2-72

where ρ_F and ρ_R are the densities of the fluid and the solid half space respectively. Likewise, C_F and C_R are the wave speeds of the two mediums. Tangential displacement is assumed not to be transferred to the fluid, since it does not support shear modes but more information on this matter can be found in a recent paper by (Vanneste and Bühler, 2010). Upon inspection it can be seen that as ρ_F tends to zero, the equation reverts back to a pure Rayleigh wave. This equation has one real root and one complex root. The real root corresponds to a Scholte wave and will be discussed later. The complex root corresponds to a modified Rayleigh wave. It can be shown that given the condition $C_F < C_R$, which is true for most media, then Equation 2-72 has a complex root that corresponds to a system of three waves (Brekhovskikh, 1957). One wave is found in the fluid and two in the solid. A simple physical interpretation of this is that the Rayleigh wave radiates energy at an angle into the fluid. This must be the case since we are dealing with a complex root, therefore it must be losing energy and this is the radiation of energy away from the boundary into the fluid (Cheeke, 2002). It can be shown that the velocity of the loaded Rayleigh wave is higher than that of the unloaded wave (Viktorov, 1967); however, upon further analysis the difference can be shown to be very small. As the fluid has little effect on the velocity of the Rayleigh wave, the following approximation can be made about the angle at which the wave propagates into the material, see Figure 2-7.

$$sin\theta = \frac{C_F}{C_R}.$$

Equation 2-73

This is a variation of Snell's law achieved by setting the initial angle to 90°. This is found by phase matching the wave in the fluid with the Rayleigh wave. As the wave travels along the interface it can be seen to "leak" energy into the fluid, at this angle. For common gases such as air this is near normal to the surface. It should be noted that a Rayleigh wave can be generated on the surface of a substrate if a wave travels through the fluid at the correct angle towards the interface.

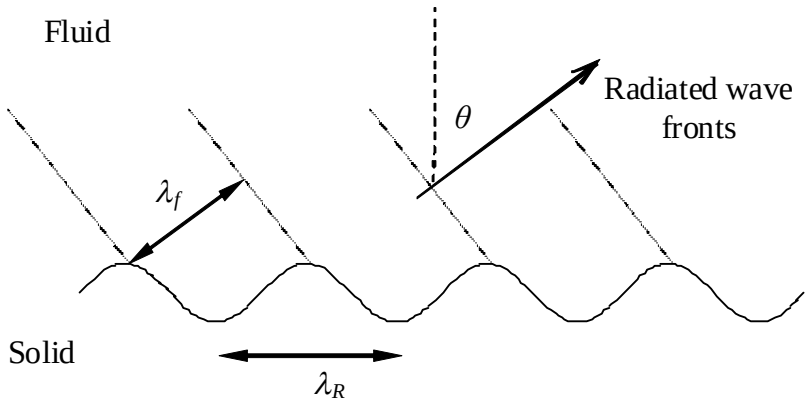

Figure 2-7 Schematic of a Rayleigh wave "leaking" from a solid into a fluid. Reproduced from (Gedge and Hill, 2012) with permission from The Royal Society of Chemistry.

In contrast to velocity, the attenuation of the wave is greatly affected by the presence of the fluid. It is this characteristic which makes Rayleigh waves excellent choices for the efficient transfer of energy into cavities or droplets. The attenuation coefficient for a leaky Rayleigh wave travelling along a solid-fluid interface is given by (Cheeke, 2002);

$$\alpha_{\mathrm{L}} = \frac{\rho_{\mathrm{F}} C_{\mathrm{F}}}{\rho_{\mathrm{R}} C_{\mathrm{R}} \lambda_{\mathrm{R}}}\ cm^{-1},$$

Equation 2-74

where λ_{R} is equal to the Rayleigh wavelength. This describes energy loss resulting from the transmission of a bulk wave into the fluid. The attenuation of the surface wave per wavelength travelled is proportional to the ratio of the fluid and solid impedances. For a typical combination of liquid and solid this factor is $\alpha_{\mathrm{L}} = 0.11$ resulting in the amplitude of the surface wave being attenuated to $1/e$ of its initial value over approximately 10 wavelengths (Viktorov, 1967). The attenuation coefficient is relatively small for atmospheric air, so for most practical purposes can be ignored (Dransfield and Salzmann, 1970).

So far it has been assumed that the attenuation of the leaky Rayleigh wave is due to the radiation of a compression wave into the fluid; however there will also be frictional losses from the transverse motion of the surface. This can be given by the following equation (Cheeke, 2002):

$$\alpha_s = \frac{\left(\rho_F \eta \frac{\omega^3}{2}\right)^{\frac{1}{2}}}{4\pi^2 \rho_R {c_R}^2} \text{ cm}^{-1}$$

Equation 2-75

where η is the viscosity of the medium and ω is the angular frequency of the leaky Rayleigh wave. These forces are typically small compared to the longitudinal contribution to attenuation. Typical calculated attenuation factors for Leaky Rayleigh waves in $LiNbO_3$ are shown in Table 2-1. To convert from cm^{-1} to dB cm^{-1} requires a multiplication of approximately 4.3 (Dransfield and Salzmann, 1970).

Table 2-1 Calculated values for the attenuation of Rayleigh waves in Lithium Niobate by ambient media.

		Attenuation (dB cm^{-1})		
Constant	Medium	10 MHz	100 MHz	300 MHz
α_L [a]	Atmospheric Air	0.00314	0.0314	0.0942
α_L [a]	Water	11.2	112	336
α_s [b]	Water	0.00673	0.213	1.107

[a] Attenuation due to radiation of longitudinal waves.

[b] Attenuation due to frictional loss

From Table 2-1 it can be seen the longitudinal component of attenuation increases linearly with frequency and that in air this is negligible for all frequencies. The frictional component of attenuation increases proportionally with the angular frequency to the power of 1.5 and is negligible except for extremely high frequencies, which are not reached in the particle and droplet manipulation devices mentioned later.

2.1.2.3 Scholte Waves

As mentioned earlier, there is a real solution to Equation 2-72. Further analysis shows that it is quite different from a Rayleigh wave and that they exist for any combination of fluid and solid (Ewing, 1957). It can be shown that the wave corresponds to a surface wave travelling along the boundary with a velocity less than the wave velocity of the fluid and the longitudinal and transverse wave speeds of the solid (Gogoladze, 1948). For lossless media they do not attenuate and therefore propagate along the interface, they are therefore pure interface waves. For fluids where the acoustic impedance is less than that of the solid, decrease in displacement amplitude with depth is significantly higher in the solid than the fluid and most of the energy is contained within the fluid, in contrast to the Leaky Rayleigh wave (Viktorov,

1967). Scholte wave generation efficiency increases as the acoustic impedance of the fluid increases so little Scholte wave generation is seen when air is the fluid. As the impedance of the fluid increases compared to the solid, the Scholte wave penetrates deeper into the solid (Glorieux et al., 2001).

2.1.2.4 Interface Waves

All waves discussed in this section so far have propagated along a *solid-vacuum* or *solid-fluid* interface. A solid-solid interface shall now be considered. For the purpose of this work only Rayleigh-like modes will be considered. Love modes, with motion perpendicular to the direction of propagation are currently of little interest for ultrasonic particle manipulation.

The addition of a thin layer (thickness h) on a substrate carrying a Rayleigh wave provides geometric constraints which will alter the characteristics of propagation, making the wave dispersive. This property has been used to great effect for SAW devices, as particular dispersion characteristics can be designed for (Farnell and Adler, 1972). As the layer thickness tends to zero, the wave transforms into a standard Rayleigh wave. The added thin layer can have several different effects on the wave velocity. The following inequality can be used to predict the behaviour of the dispersion curve as kh tends to zero (Tiersten, 1969)

$$\frac{C_{T2}}{C_{T1}} > \sqrt{\frac{1-\left(\frac{C_{T1}}{C_{L1}}\right)^2}{1-\left(\frac{C_{T2}}{C_{L2}}\right)^2}},$$

Equation 2-76

where subscripts *1* and *2* represent the substrate and added layer respectively, whilst $_T$ and $_L$ represent transverse and longitudinal as before. The limits of the right hand side are $\sqrt{2}$ and $1/\sqrt{2}$. If the above inequality is true the dispersion curve will be positive as the layer thickness approaches zero. If the above inequality is false, the dispersion curve will have a negative gradient as the layer thickness approaches zero. The case in which the solution lies between these boundaries is more difficult and shall be covered later. This inequality can be presented using shear moduli and density ratios as the ordinate and abscissa axis respectively, see Figure 2-8 (Farnell and Adler, 1972).

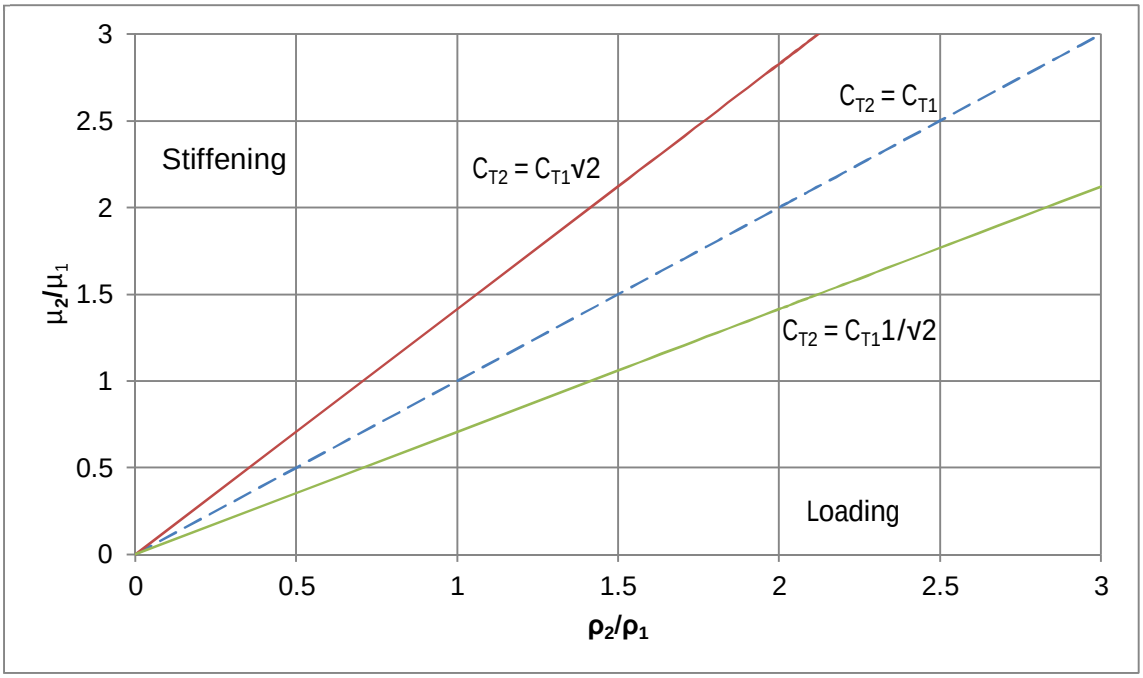

Figure 2-8 Diagram showing the limits of the inequality that determines stiffening or loading of a rayleigh wave. A stiffening substrate will cause an increase in the rayleigh wave speed. A loading substrate will cause a drop in the rayleigh wave speed. It is not possible to generalise on the Rayleigh wave speed if it lies between these two lines (Farnell and Adler, 1972). Reproduced from (Gedge and Hill, 2012) with permission from The Royal Society of Chemistry.

Should the inequality be true, then the layer is said to stiffen the substrate because the presence of the substrate leads to an increase in the surface wave velocity above the unloaded Rayleigh wave velocity. As the layer thickness increases the wave speed increases monotonically up to the shear velocity of the substrate.

As kh increases further, the wave leaks into the substrate and is no longer a true interface wave. Therefore Rayleigh type propagation is only possible for small values of kh, see Figure 2-9. The variation in wave speed is minimal for these material parameters, as it is dominated by the substrate material parameters. It should be noted that this set of material conditions is an unlikely scenario for ultrasonic particle manipulation devices.

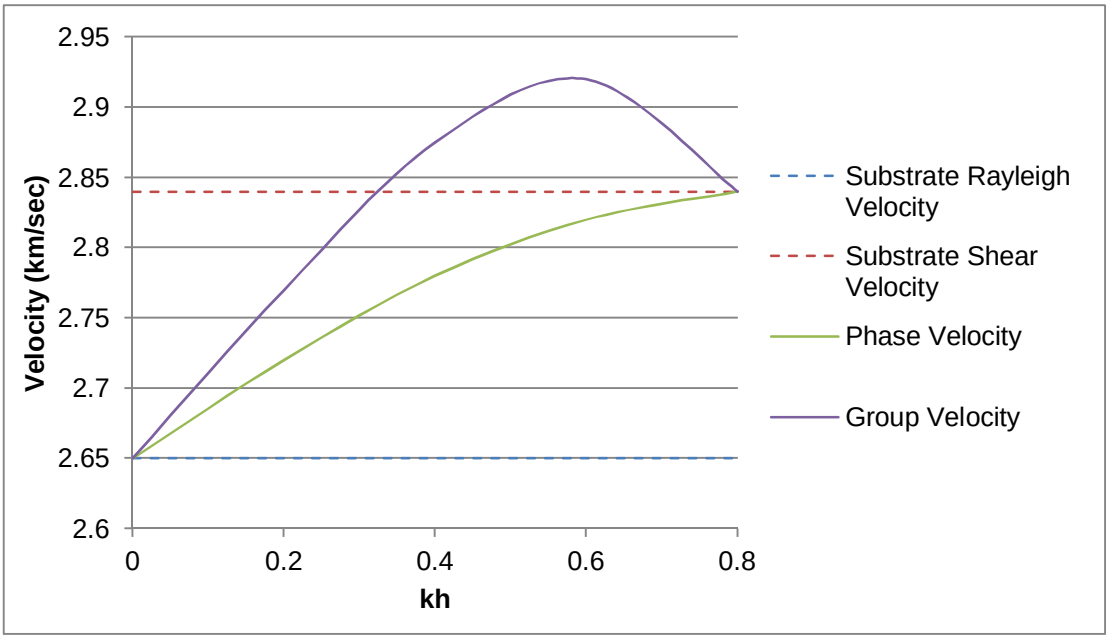

Figure 2-9 An example graph showing variation in group and phase velocity with varying layer thickness. This is for a layer on a substrate when the layer transverse wave speed is > $\sqrt{2}$ substrate transverse wave speed (Farnell and Adler, 1972).

Should $C_{T2} < C_{T1}/\sqrt{2}$ then the layer loads the substrate and the phase velocity of the Rayleigh-like mode decreases as kh increases, until it approaches the Rayleigh velocity of the layer. This is for a layer thickness large in comparison to the wavelength. At higher values of kh, the group velocity and phase velocity converge, as characteristics imposed by the layer are less important in regards to the wavelength, see Figure 2-10. An unlimited number of higher order Rayleigh type modes exist which tend to have a high frequency asymptote equal to the layer shear velocity (Farnell and Adler, 1972). The interface waves described so far radiate energy away from the interface.

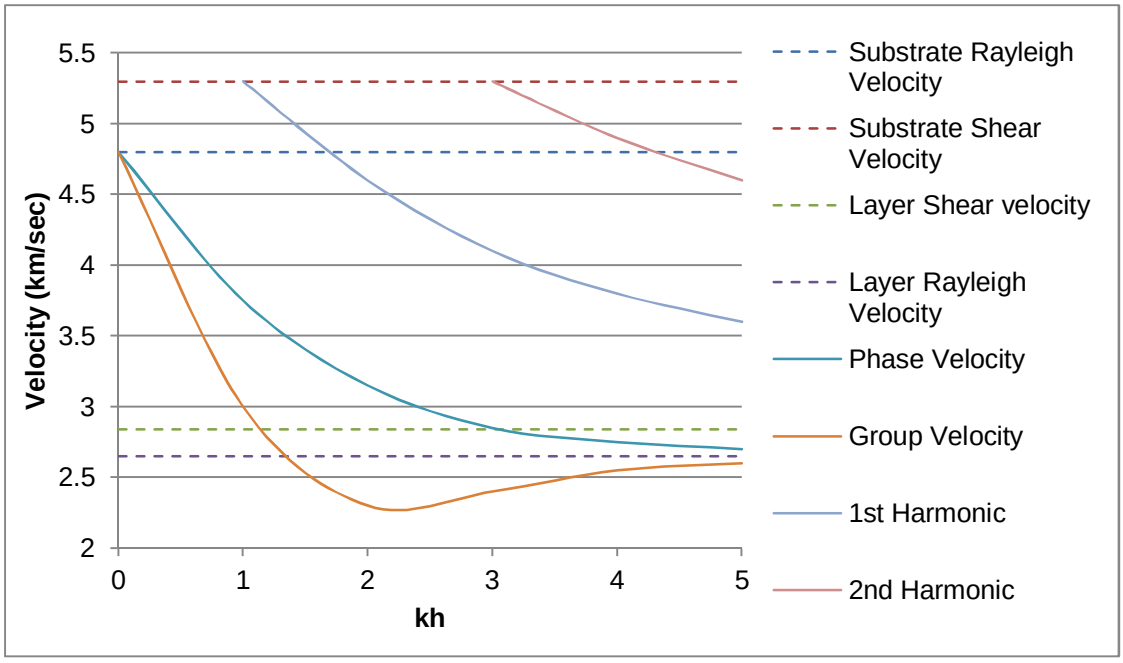

Figure 2-10 An example graph showing variation in group and phase velocity with varying layer thickness. This is for a layer on a substrate when the layer transverse wave speed is < 1/(√2) substrate transverse wave speed [6].

2.1.2.5 Stoneley Waves

There exists a particular set of conditions such that a Rayleigh-like wave can propagate at the interface between two solids; this type of wave is called a Stoneley wave which is evanescent in both media (Farnell and Adler, 1972). For a Stoneley wave to exist both the longitudinal and transverse displacements must be transferred in such a way that energy is confined to the interface. The derivation of a Stoneley wave is similar to that of a Rayleigh wave, except for the efficient transmission of displacement and stress across the boundary. The velocity of the Stoneley wave must be less than the transverse wave speeds of both media but more than the Rayleigh wave speed of the denser medium. The transverse wave speeds of both media need to be similar for Stoneley waves to exist. Stoneley wave velocity is not dependent on frequency, so the wave is therefore non dispersive. Stoneley waves do not attenuate along the path of propagation so are ideal for the efficient transfer of energy into a sealed fluid chamber.

2.1.2.6 Anisotropic Media and Piezoelectric Considerations

The description so far has been based on isotropic non-piezoelectrically active materials. Most materials used for surface acoustic wave devices are anisotropic and in

many cases single crystal. The Rayleigh wave and associated Rayleigh-like waves still exist for any given direction of propagation but the characteristics will differ based on orientation. $LiNbO_3$ is often used and it has a typical Rayleigh wave speed between 3500 m s^{-1} and 4000 m s^{-1} depending upon orientation. Depending on the materials used, the ellipse of motion need not be normal to the surface and displacement in the x and z direction may oscillate with depth (Farnell and Adler, 1972, Farnell, 1970). Wave propagation in anisotropic materials is less straightforward than isotropic materials however, gains can be made in piezoelectric coupling and the correct orientation will suppress other undesirable wave modes (Farnell and Adler, 1972). In an anisotropic solid there are two different transverse modes as well as the longitudinal mode, as a result a more general surface wave is produced with displacements in three dimensions. This type of wave can be regarded as a combination of Rayleigh and Love waves. It is possible to find orientations that decouple these waves into their respective pure Rayleigh and Love components (Pollard, 1977).

2.1.2.7 Generation of Surface Waves

There are several methods of generating surface waves. A transducer coupled through a wedge can be designed using the inverse of Equation 2-73, see Figure 2-11, (Viktorov, 1967). In this case the Rayleigh wave generated will propagate in one direction only and the coupling angle is independent of the required frequency (Rose, 1999). The wedge material must have a low longitudinal wave speed, as for this to work requires that $C_W < C_R$.

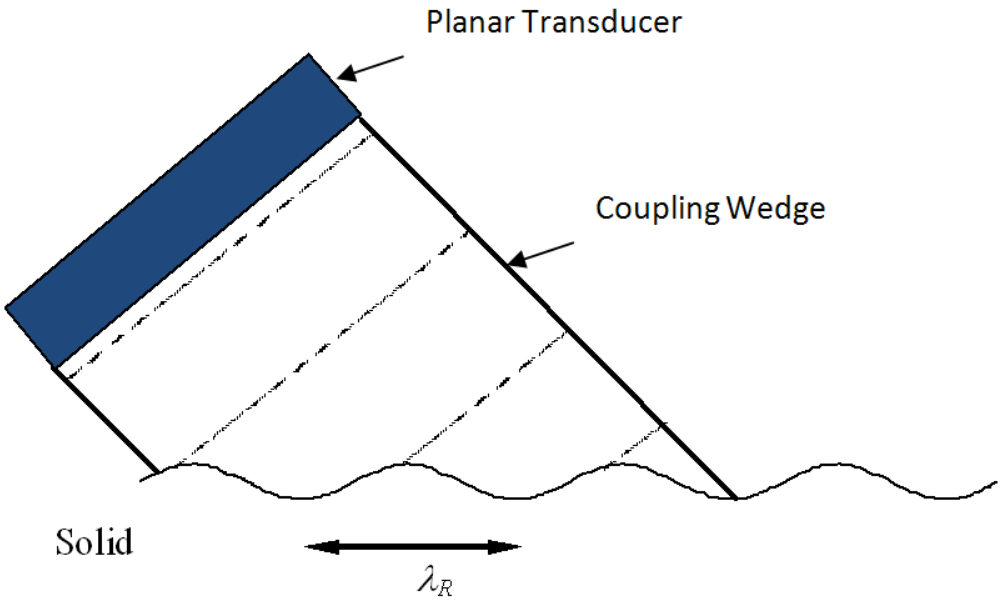

Figure 2-11 Wedge coupling to generate Rayleigh waves in a solid, the waves produced will be unidirectional. Reproduced from (Gedge and Hill, 2012) with permission from The Royal Society of Chemistry.

Alternatively a periodic transducer array, with contacts coupling to the surface at a spacing of λ_R can be used, this will radiate both to the left and the right, see Figure 2-12.

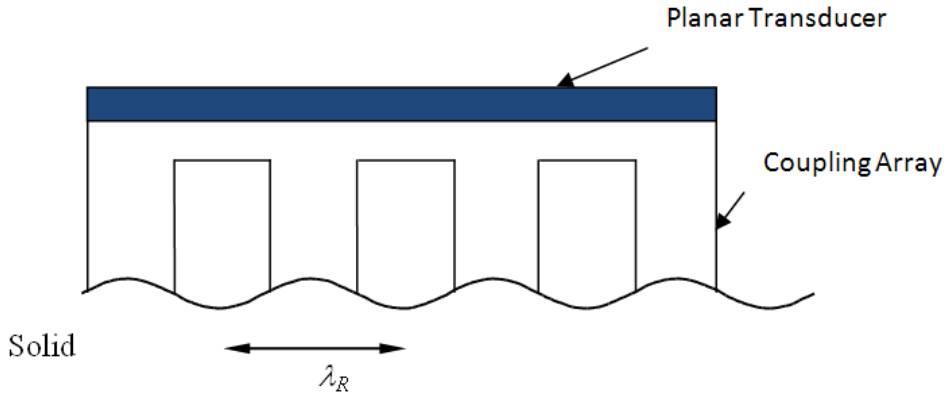

Figure 2-12 Periodic array for the generation of SAWs. The waves produced will be bidirectional and the frequency efficiency. The coupling array is usually made from metal (Viktorov, 1967). Reproduced from (Gedge and Hill, 2012) with permission from The Royal Society of Chemistry.

These transduction methods rely on coupling the energy from an active transducer into a passive substrate, but the most common means of generating SAWs is to use a piezoelectrically active substrate or a thin piezoelectric layer on a substrate.

In such a case the excitation (and reception) of the SAW is provided by sets of interdigital transducers (IDTs) which are comprised of metallic strips deposited directly onto the piezoelectric surface. Figure 2-13 shows a simple IDT electrode pattern with two sets of interleaved combs extending from the two electrode rails. When a signal is applied to these rails an electric field is established with the spatial period of the comb. This then excites a strain field via piezoelectric coupling. The response will be strongest when the spatial period of the electrodes equals the SAW wavelength in the substrate. For a single electrode pair the Q factor is small and the response is broadband, but as more identically spaced electrode pairs are added, the Q factor increases and the IDT develops a sharp resonance peak. Such an IDT will generate a SAW that will propagate in both directions. If designing for a wave that travels in one direction only attention must be given to absorbing (or reflecting) the opposite-going wave.

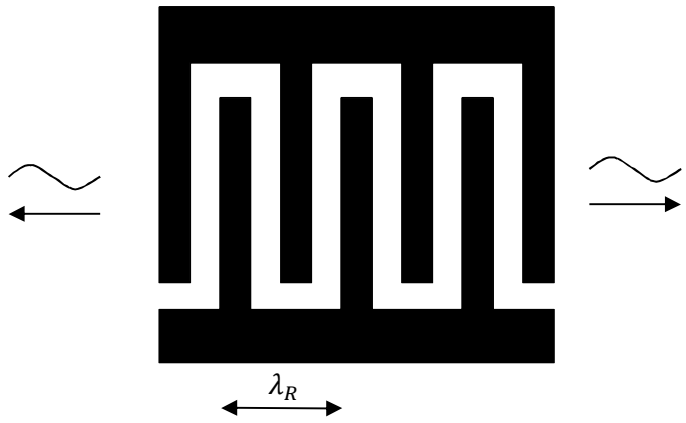

Figure 2-13 Uniform, periodic IDT array deposited on piezoelectric substrate. Reproduced from (Gedge and Hill, 2012) with permission from The Royal Society of Chemistry.

A number of additional practical considerations need to be taken into account when designing SAW systems, including the facts that: temperature effects may be significant and may also vary with orientation. It should also be noted that models for SAW propagation in passive substrates do not fully describe SAW behaviour in a piezoelectric substrate as the electromechanical coupling complicates the material's mechanical characteristics.

When generating waves it is important to note that the electrodes themselves will modify the impedance presented to the SAW, through mechanical loading and modification of the electromechanical coupling in the substrate adjacent to the electrode. For this reason each electrode finger can be broken down into two,

maintaining the periodicity in terms of the electric field but breaking the periodicity in terms of reflection characteristics. It is normal for the spacing between fingers to be of equal width to the electrodes, this means they are $\lambda/4$ for single electrode configurations or $\lambda/8$ for double electrode configurations. Devices for ultrasonic particle manipulation tend to work at frequencies of 20-40 MHz which corresponds to electrode widths of approximately 50-100 µm for a typical $LiNbO_3$ device, (Franke et al., 2010, Frommelt et al., 2008). Most devices are no bigger than a standard microscope glass slide. Electrode fingers need not be parallel to each other and can even be concentrically curved to allow for tight focusing into a point on the surface, (Luong et al., 2010).

2.1.3 Acoustic Radiation Force

Particles experience forces when in an acoustic field (Gröschl, 1998, Wang and Lee, 1998)These forces are called acoustic radiation forces and they cause particles to fall to the pressure node or anti-node of a wave. Acoustic radiation forces have been know about since the late 19th century (Kundt, 1894) but have only found applications more recently. The mathematics behind this phenomenon was investigated by King in 1934 (King, 1934), which described incompressible particles in an inviscid medium subjected to an ultrasonic field. He integrated the pressure field over the surface of the sphere to calculate the radiation pressure (Gröschl, 1998). The particle scatters the acoustic wave which produces a net force on the particle. His work was furthered by Yosioka and Kawasima to include compressible spheres (Yosioka and Kawasima, 1955) and was later summarized by Gor'kov (Gor'Kov, 1962), (Bruus, 2012). Later work by Doinikiv included the effects of viscosity (Doinikov, 1994). However, for most practical applications the Gor'kov equations suffice as the Doinikov work is lengthy and challenging.

When a sound field is propagated through a fluid, there are associated oscillating velocity and pressure fields. In a linear approximation, these forces time average to zero. To fully describe the phenomenon, 2nd order effects need to be considered. The theory is difficult and beyond the requirements of this work, however, a basic description will be given. For non-linearities to exist, the sound wave must have a high amplitude velocity, so that the wave becomes distorted. If one considers a particle in a sound field, there will be a difference in the pressure on either side of the particle, due to the superposition of the incoming wave and the scattered wave. For this to happen, the particle must differ in properties from the fluid, otherwise the wave

would not be affected by the particle. As the particle properties are different to the fluid, the particle will oscillate with a different speed to the fluid, thus radiating a wave.

Standing waves will create much larger forces, as the amplitudes of the two counter propagating waves superimpose. It can also be shown that the force exerted in a progressive wave scales with $(kr)^6$ whilst for a standing wave it is $(kr)^3$, where k and r are the wave number and particle radius respectively (Gröschl, 1998). The force in a progressive wave is constant in space, whilst in a standing wave it shows a spatial dependence according to $\sin(2kx)$, where x denotes position.

In a standing wave, the components reach the particle from each side, but with different magnitudes. This assumes that the particle is not already at its equilibrium position and that its material properties are the same on each side. This difference in velocity magnitude on either side of the particle creates a net force acting normally to the incoming waves. If one considers a stiff heavy particle, the radiation force is directed inwards, but is stronger on the side with the lowest velocity, hence a movement to the velocity antinode. For a light flexible particle, on the other hand, the force is directed outwards, but stronger on the side with the highest velocity, hence it moves to a velocity node.

As a planar wave travels through a medium, the wave carries energy, intensity and momentum. The total time averaged energy, E_{AC}, can be separated into potential energy, $E_{P,}$ and kinetic energy, E_K,

$$\langle E_{AC} \rangle = \langle E_K \rangle + \langle E_P \rangle,$$

Equation 2-77

$$\langle E_K \rangle = \frac{1}{2} \rho_F \langle {C_F}^2(x) \rangle,$$

Equation 2-78

$$\langle E_P \rangle = \frac{1}{2\rho_F {C_F}^2} \langle P^2(x) \rangle.$$

Equation 2-79

Where ρ_F, C_F, x and P denote the fluid density, wave velocity, direction and pressure respectively.

Numerical solutions to the forces acting on a particle in an acoustic field are well documented (King, 1934, Gor'Kov, 1962). The following solution by Yoshioka and Kawasima is most frequently used, it predicts the radiation force acting on a compressible sphere within a planar field (Yosioka and Kawasima, 1955).

$$F = 4\pi k r^3 \epsilon \phi(\rho, \beta) \sin(2kx)$$

Equation 2-80

Where ϵ denotes the energy density, ϕ the acoustic contrast factor and k the wave number in the fluid, given by $k = 2\pi/\lambda$. The acoustic contract factor controls the direction of the force on the particle. A positive acoustic contrast factor results in particles moving to the pressure node. A negative acoustic contrast factor will move particles to the pressure antinode. The acoustic contrast factor is defined by the following equation.

$$\phi(\rho, \beta) = \frac{\rho_F + \frac{2}{3}(\rho_P - \rho_F)}{2\rho_P + \rho_F} - \frac{\beta_P}{3\beta_F}$$

Equation 2-81

Where ρ denotes density and β compressibility, with $_P$ and $_F$ denoting the particle or the fluid. Hard dense objects such as glass will have a high positive acoustic contrast factor. Compressible buoyant particles such as lipids will have a high negative acoustic contrast factor. Generally speaking, cells have a positive acoustic contrast factor thus will be forced to the pressure nodes.

2.2 Microfluidics

Microfluidics is a relatively new field which came about from the explosion of Micro Electro-Mechanical Systems (MEMS). It was noticed that fluids operating in MEMS devices behaved in unexpected and unknown ways, thus the study of microfluidics was born (Tabeling, 2003). The first microfluidic system of note was a miniaturised gas chromatography chip produced in the mid 1970's (Terry et al., 1979), however the field really began to grow in the 1990's with the production of various microfluidic systems such as electrophoretic separation systems (Manz et al., 1992), electro-osmotic pumping systems (Harrison et al., 1991), diffusive separation systems (Weigl and Yager, 1999), micromixers (Knight et al., 1998), DNA amplifiers (Wilding et al., 1998), cytometers (Fu et al., 1999) and chemical reactors (Eijkel et al., 1998). Perhaps one of the main driving forces of microfluidic systems has been the desire to integrate it with MEMS to produce Lab-on-a-chip devices, capable of detecting, transporting, mixing and characterising samples on a single chip.

Whilst microfluidic systems seem extreme to a macro scale mind such as that of a human, in reality our bodies and surrounding world is abundant with them. A prime

example is the way in which trees transport water and nutrients to its leaves through a complex network of capillaries ranging from micro to nanofluidic size (Tabeling, 2003). The list of microfluidic systems in nature is near endless and they are quite remarkable.

Microfluidic analysis offers several advantages over conventional laboratory based analysis methods; perhaps the most important being costs. Running laboratories is expensive, even more so in remote areas such as at sea. Miniaturisation and automation of chemical reactions does away with the need for bulky expensive equipment and skilled operators. The time scales involved for microfluidic devices is also significantly reduced. When such small volumes are used, heating and mixing of fluids is quick, as are the chemical interactions to be monitored. For these reasons and more, microfluidics has found applications in biology, chemistry, pharmaceutics and more. The discipline is comparatively young but has expanded substantially in recent years (Tabeling, 2003).

Microfluidic manipulation is being driven by a desire to work with smaller volumes, lower sample concentrations but in less time and with lower costs. An example being work being carried out looking into bacteria found in the human digestive system, (Turnbaugh, 2007). Such work poses several problems; current bacteria biological tests would be dominated by the human cells found in any sample taken. Therefore the human cells need to be separated from the bacterial cells. Secondly, the separation needs to be quick to limit changes in mRNA or protein expressions. The separation also has to work with small sample volumes in the order of mm^3 that have relatively low bacteria cell counts of 10^6-10^7 cells/biopsy. Fluorescence activated cell sorting (FACS) is frequently used for this, but it is time consuming and expensive and limited by sample volume and dilution, (Wang et al., 2005). Factors such as these are pushing the desire for miniaturisation and have yielded several different microfluidic manipulation techniques.

At the micro scale there are several physical factors which come into play which may not necessarily be of interest in macro scale operations. For instance, gravitational forces can be overcome by surface forces. Despite the complications of working at the micro scale these devices offer several advantages over their macro scale counterparts. It can be cheaper to work in microfluidic systems, as less reagent is used and tasks can be carried out which would otherwise require expensive equipment. It is also possible to control heating and pumping more accurately in microfluidic systems, on the other hand, viscous forces can be difficult to overcome at the micro scale meaning that the mixing of fluids can be problematic. The following section will cover in

greater detail some of the physics associated with the microscale and how it can be utilised for the advantage of the user.

There are several situations in microfluidic systems in which the laws and observations made in the macro scale world do not hold true. This section will explain notable examples and briefly discuss some of the more exciting phenomena. Initially, it is hard to imagine what would be different, considering the length scales involved are still many orders of magnitude higher than the size and reach of atoms and their associated forces. However, upon closer inspection forces such as gravity can be overcome by capillarity and wetting.

2.2.1 Reynolds number

The Reynolds number is a dimensionless parameter that gives a value describing the ratio of internal forces to viscous forces. A low Reynolds number indicates a laminar flow whilst a high number indicates turbulence. The Reynolds number is given by the following equation,

$$Re = \frac{Ul}{\zeta},$$

Equation 2-82

where U is the mean velocity of the fluid, l is the length scale and ζ is the kinematic viscosity. For flow in a rectangular pipe, l is defined as,

$$l = \frac{4A_{Re}}{P_{Re}},$$

Equation 2-83

where A_{Re} is the cross sectional area and P_{Re} is the perimeter. Miniaturisation tends to favour low Reynolds numbers and therefore laminar flow. The speeds required to generate a turbulent flow are simply too high and would require an unattainable pressure difference across the device. Because of this unavoidable laminar flow, mixing within microfluidic channels does not readily happen. To understand why the pressure differences required for turbulent flow are so high, it is necessary to look at hydrodynamic resistance.

2.2.2 Flow in a channel

It is important to understand how a fluid travels along a microfluidic channel. For the purpose of this work it is enough to look at liquids only. The Navier-Stokes equations can be analytically solved for pressure driven steady state, continuous geometry micro channels. This class of solutions are known as Poiseuille flow or Hagen-Poiseuille flow (Bruus, 2008). There is no analytical solution for an arbitrary cross sectional channel, but solutions exist for some channel geometries. The easiest of these solutions is for a channel made from two infinite plates (channel height, h_c), as one of the dimensions drops out of the equations. The result is an ordinary differential equation,

$$\partial_z^2 v_x(z) = -\frac{\Delta p}{\eta l},$$

Equation 2-84

$$v_x(0) = 0,$$

Equation 2-85

$$v_x(h_c) = 0.$$

Equation 2-86

The solution leads to a simple parabola describing the flow profile,

$$v_x(z) = \frac{\Delta p}{2\eta l}(h_c - z)z.$$

Equation 2-87

This solution can be integrated over the height and width (w_c) of the channel to find the flow rate, Q,

$$Q = \frac{{h_c}^3 w_c}{12\eta l}\,\Delta p.$$

Equation 2-88

This equation loses accuracy as the ratio of the height to width increases, however, for a wide channel ($h < w/10$) the results are a sufficient approximation ($\leq 7\%\ Error$) (Bruus, 2008). Solutions also exist for elliptical, circular and equilateral triangular cross sections however these are not of direct importance to this work. Many lab-on-a-chip devices have fluid channels where the height is comparable to the width.

In these devices a more accurate method is required to describe the fluid flow in the channel. There is no analytical solution for a rectangular cross section, so a Fourier sum is used to represent the solution, which ultimately generates the following flow rate equation,

$$Q = \frac{{h_c}^3 w_c \Delta p}{12\eta l}\left[1 - 0.63\frac{h_c}{w_c}\right],$$

Equation 2-89

valid for $h_c < w_c$. The equation has an error of 13% when $h_c = w_c$, but this falls away sharply and is as small as 0.2% when $h_c = w_c/2$. An improved approximation exists for the case of a square channel and is shown below,

$$Q = \frac{{h_c}^4 \Delta p}{28.4\eta l},$$

Equation 2-90

this equation has an error of just 0.06%. A more thorough description of this section can be found in *Theoretical Microfluidics* by Henrik Bruus (Bruus, 2008).

Whilst the above equations are important, they are not in their most useful format for this work. The majority of the flows produced in this work will have a set flow rate, in which case it may be useful to calculate the pressure being applied,

$$\Delta p = Q R_{hyd},$$

Equation 2-91

where R_{hyd} is the hydrodynamic resistance. The following equations are re-arranged versions of Equation 2-88, 1.86 and 1.87. For completeness the equation describing flow through a circular pipe has been included, see Table 2-2: Equations describing the hydrodynamic resistance in some common channel shapes. Reference values are given for η= 1 mPa s (water), l= 1 mm, r = 100 μm, h_c = 100 μm and w_c = 300 μm.

Table 2-2: Equations describing the hydrodynamic resistance in some common channel shapes. Reference values are given for η = 1 mPa s (water), l = 1 mm, r = 100 µm, h_c = 100 µm and w_c = 300 µm.

Shape	**R_{hyd}**	**R_{hyd}** x 10^{11} Pa s m^{-3}
Circle (Radius r)	$\frac{8}{\pi}\,\eta L\frac{1}{r^4}$	0.25
Two Plates (h × w)	$12\eta L\,\frac{1}{h^3 w}$	0.4
Rectangle (h × w)	$\frac{12\eta L}{1-0.63(\frac{h}{w})}\frac{1}{h^3 w}$	0.51
Square (h × h)	$28.4\,\eta L\frac{1}{h^4}$	2.84

As an example, the hydrodynamic resistance of a 100 µm square channel, 1 mm long and filled with water is 2.84 x 10^{11} Pa s m^{-3}. Reducing the cross sectional area by 10% (h = 94.87 µm) produces a hydrodynamic resistance of 3.51 × 10^{11} Pa s m^{-3}, an increase of more than 23.5%. From this it is easy to see that as fluid channels get smaller the hydrodynamic resistance grows disproportionately. This means that as channels approach µm dimensions, the pressures required to force fluid through at a suitable flow rate are incredibly high, this may result in breakages and burst in the systems.

2.2.2.1 Channels in Series

All of the previous work on flow in channels is based on a continuous channel with no spatial variation, however this is an unlikely situation for many microfluidic devices. Fortunately, hydraulic resistance shares many traits with electrical resistance, allowing the summation of individual hydraulic resistances.

$$R_{\text{hyd}} = R_{1\text{hyd}} + R_{2\text{hyd}}$$

Equation 2-92

It should be noted that this is based on flow through two individual channels, the transition from one channel to the other is likely to increase the actual hydraulic resistance. The equation becomes increasingly invalid as the Reynolds number increases, as re-circulating streamlines form at sharp changes in shape.

2.2.2.2 Channels in parallel

Whilst not of immediate use in this work, it should be noted that microfluidic channels in parallel continue the similarities with electrical resistance, i.e. they follow this equation;

$$R_{\text{hyd}} = \left(\frac{1}{R_{1\text{hyd}}} + \frac{1}{R_{2\text{hyd}}}\right)^{-1} = \frac{R_{1\text{hyd}}R_{2\text{hyd}}}{R_{1\text{hyd}} + R_{2\text{hyd}}}$$

Equation 2-93

As in the case for flow in series, this equation is based on no interaction between the two channels. This means that it is valid for two channels with distance between them and at low Reynolds numbers.

2.2.2.3 Hydraulic Compliance

The analogy to electrical resistance can be furthered to describe hydraulic compliance, which is the equivalent of electrical capacitance. As pressure (Δp) is applied to a fluid in a microfluidic channel, a flow will be generated of rate (Q), which can be given in volume per time (v). The electrical equivalents are voltage (V), current (I), and charge per time (q). Knowing that electrical capacitance is given as, $C = dq/dV$, it is possible to deduce an equation for hydraulic compliance,

$$C_{hyd} = \frac{dv}{dp},$$

Equation 2-94

which simply describes the change in volume of a system as the pressure increases, (Bruus, 2008). It is easy to understand that fluids in microchannels will experience changes of volume when put under pressure, especially gases. It is less intuitive that the microchannel will experience changes in volume as the pressure is applied, however in soft polymers such as PDMS these changes in volume could be quite noticeable. The existence of hydraulic compliance means that microfluidic systems will often require a settling time before the system can be considered in equilibrium.

There are three reasons for the existence of hydraulic compliance;

1) The compressibility of the fluid (K_{Fluid})
2) The existence of bubbles within the fluid which can be compressed
3) The expansion of the micro channel as a pressure is applied

In this work, only liquids will be used, therefore the compressibility of the fluid is negligible. For water this is approximately, $5 \times 10^{-10}\ Pa^{-1}$, which would require unattainable pressure differences to have an effect on the devices to be used in this work.

It is highly likely that bubbles will be present in the liquids being used, however, steps can be taken to minimise this, such as vacuum desiccation prior to use. Bubbles may also be produced by excessive heating of an ultrasonic transducer, which will affect the response time of a microfluidic channel.

The final reason is likely to have the largest consequences to this work. There are two main factors to this, firstly, compressibility of the material being used, which will include a soft compliant polymer called PDMS. The second factor is the shape of some of the channels. Particularly wide channels with thin walls will be more susceptible to volume changes than square channels with thick walls.

Take Equation 2-94 and assume that the pressure changes over time,

$$C_{hyd}\frac{dp}{dt} = -\frac{dv}{dp}\frac{dp}{dt},$$

Equation 2-95

which by using the chain rule yields the following,

$$C_{hyd}\frac{dp}{dt} = \frac{dv}{dt} = Q.$$

Equation 2-96

Where Q is a volumetric flux (Kirby, 2011). For a compressible fluid the hydraulic compliance can be defined as follows,

$$C_{hyd} = K_{Fluid}V,$$

Equation 2-97

where V is equal to the volume of the fluid channel and the compressibility of the fluid (K_{Fluid}) is a measured variable.

Similar equations can be produced for the dilation of the microchannel, in this situation the compressibility is approximated as the inverse of the materials Young's modulus,

$$K_{Material} \sim \frac{1}{E_{material}},$$

Equation 2-98

which yields the following for the hydraulic capacitance,

$$C_{2hyd} = K_{Material} V.$$

Equation 2-99

It should be noted that this assumes a uniform pressure in the channel which is incorrect for a long tube. This equation also fails to incorporate dilation effects due to the shape factor of the channels. If required this could be measured on an individual basis for each microchannel, however this is beyond the scope of this work.

Similarly to electrical capacitance, there is a time characteristic, $R_{hyd}C_{hyd}$, that determines how long a channel will take to reach equilibrium (Manneberg et al., 2009a). Steps can be taken to minimise this, such as minimise lengths of auxiliary tubing; avoid bubbles in the system as the compressibility of air is significantly higher than that of water, use glass syringes rather than plastic, minimise the dead volume of fluid in the system; i.e. use a smaller syringe. It should be noted that using a smaller syringe will also reduce variations in the flow rate when syringe pumps are used, as steps will be more frequent than if a larger syringe is used. Using stiffer materials such as steel and ceramics will reduce the time characteristic; however, in some cases the use of polymers, particularly PDMS, will be mandatory.

2.2.3 Capillarity

As previously mentioned, the surface to volume ratio is much larger in microfluidic systems than in macro sized systems. Appropriately this leads to situations in which interfaces play a more significant role than body forces. All interfaces are associated with a surface energy, which is defined as follows,

$$E_C = \frac{A}{12\pi D_0^2} = 2\gamma.$$

Equation 2-100

Where A, D_0 and γ are the Hamaker constant, equilibrium distance and the surface energy respectively. Therefore E_s is the required energy to separate two planes which are attracted by Van der Waals forces. The equilibrium distance, D_0, exists at the balance between attractive Van der Waals forces and repulsive quantum forces. This idea can be extended to include fluids on a plane, where the molecules in contact or near the interface will behave differently to those in the main body of fluid. Some fluid/solid pairs will interact more than others, which results in a higher surface energy.

Wetting is a phenomena caused by surface energy; when a droplet is placed on a substrate it will form a contact angle with the substrate depending on the surface energies of the 3 interfaces. There is a spreading coefficient, S, which is defined by,

$$S = \gamma_{SG} - \gamma_{SL} - \gamma_{LG},$$

Equation 2-101

where $_{S, G}$ and $_{L}$ define solid, gas or liquid. The droplet will be in equilibrium when the resultant forces are zero at the contact line. Or, put another way, if the droplet has a particularly high surface energy with the solid, the droplet will spread out until it reaches equilibrium and vice versa. The contact angle is defined as follows,

$$\cos\theta = \frac{\gamma_{SG} - \gamma_{SL}}{\gamma_{LG}},$$

Equation 2-102

where an angle $\theta > 90°$ is considered hydrophobic and an angle $\theta < 90°$ is hydrophilic (Bruus, 2008), see Figure 2-14. Using Equation 2-101 it can be written as follows,

$$\cos\theta = \frac{S}{\gamma_{LG}} + 1,$$

Equation 2-103

which shows that if S is positive or less than $-2\gamma_{LG}$, then no equilibrium position exists. A positive S would result in total wetting, i.e. a thin film spreads out completely covering the solid. In the case that $S \leq -2\gamma_{LG}$, a non-wetting situation is formed, and a sphere of fluid is formed on the substrate (Tabeling, 2003).

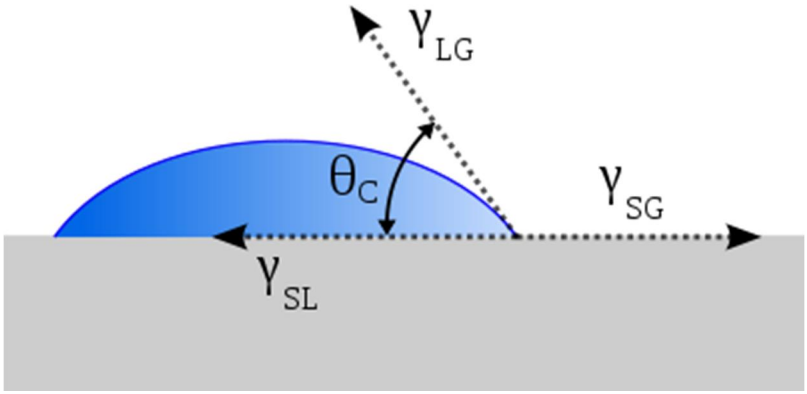

Figure 2-14 A diagram showing the contact angle formed between a droplet and a surface.

Whilst surface energies will not be of primary interest in this work, having a basic level of understanding will be useful. It is often possible to alter the properties of the substrates being used to suit the needs of the experiment. It is also possible to add chemicals to fluids to make them easier to manipulate. Examples of interest will be discussed later in the work.

2.3 Devices for Particle Manipulation

Over the years, several different applications for ultrasonic manipulation have been developed. Initial devices separated particles from the carrying fluid, but the technology has now progressed enough to separate different sizes of particles from each other, and several specific biological applications have been found. More recently, surface acoustic waves have been coupled into fluid channels allowing continuous 2 dimensional focussing on lab-on-a-chip style devices, (Shi et al., 2008).

2.3.1 Bulk Acoustic Devices

Early designs focused particles in one dimension, creating planes of particles. It is now possible to focus particles into a beam using ultrasonics in two dimensions. Recent work has also manipulated particles in the 3rd dimension, managing to move particles independently of flow, Figure 2-15. These devices usually work in the 1-10MHz region, (Manneberg et al., 2009b).

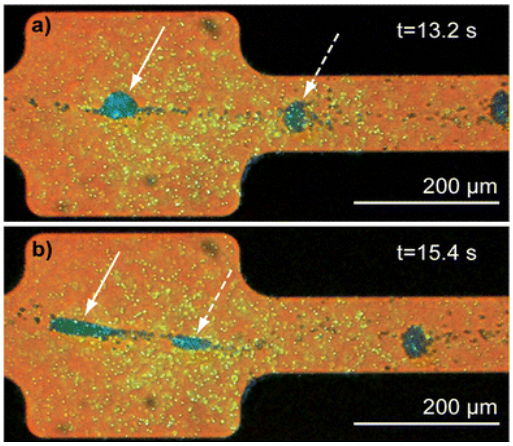

Figure 2-15 . Particles are focussed axially and laterally before being moved down the fluid channel using frequency sweeping. Reproduced from (Manneberg et al., 2009b) with permission from The Royal Society of Chemistry.

A basic ultrasonic separator was designed and built by Harris et al at Southampton, (Harris et al., 2003). The device used a standing wave half the wavelength of the chamber to force the particles to the centre of the fluid chamber. The flow was then split in two, a concentrated flow and a cleaned flow. The device was made using pre-existing micro-fabrication techniques for silicon and Pyrex. By modelling the device as a multi-layered resonant structure, the work managed to predict the resonant frequency and hence the particle focussing frequency. This modelling was then used to design a device that could support more than 1 resonant mode, (Harris et al., 2004).

The device was designed to be able to fit a half wave mode, as well as a quarter wave mode which pushes the particles to the top of the cavity. Being able to pull particles to and from the top of the cavity allows them to be pulled into focus to be counted. Once the particles have been pulled to the top of the cavity, the flow rate will generally be insufficient to move the particles further along the chamber. This type of device can also be used to push particles to chemical or biological sensors attached to the chamber roof, which will lead to enhanced sensitivity.

Most modelling up to this point had been 1 dimensional and based on resonance. The Southampton group furthered this by modelling the particle trajectory through the channel accounting for buoyancy and drag forces, (Townsend et al., 2004). The group then modelled the devices in 2 dimensions using finite element analysis (FEA), this was to investigate the striations seen across the channel due to lateral acoustic forces, (Townsend et al., 2006). The work showed the striations and that the associated forces can be of the same order of magnitude as the primary axial forces,

Figure 2-16. By designing effectively, striations can be maximised or minimised depending on the application.

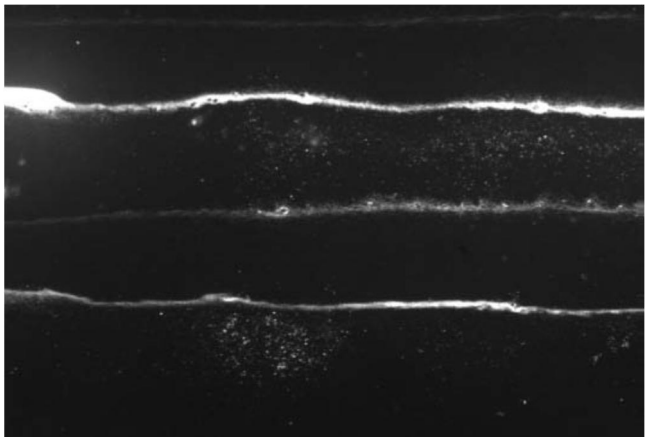

Figure 2-16 Striations seen in an ultrasonic standing wave device, particles were focused in a plane parallel to the page but secondary forces caused the particles to gather in bands too.

The group then worked heavily on quarter wave devices to separate particles from a fluid (Hill et al., 2008, Townsend et al., 2008). Quarter wavelength devices are less energy efficient, so hitting the most energetic modes is crucial. Resonant modes are affected by the thickness of the fluid layer and reflector layer, as well as the coupling and adhesive layers. The work showed that when there is a quarter wavelength (or equivalent) in the reflector and a half wavelength in the fluid layer, the position of the node will be stable with regards to changes in reflector layer thickness. However, when there is a half wavelength in the reflector and a quarter in the fluid, the nodal position will be very sensitive to reflector layer thickness.

The forces applied to particles or beads within a fluid channel vary along its length. This leads to areas of little or no focusing, and can even create areas that pull beads away from the desired position. In a flowing device, this is not an issue as the net applied force is enough to focus the particles. However, for some applications a no flow condition is desired. This allows more accurate manipulation of individual particles or cells, (Manneberg et al., 2009b). This problem can be solved by continuously ramping through frequencies close to the peak resonance. The frequency of ramping is in the order of 1 kHz. By doing this several different sections of the resonance is applied. Each frequency applies a slightly different force profile to the fluid channel which average to give a continuous focused line of beads in flow free conditions, Figure 2-17.

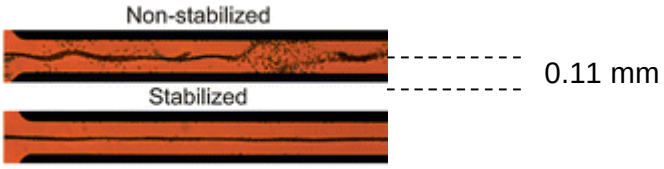

Figure 2-17 Flow free stabilization of particles in a fluid channel. Reproduced from (Manneberg et al., 2009b) with permission from The Royal Society of Chemistry.

The first ultrasonic devices excited a standing wave in a plane that was parallel to the transducer, this focused particles horizontally down the length of the fluid channel. By choosing suitable channel widths and operating frequencies it is possible to focus particles normal to the transducer down the length of the fluid channel. This can be done without changing the orientation of the transducer as long as the channel width has sufficiently different acoustic properties to the channel height, (Petersson et al., 2005). This means that for a given frequency, the channel width must equate to half a wavelength, whilst the channel height cannot be a half wavelength or a multiple of. There are other factors to consider, such as reflector layer and carrier layers thicknesses. Focussing particles in a vertical plane down the fluid channel gives advantages in optical access. Because of manufacturing methods, focussing particles vertically gives significantly more options in the design of fluid channels.

Focussing particles in a vertical plane down a fluid channel has given rise to some complex applications. It is possible to switch particles from one medium to another. This can be done with relatively little contaminant being pulled into the clean medium as long as a buffer zone is used at the outlet. For this application it is also important not to apply too much force to the particles. The greater the force, the faster particles switch stream, which causes turbulence in the flow. This mixes the two fluids and hence contaminant is pulled into the clean flow (Petersson et al., 2005). Such a procedure can be used to extract blood cells from their carrier fluid. Depending on the application, it may be vital that very little of the carrier fluid transfers into the clean fluid. If this is the case, the particles can be washed more than once, decreasing significantly the contaminant pulled across. Two washes are all that is needed to compare to current procedures, Figure 2-18 (Augustsson et al., 2009).

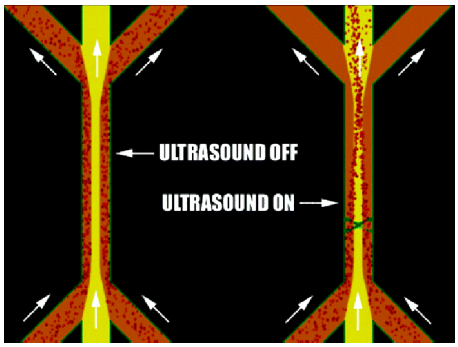

Figure 2-18 A schematic showing how particles can be removed from their original carrier fluid using lateral acoustic forces. The channel width was 350 μm wide corresponding to an operating frequency of approximately 2 MHz. Reprinted with permission from (Petersson et al., 2005). Copyright 2005 American Chemical Society.

This ability to focus particles in a vertical plane can be used to separate particles of different size. Larger particles experience a greater force, so move to the central node faster. Smaller particles will not have moved as far towards the centre of the channel and hence can be fractionated (Petersson et al., 2007). For this to work the particles need to start at the same point, to do this they are pumped into the sides of a larger clean fluid flow. The particles are then passed through an ultrasonic field and separated based on size. Particles can be separated as long as they differ in volume, density or compressibility, or a combination of these. This device can only work if there is a noticeable difference between particles otherwise there will be an overlap of particles. Experimental work has succeeded in fractionating three different sized sets of particles. It's claimed up to 5 different sizes could be fractionated in a single device, Figure 2-19.

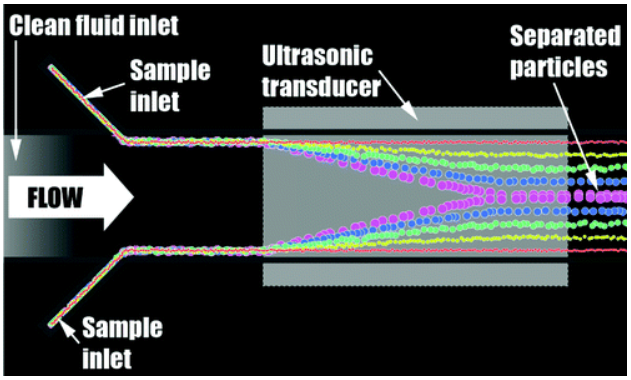

Figure 2-19 A diagram showing how particles can be fractionated using lateral acoustic forces. Reprinted with permission from (Petersson et al., 2007). Copyright 2007 American Chemical Society.

All of the devices mentioned so far use a bulk lead zirconium titanate (PZT) transducer attached to either the top or bottom of the device. The top and bottom faces have electrodes for excitation. Another option is to put two electrodes on the same side of a PZT transducer and excite them out of phase (Dougherty and Pisano, 2003). As the device hits resonance, a vertical plane of particles is formed. This is due to an effective standing wave created in the fluid chamber. The fluid chamber was made using a wet etch process, this has resulted in quite shallow side walls which may aid the focusing of the particles.

It is also possible to couple acoustic waves into a fluid channel using wedge shaped transducers (Manneberg et al., 2008). These transducers allow the PZT to be placed further from the fluid channel, which can be advantageous for optical access and will reduce heating in the fluid channel. By changing the angle at which the transducer is coupled to the device, the energy in the channel can be optimised. If two transducers are used, it is possible to focus particles into a beam in the centre of a channel rather than a plane. The ability to focus particles into a beam could have applications in cytometer devices. There are other methods to focus particles into a beam but this device has the advantage of using two distinct frequencies. This makes the behaviour of the device easier to predict and therefore easier to control.

Wedge transducers can also be used to move particles down the length of a fluid channel; the wedge needs to be coupled so that many wavelengths propagate along the channel, (Manneberg et al., 2009b). This gives many nodes which particles fall to. If the frequency is then ramped, the node positions shift along the length of the channel taking the particles with it. The frequency shift needs to be slow enough to allow the particles to move against drag forces, which is approximately 0.5Hz. If a large enough range is used, it is possible to move particles far enough along the channel that when the frequency ramp begins again, the particles will fall to a node position one place different to where it started. By repeating this frequency ramping particles can be made to traverse along the entire channel length.

2.3.1 Surface Acoustic Devices

Interdigitated transducers designed to radiate surface waves also radiate bulk waves, (Mitchell and Read, 1975) and the level of this radiation limits the performance. This is because the bulk acoustic waves interfere with the surface acoustic waves. In general 3 types of bulk excitation can exist, one longitudinal mode and two shear modes. The angle at which a longitudinal wave is radiated from interdigitated

transducers can be calculated simply from the wave velocity and the requirement that the wave shall phase match with the applied electric field.

There is a cut off frequency below which no bulk waves are generated, as the frequency increases a wave a bulk wave will be generated running parallel to the surface. As the frequency increases further the direction of the radiated wave rotates towards the bottom of the substrate, Figure 2-20.

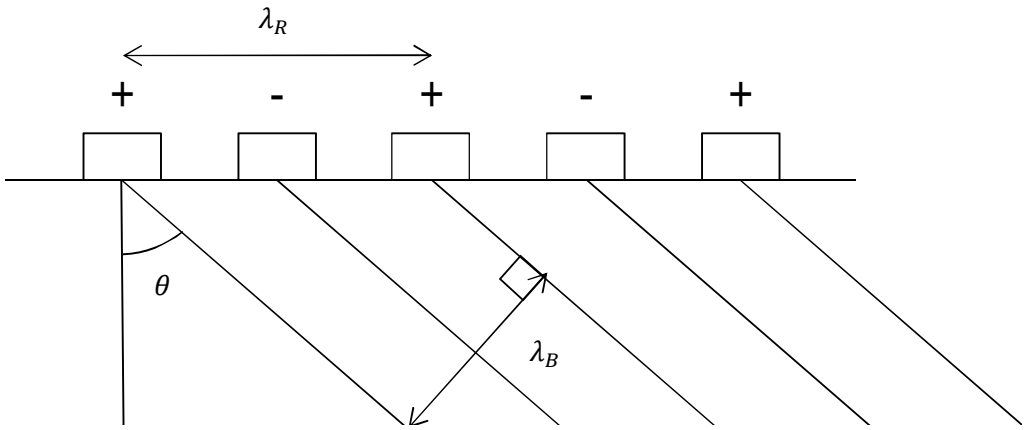

Figure 2-20 Diagram explaining bulk wave radiation in a SAW device . Reproduced from © (Mitchell and Read, 1975) [1975] IEEE.

If the radiated wave direction is different enough from the surface wave direction there will not be interference, unless it is reflected, this can be avoided by choosing a sufficiently thick substrate or roughening the underside of the substrate. Another option is to attach an acoustically absorbent material. If the wave radiation direction is sufficiently close to the surface it is likely to interfere with the device, potentially changing the expected characteristics of the device. A solution to this would be to work at a high enough frequency so that radiated waves are directed away from the surface. Other techniques rely on selecting the correct orientation of an anisotropic material to minimise bulk wave radiation. Some cuts that minimise longitudinal waves may or may not suppress shear waves. Such knowledge has led to fairly standardised cuts of materials for use as SAW devices, an example being Y+128° lithium niobate. This means that the surface of the crystal is perpendicular to the Y orientation + 128° and the chip will be orientated in such a way that the SAWs will travel along the X axis, therefore they will be X propagating. Figure 2-21 and Figure 2-22 describe the crystal orientation.

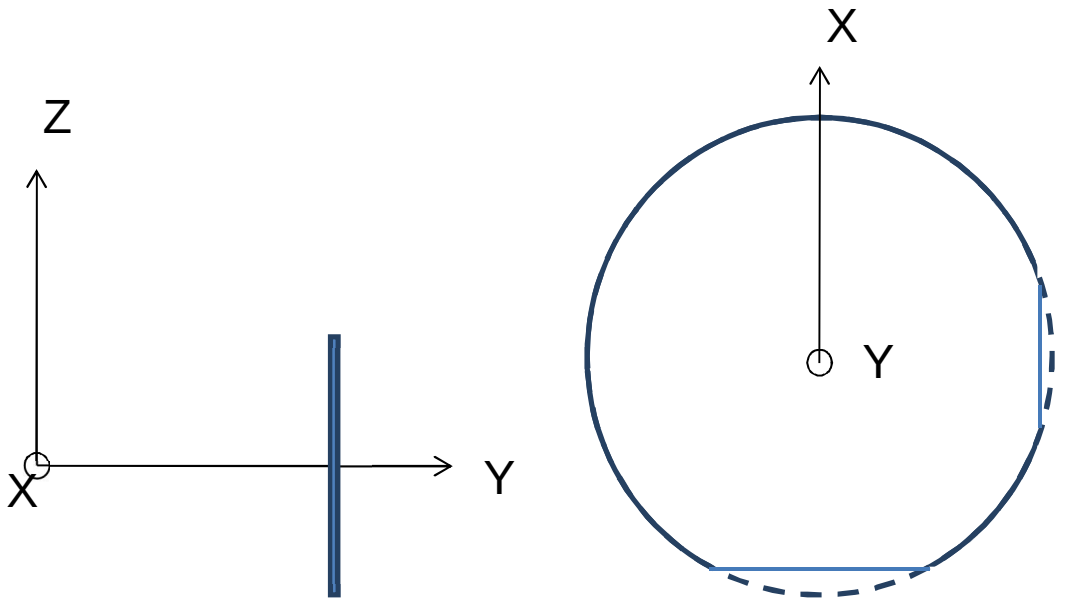

Figure 2-21 A diagram showing the crystal orientation of a Y cut X propagating wafer. The wafer is cut perpendicular to the Y axis of the crystal. Two cuts are then made across the surface of the wafer so that the direction of propagation along the wafer can be ascertained. The larger cut is made perpendicular to the X axis and the smaller cut parallel.

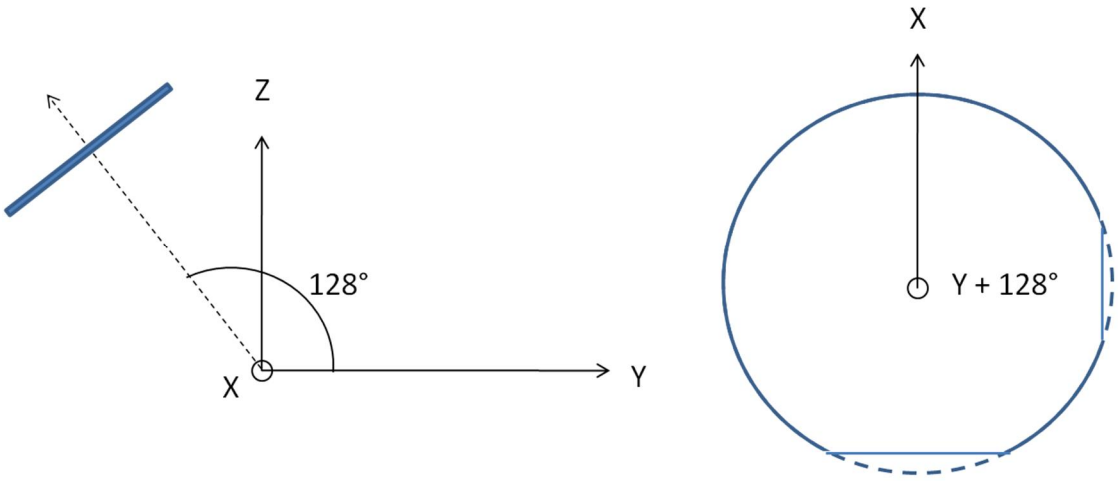

Figure 2-22 A diagram showing the crystal orientation of a Y + 128° cut X propagating wafer. The wafer is cut perpendicular to the Y axis + 128° of the crystal. Two cuts are then made across the surface of the wafer so that the direction of propagation along the wafer can be ascertained. The larger cut is made perpendicular to the X axis and the smaller cut parallel.

2.3.1.1 Travelling Wave Devices

There are several examples of how surface acoustic waves can be used to manipulate fluids and particles within fluids. One method is to move droplets of fluid on the surface of a chip (Wixforth, 2003). By applying a surface acoustic wave across the

surface of the chip, the droplet absorbs the energy and can be moved in the direction of the propagating SAW.

Most of the energy of the wave is absorbed, very little escapes to propagate further across the chip. This means two droplets can be pushed together and mixed. Such a technique can be used to conduct small chemical experiments. It is even possible to force a droplet of oil over other droplets of interest. This has two uses; firstly the chip can be heated and the oil can be used to carry the heat to the droplet, secondly by covering the droplet, the reactants in the droplet cannot evaporate, (Guttenberg et al., 2005). By printing hydrophilic tracks on the surface, the particle movement can be confined to certain directions. There are further uses to this technology; a reactant can be printed on to the surface of the chip, then a droplet moved over it. Acoustic streaming can then be induced to force the reactant into the droplet. This speeds up chemical reactions. These devices work using travelling waves, shown below, Figure 2-23.

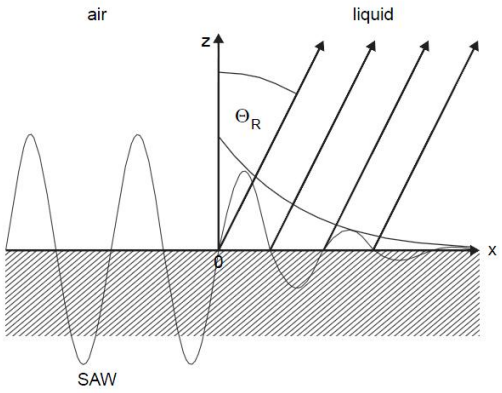

Figure 2-23 Diagram showing how a SAW can generate motion in a droplet. Reproduced from (Guttenberg et al., 2005) with permission from The Royal Society of Chemistry.

The mechanism which causes droplets to move across a surface has been explained (Beyssen et al., 2006). Surface acoustic waves travel across the substrate until they come into contact with the droplet. At this point a leaky SAW wave is generated, transferring energy into the fluid. Streaming and radiation forces are both present, which cause the droplet to distort. The energy is directed at an angle into the droplet, causing the droplet to be propelled across the surface of the substrate, providing the amplitude is high enough. This mechanism is cyclical at approximately 120 Hz for pure water. If a suitable hydrophobic film with a low sliding force is used, droplet velocities of 40 mm s^{-1} are achievable, Figure 2-24. Typical droplet volumes are

2-20 µL and typical hydrophobic coatings are polyvinylideneflouride and carbon monoflouride.

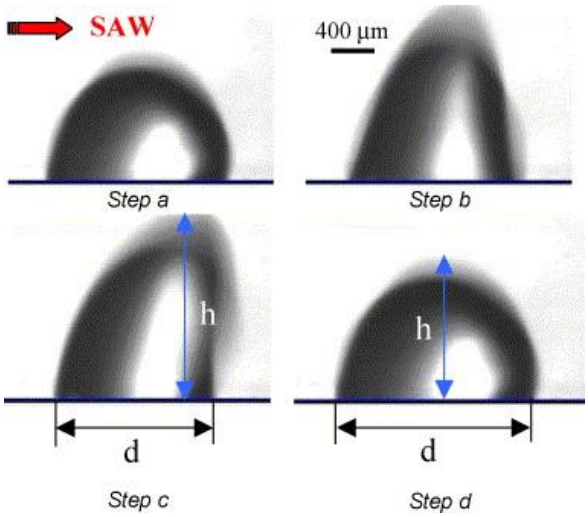

Figure 2-24 . Diagram showing the mechanism behind droplet motion. Step a; the droplet is visible on the surface with a contact angle almost perpendicular to the surface. Step b; The SAW is absorbed by the droplet causing an elongation and a reduction in the contact angle. Step c; the droplet leans with the direction of the SAW. Step d; the droplet falls to form a standard droplet but has shifted in the direction of the SAW. This happens at a frequency of approximately 120 Hz. Reproduced from (Beyssen et al., 2006) Copyright 2006, with permission from Elsevier.

2.3.1.2 Flow Free Standing Wave Devices

The devices previously mentioned are open to the air, confining the fluid causes other effects. If a droplet is placed on a substrate and a glass slide is placed over the top the liquid cannot move. If a pair of electrodes are used either side of the fluid droplet, a standing wave can be created. This standing wave generates pressure differences across the fluid. Particles within the fluid will fall to a pressure minima. This would create lines of particles, however if a second pair of electrodes perpendicular to the original are also used, particles can be focused to spots (Wood et al., 2009). This device can be used to enhance sensor detection. Lithium niobate is the most common material for this type of device. To keep the excitation frequency the same, the wavelength in each direction will be different. This is due to the anisotropic properties of lithium niobate. There will also be higher losses in the secondary direction due to a lower piezoelectric coupling coefficient. The device can focus 0.5 µL at a time, however this could be scaled up, Figure 2-25.

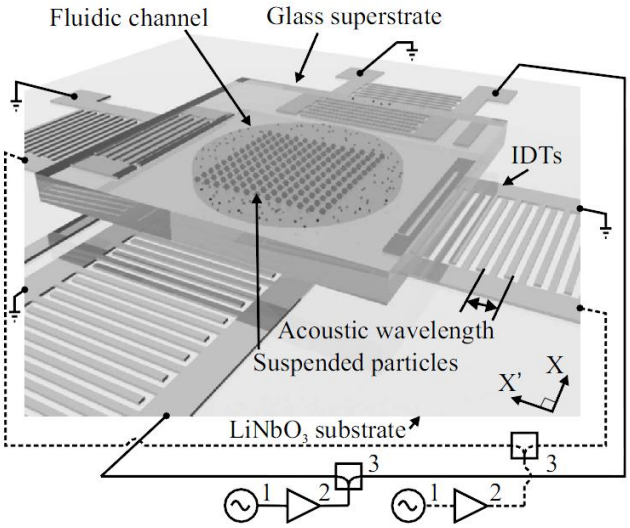

Figure 2-25 Diagram showing how two pairs of SAWs can trap particles. Reprinted with permission from (Wood et al., 2009). Copyright [2009], AIP Publishing LLC.

Surface acoustic waves can also be used to clean surfaces (Sankaranarayanan et al., 2008). Biofouling is the term used to describe the adhesion of non-specific proteins to surfaces. This can affect any biological lab on chip device. If these proteins can be removed more accurate readings from sensors can be taken and the possibility of re using devices becomes a reality. High frequency surface acoustic waves can induce acoustic streaming; this continuous flow provides enough viscous drag to pull loosely bound protein molecules away from the substrate. Acoustic streaming generates a fluid flow tangential to the substrate which drags the proteins off. A significant amount of lift is also produced which stops the proteins re-bonding.

The generated flow rate is directly related to the applied voltage, a particular device generated flow speeds of 1 cm s^{-1} using voltages as low as 1 V_{pp} (Sankaranarayanan et al., 2008). Higher frequencies also results in higher streaming flows, however a higher frequency requires more expensive electronics and there is a limit to the minimum width and spacing of interdigitated fingers that can be produced. Increasing the density and viscosity of the fluid will reduce the speed of the streaming flow, which will result in lower lift forces.

2.3.1.3 Flowing Standing Wave Devices

In a similar method to that above, a standing wave can be set up in a fluid. However, if the fluid channel is only half a wavelength, there is only one pressure minimum for particles to fall to (Shi et al., 2008). This should theoretically cause the particles to fall to the centre of the bottom of the channel as this is where a node is usually created in a standing wave device. However, the standing wave couples with

the opposite corners off the channel to lift the particles to the centre of the channel. There has been little computational work published on this, such work may generate a better understanding of the mechanisms at work.

For the device to work, a relatively soft plastic such as PDMS needs to be used. This allows the channel walls to resonate, forcing particles to the channel centre. This device has quite a high throughput, and could have applications in a flow cytometer because it is continuously flowing. The extent to which the particles focus is dependent on the excitation frequency. Higher frequencies will lead to a higher pressure gradient, which will push particles closer together. This is because the acoustic radiation forces are balanced against interparticle forces such as Bjerknes, van der Waals and electrostatic forces. However, higher frequencies require smaller fluid channels, limiting the flow rate, Figure 2-26.

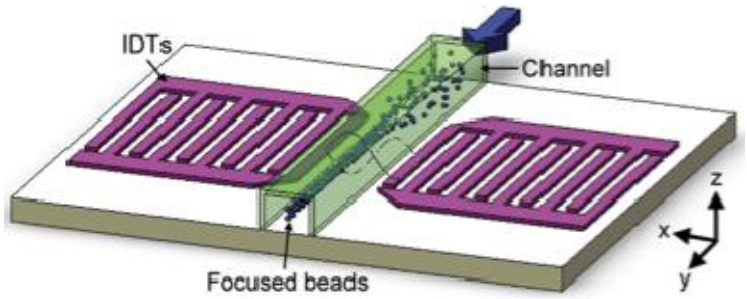

Figure 2-26 Diagram showing how a SAW can focus particles in a fluid flow. Reproduced from (Shi et al., 2008) with permission from The Royal Society of Chemistry.

2.3.2 Hydrodynamic Devices

It is possible to focus, order and separate particles within a microfluidic channel using only geometry effects and secondary flows. An example is the sheath flows used to focus a stream of particles for μ-FACS. Devices like this do not require the integration of powered components, so are less complex and in general cheaper, (Hsu et al., 2008). These devices can be sorted into two main categories, those with and those without secondary flows. Devices not requiring additional fluid have an advantage in that they can operate for extended periods of time without human interaction and without diluting the sample.

2.3.2.1 Flow Assisted Hydrodynamic Separation

Recent work by Wu, (Wu et al., 2009), separated bacteria from human blood cells by manipulating fluid flow characteristics. The device uses a sheath flow and an acting flow to focus the stream of blood cells and bacteria. By choosing suitable channel

geometry the two particle fractions are separated. The device has a throughput of 18 µL min^{-1}, which is of similar in magnitude to ultrasonic devices. The cells were tested after and were viable. The work overcame several specific problems; High throughput requires high flow rates. These high flow rates will lead to high shear stresses at the walls, which will damage the cells, (Hu et al., 2005). To protect the cells a sheath flow was incorporated into the design. This sheath flow also stopped cells sticking to the channel walls. Another issue in separating the cells from bacteria is that because of the disc shape of red blood cells, the thickness dimension is very similar to bacteria dimensions. This problem was solved by using a design that distinguished between the momentum of the cells. By focusing the particles into a tight stream, they have near identical velocities; therefore the separation is based upon the different mass of particles, see Figure 2-27.

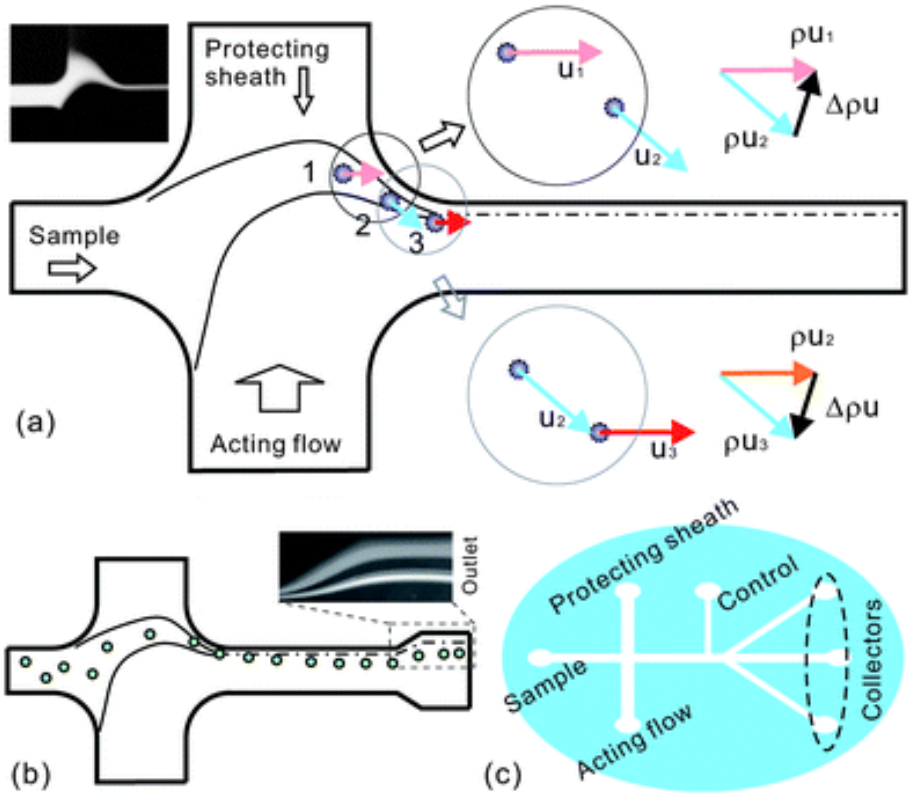

Figure 2-27 A series of images showing how cells can be sorted based on momentum using sheath flows and changes in direction. Reproduced from (Wu et al., 2009) with permission from The Royal Society of Chemistry.

In Figure 2-27(a), from points 1-2, the flow is compressed, resulting in an acceleration of the fluid. Drag forces also cause the particles to accelerate. The particles then have near identical velocities. From points 2-3, the flow changes direction, the heavy red blood cells (RBC's) take longer to change direction as they

have a higher inertia, so leave the stream line containing the bacteria. This can be seen Figure 2-27(b), where the green particles denote RBC's and the dashed line denotes the path of the bacteria. At the end of the channel the fluid flow is expanded. This slows the fluid which amplifies the different particle streams, enabling the different fractions to be collected.

The device is simple in principle though it needs careful balancing. The acting flow adds a considerable volume, approximately 10 times that of the sample, this will potentially dilute the sample. The flow rate is not particularly high at only 1 mL hr^{-1}, but it would be easy to run several devices in parallel. For the device to work the two different fractions need to have different quantities of inertia, which may not always be the case. Whilst this technique requires little power, it may be unusable in a remote sensing system, due to the heavy dependency on additional fluid, which would also require pumps and reservoirs to be integrated into the system.

2.3.2.2 Hydrodynamic Separation and Focusing

It is possible to guide particles across a fluid flow using a device with a chevron pattern on its roof, (Hsu et al., 2008). The chevrons cause micro vortices to form, which guide particles to the apex of a chevron. This movement occurs over several chevrons, provided the particle is denser than the fluid it is immersed in. By placing sets of chevrons on the roof of the channel it is possible to traverse a particle almost the entire width of the channel. For this to work there must be sufficient gap between the sets of chevrons, allowing the flow to return to laminar conditions. The width of the chevrons must also be wide enough to encompass the apex of the previous chevrons. Typical Reynolds numbers for such a device are Re=0.003. Figure 2-28 shows a particle trajectory. It can be seen that the particles always leave a set of chevrons in the centre, before being picked up by the micro vortices created by the next set of chevrons and are pulled across the channel

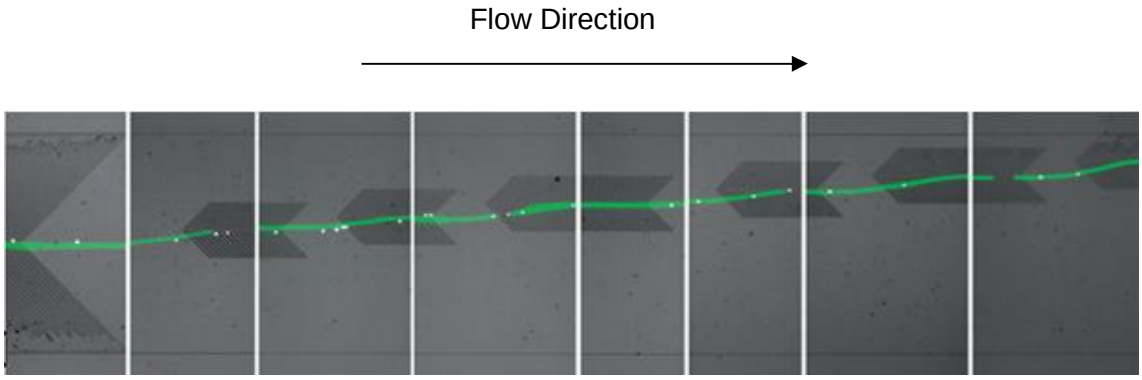

Figure 2-28 Diagram showing the path of a particle passing through chevrons. Reproduced from (Hsu et al., 2008) with permission from The Royal Society of Chemistry.

As previously stated, particles denser than the fluid will be guided to the apex of the chevron; they will also sit at the bottom of the fluid channel. If a second set of particles were added; which were lighter than the fluid, they would be guided to the edge of the chevrons and sit at the top of the channel. By placing sets of chevrons next to each other, both forward and backward apexes are created. This herringbone pattern can separate particles that are denser than the fluid from particles that are less dense. The limiting factor here is the slow flow rate. It would be possible to extend the width of the device to allow more chevrons. Issues may arise in keeping a constant flow rate across the entire width of the device, Figure 2-29.

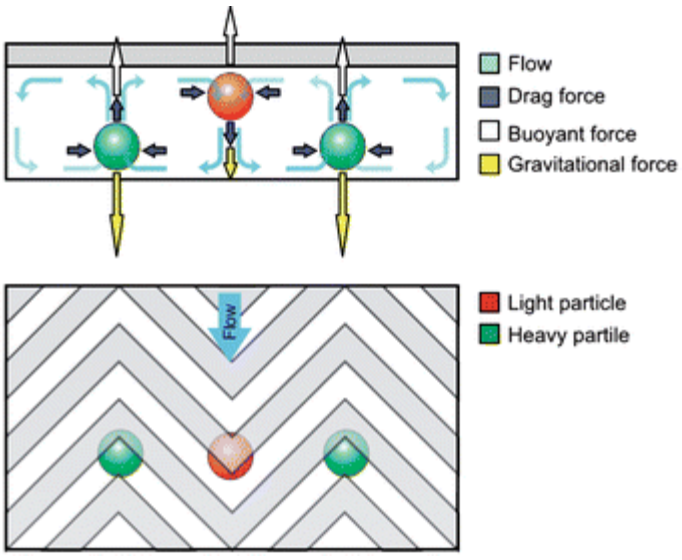

Figure 2-29 Diagram showing the mechanism which causes particles to separate. Reproduced from (Hsu et al., 2008) with permission from The Royal Society of Chemistry.

This method provides a cheap, simple way of separating two fractions, depending on the fluid density. For many tasks this may require a secondary fluid to be

mixed into the fluid before it reaches the separator. This is because it is unlikely the natural carrier fluid has a density in between the two fractions to be separated. This will ultimately make the device design more complicated. It is also limited in that it can only separate two different fractions of particles. The slow flow rate and potential need for additional fluid will limit its potential in remote sensing.

Sending a flow through a repeatedly curving fluid channel can cause particles to focus into a tight beam, Figure 2-30. In the case of red blood cells, they are also rotated so they travel with the same orientation, (Di Carlo et al., 2007). This effect is due to secondary Dean forces created within the fluid channel. Such a device has a relatively high throughput of 1.5 mL min^{-1} with a Reynolds number in the order of 100. The device places different sized particles in different places within the channel, but does not differentiate between particle densities. The separated positions in reality are very similar, so it may be difficult to fractionate particles using such a device. The main advantage of this device is that it can focus 10 µm particles to within a 0.8 µm tolerance and also rotate non spherical particles to the same orientation. This method could prove useful in remote sensing because of its low power requirements and the fact it does not need sheath flows, meaning that the sample is not diluted.

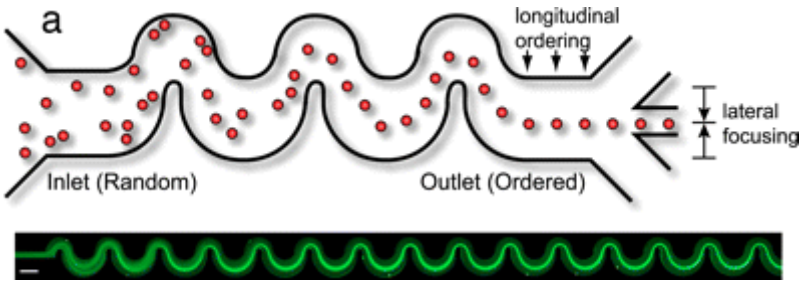

Figure 2-30 Images depicting how particles can be focused using only channel geometry, such a device could increase particle concentration and also align particles for sensing later in the channel. Reproduced from (Di Carlo et al., 2007). Copyright 2007, National Academy of Sciences, USA

2.4 Summary

This chapter has described the physics behind ultrasonic particle manipulation devices. The work initially derives the equations governing bulk acoustic waves before describing how such waves interact at boundaries and how matching layers can be used to increase acoustic efficiencies between materials of differing impedance. The chapter goes on to derive the equations governing surface acoustic waves and present key ideas such as leaky Rayleigh waves and generation techniques. Much of this work was presented in “Acoustofluidics 17: Theory and applications of surface acoustic wave

devices for particle manipulation, Lab on a Chip, Volume 12, Issue 17, 2998-3007, (Gedge and Hill, 2012)". The chapter goes on to describe the acoustic radiation force and the key equations.

The work then describes key microfluidic principles such as reynolds number, hydraulic resistance, hydraulic compliance and capiliarity. The work highlights potential problems and solutions likely to be encountered when undertaking microfluidic experiments. The last section describes the progression of ultrasonic particle manipulation devies from 1 dimensional to 3 dimensional manipulators and the associated techniques and methods. The work describes surface acoustic wave devices, in particular the state-of-the-art device presented by Shi et al (Shi et al., 2008). Finally, the section describes some hydrodynamic particle manipulation devices that are of interest due to the fact they do not require power, which make them suitable for use in an *in-situ* oceanographic device.

Chapter 3 Manufacturing and Design Techniques

The following chapter identifies manufacturing techniques that will be useful in the design of remote *in-situ* oceanographic sensors. The chapter looks at methods to generate a piezoelectric substrate and the general design of bulk acoustic wave devices. The chapter goes on to look at the properties of PDMS and why it is popular in microfluidic devices. Manufacturing techniques for PDMS are covered along with some example uses. The chapter finishes by looking at some techniques for building microfluidic devices.

3.1 Piezoelectric Materials

Ultrasonic particle manipulation takes advantage of the piezoelectric properties of certain ceramics. When loaded, these ceramics develop a charge, proportional to the mechanical strain. This effect is reversible, producing mechanical strains when electrically loaded. Depending on the electrical loading, different structural resonances can be achieved. These high frequency sound waves can be coupled into other mediums, such as solids and liquids, which in turn can manipulate particles in suspension. PZT is commonly used for bulk excitation devices whilst lithium niobate is commonly used in devices generating surface waves. The following section looks at different manufacturing techniques that can be used in conjunction with piezoelectric materials.

3.1.1 PZT

Early ultrasonic devices were predominantly made from metal. The PZT was attached to a steel base plate and matching layer, with a brass spacer and steel reflector (Hawkes and Coakley, 2001). As the technology has improved, new materials have come into use. It became common for silicon to be used for the majority of the device coupled with a Pyrex reflector layer (Harris et al., 2003). More recently, Macor has been used because of its superior acoustic properties and machinability (Hill et al., 2008). Soda glass is now commonly used as a reflector as it is easily available. It has also recently been shown that Lithium Niobate can be used instead of PZT, which gives advantages in terms of optical access (Shi et al., 2008). Polymers are

increasingly being used for ultrasonic devices, predominantly because of the quick and easy fabrication techniques.

Most acoustic excitation devices use bulk PZT bonded to the structure or bonded via a carefully angled wedge to transmit the acoustic energy (Harris et al., 2006, Manneberg et al., 2008). In many cases, this requires careful alignment which takes time and is not always repeatable. The bonding layer also affects the characteristics of the device.

3.1.2 Lithium Niobate

Lithium niobate is predominantly used in the generation of surface acoustic waves, but there are orientations that exist which allow the generation of bulk waves. This is due to the anisotropic nature of the crystal. The following section looks at potential manufacturing techniques that could be used on lithium niobate which would retain the transparent optical properties.

3.1.2.1 Conducting Polymers

Conducting polymers have received much interest in recent years in particular poly(3,4-ethylendioxythiophene), or more commonly, PEDOT. This is due to its high stability, optical transparency and electrical conductivity (Groenendaal et al., 2000). Initially its insolubility limited its use, but it has since been dispersed in poly(styrenesulphonic acid), or PSS. This results in a dark blue aqueous solution that is available commercially and can be spin coated (Zhang et al., 2005). It is used in antistatic coatings and as an electrode material (Ha et al., 2004). The chemical backbone of PEDOT and PSS is shown in Figure 3-1.

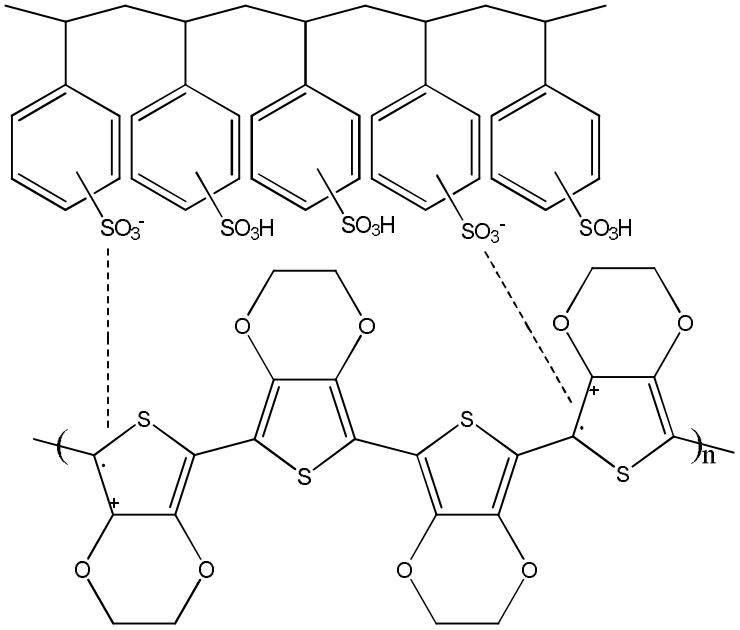

Figure 3-1 The chemical backbone of PEDOT:PSS. The PSS chain is shown above the PEDOT chain. The double bonds in the thiophene rings interact with the sulphonic acid associated with the PSS. Reprinted from (Groenendaal et al., 2000). Copyright 2000, with permission from John Wiley and Sons.

As expected, the composition of the PEDOT:PSS will affect the conductivity and optical transmittance of the generated film as will the thickness. There are many similar compounds available with various other chemical groups attached or involved, all with varying optical, electrical and mechanical properties. PEDOT:PSS has been identified as a possible coating for use with lithium niobate for the production of a transparent bulk acoustic wave transducer.

3.1.2.2 Indium Tin Oxide

Indium Tin Oxide (ITO) films are electrically conductive and also transparent. The thickness of the film will determine its electrical conductance and light transmittance. As expected, the thicker the film the lower the resistance, see Figure 3-2. However, more light is absorbed (Pokaipisit et al., 2007). Films can be prepared in numerous ways such as laser deposition, thermal deposition, reactive evaporation or D.C. magnetron sputtering (George and Menon, 2000). For the purpose of this work, only electron beam evaporation (e-beam) will be covered as this is the process available. E-beam evaporation is a type of physical vapour deposition, which involves releasing a material from a source and transferring it to a substrate. In the case of e-beam evaporation, this is done by evaporating the material using electron bombardment and allowing the vapours to condense on an overhead substrate. The electron beam is

controlled using a magnetic field so that the electron source can be positioned below the evaporation line (Ferrotec, 2012).

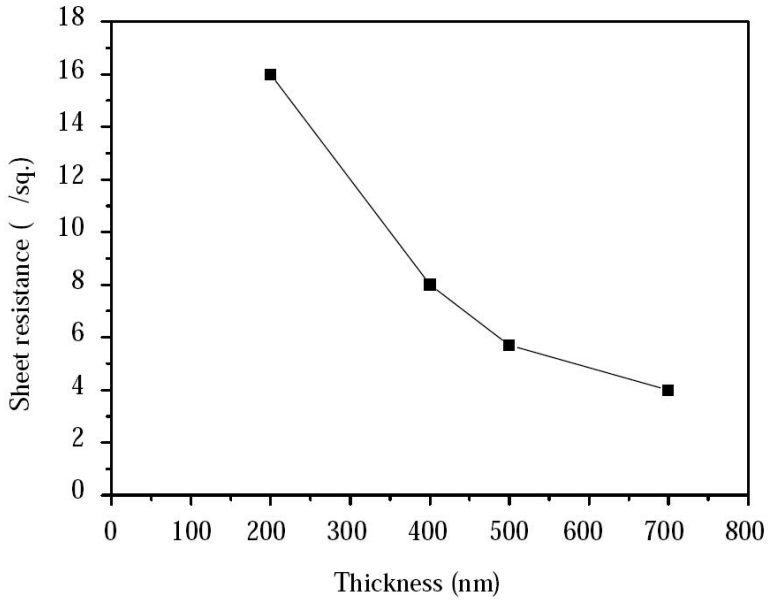

Figure 3-2 The effect of film thickness on the sheet resistance of an ITO film prepared by e-beam evaporation. Reproduced from (Pokaipisit et al., 2007). Copyright 2007, with permission from kasetart.

To coat a substrate a mixture of In_2O_3 and SnO_2 is vaporised under a partial pressure of oxygen. Typical ratios of indium oxide to tin oxide are 4:1 by weight for optimum electrical conductance, see Figure 3-3 (George and Menon, 2000). The electrical conductance comes from oxygen vacancies within the lattice as well as the incorporation of Sn atoms in the indium oxide (Karasawa and Miyata, 1993).

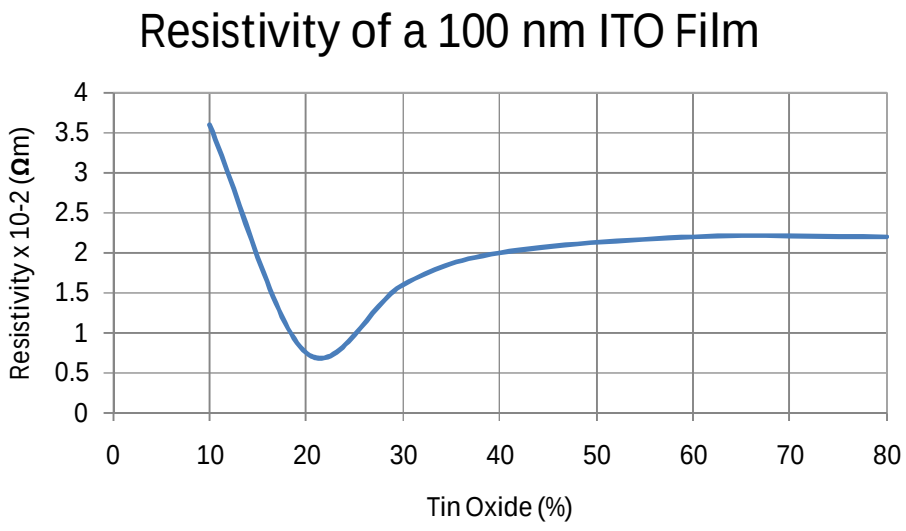

Figure 3-3 Resistivity of a 100 nm thick ITO film of varying composition. Reproduced from (George and Menon, 2000). Copyright 2000, with permission from Elsevier.

For improved optical transmittance, the film needs to be heat treated. This is usually an annealing process after deposition (Kobayashi et al., 1992). The annealing process also improves the electrical conductivity of the film and is usually carried out at temperatures between 350-550 °C. Higher annealing temperatures lead to better conductivity and optical transmittance. This is due to improved crystallinity of the film (Fallah et al., 2007). Some e-beam techniques deposit the ITO film at an elevated temperature; higher temperatures (350°C) lead to better conductivity and optical transmittance (George and Menon, 2000). ITO has been identified as a possible coating for use with lithium niobate for the production of a transparent bulk acoustic wave transducer.

3.2 Polydimethylsiloxane (PDMS)

The first microfluidic devices were constructed from silicon (Terry et al., 1979); subsequently, ceramics such as Pyrex, soda glass and fused silica were used. This was because the techniques needed to make such devices were readily available from the semiconductor industry (Becker and Locascio, 2002). The main draw back with using ceramics is the time and money needed to produce devices. Wet and deep reactive ion etching (DRIE) both require expensive equipment, skilled technicians and the use of a clean room. Wet etching also requires chemicals, which need to be dealt with properly after use. Micro machining and anodic bonding of these ceramics is also time consuming and expensive. These factors have led to the increased use of polymers as microfluidic chips. Of particular interest is Polydimethylsiloxane, an organosilicon that is considered inert and non-toxic (McDonald and Whitesides, 2002, Mark, 2009). PDMS lends itself particularly well to casting; a Silicon master can be re-used approximately 100 times without degradation (Thibault et al., 2006).

3.2.1 Curing

A PDMS called Sylgard 184, produced by Dow Corning, is frequently used for microfluidic chips. The PDMS comes in two parts, a base agent and a curing agent. The ingredients of interest being dimethylvinyl-terminated dimethyl siloxane and dimethyl methylhydrogen siloxane for the base and curing agent respectively. The curing agent also contains Speier's catalyst, H_2PtCl_6 (IMSLab, 2010). The base and curing agent are mixed together typically at a ratio of 10:1, and a hydrosilylation reaction occurs. The double bond in the vinyl group at the end of the chain opens up and forms a bond in place of the S-H bond on the curing agent. The base agent can make a maximum of two bonds, one at each end of the chain. The curing agent can

make many bonds along its -Si-O- backbone; this explains why the ratio of base to curing agent is not 1:1. The multiple reaction sites on both chains allows a dense 3D network to be created. This reaction produces no waste products and its properties can be altered by changing the ratio of base to curing agent (Lisensky et al., 1999). More curing agent will produce a harder product as there will be more crosslinks. Heating also accelerates the rate at which the bonds form.

The base agent usually has a chain length of approximately 60 units compared to approximately 10 units for the curing agent (Lisensky et al., 1999). The hydrosilylation reaction is shown in Figure 3-4.

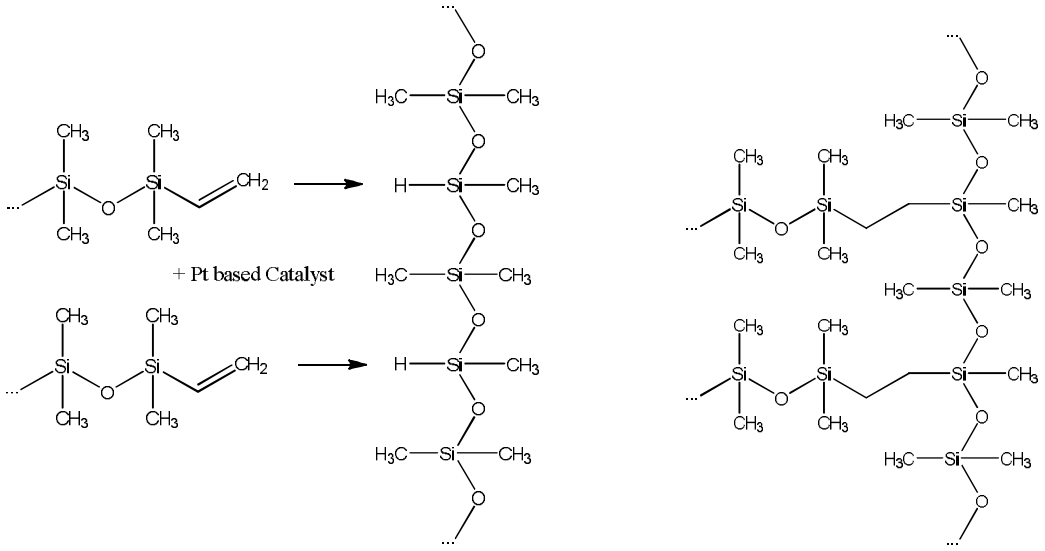

Figure 3-4 Diagram showing how the base agent of PDMS attaches to the curing agent. The base agent is shown horizontally and the curing agent vertically. Reprinted with permission from (Lisensky et al., 1999). Copyright 2000, American Chemical Society.

3.2.2 Surface Treatments and Forming Channels

An advantage to using PDMS is that it can seal to itself or other surfaces reversibly or permanently with minimal distortion of channels (McDonald et al., 2000, Duffy et al., 1998, Jo et al., 2000). The process of sealing PDMS is significantly easier than sealing channels in glass, silicon or thermoplastics (Soper et al., 2000, Madou, 2002, Martynova et al., 1997). A reversible seal can be formed by van der Waals contact, however the seal cannot withstand pressures of more than 5 psi (McDonald et al., 2000). The seal can be broken by simply peeling the PDMS off the surface it is in contact with. The PDMS can then be cleaned and re-sealed with minimal degradation of the PDMS (McDonald et al., 2000). Cellophane or silicone tape can be used to seal devices, but such methods are temporary and not as strong as irreversible bonding techniques such as oxygen plasma (McDonald et al., 2002).

3.2.2.1 Oxygen Plasma Bonding

Exposing a polymer to a plasma results in fundamental changes to its surface properties. Most notably, wettability and the molecular weight and composition of the surface change. On the whole, these effects only protrude 1-10 µm in depth. As a result, the bulk properties of the samples don't change. The contact angle formed between a water droplet and a surface defines its wettability (Adamson, 1960). Plasma processes are able to alter the wettability making surfaces more susceptible to the adherence of dyes, inks, adhesives and other polymers. These processes can be used to print and label on inert polymers such as electrical wiring. Plasma processes can also be used to alter the chemical composition of a surface to better suit its requirement, an example being the doping of medical polymer tubing with amines which can then be coated with a coagulant such as heparin to minimise clotting (Bell et al., 1974).

Oxygen plasma treatment of silicones has been studied for over 40 years. Initial work by Hollahan and Carlson investigated surface changes using infrared spectroscopy (Hollahan and Carlson, 1970). By soaking plasma treated samples in D_2O and looking at changes in the infrared spectra the group showed that an oxygen plasma treatment increased the number of –OH groups on the surface of the silicone. The group concluded that more Si-CH_2OH bonds were formed than Si-OH. This idea has changed over the years and it is now believed more Si-OH bonds are formed (McDonald and Whitesides, 2002, Owen and Smith, 1994, Chaudhury and Whitesides, 1991). This hydroxylation of silicones can be used to form irreversible bonds, that is to say the silicone will mechanically fail before de-bonding. Oxidized PDMS can seal to itself, glass, silicon, polystyrene and many other materials provided the bonding substrate has undergone the same oxygen plasma technique (McDonald and Whitesides, 2002). The mechanism for bonding PDMS to PDMS is shown below, Figure 3-5. Initially, the two surfaces are exposed to oxygen plasma which scissors off CH_3 molecules and replaces them with OH molecules. When these two treated surfaces come into contact, the hydroxyl groups condense releasing water molecules, forming permanent bonds between the two samples (IMSLab, 2010).

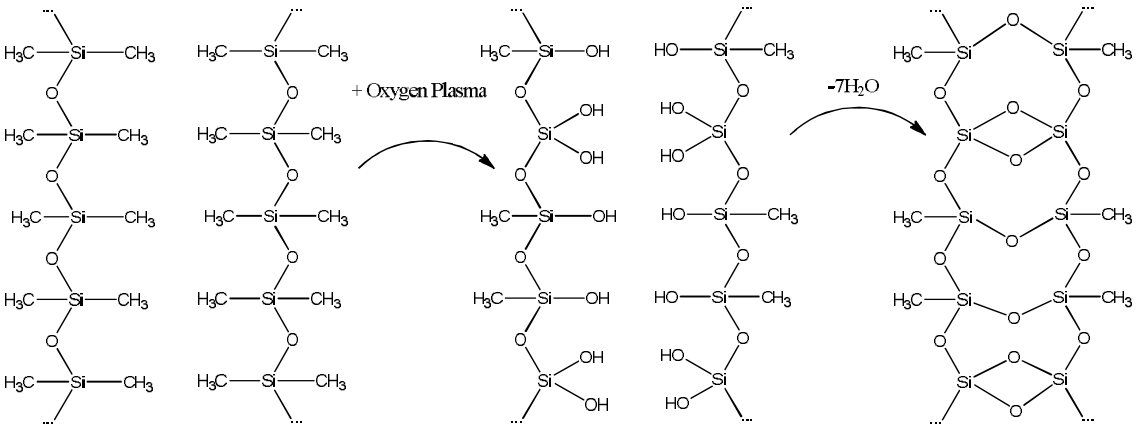

Figure 3-5 Schematic showing the process of covalently bonding two PDMS surfaces using the oxygen plasma technique.

The effectiveness of the bonding is heavily dependent on the reactor pressures, plasma powers and time (Jo et al., 2000, Bhattacharya et al., 2005). Generally speaking, best results can be obtained with high reactor pressures, low plasma power and short times. Low pressures cause the sample to be bombarded with high energy ions which break down the –Si-O- backbone and weaken the surface layer. Prolonged exposure to oxygen plasma causes too much SiO_2 to form which is weak and brittle (IMSLab, 2010). It has also been suggested that prolonged exposure will cause damage to the -Si-O-backbone, yielding shorter chains, which ultimately will not be able to bond as well as long interlocking chains (Awaja et al., 2009). One advantage of plasma treatments is that they can change the surface of the sample without changing the properties of the bulk of the material (Egitto and Matienzo, 1994).

3.2.2.2 Oxygen Plasma Surface Treatments

PDMS is hydrophobic which gives it applications where repelling water is desirable, such as outdoor electrical cable (Simmons et al., 1997, Hillborg and Gedde, 1998). After oxygen plasma treatment, the exposed surface becomes hydrophilic as a layer of SiO_2 forms on the surface, approximately 8-10 nm thick (Owen and Smith, 1994). This layer of SiO_2 can be dissolved by leaving the sample in a solution of hydrogen fluoride. The PDMS can then be plasma treated again (Chou et al., 1985). Oxidised PDMS is unstable in air and undergoes hydrophobic recovery; near total hydrophobic recovery can be obtained within one week (Owen, 2005). The useful lifetime of oxidised PDMS in air for bonding is in the order of minutes. This hydrophobic recovery has been extensively studied over the years, but only recently has a general consensus been formed. It is believed the migration of untreated polymer chains from the bulk of the PDMS onto the surface of the PDMS is the main mechanism. Surface

cracks in the brittle SiO_2 layer allow this to happen, Figure 3-6 (Owen and Smith, 1994). Owen and Smith showed that treated samples of PDMS would recover hydrophobicity quicker if they were deformed, causing cracks in the surface, thus allowing untreated PDMS to diffuse to the surface. The SiO_2 layer on the surface of the PDMS is considerably denser than the bulk PDMS. This glassy top layer will therefore experience tensile stresses that would cause cracking. These cracks would allow for the transport of PDMS to the surface and render the surface hydrophobic again (Hillborg and Gedde, 1999, Hillborg and Gedde, 1998). Other suggested mechanisms include the condensation of hydroxyl groups on the surface or the reorientation of the surface silicone chains (Morra et al., 1990).

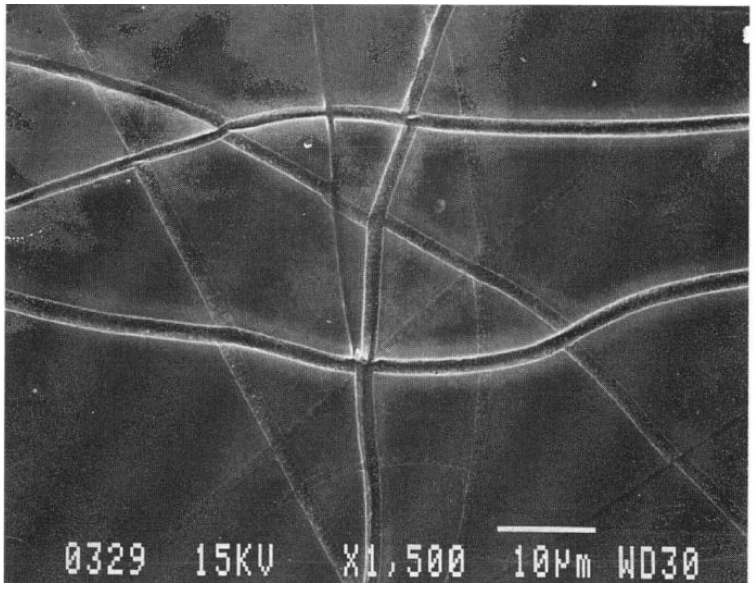

Figure 3-6 SEM image of the surface cracks that appear on plasma treated PDMS. Reproduced from (Owen and Smith, 1994). Copyright 1994, with permission from Taylor & Francis.

There are several methods available to prolong the hydrophilic nature of oxygen plasma treated PDMS, such as ageing the sample in water rather than air (Morra et al., 1990). Methanol has also been used to prolong hydrophilicity and allows for the orientation and alignment of different layers. This method was used to construct a five layer thick 3D mixer, Figure 3-7 (Jo et al., 2000). The same group showed that untreated PDMS that had been aged in air for two months could be cleaned with dilute hydrochloric acid (HCl) before oxygen plasma treatment and complete bonding will still occur.

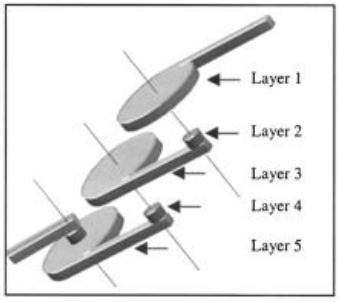

Figure 3-7 Diagram showing how 3D structures can be manufactured in PDMS. Reprinted, with permission, from (Jo et al., 2000). © 2000, IEEE.

The group also partially covered samples of PDMS during the oxygen plasma treatment, the covered parts of the sample retained hydrophobicity whilst the uncovered parts became hydrophilic. This effect has been used by other groups to pattern PDMS surfaces with various different metals for use in assay applications (Séguin et al.). A different application of this method showed different effects. The formation of hydrophilic channels on PDMS, where a copper mesh was in contact with the PDMS during oxidising, see Figure 3-8. The area of the PDMS exposed to the oxygen plasma showed no chemical change. The group concluded that this was down to the charging of the copper mesh which attracted the plasma ions, stopping them from reacting with the unmasked PDMS. The group also believe the charging of the copper mesh caused a reaction between the copper oxide and the surface of the PDMS (Hsieh et al., 2009).

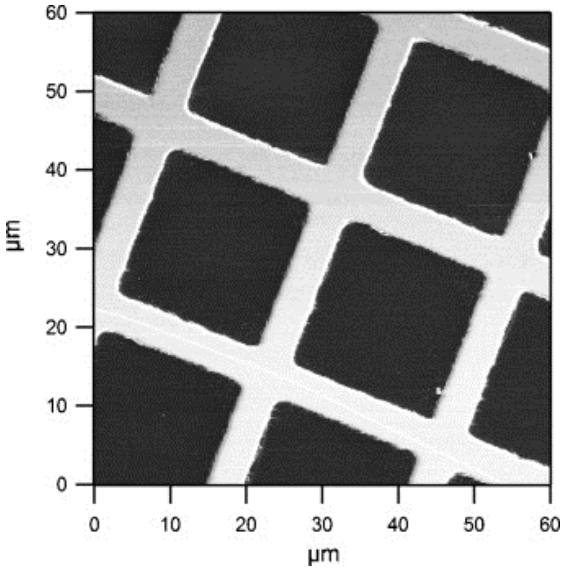

Figure 3-8 A friction image depicting the difference between plasma treated PDMS and the PDMS that was covered by a copper mesh. Light areas depict high friction areas. The image shows that there are chemical differences between exposed areas and covered areas. Reprinted from (Hsieh et al., 2009). Copyright 2009, with permission from Elsevier.

Using the oxygen plasma treatment on PDMS brings another advantage. Normally PDMS is hydrophobic which causes problems in filling PDMS channels with solutions and in supporting electroosmotic flow (Paul, 2010). This problem can also be solved by priming the channels with chemicals such as ethanol or HCl (Linder et al., 2001), or gases such as CO_2 (Folch et al., 2000). These alternatives do not change the hydrophobicity to the extent of oxygen plasma treatments; however, the effects of oxygen plasma can be short lived, (15 min) as the surface regains hydrophobicity (Paul, 2010).

Another group has shown that small drops in the hydrophobic nature of PDMS can be accomplished by increasing the fraction of curing agent in the PDMS. Samples of PDMS were prepared at ratios of 10:1, 10:2, 10:3 and 10:4. The samples showed a decrease in hydrophobicity, but an increase in surface roughness was also noted (Choi et al., 2009).

3.2.2.3 Chemical Bonding

There are other methods of irreversibly bonding PDMS to itself and other substrates. One method involves using semi cured PDMS samples of different ratios, 3:1 and 30:1 base to curing agent. These samples can then be brought into contact and aligned. A second curing stage allows the excess of chemicals in each sample to diffuse and then bond (Unger et al., 2000). Another method that has recently been described is a vapour assisted method. Sheets of PDMS were put in contact with glass

and placed inside a 1 litre container. Drops of tridecafluoro-1,1,2,2-tetrahydrooctyl were also placed in the container, but not touching the glass or PDMS. The samples were left for between 6 and 24 hours resulting in different strength bonds between the glass and the PDMS (Sofla and Martin, 2010). This method requires very little equipment and is very straight forward.

Chemical gluing has also been used to seal PDMS to PDMS. The surfaces to be bonded are altered to contain the functionalities found in amine-epoxy glues, and when brought into contact they seal irreversibly (Lee and Chung, 2009). The same method can be used to bond PDMS to other polymers, such as to poly(ethylene terephthalate). The method requires the use of oxygen plasma to anchor the amine and epoxy groups to the PDMS, but has a longer shelf life than standard plasma bonding. These last two methods have the advantage that no heating is required. This means temperature sensitive chemicals and components can be put through this process without being damaged.

These methods provide simple and low cost methods for the production of PDMS devices and could lead the way in terms of large scale production. Whilst oxygen plasma techniques can be very reliable, they require great care and attention as well as access to specialist equipment (Cai and Neyer, 2010).

3.2.3 PDMS in Microfluidics

There are numerous other reasons why PDMS has become so widely used in microfluidic applications. Its high gas permeability has allowed the culture of several different organisms (Chang et al., 2003) and could be useful in any application requiring exchange of gases but not liquids. It is possible to saturate PDMS with CO_2 to aid the long term growth of cells (Hirano et al., 2010). PDMS has a low thermal conductivity which could be an advantage or disadvantage depending on the application. In electrophoresis, excess heating may occur in the chip which will affect its resolution. Conversely, the low thermal conductivity of PDMS is an advantage in applications such as incubators (Hong et al., 2001). The low surface energy and elasticity of PDMS allows cured pieces to be removed from masters with relative ease (McDonald and Whitesides, 2002). Polymers can suffer from dielectric breakdown, but PDMS has good electrical insulation properties which allows it to be used in electrophoresis applications (Effenhauser et al., 1997).

PDMS also has good optical properties compared to other polymers; it is transparent down to 280 nm, making it useful for ultraviolet (UV) based detection

(McDonald et al., 2000, Tabeling, 2003). It also has a relatively low refractive index, which reduces reflectance and hence the amount of reflected excitation light.

Another reason that PDMS is frequently used in microfluidics is its solvent compatibility. A thorough study was carried out by Whitesides et al, investigating the effects of various different solvents. The group showed that PDMS is virtually unaffected by water, polar solvents and perfluorinated compounds. The work identified diisopropylamine, dipropylamine and triethylamine as solvents that caused excess swelling of PDMS. Samples were bonded to glass using the oxygen plasma technique; it was shown that some solvents induced such swelling that the PDMS will tear or even cause the glass to crack (Lee et al., 2003). When PDMS is cured, not all the polymer chains crosslink. These oligomers are likely to be involved in the return of hydrophobicity to plasma treated PDMS as they are able to move more freely than cross linked chains. By soaking PDMS samples in solvents of decreasing solubility, the group were able to extract oligomers and reduce the hydrophobic recovery of plasma treated PDMS. Samples lasted as long as four days in air whilst retaining a hydrophilic surface. Extracting the oligomers will also help reduce contaminants once the devices are in use.

The mechanical properties of PDMS have also lead to its increased use in microfluidics (Ismagilov et al., 2001a). Its elastomeric nature allows for the easy connection of fluidic inlets and outlets (Tabeling, 2003). Syringe needles can be punched directly into the PDMS to connect inlet and outlet tubes (Ismagilov et al., 2001b). The relative ease with which PDMS can be deformed has also caused issues, such as channel collapse, either under gravity or suction, Figure 3-9 (Delamarche et al., 1997). This problem can be minimised with the addition of support pillars (Chou et al., 1999). The lateral collapse of channels can also be seen when they are positioned too close together (Delamarche et al., 1998).

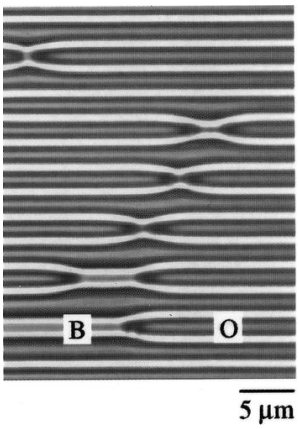

Figure 3-9 An optical micrograph showing the lateral collapse of PDMS walls in a microfluidic device. Channels are blocked (B) or open (O) after the stresses from being formed, handled and used. Reprinted from (Delamarche et al., 1998). Copyright 1998, with permission from American Chemical Society.

The elasticity of PDMS makes it ideal for use in valves and pumps. By applying a relatively small force to the PDMS it is possible to cause a deformation that stops flow. The ability of PDMS to deform also makes it ideal for pumps as it allows for small particulates to pass through without damaging the pump (Unger et al., 2000). The relative inertness of PDMS has also led to its use as a micro reactor; it is possible to dope a PDMS sample with a catalyst, opening up the possibility of more chemical processes in PDMS devices (McCreedy and Wilson, 2001).

All of the properties and processes described above have led to the widespread use of PDMS in microfluidic applications. Coupled with the fact it is tolerant to sterilisation processes such as autoclaving, UV sterilisation and ethanol means that PDMS can be used in a wide variety of biological applications (Hirano et al., 2010). A study carried out in 2010 (Paul, 2010) counted more than 80 examples of PDMS microfluidic devices carrying out biological or chemical reactions; this number is only going to increase with the availability and depth of knowledge of PDMS.

3.3 Processes

The following section looks at the techniques used to build microfluidic devices. It discusses the different methods available to construct a microfluidic channel. Some involve creating a master and producing copies, other techniques produce the final piece directly. The work then covers spin coating and how it could be used with a lithium niobate transducer.

3.3.1 Forming Channels

There are a variety of methods available to build microfluidic devices. The following section describes some of these techniques and discusses the associated advantages and limitations. The work looks at how techniques can be adapted to improve the fluid flow through a device which will ultimately lead to improved performance.

3.3.1.1 Photlithography

Photolithography is often used in the fabrication of microfluidic chips. For this process, a photoresist is spun onto a wafer, usually silicon. A mask is then used to define channels in the photoresist before being exposed to light, often UV. There are two types of photoresist: negative and positive. When a positive photoresist is used the sections of resist that are exposed to the light become soluble. Vice versa, when a negative photoresist is used the portion of the resist that is exposed to light becomes insoluble. Once the process is finished, the mask is removed leaving a silicon master with defined channels. PDMS can then be poured onto the mold; a silicon master can be re-used approximately 100 times without significant degradation, Figure 3-10 (Paul, 2010).

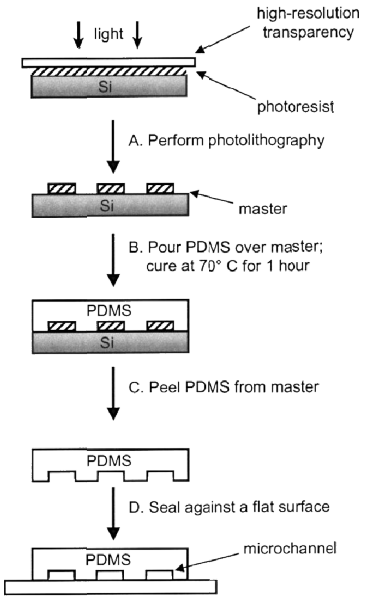

Figure 3-10 Process flow for photolithography. Reprinted from (McDonald and Whitesides, 2002). Copyright 2002, with permission from Elsevier.

Duffy et al showed in 1998 the possibility of rapid prototyping PDMS micro channels (Duffy et al., 1998). A computer-aided-design programme was used to design the fluid channels which were then printed onto a photoresist using a high resolution printer. Photolithography was then used to produce a master on a silicon wafer. PDMS was then poured onto the master and cured. The final piece was then bonded irreversibly to a blank piece of PDMS. This is now a standard technique for the rapid prototyping of microfluidic chips; less than 24hr is required from design to chip completion. Such a technique is limited by the resolution of the printer and features are usually in the order of 8 µm and larger (Fiorini and Chiu, 2005). The resolution of the printer will also give a wavy edge to the fluid channels which is not experienced by wet etching or micromachining, Figure 3-11.

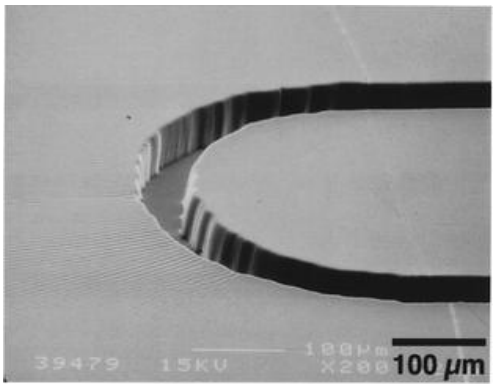

Figure 3-11 SEM image of the wavy fluid channels produced using rapid prototyping methods, Reprinted with permission from (Duffy et al., 1998). Copyright 1998, American Chemical Society.

3.3.1.2 Etching

The purpose of etching is to remove unwanted material. Wet etching is the most basic form and can be used on metals, semiconductors and some ceramics. A mask is used to stop desired areas dissolving away. This process is used to create tracks on printed circuit boards. Wet etching can dissolve away millimetres of material making it ideal for the production of fluid channels and reservoirs for use in microfluidics (SiliconFarEast, 2009).

Photolithography is commonly used in the etching of ceramics. During this process, a substrate is coated with a chrome and gold layer before a photoresist is spin coated onto the metal layer. Photolithography is then used to define the channels before the partial removal of the metal layer. The silicon is then exposed where the fluid channels are desired. The silicon is then etched to the required depth before the metal layer and photoresist layer are removed, Figure 3-12 (Fan and Harrison, 1994).

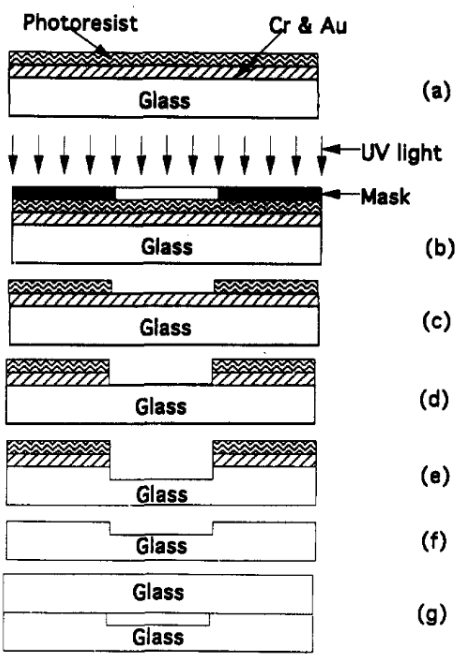

Figure 3-12 Diagram depicting the sequence of photolithographic lithography. Reprinted with permission from (Fan and Harrison, 1994). Copyright 1994, American Chemical Society.

Wet etching usually dissolves equally in all directions; however, some anisotropic materials have different etch rates in different planes. This characteristic makes some shapes difficult to manufacture. For example, the etch rate of silicon in one particular plane is 3 orders of magnitude lower than other planes. These particular planes are referred to as stop etch planes (VirginiaSemiconductorInc., 2011).

DRIE is a more costly process but can give vertical side walls that are not always attainable by wet etching. The material is etched using ions applied vertically. A passivation layer is then applied before the next vertical etch. The passivation layer on the side of the etch is not attacked directly, but the ions splutter off the bottom of the channel and damage the side walls. The next passivation layer is then applied over the bottom and side walls. This process is cyclic; between 100-1000 repetitions are required to etch 0.5 mm. The finished etch gives a near vertical side wall, but they do undulate with an amplitude of approximately 100-500 nm, (Micronit, 2009). The passivation layer acts to reduce the amount of sideways etching. Decreasing the etch time produces smoother side walls but the overall manufacturing time increases, Figure 3-13 (Knol, 2011).

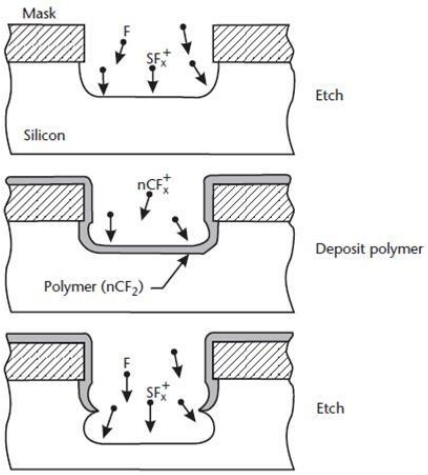

Figure 3-13 Diagram depicting the DRI etch process. The steps are repeated many times to etch channels to the required depth, (Knol, 2011).

3.3.1.3 Other Channel Forming Processes

Laser ablation has also been used to prepare polymer chips. A sheet of thermoplastic can be ablated using UV lasers. This process makes use of the fact that the majority of plastics absorb UV radiation. The width of the ablation can be controlled optically, or a protective metal mask can be used to define channels. This process lends itself to rapid prototyping and can be used to make chips directly or to make moulds, (Fiorini and Chiu, 2005).

Embossing is often used to make microfluidic devices. It involves the use of thermoplastic materials which are patterned using a master under pressure and heat. Thermoplastics can be reshaped when heated near to its glass transition temperature. Plastics commonly used include polymethylmethacrylate (PMMA), polycarbonate, cyclic olefin copolymer (COC) and polystyrene. The master, or stamp, is often made from silicon or metal. Hydraulic presses are used to stamp the thermoplastic. This can be done at elevated temperatures or at room temperature provided the applied force is high enough. The process is relatively quick and cheap and a further advantage is that the master can be re-used many times. The time consuming part of the process is the design and manufacturing of the stamp; this means the process is not great for prototyping, but is ideal for the mass production of microfluidic devices (Fiorini and Chiu, 2005).

There are other methods available for the construction of moulds. Solid object printing (SOP) involves the printing of a thermoplastic to form a series of channels and reservoirs. It is a very fast process (≈2 hr) and channel designs can be drawn using simple CAD programmes. This method can make large masters with several different layers, something that would take a long time if etched. The downside to SOP is the

relatively poor surface finish and that it can only make fluid channels in the region of 100 µm and more (McDonald et al., 2002).

Another process to make a master is micromachining, often in PMMA. This technique has a minimum diameter of approximately 50 µm for the softer plastics. The more brittle and hard the material is the bigger the minimum diameter is. Many microfluidic applications require smaller geometries than what is on offer from micromilling (Zhao et al., 2003).

3.3.2 Spin Coating

It is often required that a substrate is coated with a material either as part of a manufacturing process, such as the photoresistive mask used in photolithography, or to improve its electrical conductance. Surfaces may also be coated for a functional reason, such as the adherence of microbubbles to encourage acoustic streaming for sonoporation studies. There are several different methods available, such as spin coating, electron beam evaporation and plasma techniques.

The process of spin coating has been in existence for decades. Typically a fluid is deposited onto a wafer or substrate and rotated at speeds of 100 rpm and upwards. To hold the wafer in place, the underside is usually under vacuum. The wafer can either be stationary or spinning at low speeds before the fluid is dispersed. This dynamic dispense helps to spread the fluid evenly before the final spin speed is reached. This technique is particularly helpful for fluids with low wetting ability and it helps reduce waste, see Figure 3-14.

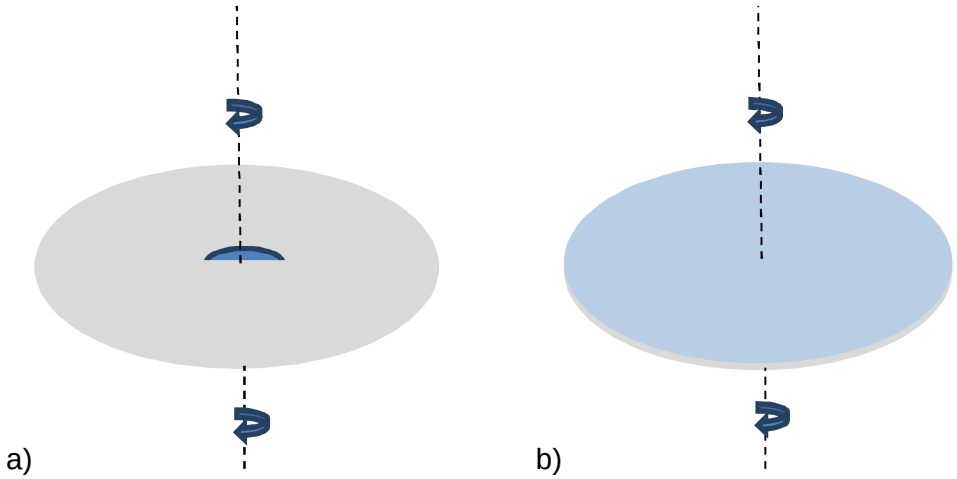

Figure 3-14 Diagram depicting spin coating. a) The droplet is placed on the wafer and spun. b) The droplet spreads across the surface of the wafer due to the centripetal forces from the spinning.

The theory of spin coating has been established from as early as the 1950s (Emslie et al., 1958). A noticeable study was published in 1982 which compared theory with

experiments and produced a concise set of guidelines (Daughton and Givens, 1982). The study identified the following parameters that govern the thickness and uniformity of a spun on film.

- Volume of fluid dispersed
- Speed of rotation during dispense
- Acceleration from dispense speed to final speed
- Final spin speed
- Elapsed time during final spin speed
- Fluid Viscosity
- Surface material of wafer
- Wafer radius

The first parameter is easily controlled using pipettes, syringes and automated dispensing systems. The next four parameters are usually programmable, the only limitations being the equipment used. Current spin coaters can reach speeds of 16,000 rpm, accelerate at 23,000 rpm s^{-1} and cost in the region of £5000 (BrewerScience, 2011). If further control is required, the material to be spun can be dissolved in a low viscosity solvent which, if used correctly, will improve the uniformity of the spun film. There is a strong desire for thinner films, so suspending the desired coating in solvents is a normal practice.

The wettability of the material being coated will affect the thickness and uniformity of the film, as will the surface roughness. The substrate material will often be pre-determined, but the surface can be polished. This allows the fluid to flow more freely, thus producing a more uniform film. Generally, larger radius wafers will be more uniform as there is a tendency for fluid to build up at the edge of the wafer. This build up continues until there is enough fluid for a drop to be expelled from the side of the wafer. One way of overcoming this problem is to discard the outer few mm of the wafer. The maximum radius of the wafer is dependent on the spin coater being used. Larger wafers will have to be spun at lower speeds, so the obtainable thickness will be higher.

The parameters that have the greatest effect on the film thickness and uniformity are fluid viscosity and final spin speed (Daughton and Givens, 1982). An example thickness profile for pure uncured PDMS is shown in Figure 3-15. It shows that as the rotational speed reaches approximately 3000 rpm, the thickness of the PDMS is

approximately 10% of its initial (100 rpm) thickness. Increasing the rotational speed further will yield marginal reductions in the thickness of the film (Zhang et al., 2004).

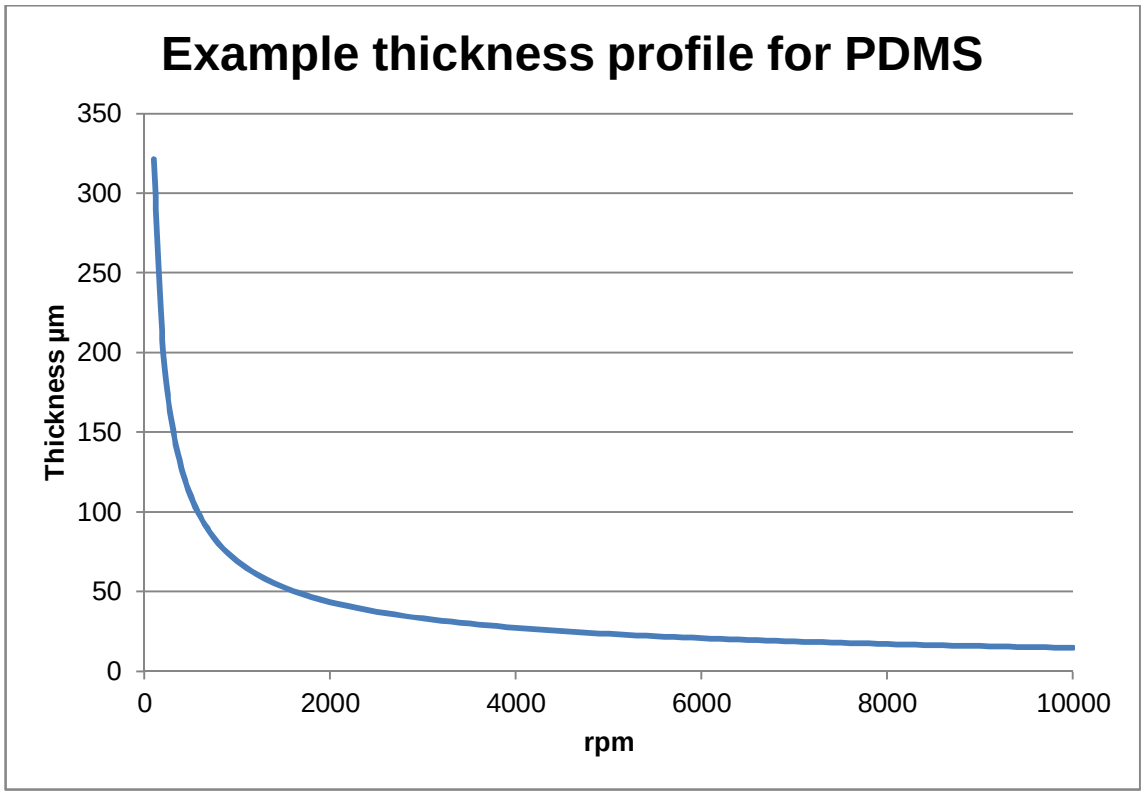

Figure 3-15 An example thickness profile for spin coated Sylgard 184 PDMS. © 2004, IEEE. Adapted, with permission, from (Zhang et al., 2004).

The amount of time a film is spun for has limited effect after the initial dispersion, approximately 20 s for low viscosity fluids. As previously mentioned, it is common for the desired coating to be in a suspension of solvents. As these solvents evaporate, the coating particulates adhere to the wafer. If the rate of evaporation is too fast, the coating will be thicker in the middle than at the edges. Conversely, if the rate of evaporation is too low there will be a build up of fluid at the edge of the wafer which when dry will produce a thicker film than at the middle of the wafer. By balancing rate of evaporation with spin speed it is possible to produce some very thin and very uniform films. To aid evaporation, most spin coating systems have an inert gas, such as nitrogen, released into the spin chamber. If the flow rate is too high, turbulence will cause the uniformity of the wafer to suffer. The high flow rates will also cause the solvents to evaporate faster, leaving a thicker film.

If the coating is in solution, its viscosity will change as it evaporates making it non-newtonian. This behaviour is actually helpful. If it was Newtonian the film would

thin out progressively with long spin times. The fluid evaporates readily because of the high surface area to volume ratio that comes from the spinning (Tabeling, 2003).

Spin coating can be used in many different applications, such as photolithography, indium tin oxide coatings (Stoica et al., 2000) and conducting polymer coatings (Giraudet et al., 2006, Zhang et al., 2005). ITO coatings are of interest due to their high electrical conductivity and high optical transparency (Stoica et al., 2000). More recently, conducting polymers have been used, primarily in the production of organic LEDs or organic thin film transistors. These conducting polymers are also transparent (Zhang et al., 2005, Giraudet et al., 2006). A lot of work has been carried out on spin coating, much of which is readily available in online forums (Groupsrv, 2011). The work is highly detailed, discussing 500 nm films of PDMS with uniformity of 50 nm. As a result, finding approximate guidelines to spin Sylgard 184 PDMS films was not difficult (Engen, 2011).

3.4 Summary

This chapter presents key information, methods and materials used or investigated during the course of this project. The chapter begins by describing the use of PZT and lithium niobate as bulk and surface acoustic wave transducers respectively. The work describes the advantages of using lithium niobate but also the difficulties in regards to applying an electric potential through the use of conducting polymers and ITO. The following section describes PDMS and the chemistry behind it. This was useful in the construction of a SAW device with a PDMS channel. The next section describes potential techniques for making microfluidic channels and some of the advantages and disadvantages of different techniques. Finally, the chapter gives a brief description of spin coating and the key factors affecting performance. This work was useful in developing surface acoustic wave devices.

Chapter 4 Bulk Acoustic Wave Devices

Bulk acoustic wave devices are the more traditional method for manipulating particles within fluid chambers using acoustic radiation forces. The technology is well advanced, with devices being able to manipulate particles into layers, beams and even collect them in a 3 dimensional trap, (Manneberg et al., 2009b). Few of the devices created so far are capable of operating outside a laboratory environment and therefore there are opportunities to develop the robustness of such devices. Many of the devices which use ultrasonic standing wave techniques are custom made for specific applications and require characterization on a device by device basis. For ultrasonic standing wave techniques to be used in an oceanographic environment they will need to be produced in polymers and be suitable for mass deployment over a range of environments. The work in this chapter develops a PMMA particle manipulation device that is repeatable can be manufactured easily. The device also uses a novel approach to particle manipulation that makes it more robust to changes in the fluid which is a key requirement given the diverse properties of the world's oceans and coastal waters.

Many wide channeled devices rely on an opaque lead zirconium titanate (PZT) transducer to manipulate particles into planes. This can lead to difficulties in imaging or constraints as to the types of microscope that can be used. The work in this chapter will also investigate novel transducers that could increase the range of activities that ultrasonic standing wave techniques could be used for.

4.1 Polymer Devices

There is much interest in polymer ultrasonic particle devices despite the associated higher losses: this is because they can be produced cheaply, allowing them to be used as disposable devices. Polymer devices are already used in a wide variety of biological applications, so being able to incorporate ultrasonic manipulation techniques would enhance the number of operations available to the cell biologist. Polymers are also often transparent, making them ideal for imaging. For this work, a series of polymer devices were developed, with the intention of creating a 2 dimensional focussing device and a more conventional 1 dimensional device.

4.1.1 Milled microchips

An easy and quick method for producing polymer devices for ultrasonic particle manipulation was to mill them from readily available 1 mm thick PMMA sheets. Fluid channels were milled into one piece of PMMA and a cover slip was milled into a second piece of PMMA. The chips were bonded together using a solvent technique involving 33 % acetone with 67 % ethanol (Harris et al., 2010). The solution was placed on the surface to be bonded and the two pieces were brought into contact. Force was applied to the chips and after 15 min excess solution was syringed from the chip. The finished chips were annealed for 4 h at 85 °C to relieve internal stress. A diagram is shown in Figure 4-1. For this work a 1 mm thick PZT transducer will be used which corresponds to a resonance of approximately 2 MHz. This equates to a half wave in water of approximately 350 µm which is the right order of magnitude for integration into microfluidic oceanographic sensors.

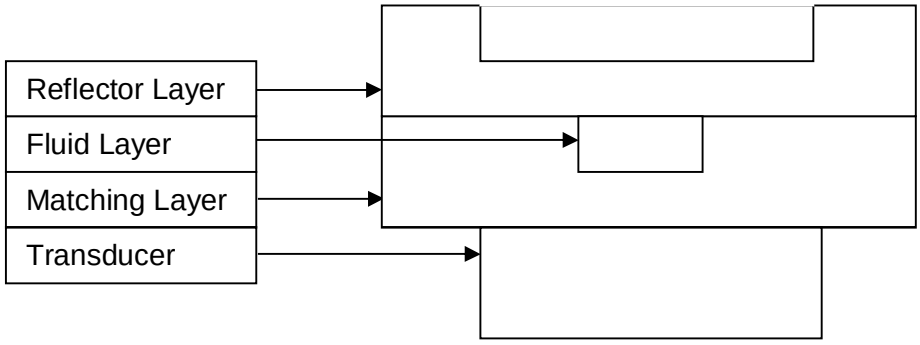

Figure 4-1 A schematic of the polymer devices. The matching layer and reflector layer are made from 1 mm thick PMMA sheets. The matching layer has a fluid cavity milled into it, thus the total thickness of the two layers is constrained to 1 mm. The reflector layer can be milled to any thickness but for these designs an area at the edge of the layer was left at 1 mm for strength and ease of manufacturing. The PZT used for these designs was 1 mm which corresponds to a 2 MHz resonance and approximately 350 µm half wavelength in water.

The devices were designed to have a fluid channel half a wavelength wide in water and less than half a wavelength tall when operating with a 1 mm thick PZT transducer (PZ26, Ferroperm Piezoceramics, Denmark). The width of the fluid channel was designed to be a half wavelength to encourage lateral manipulation (Harris et al., 2010). To achieve focusing planar to the transducer a sub half-wavelength design would be designed. The following sections show how the dimensions for the chips were decided using computational modelling.

4.1.1.1 Device Design

A 1 dimensional Matlab (The MathWorks Inc., USA) model will be used to design devices in PMMA with the aim of producing a 2 dimensional particle focusing device, (Hill et al., 2002). The model uses an “impedance transfer” approach to relate the mechanical impedances between different layers within the device, and then uses this to derive an input electrical impedance which is driven by an electromechanical representation of the piezoceramic transducer. Lateral focusing should occur through setting the width of the device to a half wavelength (or multiple of), (Harris et al., 2010), so the modelling aims to achieve axial focusing which requires a single pressure node near the midpoint of the channel, with forces throughout the channel forcing particles towards that pressure node.

The properties of the materials used in a 1 dimensional Matlab model are shown in Table 4-1. A Q factor is included which corresponds to a loss factor for each material and are based on empirical knowledge. The particles modelled are 5 µm radius polystyrene beads (FluoroSpheres) and an electric voltage of 10 V_{pp} is modelled across the PZT, (Carugo et al., 2014). A fluid channel 300 µm deep results in a matching layer 700 µm deep as the channel is milled from a 1 mm PMMA sheet. Several thicknesses for the reflector layer were modelled, with the aim of reducing the thickness to increase the efficiency of the device whilst designing a device that is capable of being milled. The properties of water are well documented and can be calculated, (Coates, 1989), see Appendix A for further details. PMMA density is taken from the Plexiglas acrylic data sheet (Cadillac plastic limited, Swindon, U.K.) and some iteration was carried out to inform the speed of sound along with values widely available online. The purpose of the model is primarily to generate information on node position.

Table 4-1 The material properties of the layers and particles in a 1 dimensional model.

	Density kg m^{-3}	**Speed of Sound m s^{-1}**	**Thickness mm**	**Q Factor**
PZT	7700	4530	1	100
PMMA	1160	2260	Varied	30
Water	1000	1480	Varied	100
Polystyrene Bead	1055	1962	N/A	N/A

When a reflector layer of 350 µm is modelled a pressure node is predicted in the centre of the fluid channel with an operating frequency of 2.1 MHz, Figure 4-2. Modelling showed that a force would be present acting on particles away from the roof and floor of the channel,Figure 4-3. This is ideal as the positive force should be able to

lift any particles that sediment to the floor of the channel. In a half wavelength design there would only be a small force lifting particles off the bottom of the channel.

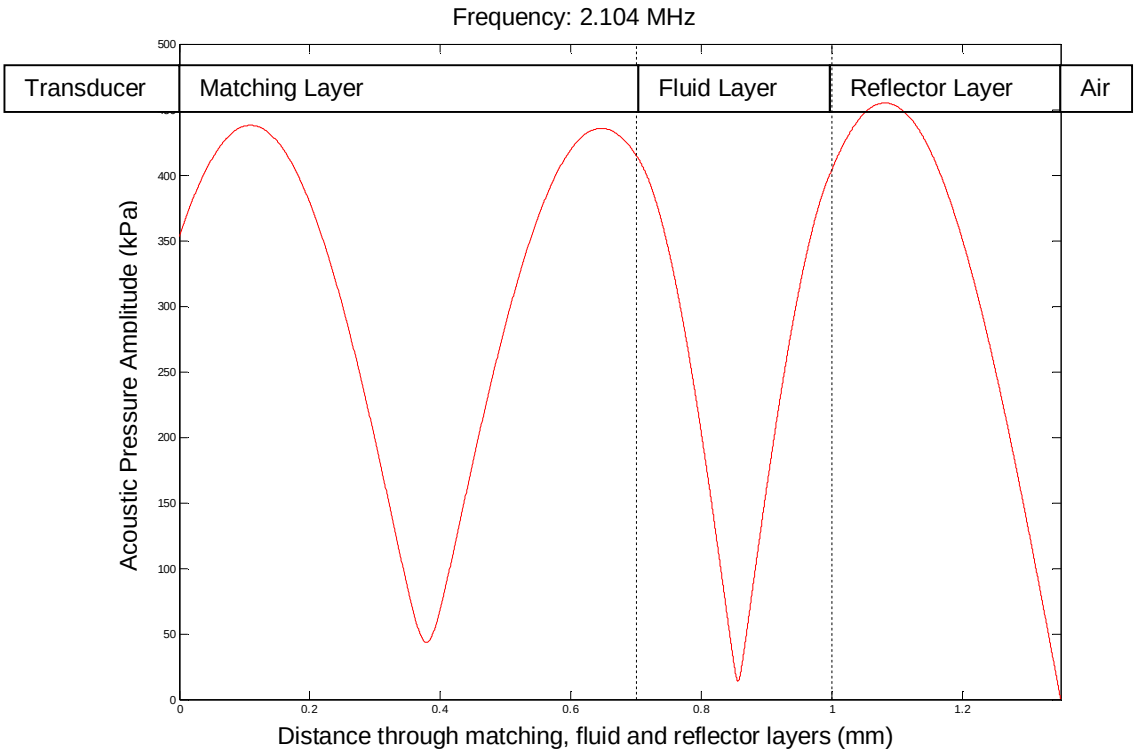

Figure 4-2 The predicted pressure amplitude in a PMMA device 0.7, 0.3 and 0.35 mm thick.

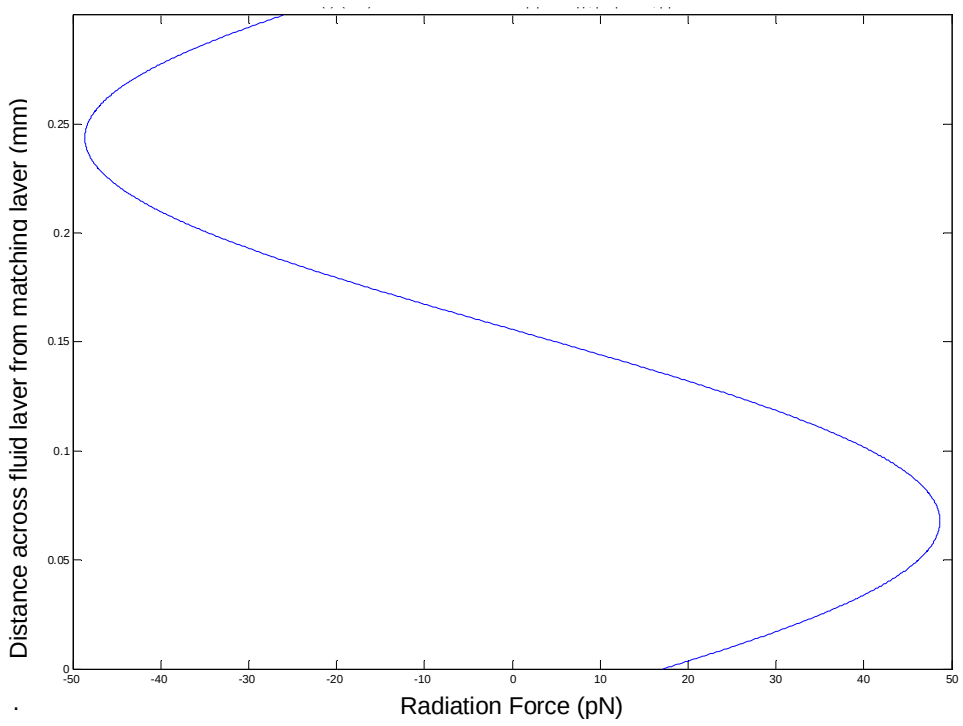

Figure 4-3 The corresponding force profile at 2.104 MHz. Note that forces at the boundaries are more than 0 as slightly less than a half wavelength is present in the fluid channel.

As the predicted operating frequency is 2.1 MHz, the channel width needs to be 350 µm to fit an exact half wavelength. Chips were milled into PMMA and measurements of the manufactured chips showed that the dimensions were different from the design and are shown in Table 4-2.

Table 4-2 Design specs and actual channel dimensions

	Design Spec	1st Batch (20 samples)
Channel Width µm	350	398±4
Channel Height µm	300	325±10
Matching Layer µm	700	371±25
Reflector Layer µm	350	237±13

When these dimensions were loaded into Matlab the predicted pressure amplitude included an anti-node present in the fluid channel, Figure 4-4.

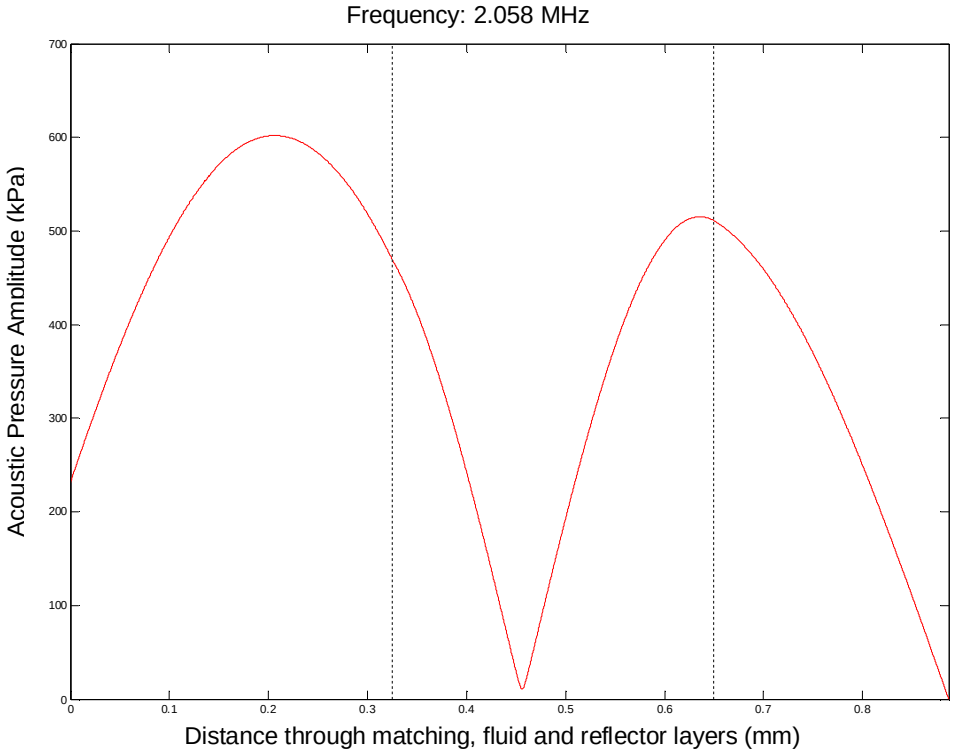

Figure 4-4 The predicted pressure amplitude across the device based on actual measured dimensions.

Devices were assembled and impedance analysis was carried out using a Cyphergraph C60 impedance analyser, Figure 4-5. The measurements identified impedance minima at 1.95 and 2.09 MHz, whilst the one dimensional model only predicted a resonance at 2.06 MHz. The other resonance is likely to be caused by a

lateral resonance. A frequency of 1.95 MHz corresponds to a wavelength of 770 µm in water (1500 ms^{-1}) and a half wavelength of 385 µm. This is a close match to the measured channel width of 398 ±4 µm, see Table 4-2. The modelling matches well with the measured impedance in terms of the frequency of the main planar resonance.

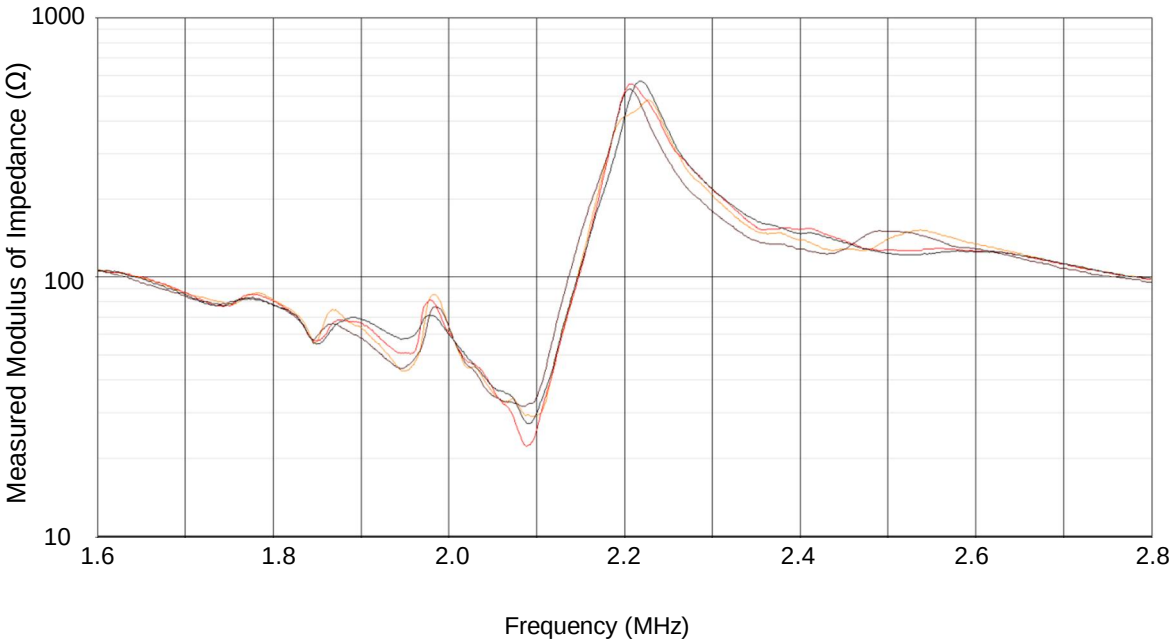

Figure 4-5 Impedance measurements for four PMMA chips with a 0.370, 0.325 and 0.240 mm thick matching, fluid and reflector layer respectively. The chips have good repeatability with a visible resonance at just under 2.1 MHz. A less pronounced resonance is apparent at approximately 1.95 MHz and is likely to be caused by a lateral resonance in the 0.4 mm wide fluid channel.

4.1.1.2 Voltage Drop Analysis

To measure the acoustic pressure within the fluid chamber, voltage drop analysis experiments were undertaken. The gravitational force, F_g, on the bead can be calculated as follows;

$$F_g = \Delta\rho \times V_B \times g$$

Equation 4-1

Where $\Delta\rho$, V_B and g represent the density difference of the bead and the fluid, the bead volume and gravitational constant respectively. The bead is spherical, therefore $V_B = \frac{4}{3}\pi r^3$. The fluid is water and can be calculated as follows, $\Delta\rho = \rho_B - \rho_F$, where subscripts represent the bead and the fluid respectively. The following parameters were used to calculate the gravitational force on the bead, Table 4-3. The

gravitational force acting on a 10 µm bead in water is equal to 0.282 pN. For simplicity, Milli-Q water was used rather than seawater. If required, it will be possible to calculate the expected force on a bead if the fluid was changed to seawater, assuming the density of the new fluid is known.

Table 4-3 The parameters used to calculate the gravitational force acting on a 10 µm bead in water.

Parameter	Value
ρ_B	1055 kg m^{-3}
ρ_F	1000 kg m^{-3}
r	5 x 10^{-6} m
g	9.81 m s^{-2}

The minimum voltage which levitates a bead must be equal to the gravitational force acting on the bead. The following equation shows the force generated on the bead and is greatest when $\sin(2kx)$ is equal to 1.

$$F = 4\pi k r^3 \epsilon \phi(\rho, \beta) \sin(2kx)$$

Equation 4-2

The compressibility of the bead can be calculated from the following equation;

$$\beta_B = \frac{1}{\rho_B \times {c_B}^2}$$

Equation 4-3

Where c_B is the speed of sound in the bead. The following parameters were used to calculate the compressibility, Table 4-4;

Table 4-4 Parameters used to calculate compressibility of the particle.

Parameter	Value
C_B	1962 m s^{-1}
ρ_B	1055 k gm^{-3}

From here it is possible to calculate the acoustic contrast factor using the following equation,

$$\phi(\rho,\beta) = \frac{\rho_F + \frac{2}{3}(\rho_B - \rho_F)}{2\rho_B + \rho_F} - \frac{\beta_B}{3\beta_F}$$

Equation 4-4

along with a compressibility of water of 4.5 x 10^{-10} m^2 N^{-1}. The acoustic contrast factor for a polystyrene bead in water is equal to 0.151. From here the energy density can be calculated using a value of k of 8700 m^{-1} and is equal to 0.137 J m^{-3} when the bead is just levitating. From here the following equation can be rearranged to calculate the pressure, P_d.

$$\epsilon = \frac{1}{4} \times \frac{{P_d}^2}{\rho_F {c_F}^2}$$

Equation 4-5

By recording the voltage at which a bead is just levitated, it is possible to calculate the pressure at a higher voltage, P_1.

$$P_1 = P_d \times \frac{V_1}{V_d}$$

Equation 4-6

A chip was tested with green fluorescent beads (FluoroSpheres, yellow-green microspheres, ex 502 nm, em 513 nm, fluorescein isothiocyanate (FITC filter)) to check the ultrasonic capabilities of the device. Vertical focusing was observed at a relatively low voltage of 1.8 V_{pp} and lateral focusing was seen but only at voltages of 10 V_{pp} and above. Whilst lateral focusing was desired, high voltages were required along with low flow rates. This will result in acoustic streaming which will disrupt the uniformity of the focused particles. The acoustic pressure (*P*) within the chips, measured through voltage-drop analysis on a 10 µm polystyrene bead was equal to 3.5 x 10^4 Pa, at 1.8 V_{pp}. This corresponds to an energy density of 4.25 J m^{-3} at a voltage of 10 V_{pp}. The device did not exhibit good lateral focusing, which is assumed to be because the width of the fluid channel does not correspond to a half wavelength.

4.1.1.3 Repeatability

Whilst the results of this experiment were promising, the actual dimensions of the devices used were significantly different from the design specifications. The acoustic excitation was favorable; however it could have had the opposite effect. Measurements were taken of chips used in this experiment and of two other batches (20 samples per batch), results can be seen in Table 4-5.

Table 4-5 Design specifications compared with actual manufactured devices.

	Design Spec	1st Batch	2nd Batch	3rd Batch
Channel Width µm	350	398±4	353±10	335±19
Channel Height µm	300	325±10	297±11	308±6
Matching Layer µm	700	371±25	561±25	406±12
Reflector Layer µm	350	237±13	406±17	256±8

The results show that the variation within batches is significant and that accuracy in terms of the depth of milling is poor. This will lead to differences between chips in terms of acoustic performance as well an unrepeatable coupling effect between the width of the channel and the height of the channel. Variation between batches of chips is particularly poor, which makes the possibility of repeating this experiment difficult.

4.1.2 Polymer Slides

Due to the lack of repeatability available from milled PMMA chips alternatives were sought which would limit variations in the thickness dimensions of the devices. PMMA films (Plexiglas Acrylic, Cadillac plastic limited, Swindon, U.K.) were identified as a suitable material for the production of polymer ultrasonic devices. Films were available in the following three thicknesses; 0.175, 0.25, and 0.375 mm. Every combination of matching, fluid and reflector layer thickness was modelled using the given thicknesses. An air backing was assumed as the terminating material. Using set thickness polymer slides will give greater control over the thickness of layers but will not solve the problem of the variation in the width of milled components. For this reason, the work will concentrate on producing a robust 1 dimensional planar focusing polymer device.

4.1.2.1 Acoustic Pressure and Force Profile

Many of the combinations predicted strong ultrasonic performance, but with poor pressure node position, such as too close to or within the matching or reflector layer. An example pressure plot is shown in Figure 4-6.

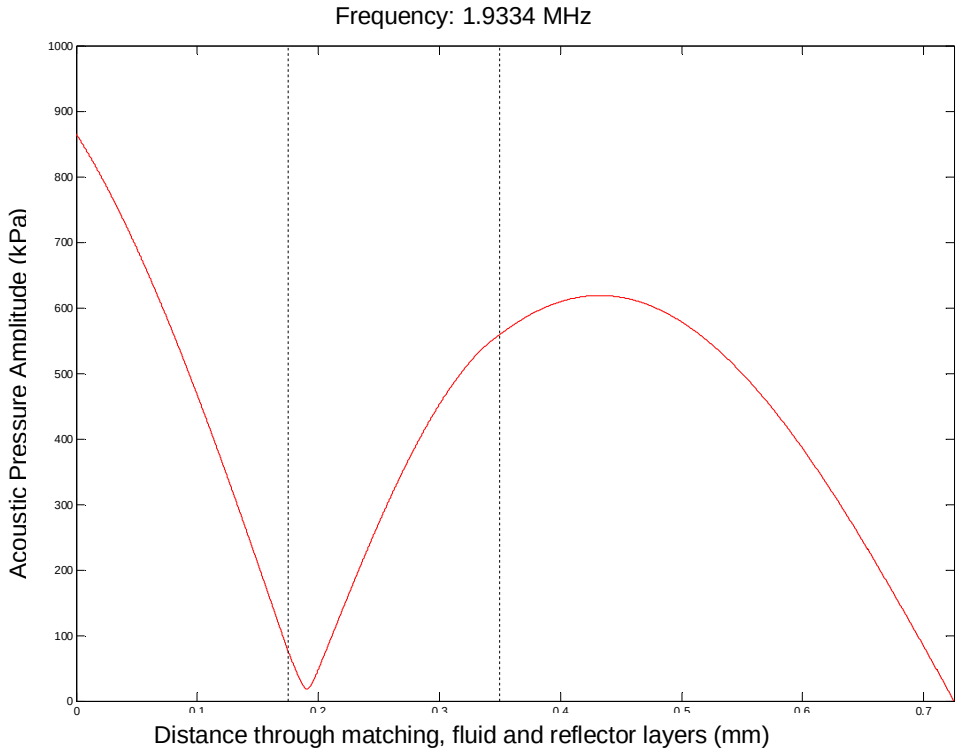

Figure 4-6 An example pressure plot of a PMMA device with a matching, fluid and reflector layer 0.175, 0.175 and 0.375 mm thick respectively. Whilst the pressure amplitude generated across the device is strong, the position of the node is close to the matching layer, this would invariably lead to particles being moved within very close range of the matching layer. Few applications require such manipulation.

Some of the combinations showed excellent node positioning and maximum force acting on particles near the fluid boundaries. In fact, the same design at a higher frequency gave a good node position. However, the magnitude of the force was not particularly high, due to the fact that the operating frequency was far from the natural frequency of the transducer, approximately 2 MHz. An example of this is shown in Figure 4-7. The forces generated on a 10 µm diameter particle are shown in Figure 4-8. It can be seen that whilst the forces at each boundary are at a maximum, the magnitude of the forces is still relatively small.

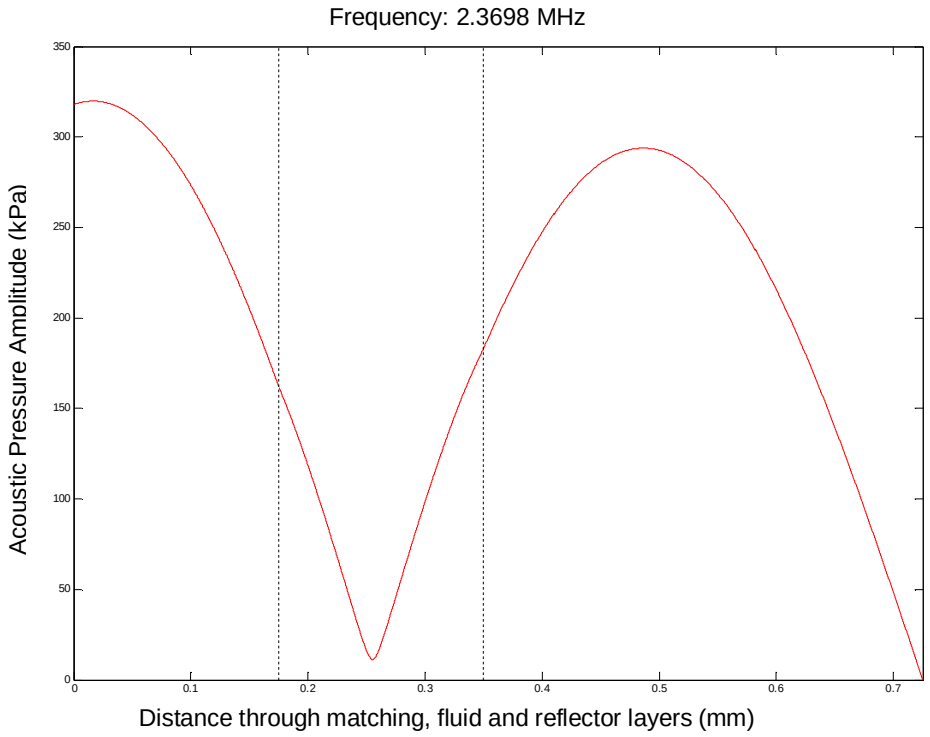

Figure 4-7 An example pressure plot of a PMMA device with a matching, fluid and reflector layer 0.175, 0.175 and 0.375 mm thick respectively. The operating frequency is higher than Figure 4-6 which causes the pressure node to fall into the middle of the fluid chamber. Unfortunately the generated pressure field is significantly smaller than before as the device is operating away from the natural frequency of the PZT.

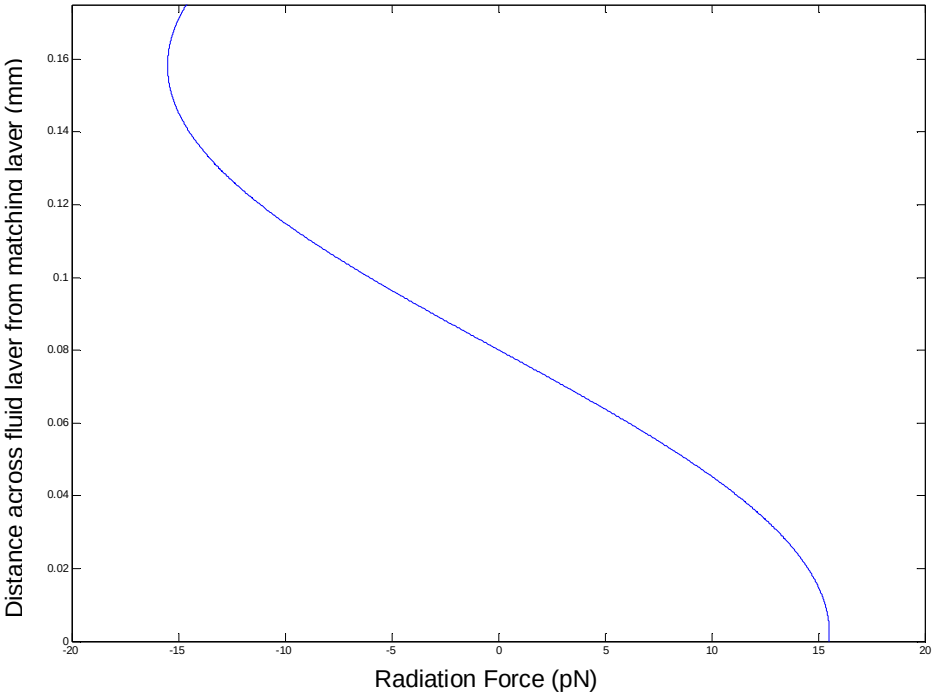

Figure 4-8 The predicted forces acting on a 10 µm diameter bead in the fluid channel.

The combinations that used a 0.375 mm fluid layer resulted in a pressure amplitude across the device that would have caused the majority of particles to focus towards the inside of the channel, but a fraction would experience a force towards one of the boundaries. An example of this is shown in Figure 4-9. Particles that are close to the reflector would experience a force towards the reflector layer whilst the majority of particles would collect towards the middle of the channel.

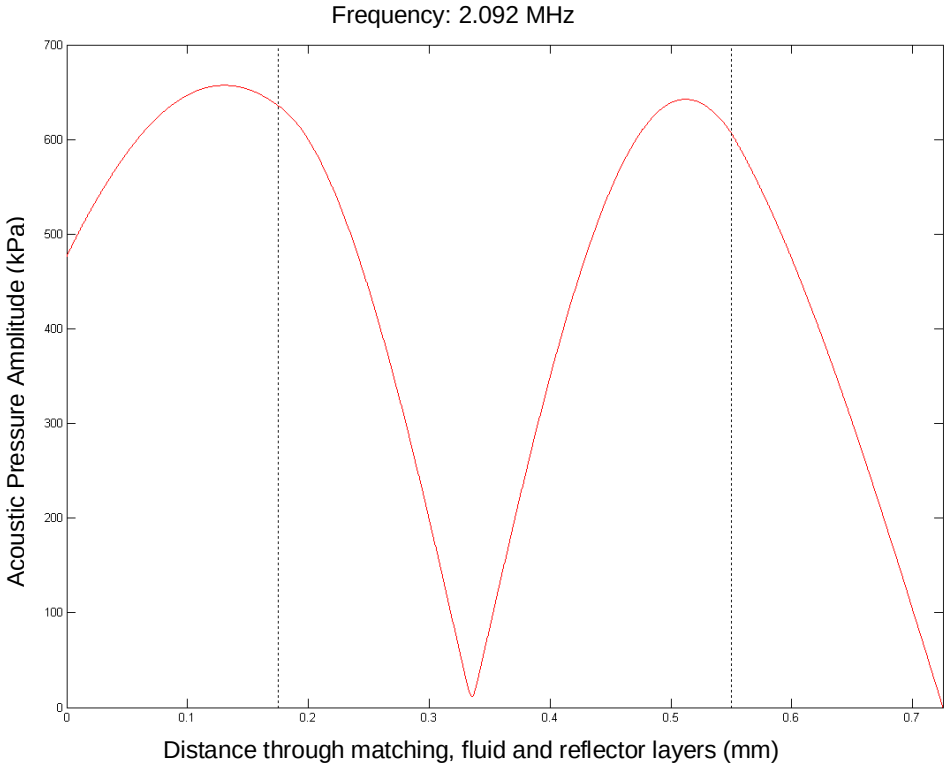

Figure 4-9 An example pressure plot of a PMMA device with a matching, fluid and reflector layer 0.175, 0.375 and 0.175 mm thick respectively. Whilst the pressure amplitude created across the device is strong and the pressure node is fairly well centralised an anti-node is present in the fluid layer. This would cause some particles to collect at the reflector.

Some combinations predicted an anti-node in the fluid channel near both boundaries, Figure 4-10. Such devices would have little or no practical purpose and are therefore not of interest. It should also be noted that they would not be robust as any increases in the speed of sound in the fluid or density would tend to lead to the anti-nodes moving further into the fluid layer.

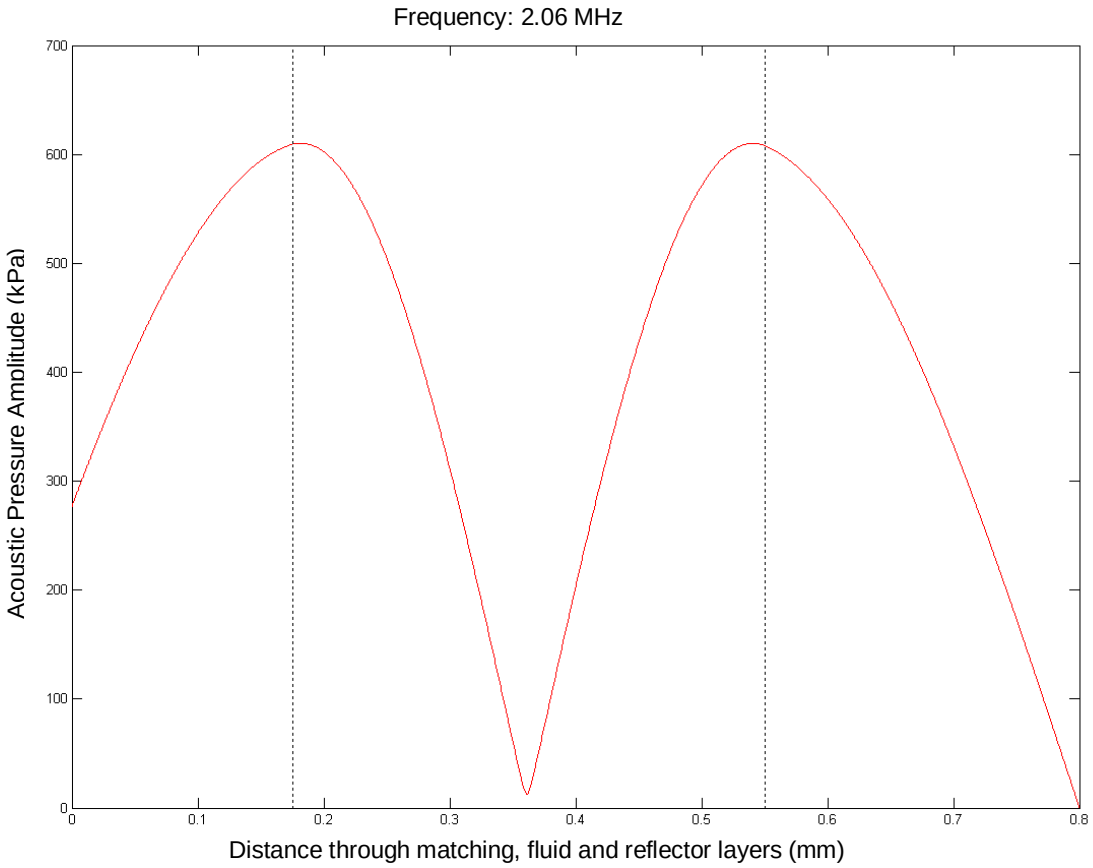

Figure 4-10 An example pressure plot of a PMMA device with a matching, fluid and reflector layer 0.175, 0.375 and 0.250 mm thick respectively. Whilst the pressure amplitude is relatively high particles would be focused at both boundaries and in the middle of the channel. Variations in the density and speed of sound of water would tend to make this effect worse.

After modelling all the combinations, 2 combinations predicted strong acoustic forces with good node positioning and no anti-nodes in the fluid chamber. 1 design showed a quarter wave and half wave resonance. A summary of these devices is shown below, Table 4-6. Pressure amplitude plots and force potentials are shown in Figure 4-11 through to Figure 4-18.

Table 4-6 Results from 1 dimensional modelling based on a 10 µm bead and 10 V_{pp} excitation.

Combination: matching-fluid-reflector, mm	Force from matching layer, pN	Force from reflector layer, pN	Node – distance from matching layer, mm	Node – distance from reflector layer, mm	Predicted operating frequency, MHz
0.25, 0.25, 0.375	54	-44	0.115	0.135	2.12
0.375, 0.25, 0.375	36	-48	0.11	0.14	2.062
0.175, 0.175, 0.375	16	-17	0.08	0.095	2.375 (Half)
0.175, 0.175, 0.375	17	-40	0.015	0.16	1.932 (Quarter)

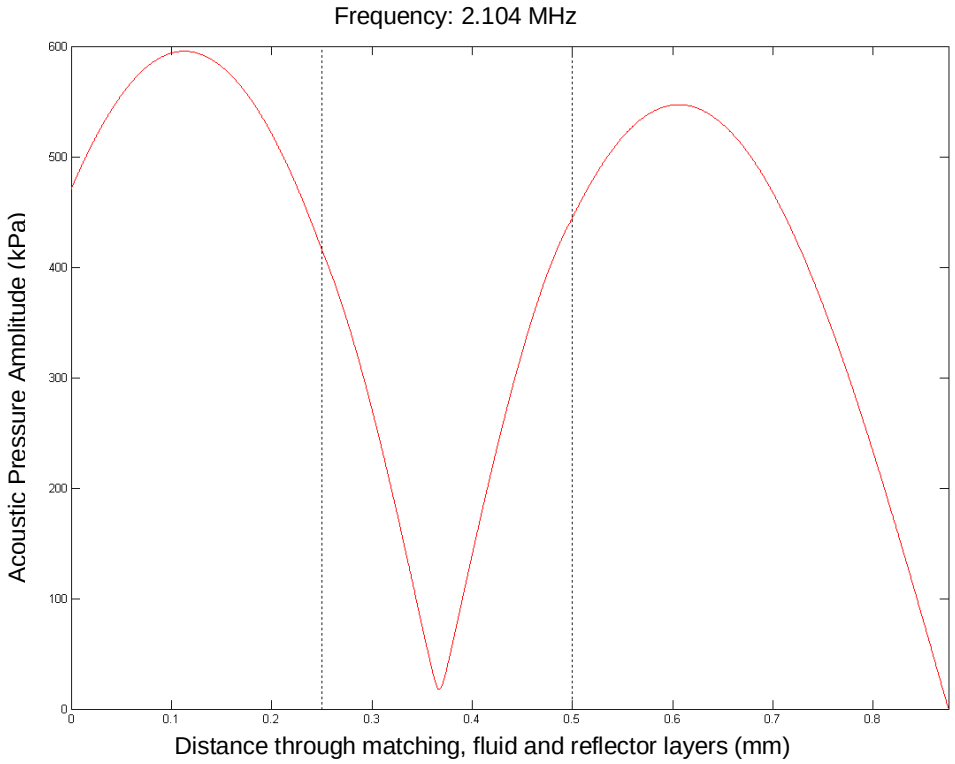

Figure 4-11 An example pressure plot of a PMMA device with a matching, fluid and reflector layer 0.25, 0.25 and 0.375 mm thick respectively.

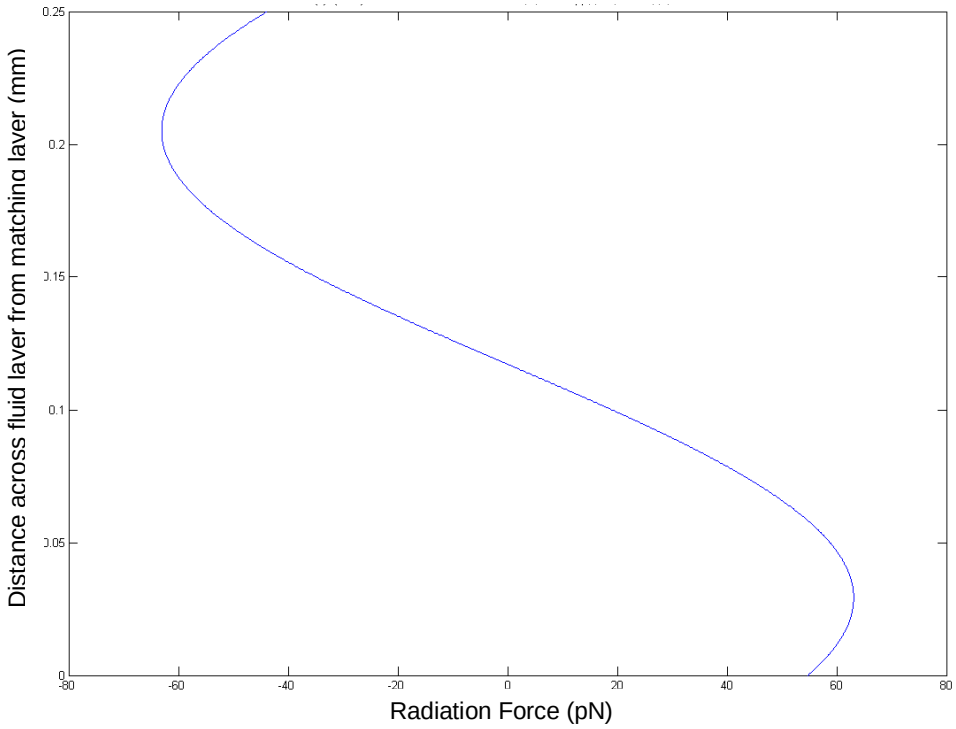

Figure 4-12 The corresponding force profile for Figure 4-11 for a 10 µm bead in the predicted acoustic pressure field.

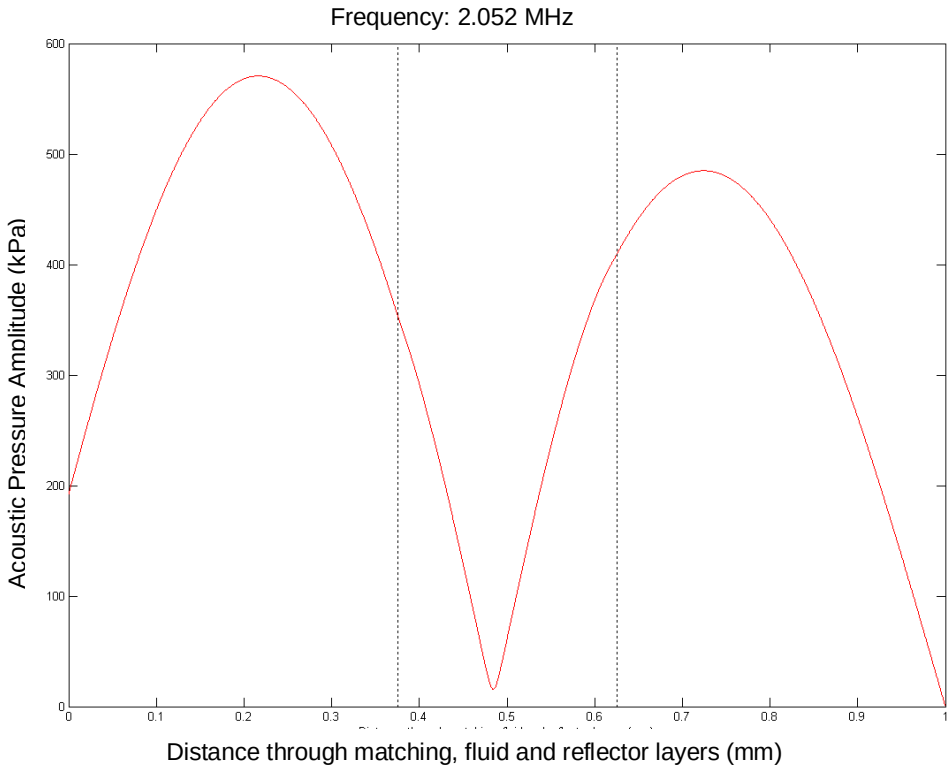

Figure 4-13 An example pressure plot of a PMMA device with a matching, fluid and reflector layer 0.375, 0.250 and 0.375 mm thick respectively.

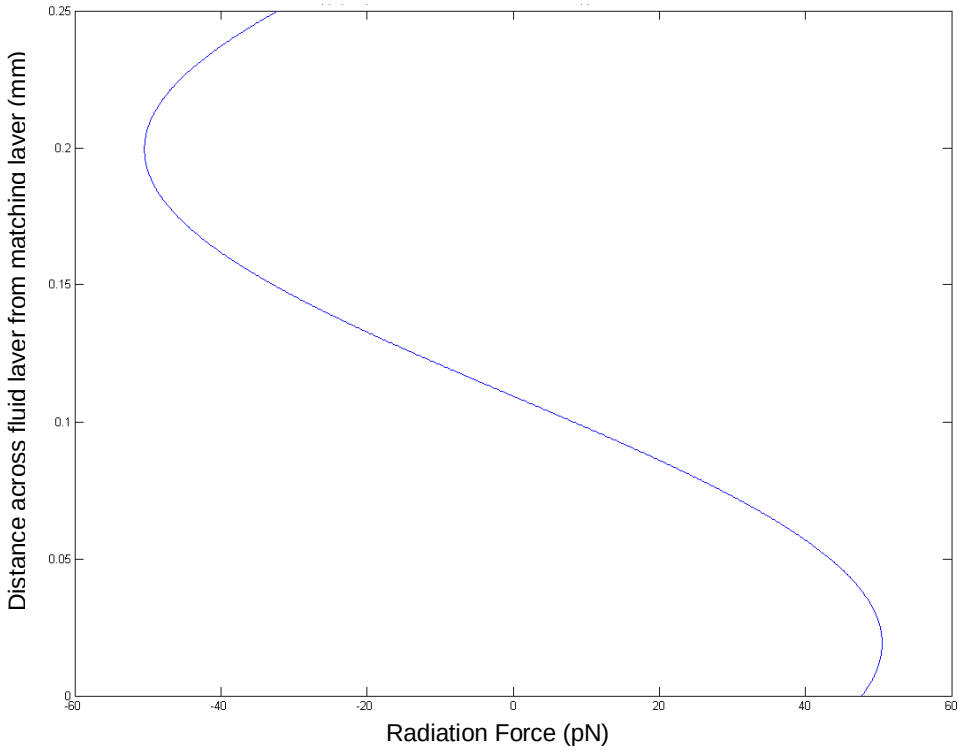

Figure 4-14 The corresponding force profile for Figure 4-13 for a 10 µm bead in the predicted acoustic pressure field.

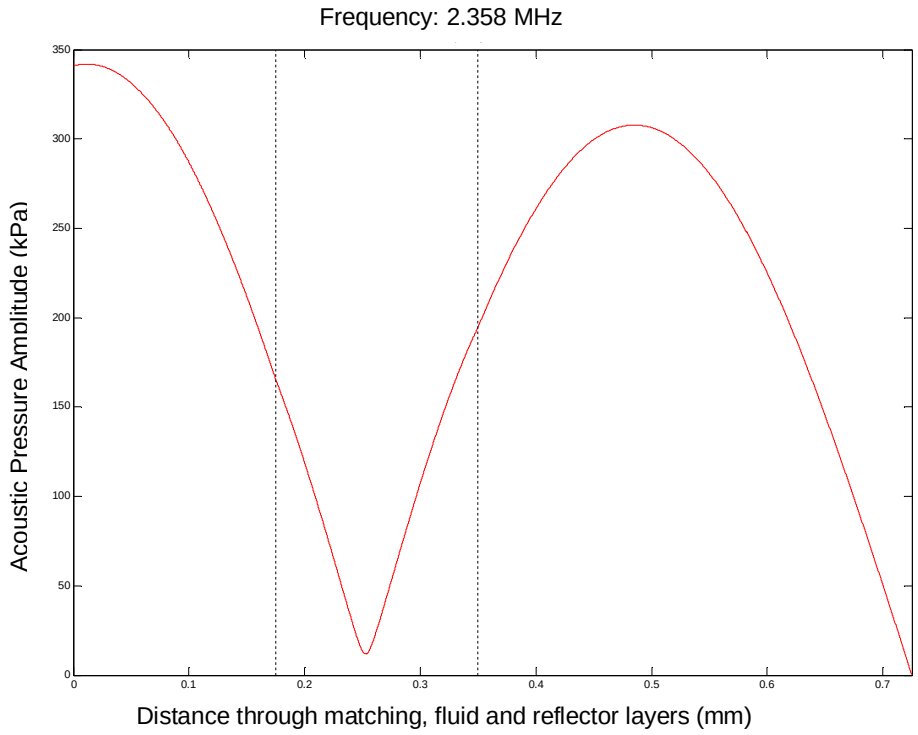

Figure 4-15 An example pressure plot of a PMMA device with a matching, fluid and reflector layer 0.175, 0.175 and 0.375 mm thick respectively.

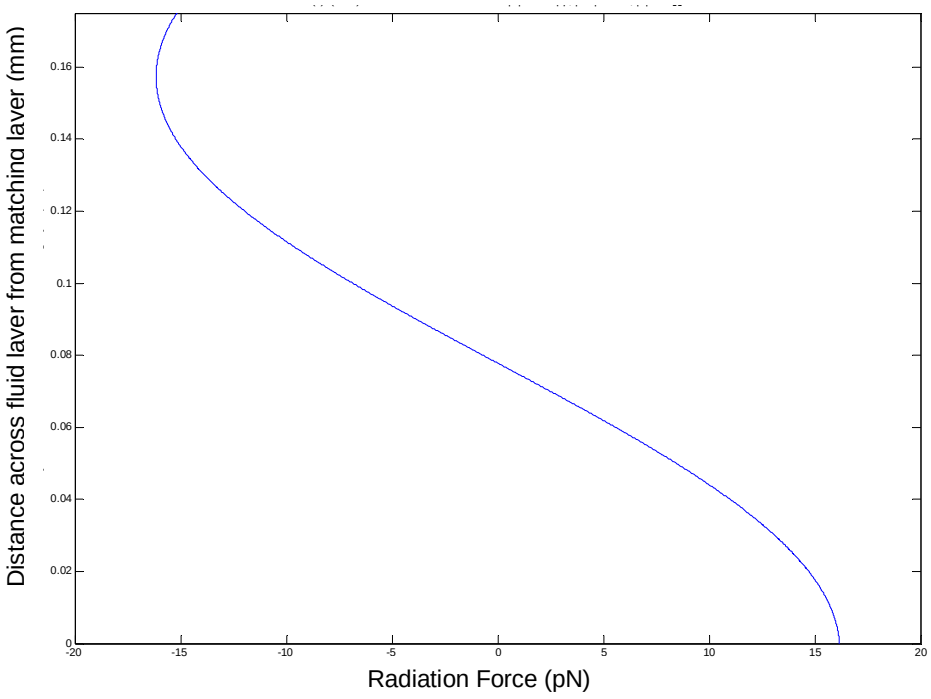

Figure 4-16 The corresponding force profile for Figure 4-15 for a 10 µm bead in the predicted acoustic pressure field.

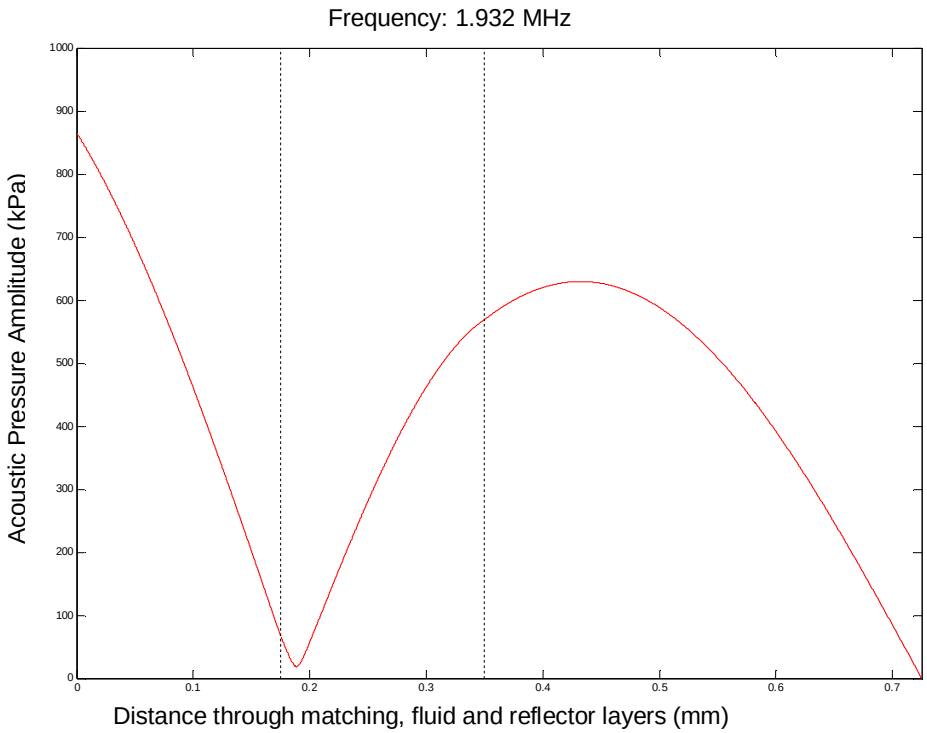

Figure 4-17 An example pressure plot of a PMMA device with a matching, fluid and reflector layer 0.175, 0.175 and 0.375 mm thick respectively.

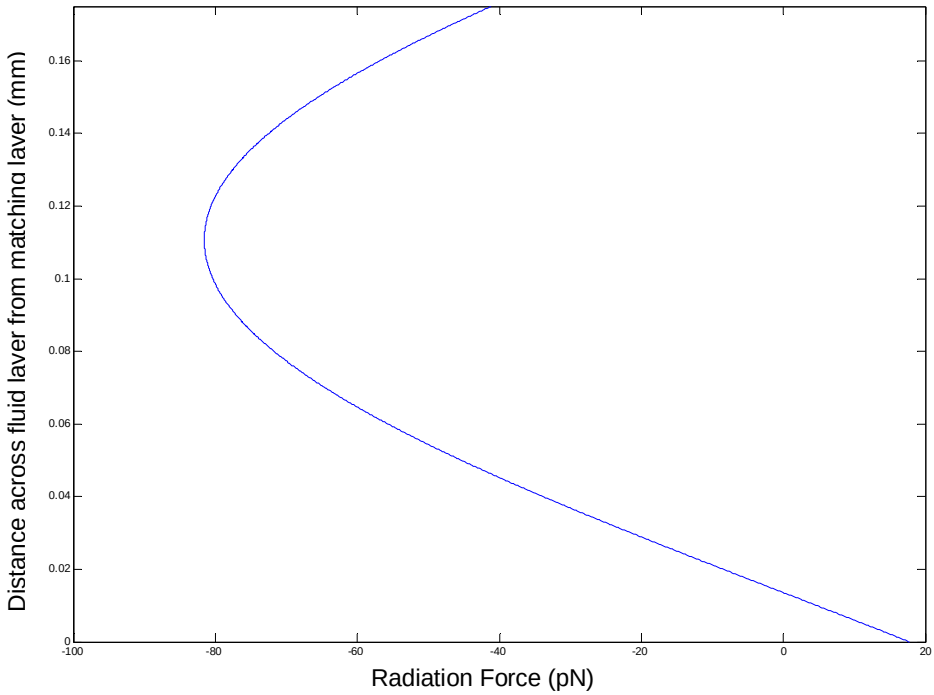

Figure 4-18 The corresponding force profile for Figure 4-17 for a 10 µm bead in the predicted acoustic pressure field.

The above figures show the generated acoustic pressure field and the associated force profiles for a series of devices. One of the demands of an ultrasonic polymer microfluidic device for *in-situ* oceanographic sensing is the ability to work in a range of conditions. These conditions will invariably lead to changes in the speed of sound of the fluid so it is important to understand how this will affect device performance.

4.1.2.2 Speed of Sound of Fluid

To investigate the effects of a changing fluid the model was re-run with the speed of sound in the fluid varying from 1350 – 1700 m s^{-1} in steps of 50 m s^{-1}. This range covers any global position as far as 6000 m deep for temperatures between -2 and 35 °C, for salinity readings from 0 parts per thousand (ppt) to 70 ppt, (Coates, 1989), see Appendix A for further details. The results are summarised below in Table 4-7. The table shows that the device is stable across a wide range fluid sound speed. A small shift in the operating frequency is seen and the node shifts slightly towards the matching layer.

Table 4-7 Summarised results of the investigation into the effects of the speed of sound of the fluid on the predicted acoustic performance of the 0.375, 0.25, 0.375 mm device.

Speed of Sound, ms^{-1}	Pressure at matching layer, kPa	Pressure at reflector layer, kPa	Frequency, MHz	Node distance from matching layer, mm
1350	400	420	2.053	0.12
1400	390	415	2.056	0.12
1450	375	415	2.059	0.12
1500	360	410	2.062	0.115
1550	350	405	2.065	0.115
1600	330	400	2.068	0.11
1650	315	400	2.068	0.105
1700	300	400	2.071	0.105

The differences in the pressure field generated are relatively small and are still large enough to generate a significant force on any particles in the fluid channel. The predicted pressure variations across a device are shown for the two extreme cases, Figure 4-19 and Figure 4-20. The diagrams show that the node position moves towards the matching layer as the speed of sound in the fluid increases. The operating

frequency also increases. The devices appear to be robust, as significant changes in the speed of sound in the fluid do not drastically alter the acoustic characteristics of the device.

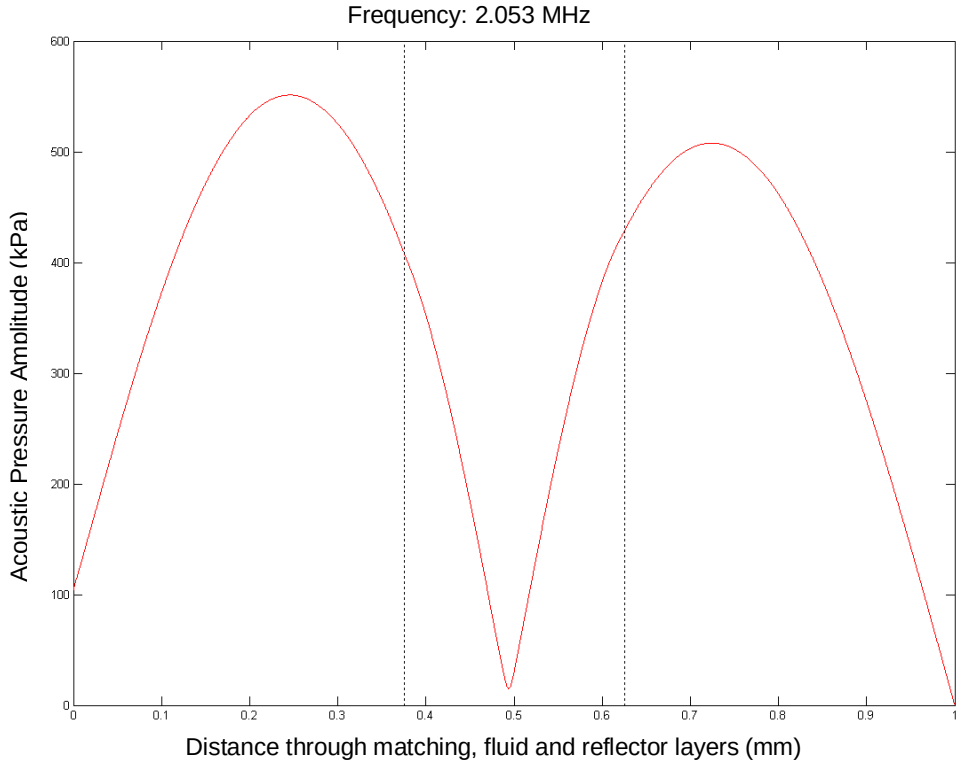

Figure 4-19 An example pressure plot of a PMMA device with a matching, fluid and reflector layer 0.375, 0.250 and 0.375 mm thick respectively with the speed of sound in the fluid set to 1350 m s^{-1}.

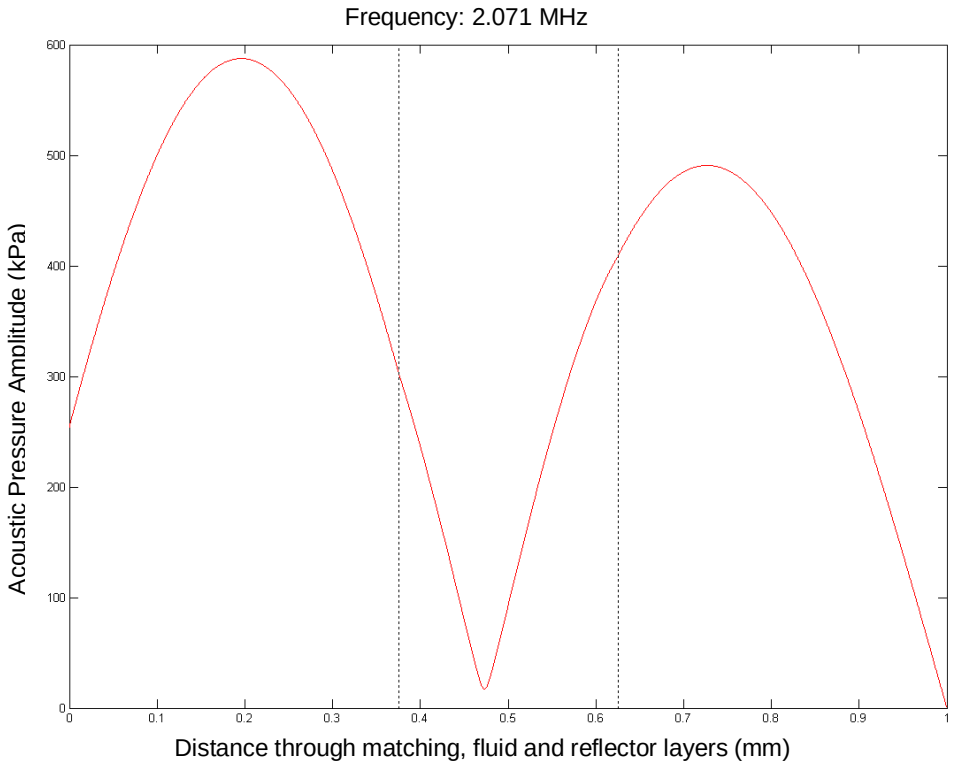

Figure 4-20 An example pressure plot of a PMMA device with a matching, fluid and reflector layer 0.375, 0.250 and 0.375 mm thick respectively with the speed of sound in the fluid set to 1700 m s^{-1}.

4.1.2.3 Discussion

Usually, ceramic devices are designed to fit an exact half wave in the fluid chamber, when this occurs the magnitude of forces generated are higher, but can be sensitive to changes in the speed of sound in the fluid layer as anti-nodes can appear in the channel. In the polymer devices, the impedance differences between the PMMA and the fluid layer are small. This allows any part of a wavelength to be set up across the fluid channel. Because of this, the important dimensions are that of the thickness of the structure as a whole, rather than its individual components. If this can be matched to that of the free transducer, a strong pressure amplitude will be set up across the device. It is then down to the ordering of the layers to position the node as required in the fluid chamber.

One of the disadvantages of designing in ceramic devices when the speed of sound of the fluid is going to change is that the variations may cause an anti-node to appear close to either the matching/fluid or reflector/fluid boundary, see

Figure 4-21 and Figure 4-22. This will usually be against the objectives of the device. By designing in polymers, any fraction of a wavelength can be set up across the fluid channel, meaning that changes in the speed of sound of the fluid are less likely to result in an anti-node in the device, Figure 4-23.

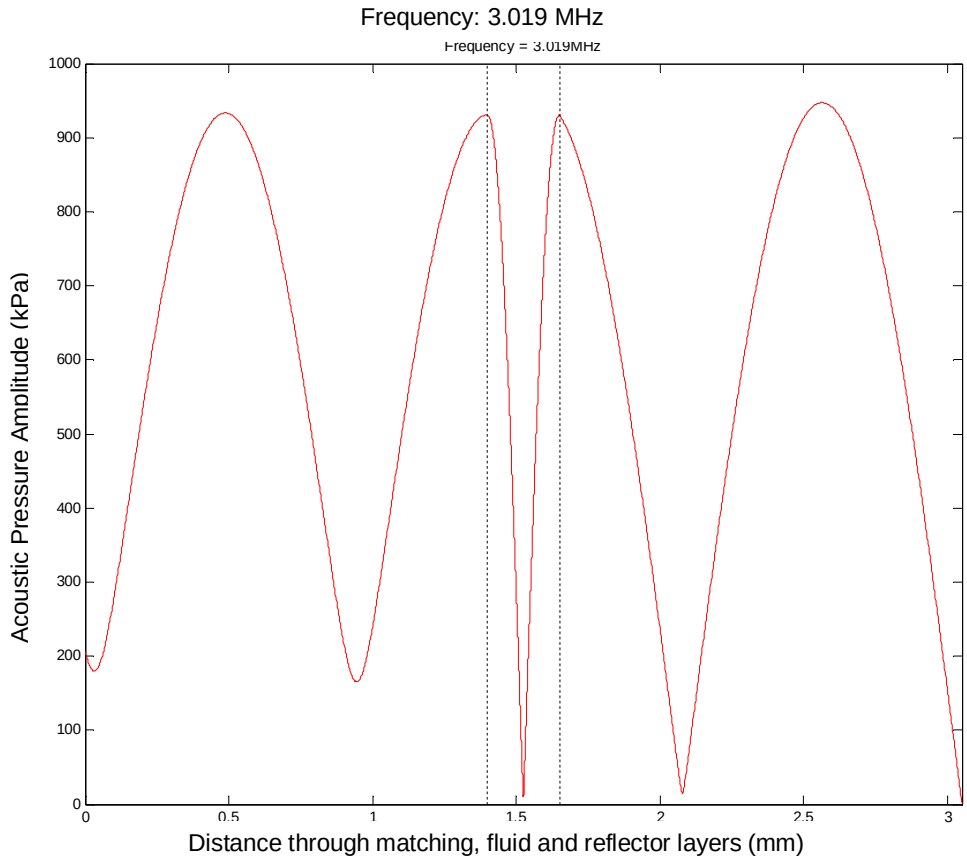

Figure 4-21 An example pressure plot of a ceramic device with a matching, fluid and reflector layer 1.4, 0.250 and 1.4 mm thick respectively with the speed of sound in the fluid set to 1500 m s^{-1}. At both fluid boundaries the pressure anti-node is just within the solid layers.

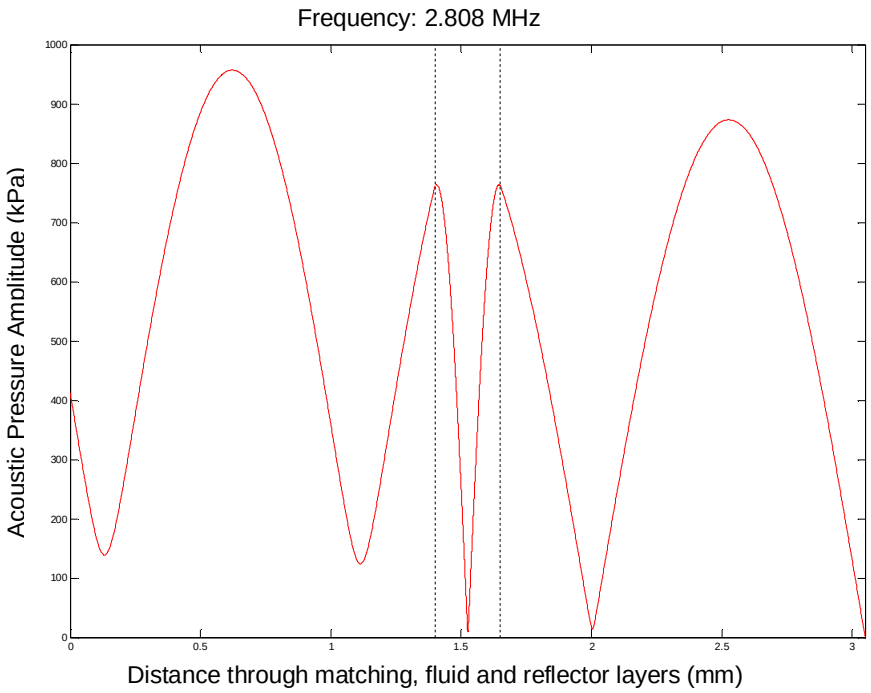

Figure 4-22 An example pressure plot of a ceramic device with a matching, fluid and reflector layer 1.4, 0.250 and 1.4 mm thick respectively with the speed of sound in the fluid set to 1350 m s^{-1}. At both fluid boundaries the pressure anti-node is just within the fluid layer.

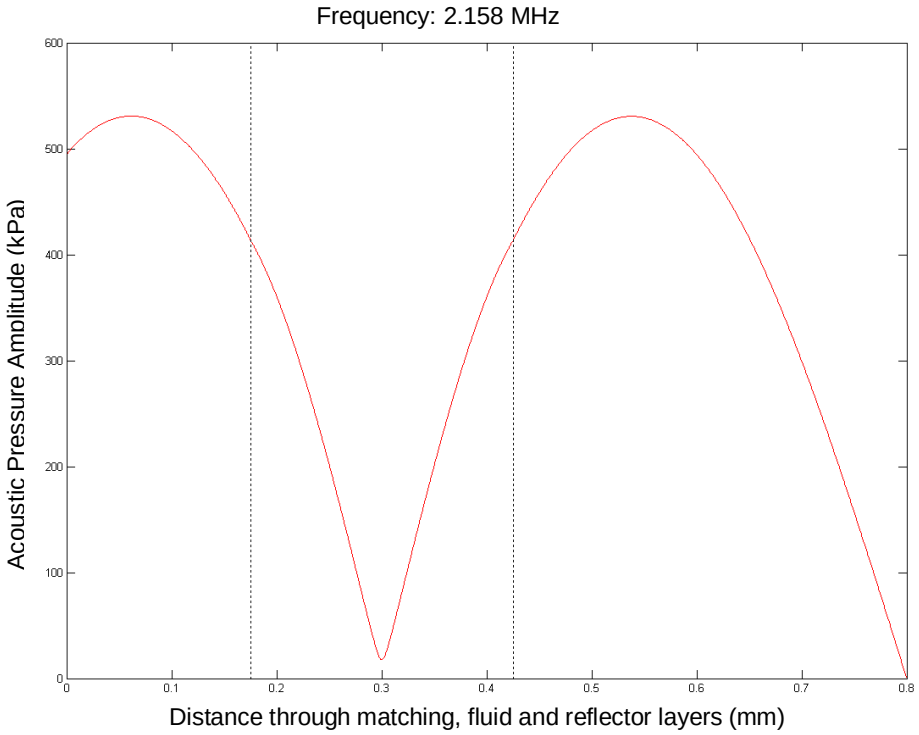

Figure 4-23 An example pressure plot of a PMMA device with a matching, fluid and reflector layer 0.175, 0.250 and 0.375 mm. The pressure anti-nodes are well within the matching and reflector layers and it will not be possible for them to form in the fluid layer.

Another advantage of polymer devices is the positive force away from the fluid/solid boundaries towards the centre of the channel. In a more conventional ½ wave device the force at the boundary is 0, meaning that particles close to the boundary experience very small forces, Figure 4-24. This means that some particles may not experience high enough forces to overcome sedimentation effects. In the polymer device, less than half a wavelength is present in the fluid channel, meaning there are forces acting on particles very close to each boundary layer, Figure 4-25. In fact, the design of the device can be tailored to ensure that a large enough force is present at the matching layer to overcome sedimentation. To maximise the forces on particles at the boundary requires the design of a ¼ wavelength device with a central node, meaning there is a force maximum at each fluid/solid boundary.

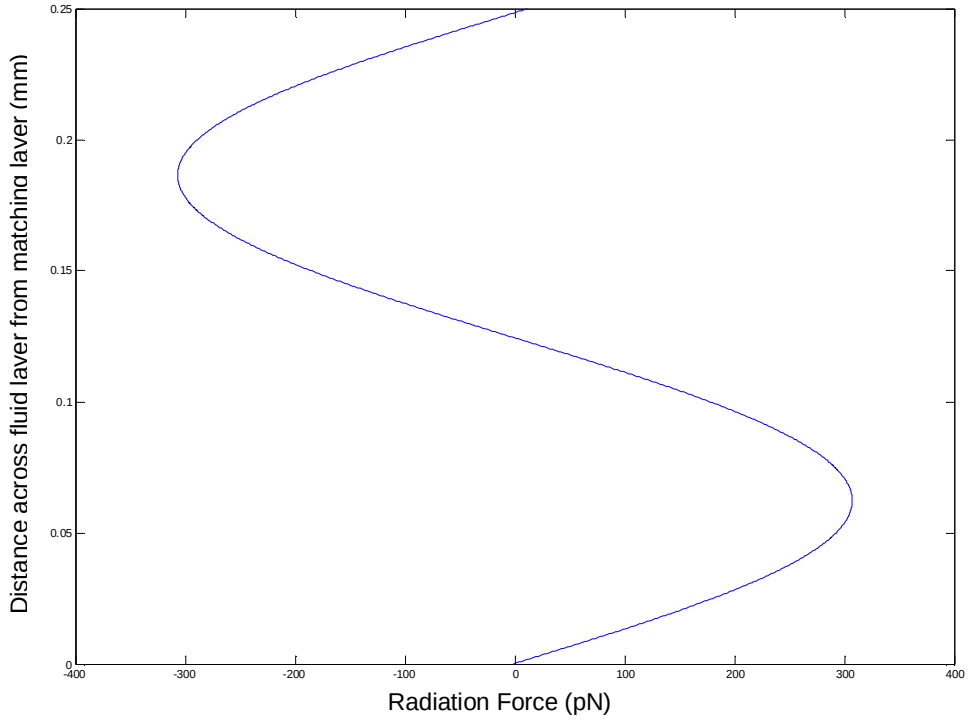

Figure 4-24 The predicted forces in a conventional ceramic ultrasonic particle manipulation device. At each boundary the force is 0, which would allow particles to sediment on the lower surface of the device.

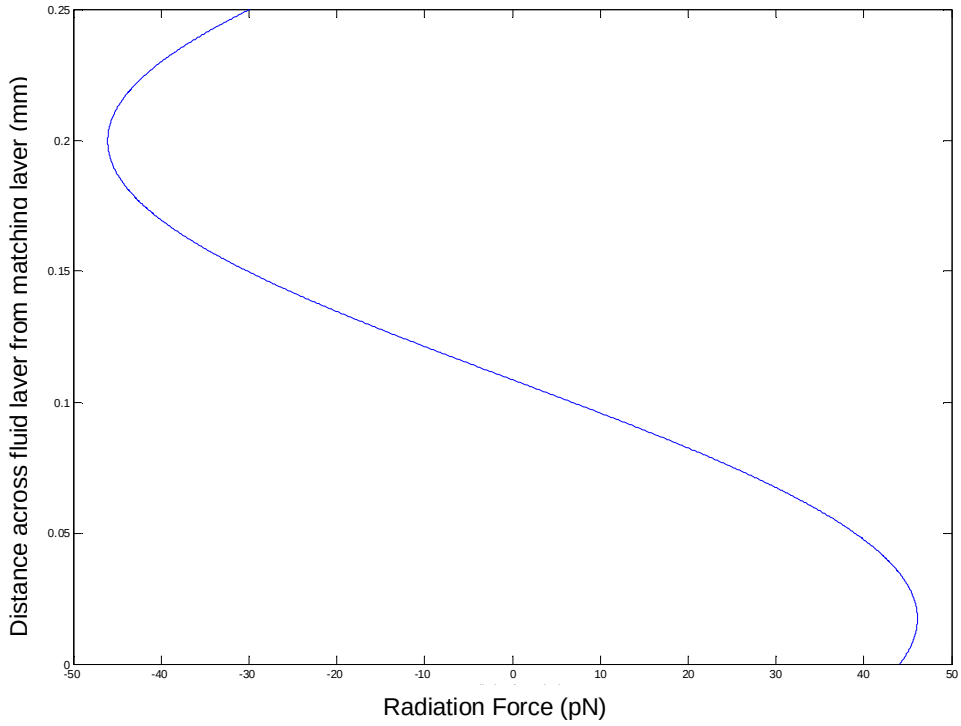

Figure 4-25 The predicted forces in a polymer ultrasonic particle manipulation device. At the matching layer there is an upwards force of 45 pN which is of the right magnitude to stop particles sedimenting. At the reflector layer there is a negative force acting on the beads which ensures they do not adhere to the reflector layer. By designing the device correctly a stronger force can be generated at the matching layer to overcome sedimentation.

4.1.2.4 Conclusions

In conclusion, the 1 dimensional modelling has predicted that robust polymer devices can be made from PMMA. The work has shown that it is important to design for the total thickness to have a similar resonance to that of the free transducer. It then just requires the correct combination of layers and thicknesses to ensure that the node is positioned correctly in the fluid layer; this is because the resonance is dominated by the total thickness due to the similarities in the impedance of the PMMA and fluid. It is possible to design devices that set up less than half a wavelength across the fluid channel, which has the benefit of strong forces acting on particles away from the solid/fluid boundaries. The devices will be robust to changes in the speed of sound of the fluid compared to a traditional half wave ceramic device.

4.1.3 Experiments

To verify the results from the modelling experiments were carried out on the following polymer slide combinations. Dimensions are for the matching, fluid channel and reflector layers respectively;

1) 0.25, 0.25, 0.375 mm
2) 0.375, 0.25, 0.375 mm
3) 0.175, 0.175, 0.375 (half and quarter wave device) mm

The PMMA sheets were cut into approximately 25 x 75 mm slides. Channels approximately 5 mm wide were cut into some of the slides and holes were punched through others for fluidic access. The chips were bonded together using the solvent technique involving 33% acetone with 67% ethanol (Harris et al., 2010). Fluid connectors were glued in place and transducers approximately 10 x 15 mm long were glued over the channel. Diagrams of the device are shown in Figure 4-26 and Figure 4-27.

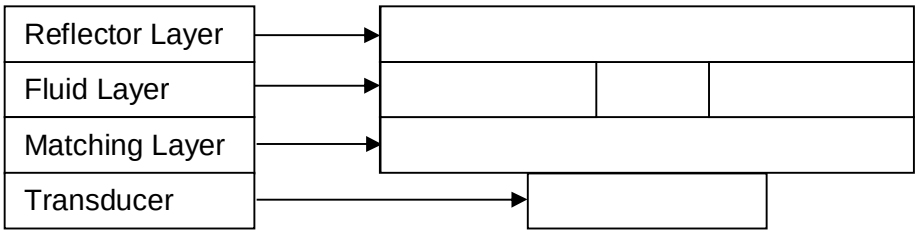

Figure 4-26 A schematic of the cross section of a polymer device. The central fluid channel is approximately 5 mm wide. Layer thicknesses are detailed above.

Figure 4-27 An aerial view of the fluid layer with the fluid channel cut out. The fluid channel was approximately 5 mm wide and 50 mm long. The total size of the PMMA sheet was approximately 25 x 75 mm to match standard microscope slides.

4.1.3.1 Impedance Analysis

Impedance analysis was carried out for comparison with the modelling. The frequency values measured matched well with what was modelled for the 0.375, 0.25

and 0.375 mm device, confirming that the properties used for the modelling were accurate. The estimated Q factors led to significant differences in the magnitude of the modulus of impedance but the frequency values matched well, Figure 4-28. The measured impedance plot identified more resonant modes than the 1 dimensional Matlab model, as it cannot predict lateral resonances.

In the 0.175, 0.175 and 0.375 mm device the modelling predicted two resonant modes, a quarter wave and a half wave. When impedance measurements were carried out on two devices, both the resonant modes were identified at approximately the right frequencies. As before, minor modes were identified in the measurements likely to be from lateral resonances, Figure 4-29. The frequency at which points of minimum impedance were measured appeared to match well with the modelling though the magnitude of the measured impedance significantly different.

In the 0.25, 0.25 and 0.375 mm device the impedance measurements also matched well with the model. In this particular device, some resonances are present in the air filled device but not in the water filled device which also matches with what was predicted. The impedance measurements also identified more minor resonances than the model predicted, again due to the model only being one dimensional, Figure 4-30. The frequency at which points of minimum impedance were measured appeared to match well with the modelling though the magnitude varied significantly.

The impedance measurements have confirmed that the properties used in the Matlab model are accurate enough for this stage of the work. The frequencies of impedance minima and maxima match but the magnitude between the points is significantly overestimated in the model. This implies the Q factors used in the modelling are overestimated. It was later confirmed that the Q factor for water would have been better represented as 30 rather than 100, (Hill et al., 2008). For the purposes of this work it is sufficient for the values of the resonant frequencies to match. This will mean the information from the model regarding node position is correct but the magnitude of the forces will be overestimated. Further development of the model is not required to fulfill the aims of this work and experiments will be used to develop the ideas further.

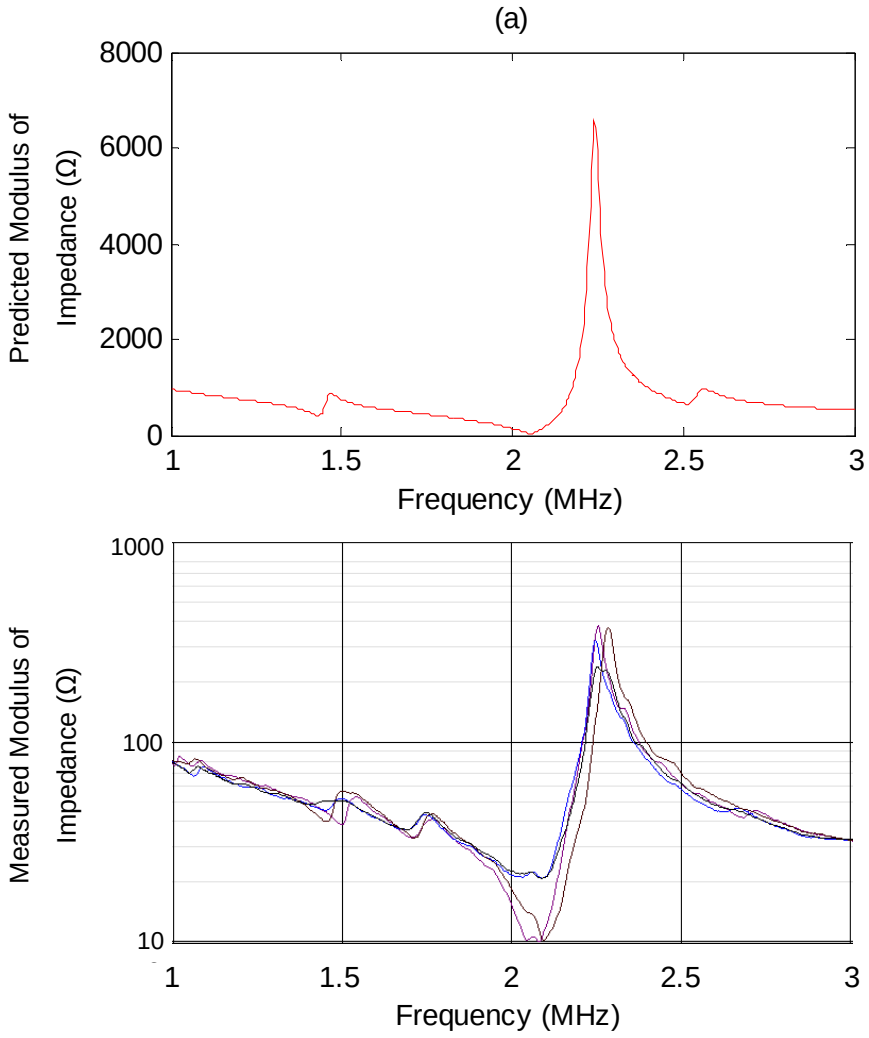

Figure 4-28 The predicted impedance plot is shown above and is compared with the measured impedance for two 0.375, 0.25, 0.375 mm polymer devices. The black and blue plots show the device with an air filled fluid chamber. The purple and pink lines show a water filled cavity. The measured plot shows a resonance at just over 2 MHz as predicted, with a smaller resonance just below 1.5 MHz. An extra resonance is seen at approximately 1.7 MHz which could be due to a resonance in a different dimension that would not be predicted using the 1 dimensional Matlab model.

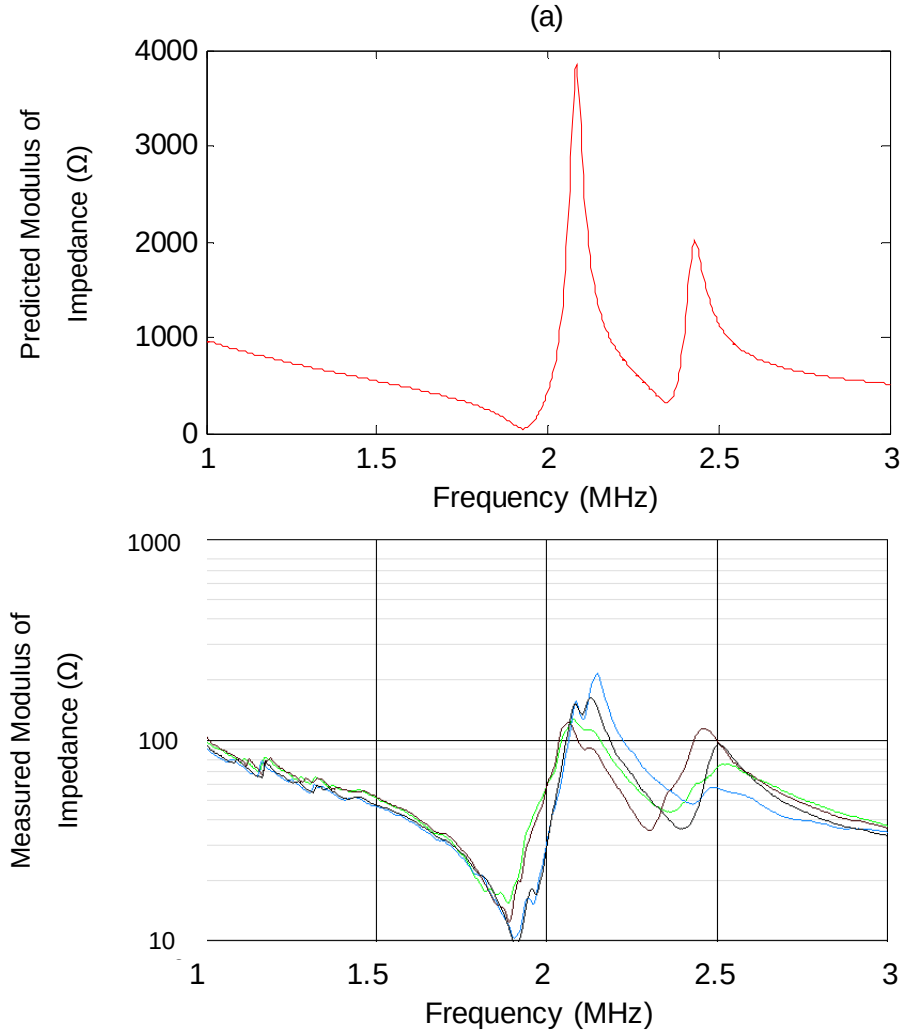

Figure 4-29 The predicted impedance plot is shown above and is compared with the measured impedance for two 0.175, 0.175, 0.375 mm polymer devices. The green and brown plots show the device with an air filled fluid chamber. The black and blue lines show a water filled cavity. The measured plot shows a resonance at just over 1.9 MHz as predicted, with a smaller resonance just below 2.4 MHz. These correspond to the quarter wave and half wave resonances predicted.

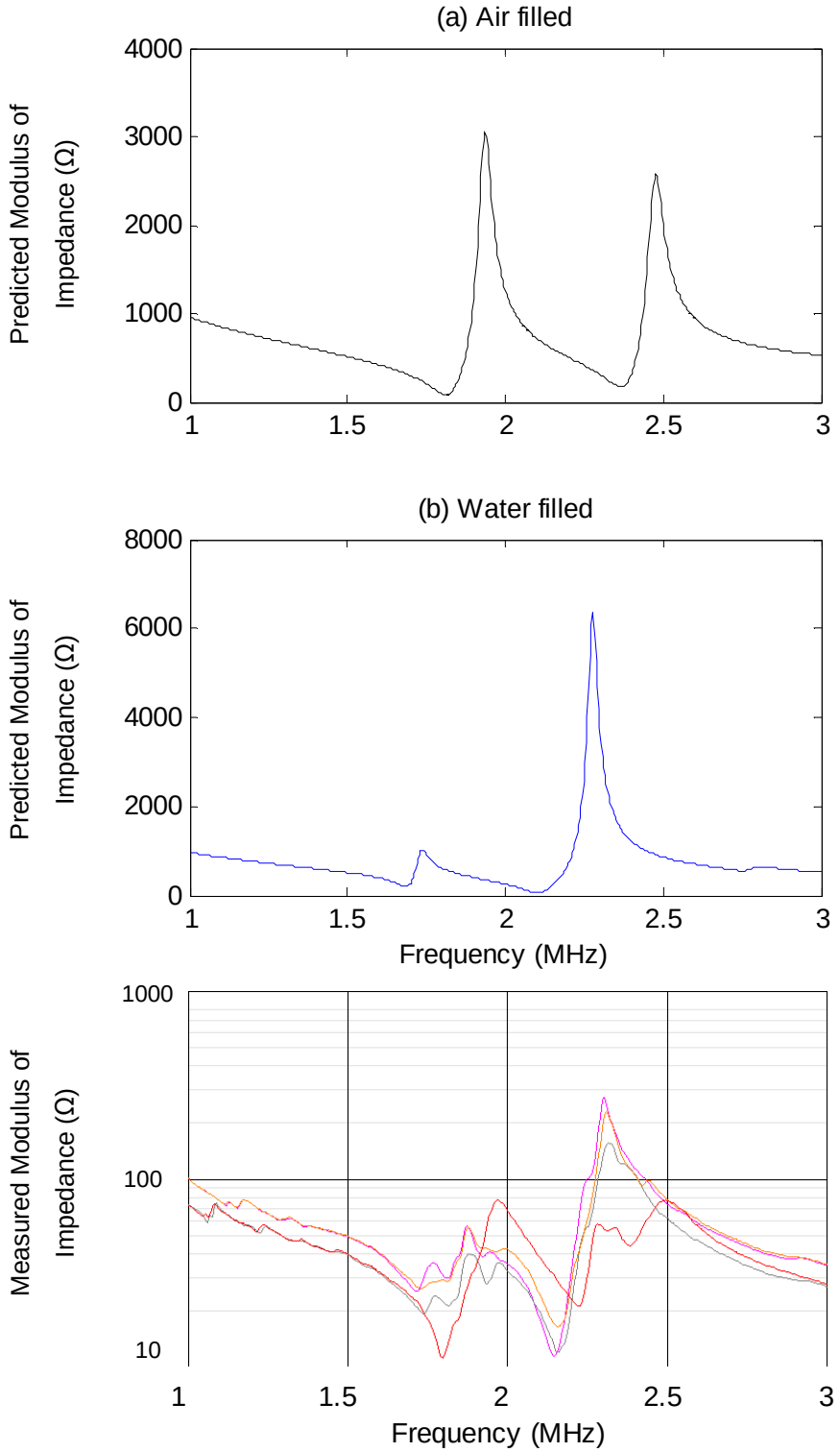

Figure 4-30 The predicted impedance plot is shown above and is compared with the measured impedance for two 0.25, 0.25, 0.375 mm polymer devices. The red and orange plots show the device with an air filled fluid chamber. The grey and pink lines show a water filled cavity. The measured plot shows a resonance at just over 2.1 MHz as predicted, with a smaller resonance at approximately 1.6 MHz. The ½ wave resonance of interest is at 2.1 MHz. In this device, the air filled resonance at 1.6 MHz becomes less pronounced in the water filled cavity, which is seen in the impedance measurements.

Impedance measurement results are summarised and compared with modelling in Table 4-8.

Table 4-8 Shows the comparison between predicted impedance minima and measured. The model tended to predict slightly lower frequencies but on the whole matched well.

Device	Configuration (mm)	Expected Resonance (MHz)	Measured Resonance (MHz)
1	175, 175, 375 (Quarter)	1.936	1.952
1	175, 175, 375 (Half)	2.36	2.426
2	250, 250, 375	2.104	2.149
3	375, 250, 375	2.052	2.086

4.1.3.2 Particle focusing method

To investigate this device further, a series of devices were made in the 0.375, 0.25, 0.375 mm thick combination. This combination of layers was chosen as the symmetrical design is less likely to lead to user errors than the 0.25, 0.25, 0.375 mm combination that has marginally higher forces predicted, see Table 4-6. The PMMA sheets were milled into 25 x 75 mm slides. PZT transducers 8, 6 and 4 mm wide and 30 mm long were made and fluid channels 0.5, 1, 1.5, 2, 3 and 4 mm wide were milled into the 0.25 mm thick layers. 1 mm diameter holes were milled into half of the 0.375 mm thick slides and then the layers were bonded together using the 1:2 acetone:ethanol technique discussed previously.

A solution containing yellow-green 10 µm diameter FluoroSpheres was prepared and flowed through the devices at various rates using a syringe pump. The transducers were connected to a signal generator and set to the measured impedance minimum in Table 4-8. Fluorescence microscopy (FITC filter, Olympus IX71 microscope) was used to view the particles in the fluid chamber. Images were taken at the far end of the transducer to allow the maximum time for the acoustic radiation force to manipulate the beads. By taking long exposure photos (300 ms) of the fluid chamber it is possible to compare how far beads have travelled in a set amount of time, indicating whether or not they are travelling at the same speed and therefore if they are in the same plane, Figure 4-31. This is possible because a parabolic fluid profile is set up in the microfluidic channel from the bottom of the channel to the top. A voltage of 10 V_{pp} was applied using a signal generator at the point of minimum impedance, approximately 2.08 MHz. The flow rate in the 4 mm wide channels was set to 0.45 mL hr^{-1} and was scaled down proportionally for the narrower channels.

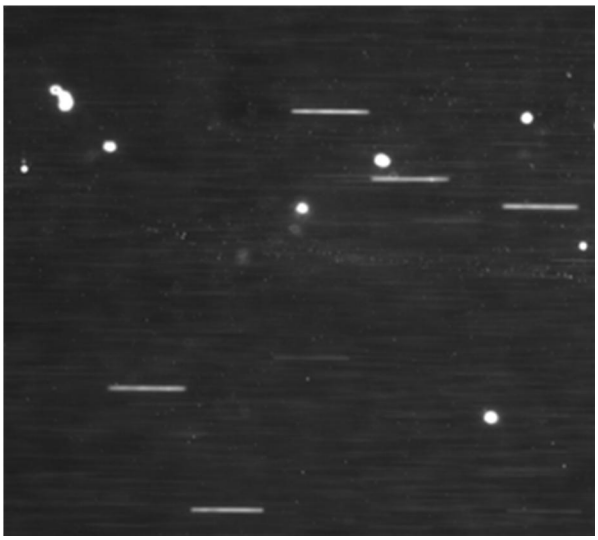

Figure 4-31 An example image of the 10 µm beads in the fluid channel. By comparing the streak lengths when the power is turned on and turned off it is possible to show the effects of ultrasonic excitation across the device. Streak lengths are approximately 200 µm.

Lateral banding was observed at high voltages (>10 V_{pp}) which is too high a power requirement for remote *in-situ* oceanographic sensors. This lack of lateral focusing is to be expected as the devices were not operating at a frequency that corresponds to a half wavelength or multiple of across the width of the device.

4.1.3.3 Width of PZT results

To test the robustness of the device, a series of PZT transducers of various widths were trialed; this will ensure that width variations in the manufacture of transducers should not hugely impact the effectiveness of the device. Images were taken across a 4 mm wide channel and the three different PZT transducers were trialed. When no ultrasonic forces were used the length of the streaks varied significantly across the width of the device, consistent with a random distribution of particles across the device, Figure 4-32. When the 4 mm wide transducer is powered at 10 V_{pp} the particles in the central 92.5 % width of the device travelled 190 µm in 300 ms, ±15 µm, Figure 4-33. Similar results are seen when a 6 mm wide transducer is used, particles within the central 90 % of the width all travel 185 µm in 300 ms, ±17 µm, Figure 4-34. The position of the pressure node, based on the Matlab modelling, is not quite centered. Therefore, a slower particle speed implies that the force acting on the particles is stronger, pulling particles into a slightly slower stream. When an 8 mm wide transducer is used, all the particles within the central 92.5 % of the channel travel 192 µm in 300 ms, ±11 ms, Figure 4-35.

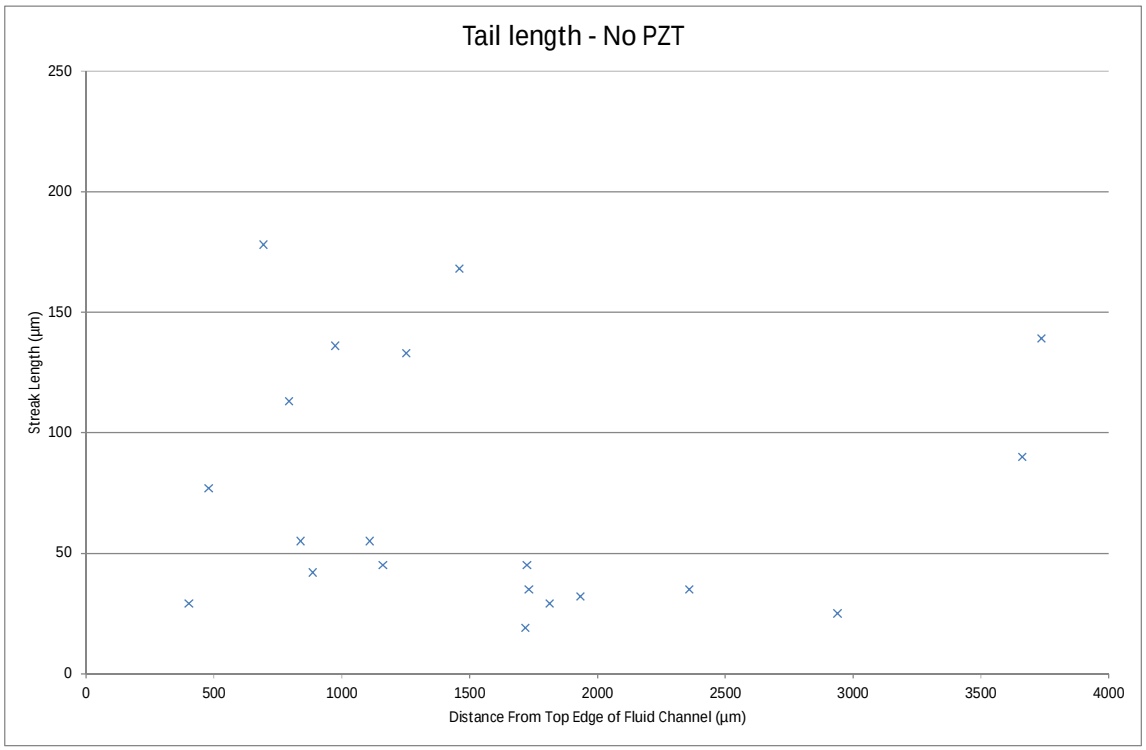

Figure 4-32 shows the distribution of streak lengths across the width of the device. Streak lengths varies significantly which implies a random distribution of particles in the device.

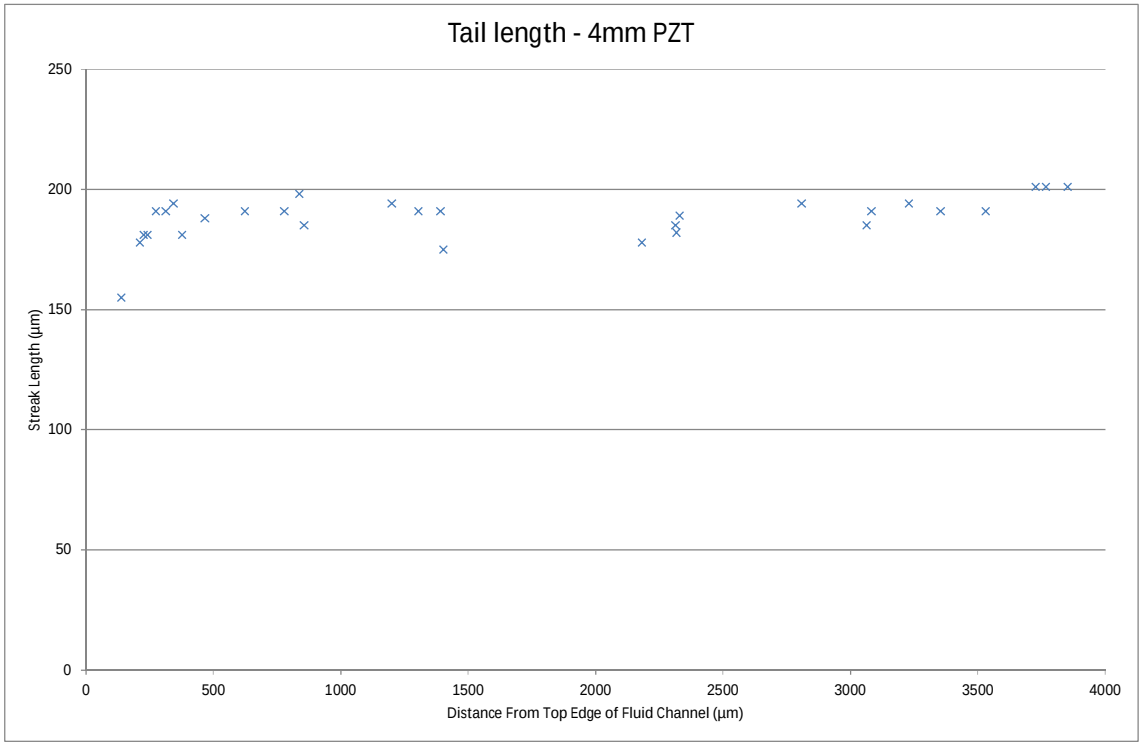

Figure 4-33 shows the distribution of streak lengths across the device when a 4 mm wide PZT transducer is powered at 10 V_{pp}.

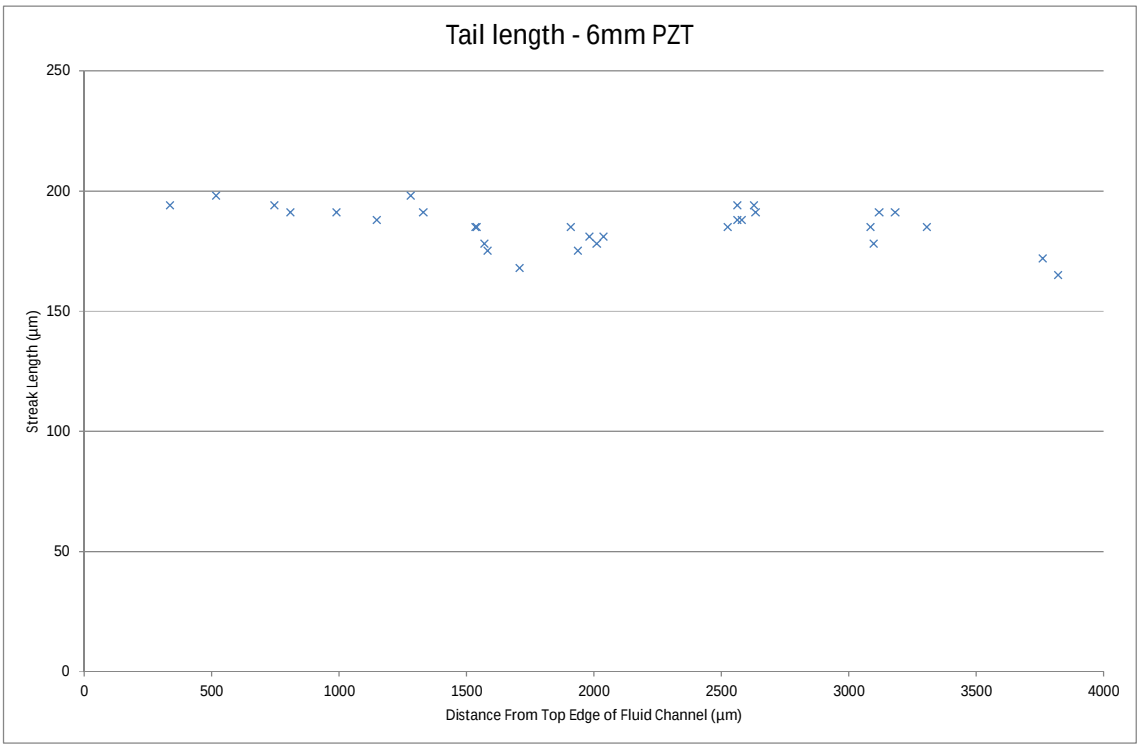

Figure 4-34 shows the distribution of streak lengths across the device when a 6 mm wide PZT transducer is powered at 10 V_{pp}.

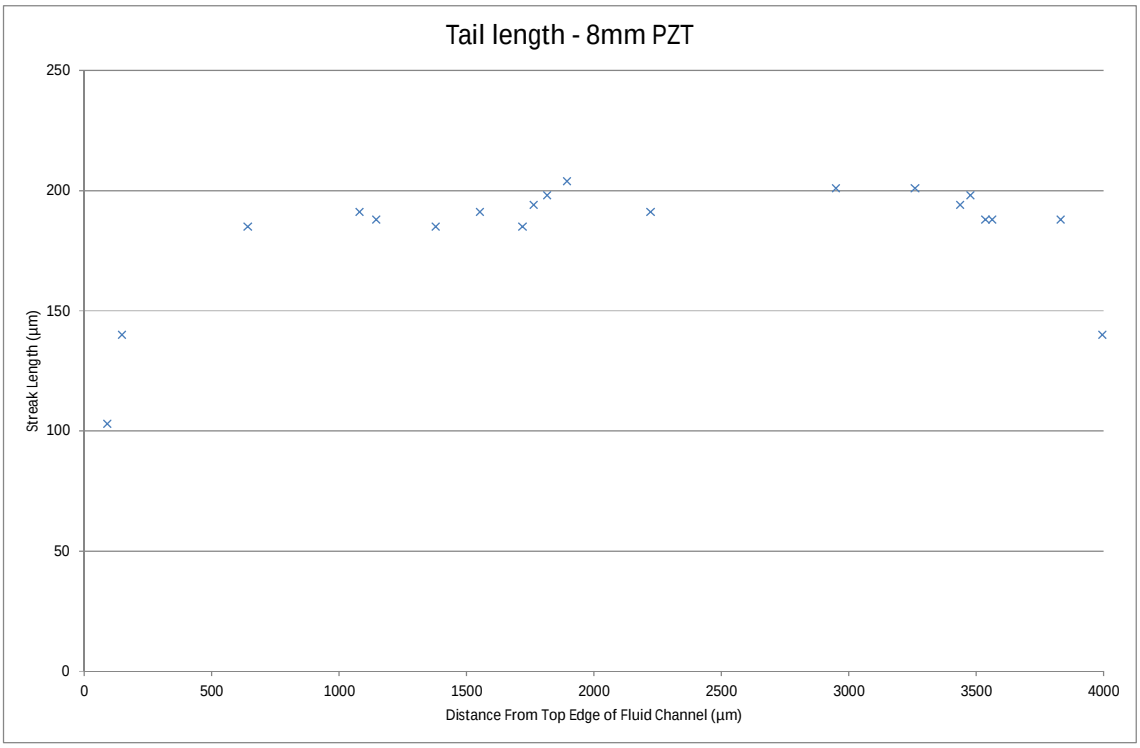

Figure 4-35 shows the distribution of streak lengths across the device when an 8 mm wide PZT transducer is powered at 10 V_{pp}.

All 3 transducers when powered at 10 V_{pp} focused particles to within a relatively tight band and speed variations across each device were minimal. This shows a consistently shaped pressure node across each device and that variations in transducer width are unlikely to change the characteristics of the device significantly. The speed of particles between different devices was also consistent, implying that changing the PZT width has little effect on the force profile generated.

4.1.3.4 Width of the fluid channel results

To investigate if variations in the channel width will affect the characteristics of the device a series of fluid channels were trialed. The 4 mm wide PZT was powered at 10 V_{pp} with a series of fluid channels. Images were taken across the width of the device, or a series of images taken in the same spot for the narrow channels.

Figure 4-36 to Figure 4-41 show particle distribution across different width channels. All channels show particle manipulation when the device is powered at 10 V_{pp}, with one dimensional focusing achieved across the majority of the device. In Figure 4-37 and Figure 4-40 a small drop in particle velocity can be seen at the centre of the channel but in general particle positioning is consistent. Average particle speed varies between devices, which is expected as the flow profile would change as the width of the channel decreases. The extreme case, a channel 0.5 mm wide shows the formation of a parabolic flow across the width of the device but still shows particle focusing.

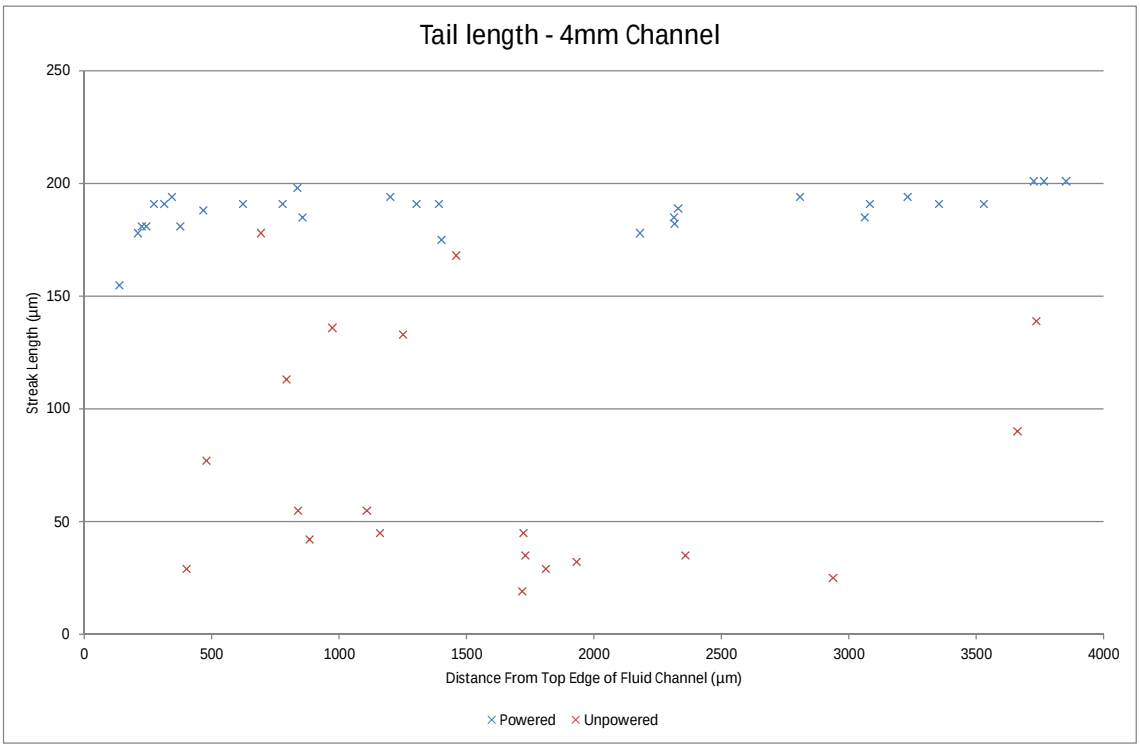

Figure 4-36 shows the distribution of streak lengths across the device with a 4 mm wide channel and a 4 mm wide PZT transducer powered at 10 V_{pp}.

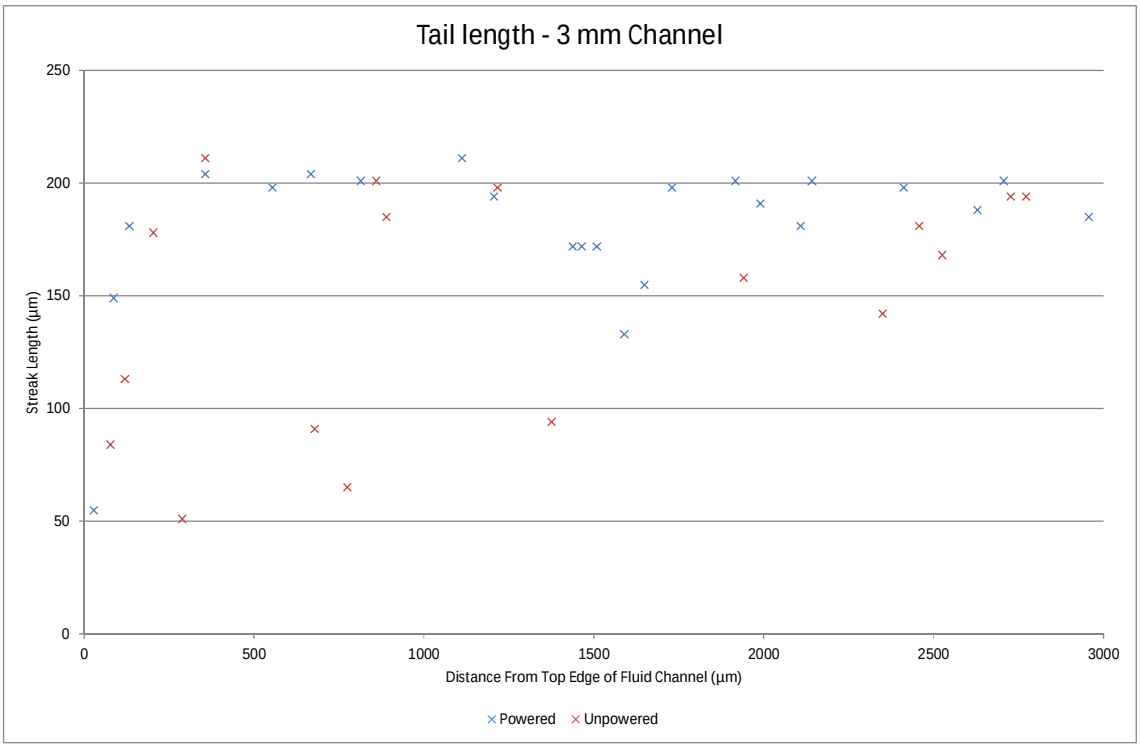

Figure 4-37 shows the distribution of streak lengths across the device with a 3 mm wide channel and a 4 mm wide PZT transducer powered at 10 V_{pp}.

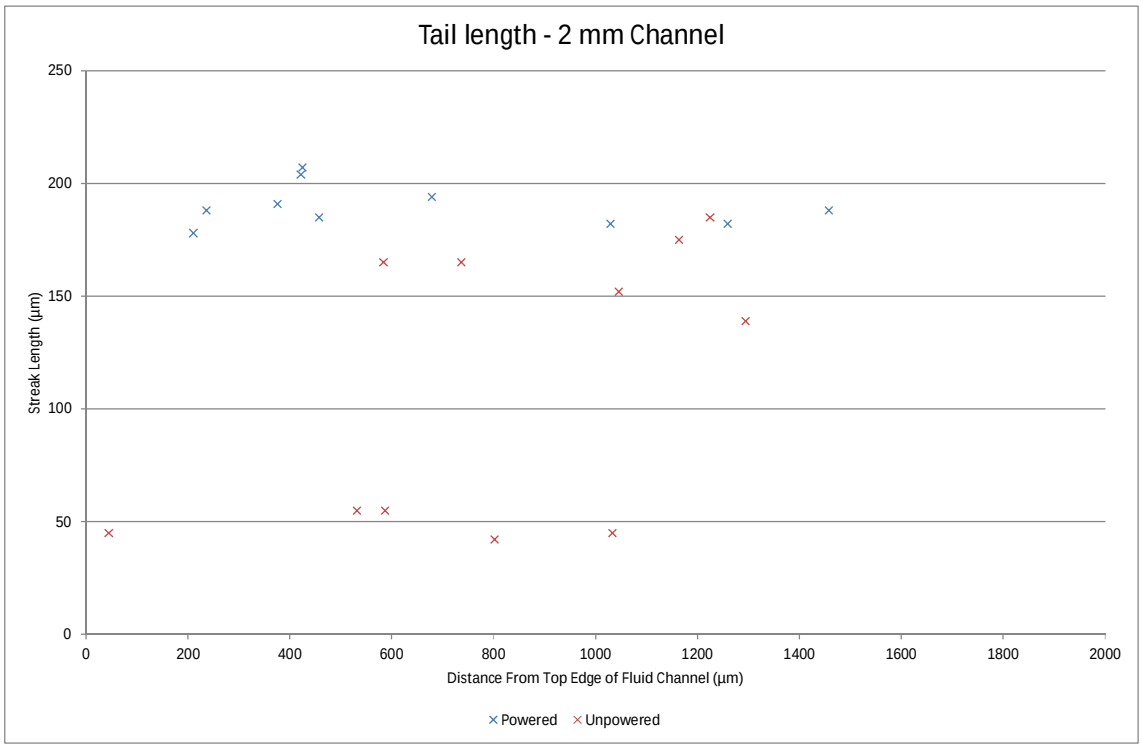

Figure 4-38 shows the distribution of streak lengths across the device with a 2 mm wide channel and a 4 mm wide PZT transducer powered at 10 V_{pp}.

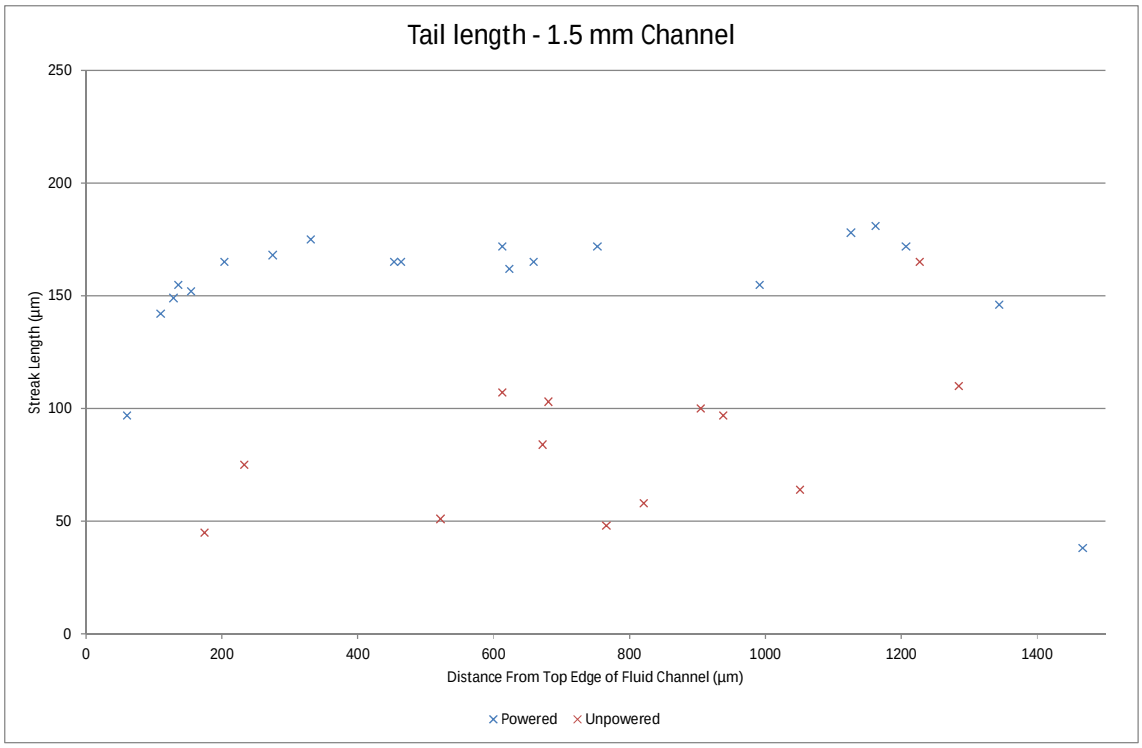

Figure 4-39 shows the distribution of streak lengths across the device with a 1.5 mm wide channel and a 4 mm wide PZT transducer powered at 10 V_{pp}.

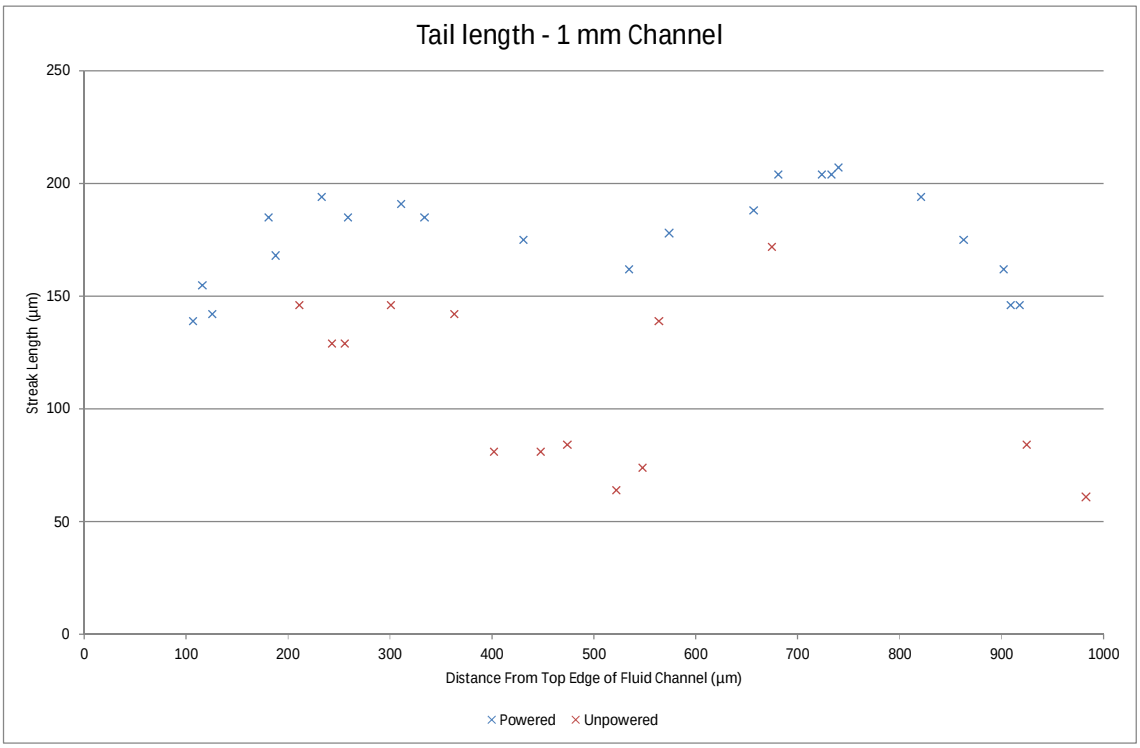

Figure 4-40 shows the distribution of streak lengths across the device with a 1.5 mm wide channel and a 4 mm wide PZT transducer powered at 10 V_{pp}.

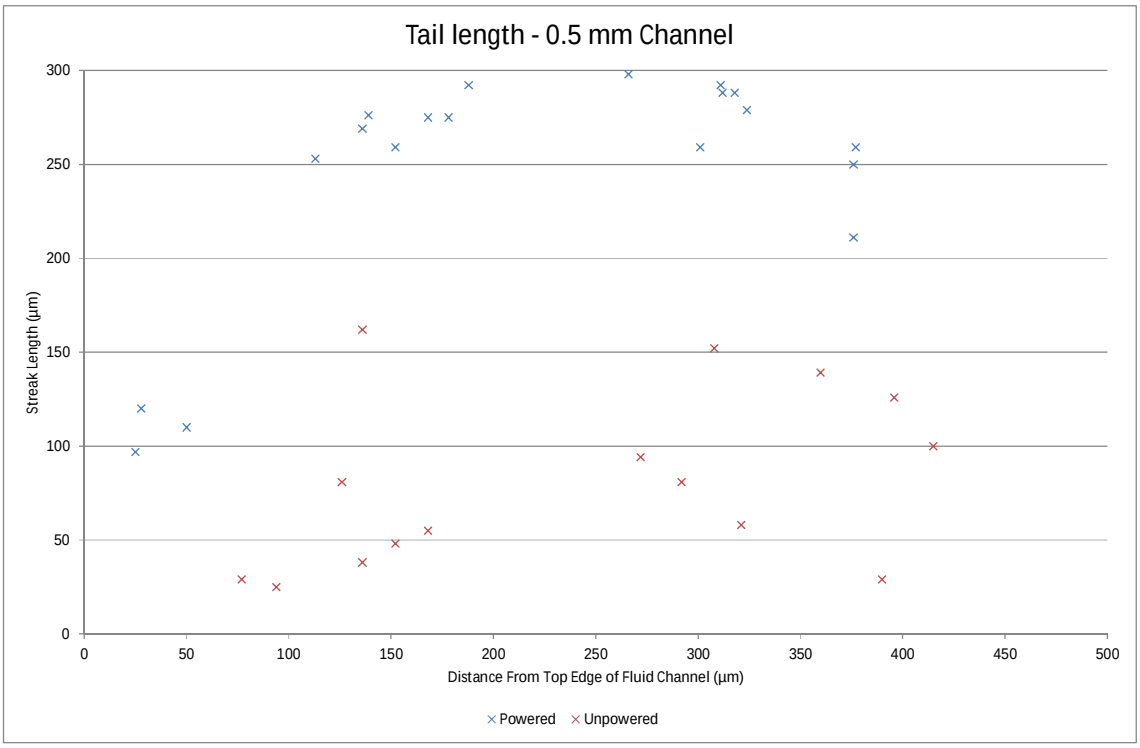

Figure 4-41 shows the distribution of streak lengths across the device with a 1.5 mm wide channel and a 4 mm wide PZT transducer powered at 10 V_{pp}.

These experiments have shown that the device is robust to variations in the width of the fluid channel. All of the devices were capable of focusing particles into a plane parallel to the transducer. No evidence of lateral banding was seen at these voltages.

4.1.3.5 Voltage Drop Analysis

A solution containing 10 µm diameter beads was fed into a 3.8 mm wide fluid chamber and 10 V_{pp} was applied to a 4 x 30 mm wide transducer. Once a bead was captured in the acoustic forces within the device, the voltage was lowered until the forces acting on the bead were insufficient to levitate the bead, 1.6 V_{pp}. The acoustic pressure (*P*) within the chips, measured through voltage-drop analysis on a 10 µm polystyrene bead was equal to 3.5 x 10^4 x Pa, at 1.6 V_{pp}. This corresponds to an energy density of 5.38 J m^{-3} at a voltage of 10 V_{pp}.

4.1.4 Conclusions

One dimensional modelling predicted sub half wavelength modes in polymer devices. This was verified experimentally, initially in milled PMMA chips and later in PMMA films. Attempts to generate a lateral mode across a half wavelength channel were unsuccessful, though weak lateral focusing was seen. Manufacturing tolerances made it difficult to repeat these experiments and so alternative methods were sought. PMMA films of consistent thickness were identified as a repeatable method. One dimensional modelling again predicted which devices would work as planar resonators and impedance readings matched well with modelling. The problem of variations in the width of components was not solved by using PMMA films, so a series of particle focusing experiments investigated these effects. A series of different width transducers and fluid channels were made and tested. No significant variation was seen between the devices which implies they will be robust to variations in the milled width dimensions. The PMMA films successfully manipulated particles to a steady plane across the width of the device with minimal lateral variations. This lack of lateral focusing can be attributed to the fact the devices were not operating at a half wavelength (or multiple of) and so lateral coupling was weak. To design a 2 dimensional focusing device in polymer will require more accurate manufacturing techniques which puts it beyond the scope of this project.

By designing PMMA devices in which the resonance of the thickness as a whole is as close to the free transducer as possible, strong acoustic manipulation devices can be created. The difficulty is in ordering the PMMA layers to achieve the desired node position. This method is a new approach to designing ultrasonic particle manipulation

devices in polymers. This method has the added benefits of noticeable forces at the fluid/solid boundaries and they are robust to significant changes in the properties of the fluid.

4.2 Lithium Niobate Devices

Lithium niobate is more commonly used in SAW devices, however, its optical transparency gives the potential for transmission microscopy to be used in a bulk excitation configuration. This could have useful applications for biologists where transmission microscopy is required. Whilst lithium niobate is transparent, electrodes tend to be opaque. For this work, the use of transparent electrodes was investigated as a suitable partner for lithium niobate.

4.2.1 Computational Modelling

The anisotropic properties of lithium niobate mean that careful consideration is required in the selection of a bulk transducer. The most common cut of lithium niobate, Y+128°, is optimised for the propagation of surface waves and to limit the generation of bulk acoustic waves, see Section 2.3.1 Surface Acoustic Devices. To test this, impedance measurements were taken of a 2 mm thick piece of Y+128 lithium niobate (Photox, Sheffiled, U.K.) with silver paint electrodes. The results showed no impedance troughs between 0.5 – 4 MHz.

A less common cut, Y+36, is capable of bulk resonance modes and 500 µm thick samples were acquired (Roditi International Corp, London, U.K.). The 1 dimensional Matlab model had the following parameters loaded into it describing the lithium niobate and polymer slides, Table 4-9. Lithium niobate density is available from the manufacturer and the Q factor was set at the same level as PZT. Approximate values for the speed of sound are available online and some iterations were performed to optimise the model. Parameters for other materials have been discussed in 4.1.1.1 Device Design.

Table 4-9 Properties used for the modelling of a 0.5 mm thick lithium niobate transducer.

	Density kg m^{-3}	Speed of Sound m s^{-1}	Thickness mm	Q Factor
Lithium Niobate	4650	4560	0.5	100
PMMA	1160	2260	Varied	30
Water	1000	1480	Varied	100
Polystyrene Bead	1055	1962	N/A	N/A

The model predicts a resonance at approximately 3.71 MHz for the free transducer, which was tested by impedance measurements on a piece of lithium niobate using silver paint electrodes, Figure 4-42. An impedance minimum was recorded at 3.75 MHz which matches well with the modelling.

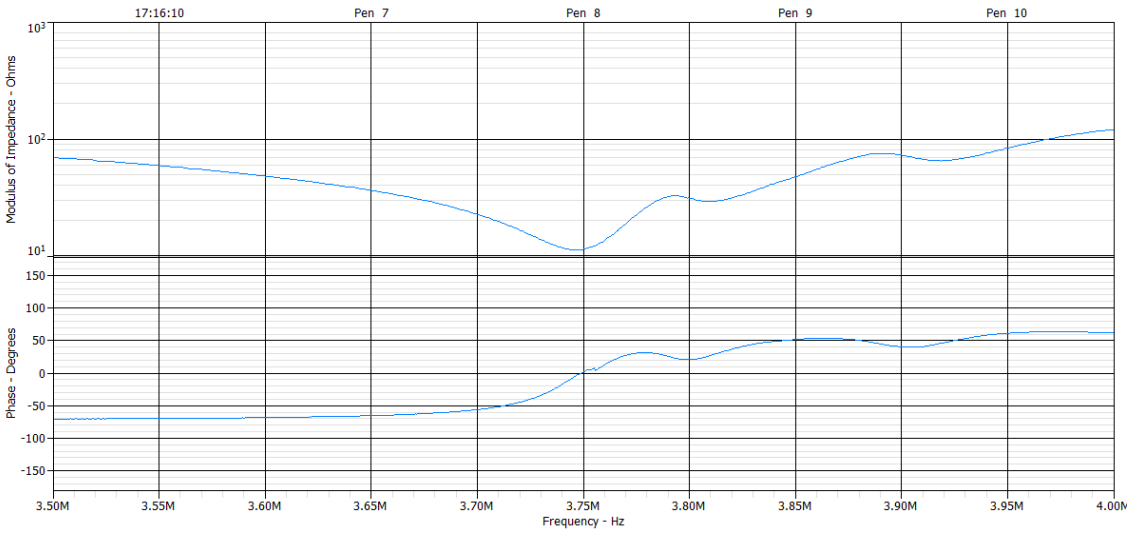

Figure 4-42 The measured impedance for a 0.5 mm thick lithium niobate Y+36 transducer from 3.5 - 4 MHz.

The modelling matched well with measurements for a free lithium niobate transducer. Further modelling was then carried out designing a polymer device to be coupled with the transparent transducer. Using 3 PMMA layers each 0.175 mm thick predicts a pressure node in the centre of the device at approximately 3.75 MHz and a minor resonance at 2.6 MHz, see Figure 4-43 and Figure 4-44. As described earlier, the use of polymers allows for less than half a wavelength in the fluid channel, resulting in strong forces at the solid/fluid boundaries, Figure 4-45.

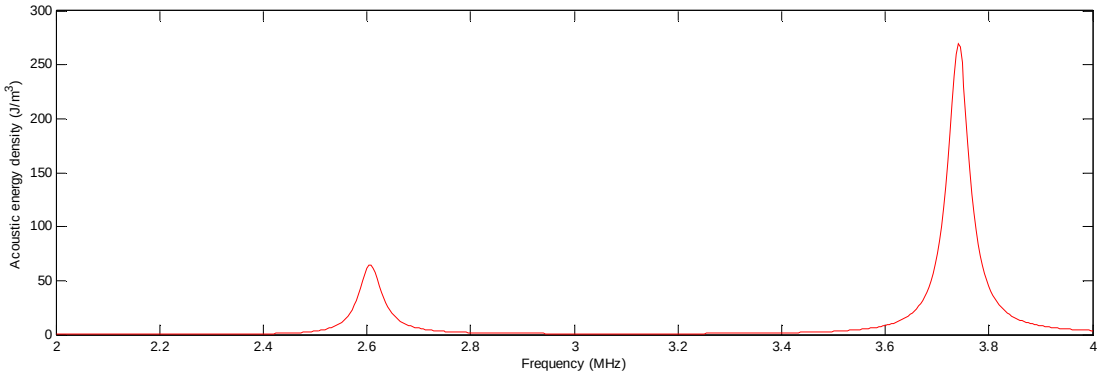

Figure 4-43 The predicted energy density in the fluid channel for a 0.175, 0.175 and 0.175 mm PMMA film device coupled with a 0.5 mm thick lithium niobate Y+36 transducer.

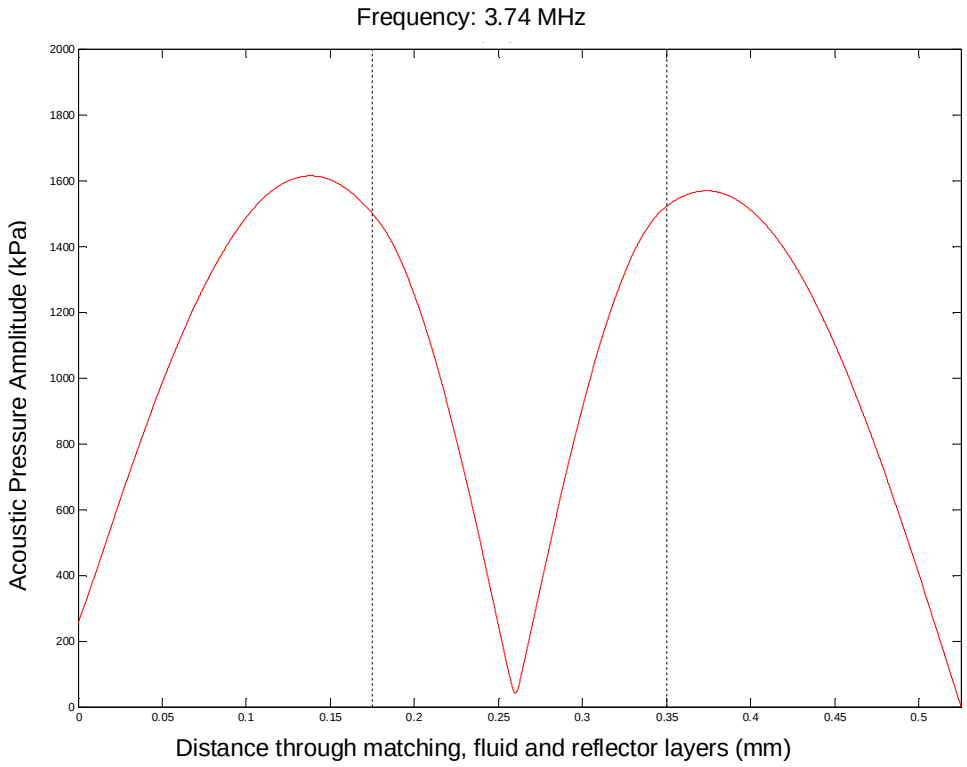

Figure 4-44 the predicted pressure amplitude through the PMMA layers when coupled with the lithium niobate transducer. A pressure node is predicted in the middle of the channel and a pressure gradient is seen at both solid/fluid boundary layers which will result in a force away from the boundaries.

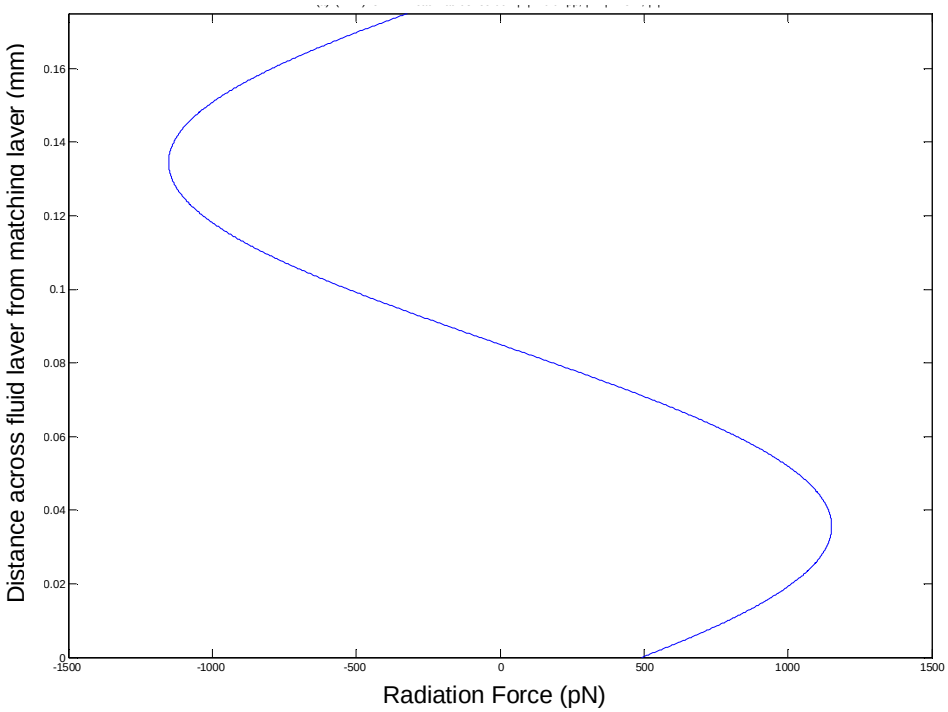

Figure 4-45 The generated force profile for the lithium niobate transducer PMMA film device. Very strong forces are predicted manipulating particles into the middle of the fluid chamber.

The modelling of a PMMA device coupled with a lithium niobate transducer predicted a half wave type particle focusing device operating at a frequency close to that of the free transducer. To verify this, devices will be built and tested whilst also investigating the feasibility of different electrode materials.

4.2.2 Experiments

Experiments were carried out on the designed PMMA devices as well as a brief investigation to check the devices would work in a more conventional glass device. Verifying the model using a glass capillary (Vitrocom Inc, New Jersey, U.S.A.) configuration helped ensure that the parameters of the model were correct.

4.2.2.1 Glass Capillary

The acoustic characteristics of glass capillaries are well known, so modelling was carried out to investigate the effects of coupling a 300 µm fluid channel capillary to a Y + 36 lithium niobate transducer. Further information on the capillaries is presented in 5.2 Initial Experiments – Glass Capillaries. The model predicted a resonance at 2.848 MHz with an antinode in the fluid channel near the matching layer and an antinode very close to the reflector. The device was built and filled with a solution containing green FluoroSpheres of 5 µm radius. The transducer was powered at 20 V_{pp}

at the frequency of minimum impedance which was measured at 2.92 MHz, close to the predicted resonance. Images were taken at the top and bottom of the capillary which showed the focusing of beads at both solid/fluid boundaries and lateral banding, Figure 4-47 and Figure 4-48. More particles were observed at the matching layer which matches with the modelling.

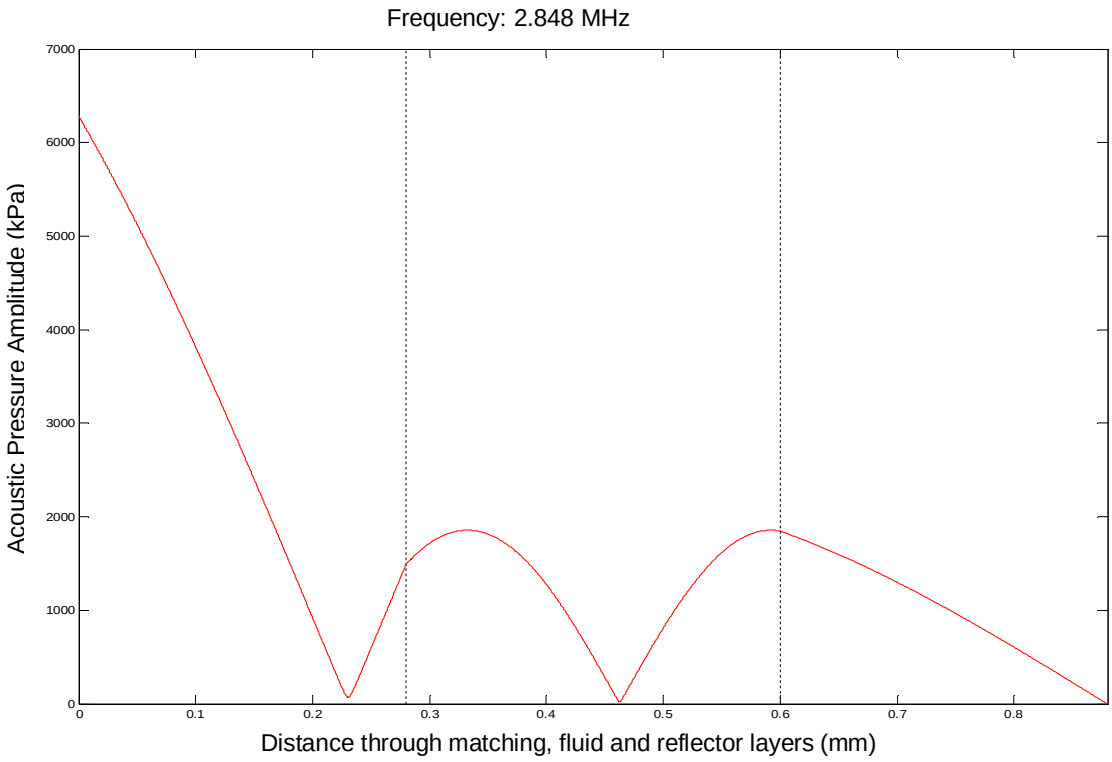

Figure 4-46 The predicted acoustic pressure generated in a 300 µm capillary. An antinode is present near the matching layer and very close to the reflector layer.

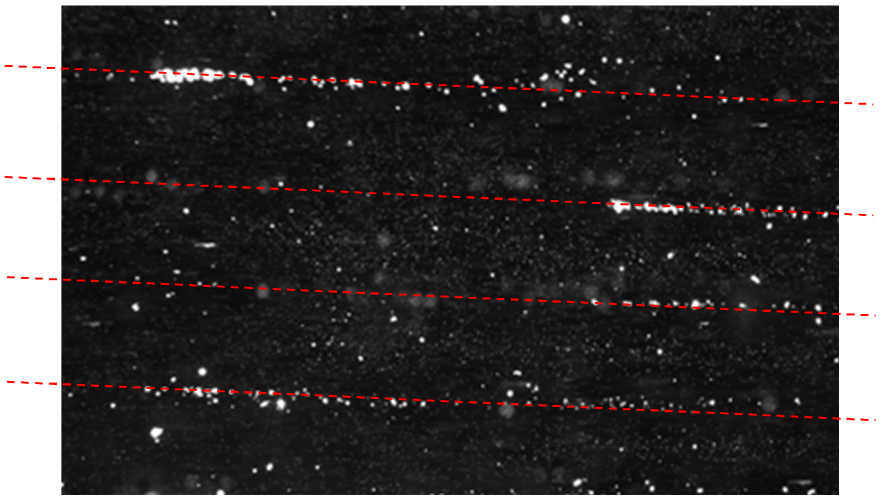

Figure 4-47 An image taken focused at the matching layer of the device. Red dashes highlight the lateral banding at a spacing of approximately 250 µm, consistent with a half wavelength when powered at 2.9 MHz. The particles are all in focus because they have all been forced into the matching layer of the device and are therefore all at the same depth.

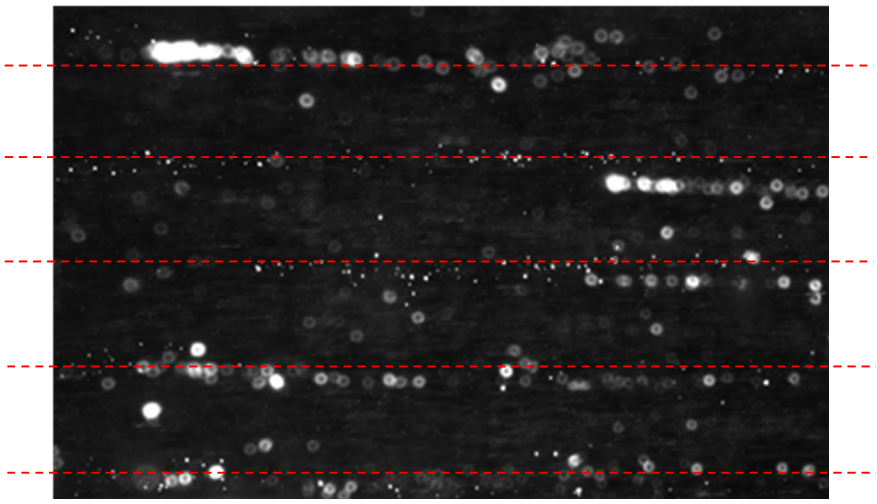

Figure 4-48 An image taken focused at the reflector layer of the device. Red dashes highlight the lateral banding at a spacing of approximately 250 µm, consistent with a half wavelength when powered at 2.9 MHz. The particles are all in focus because they have all been forced into the reflector layer of the device and are therefore all at the same depth.

Using a glass capillary showed that it is possible to generate acoustic forces in a ceramic device using lithium niobate as a bulk transducer. It also showed that the parameters used in the Matlab model were correct and that the model would be able to successfully predict modes in the PMMA devices.

4.2.2.2 Polymer slides

Three polymer devices were made using the 2:1 ethanol:acetone mix described earlier, (Harris et al., 2010). Each layer was 175 µm thick and fluid connections were glued in place. Three different transducers were prepared, each with a different electrode, Figure 4-49.

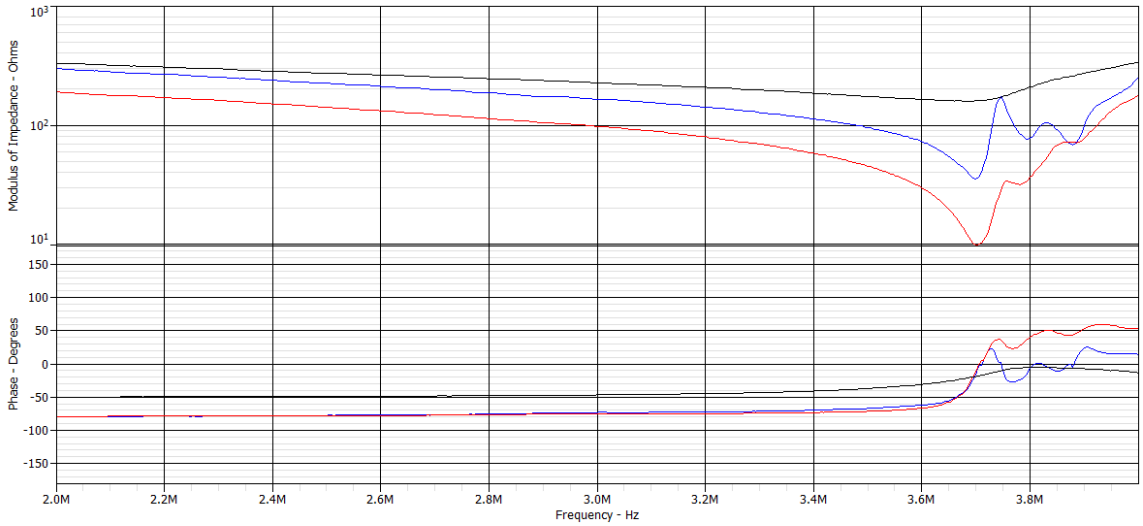

Figure 4-49 The measured impedance plots for a 0.5 mm lithium niobate Y + 36 transducer coupled with a 0.175, 0.175 and 0.175 mm thick PMMA slide device. The black line indicates a PEDOT:PSS polymer electrode, the blue line indicates the ITO electrodes and the red line indicates the silver paint electrodes.

The three electrodes were; silver paint, ITO and spin coated PEDOT:PSS conducting polymer. The figure shows the conducting polymer electrodes have insufficient conductivity to induce resonance in the device. The ITO film and the silver paint are both capable of generating the resonance at 3.7 MHz, which matches well with the predicted resonance of 3.741 MHz. As expected the resonance seen by the silver paint electrode is more pronounced than that of the ITO electrode. The modelling predicted a minor resonance at approximately 2.6 MHz which was not seen by the impedance measurements.

To confirm the presence of a half wave type focusing mode, yellow-green FluoroSpheres were used to confirm the presence of acoustic radiation forces. A solution containing 10 µm diameter beads was fed into a 4 mm wide fluid chamber and 10 V_{pp} was applied to a 20 x 20 mm wide transducer. Once a bead was captured in the acoustic forces within the device, the voltage was lowered until the forces acting on the bead were insufficient to levitate the bead, 2 V_{pp} and 3.3 V_{pp} for the silver paint and ITO films transducers respectively. The acoustic pressure within the chips, measured through voltage-drop analysis on a 5 µm radius polystyrene bead was equal to

2.6×10^4 Pa. This corresponds to an energy density of 1.93 J m^{-3} and 0.71 J m^{-3} at 10 V_{pp} for the silver paint and ITO coatings, respectively.

4.2.3 Conclusions

Lithium niobate has been shown to work as a bulk acoustic transducer using traditional ceramic devices and the novel PMMA devices. One of the main advantages of using lithium niobate is the fact it is transparent, so using it in conjunction with transparent electrodes could open up new applications for ultrasonic standing wave technology. Transparent ITO electrodes were used and it was possible to image particles using transmission microscopy rather than episcopic microscopy. Polymer conducting electrodes were trialed because of their ease of use, but did not produce a film conductive enough to generate a resonance in the device. The acoustic characteristics of the ITO films were comparable with silver paint coating, and whilst successful, had a higher power requirement for the same level of acoustic focusing. If power consumption was an issue, it would be possible to increase the thickness of the ITO film to decrease the resistance. This would have a negative effect on the optical transmittance of the device.

Chapter 5 Biofouling

Sensors left in a marine environment suffer from the effects of biofouling, in particular the build up of biofilms. Biofilms are comprised of microorganisms and extracellular polymeric substance (EPS) and are formed when bacteria adhere to a wetted surface. The bacteria then excrete slime like EPS which aids the adherence of other microorganisms such as fungi, yeast, algae and other bacteria species (Lewandowski, 2007). The presence of biofilms will have detrimental effects on the performance of marine sensors. In optical based sensors the presence of biofilms in the optical path will affect readings, lowering sensitivity and efficiency. For chemical based sensors, the uptake of nutrients and release of metabolites from the organisms in the biofilm may affect the readings (Delauney et al., 2010). These factors are especially problematic for *in-situ* sensors as regular cleaning by hand is not possible. Mechanical and chemical cleaning options exist but are either expensive or will reduce the working life of the system. The formation of biofilms in microfluidic channels will also have detrimental effects on flow rates and could eventually lead to clogging. For these reasons it is important to protect *in-situ* oceanographic sensors from the formation of biofilms.

5.1 Biofouling Mechanisms and Protection Strategies

When a device is placed in a marine environment, biofilms start to form. It has been shown that these films can have disruptive effects on sensors within a week (Lehaitre et al., 2008). Whilst in suspension, microorganisms that cause biofilms tend to be dormant. When they come into contact with a surface they attach themselves in a matter of minutes. The film grows and then starts to disperse, either by detaching itself or seeding the local environment with individual cells (Lewandowski, 2007). Bioaccumulation generally occurs in the following stages (Delauney et al., 2010);

- Adsorption of organic and inorganic macromolecules onto a surface
- Transport of microbial cells to the surface
- Reproduction of bacteria on the surface
- Development of more complex communities such as multi-cellular species, debris, sediments, and microalgae

- Attachment of larger marine invertebrates such as barnacles, mussels and macro-algae.

Some work has shown that it is possible for stages to happen in parallel and later stages can occur without earlier stages (Roberts et al., 1991). Biofilms are formed from the build-up of micro-organisms and EPS, which are excreted by the micro-organisms (Staudt et al., 2004). The film is detrimental to marine sensors in more than one way. Clogging of micro channels can occur due to the excessive build-up of microorganisms. Of greater effect, the localised environment will be affected by the organisms, either by uptake of chemicals and nutrients or the release of compounds such as EPS or waste products. This could completely change the composition of the sample being measured. For optical sensors, the formation of a biofilm will have severe impacts, either by blocking the light path, or by background radiation from autofluorescent organisms.

Bacteria found in biofilms are more resilient to antimicrobial agents than the free cells. In fact biofilms can require more than 100 times the concentration of antibacterial agents than individual cells. An individual cell has little time to respond to antibacterial agents before being overwhelmed. When in a colony, the top layer of cells slows down the advancing antimicrobial agents in the surrounding fluid, whilst signalling to the rest of the colony the incoming danger. This allows the rest of the colony to respond effectively against the agents. Also, cells further from the fluid will have less access to nutrients, resulting in a slower metabolism. This will result in a reduced uptake of the antibacterial agent. In larger colonies, the thick biofilm will stop sufficient antimicrobial agent reaching the base of the growth (David, 2011, MontanaStateUniversity, 2011).

5.1.1 Biofouling Protection

When considering biofouling protection, there are two areas of interest. Protecting the sensing area of the device and protecting the sensor housing. There are several reasons why protecting the sensor housing is as important as protecting the sensing area. Firstly it helps with the repeated use of the devices, accumulation of bio films and marine invertebrates could cause damage to sensors and sensor housings. Secondly, when it comes to the end of the deployment and the sensor is removed from the water, it needs to be cleaned before it can be calibrated. Cleaning is easier if biofouling is minimal, it can be done with high pressure water or chemicals. Another reason to minimise biofouling of the sensor housing is the effect the organisms will have on the sensor, either chemical or optical (Delauney et al., 2010). However, it will not be

possible to incorporate acoustic radiation forces into a system to keep the sensor housing free from biofouling.

5.1.1.1 Sensor

Designing systems that adequately protect the sensing area of a device is complex. Depending on the deployment the sensor may not have human interaction for a year. Biofouling can lead to a continuous shift in readings, so minimising biofilm growth is important. Development of biofilm protection systems must concentrate on three main areas.

- It should not affect the measurement or the environment
- It should not consume too much energy
- It should be reliable in all conditions; depth, temperature, salinity, etc.

Several protection systems are currently in use, and several have been proposed. Wipers or scrapers have been successfully used to clean sensor surfaces. Depending on the geometry of the device it may not be possible to incorporate such a system. Such a system will also require careful design in terms of mechanical parts and water tight seals. Several systems using biocide leaching have been reported, however one of the most effective and once widely used used, tributyl-tin, has been banned because of its damaging impact on the environment (Champ, 2003). Copper is known for its biocide properties, leading to companies manufacturing sensor devices in copper as much as possible. Copper shutters have been designed, placing the copper as close to the sensor as possible, keeping the sensor in the dark and allowing the biocide concentration to rise. Copper is also coming under scrutiny as an anti fouling paint and may face bans in several countries, (E.P.A., 2014).

Electrolysis chlorination is used to clean particular areas of a system, in particular the sensing area. This process has also been used to clean an entire system, but at the cost of heavy power requirements. Other methods including the controlled release of bleach have been used, but these systems require reservoirs of bleach, which could shorten the length of deployment. UV light has also been used to inhibit biofilm growth, as has laser irradiation but so far the power requirements for such devices are too high (Delauney et al., 2010).

The use of ultrasonic streaming to clean surfaces has been investigated computationally and verified experimentally, (Sankaranarayanan et al., 2008). It has also been shown to work in macroscale marine sensors, (Piedrahita and Wong, 1999). Whilst effective, these methods rely on acoustic streaming which places high power requirements on the sensor, (Whelan and Regan, 2006, Delauney et al., 2010). Some

experiments report power consumption in the region of 35 – 45 W for effective biofilm removal, (Mott et al., 1998). Ultrasonic excitation has been shown to have other effects on biofilms other than just removal. Whilst acoustic streaming can generate forces large enough to remove biofilms, it also acts to circulate the medium through the biofilm, which can act to increase the uptake of biocide in the biofilm if it is present in the medium, (Bott and Tianqing, 2004). Experiments have shown that antibiotic (gentamicin) alone can kill 82 % of bacteria (*E.coli*) present in a film, but the addition of an ultrasonic field can increase the effectiveness of the antibiotic to 99 %. The use of ultrasonic excitation alone did little to kill bacteria, (Peterson and Pitt, 2000). Literature suggests that the reason for this increased efficiency is that the cells deeper into the biofilm have limited access to oxygen, so metabolise slowly or are in a dormant state. The addition of ultrasound increases the supply of oxygen to the colony, increasing metabolism and therefore uptake of antibiotic, (Borriello et al., 2004, Walters et al., 2003). Other experiments have shown that if the acoustic streaming is insufficient to remove bacteria and biocide is not present, the increased circulation of nutrients and metabolites can actually increase the rate of cell growth, (Pitt and Ross, 2003). At present there are no reported cases of ultrasonic standing waves to reduce biofilm formation in microfluidic devices.

Any device being designed needs to manipulate cells effectively in a variety of environments. The temperatures will vary from 35 to -2 °C (NOAA, 2009). This will change the speed of sound in water, which will have huge effects on the resonant frequency. Other factors that affect the working frequency are salinity, depth and latitude (Coates, 1989). Salinity can vary from 16 ppt to nearly 400 ppt in the Dead Sea (OfficeOfNavalResearch, 2009). Average salinity for seas and oceans is 32-37 ppt, but if the device was to be used in a fresh water area, it would be as low as 0.5 ppt. Latitude and depth have less of an effect on the acoustic properties. The materials chosen will also have to withstand this range of temperatures, which is enough to affect the strength of many materials. Corrosion may also be an issue due to the salinity.

5.1.2 Biofouling and Ultrasonics

To counteract the problems associated with biofouling it is proposed to use ultrasonic standing waves to limit the growth of biofilms within microfluidic devices. Ultrasonic standing wave technology should be well suited to the reduction of biofilm formation as bacteria tend to have positive acoustic contrast factors, meaning cells will move to the pressure nodes, (Kumar et al., 2005). There are many species of bacteria, which leads to variations in the size of cells between 0.3 µm and 750 µm, (Chien et al., 2012). However, in general, most bacteria tend to be between 0.5-1.0 µm in diameter and 2-5 µm in length, (Srivastava, 2003). Particles of this size are well suited to the magnitude of forces generated by ultrasonic standing waves; large enough to experience ultrasonic forces whilst still noticeably smaller than a half wavelength in a microfluidic device. Whilst the ultrasonic forces generated will not affect cell viability, (Hultstrom et al., 2007), they should at least move cells away from channel walls, reducing the chance of them adhering and replicating.

As a starting point *Vibrio natriegens,* a gram negative facultative anaerobic marine strain, was chosen as the test bacteria due to the fact they are a good marine bacteria for biofilm studies as they form substantial biofilms, (Sivakumar et al., 2010). They also have a rapid growth rate (sub 10 minute replication time in optimal conditions at 37° Centigrade) and are considered non-pathogenic, (Eagon, 1962). *Vibrio natriegens* have a measured volume of 0.93 ± 0.06 μm^3 in a dormant state and 3.5 ± 0.5 μm^3 in a growing state, (Fagerbakke et al., 1996). The lower bound of the dormant state is comparable to a 0.59 µm radius sphere. Cells are typically rod shaped with dimensions 0.606 µm wide x 0.5 µm thick x 3.334 µm long, measured using atomic force microscopy, (Cheng et al., 2010). It is expected that it will be possible to manipulate cells of this size using ultrasonic standing waves.

A solution called minimal marine media with nutrients (3MN) was selected as the fluid as it is commonly used for cultivating marine bacteria in biofouling experiments, (Denkin and Nelson, 1999). The aim of this work is to significantly reduce the formation of biofilm growth in microfluidic channels.

The following parameters can be used to calculate the acoustic contrast factor of bacteria cells. Cell compressibility has been assumed to be similar to red blood cells. There is very little data available regarding cell compressibility. Red blood cells are considered compressible (Charcosset, 2012) so using this value is conservative and is expected to underestimate the acoustic contrast factor and therefore the forces generated.

Cell density: 1.031-1.212 g cm^{-3}, (Sharma et al., 1998).

Cell compressibility: 3.38 x 10^{-10} $m^2 N^{-1}$, (Malika et al., 1999).

3MN water density: 1.0235 g cm^{-3}, see Appendix B.

Speed of sound in 3MN: 1508 m s^{-1}, (Coates, 1989).

The compressibility of the fluid can be calculated using the following formula.

$$\beta_F = \frac{1}{\rho_F c_F^2}$$

Equation 5-1

The calculated compressibility of the 3MN solution is: 4.3 x 10^{-10} $m^2 N^{-1}$, this is close to the value of 4.5 x 10^{-10} $m^2 N^{-1}$ for pure water, (Fitts, 2013). From here it is possible to calculate the acoustic contrast factor of bacteria cells using Equation 2-81. The calculated acoustic contrast factor of a bacteria cell is between 0.074 and 0.126, confirming a net resultant force towards the pressure node. This is comparable to the acoustic contrast factor of polystyrene beads in pure water of 0.15, which are used frequently in ultrasonic standing wave experiments due to their cell like properties and ease of use. Whilst the acoustic contrast factor is lower than polystyrene beads, this is a conservative estimate due to the lack of data available on cell compressibility.

5.2 Initial Experiments – Glass Capillaries

As an initial experiment borosilicate glass capillaries were chosen as their acoustic performance and characteristics are well documented, (Hammarstrom et al.). Capillaries 6 mm wide, 50 mm long with a 0.3 mm high fluid channel were used, as they had been proven to have a strong half wave resonance, see Figure 5-1, (Glynne-Jones et al., 2012, Carugo et al., 2011). Literature reports an acoustic pressure amplitude (*P*) within the capillary, measured through voltage-drop analysis on a 20 µm polystyrene bead (Martin et al., 2005) was equal to 3.5 x 10^4 Pa, at a minimum operating voltage of 1 V_{pp}. This corresponds to an energy density of 13.74 J m^{-3} at a voltage of 10 V_{pp}.

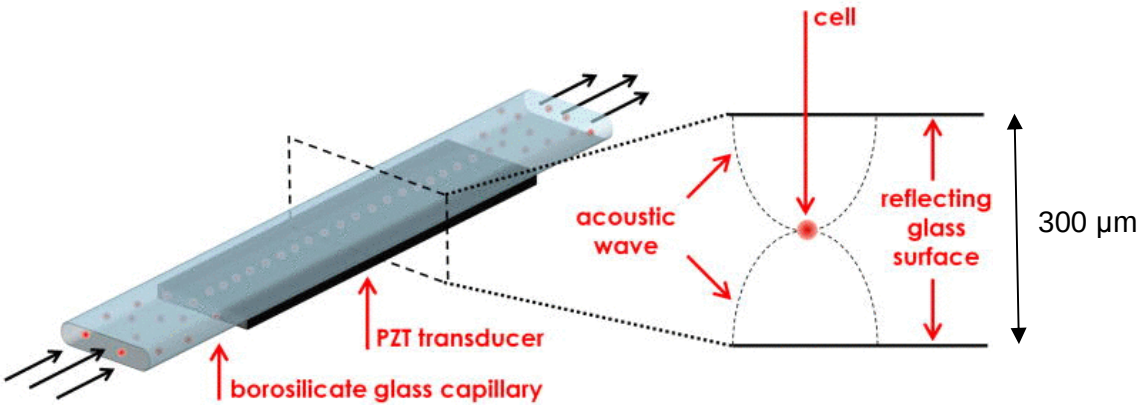

Figure 5-1 Schematic of a glass capillary ultrasonic standing wave device. Reprinted with permission from (Carugo et al., 2011). Copyright 2011, AIP Publishing LLC.

5.2.1 Experiment 1

The capillaries were sterilized in an autoclave before fluid connections were made using heat shrink. The capillaries were marked so that images could be taken at the same place during the experiment, see Figure 5-2. The capillaries were connected in parallel to a 5 L container of 3MN seeded with *Vibrio natriegens* that had been allowed to cultivate for 48 hours before being used. A sterilised magnetic stirrer was added to the solution to counteract the expected sedimentation at the bottom of the container. Flow was applied using a peristaltic pump, allowing continuous flow throughout the course of the experiment, see Figure 5-3. All ancillary peristaltic polypropylene tubing and steel connectors were also autoclaved. The flow through each of the capillaries was 6 ml hr^{-1}, which corresponds to a Reynolds number of 0.529. This confirms the flow is well within the laminar phase.

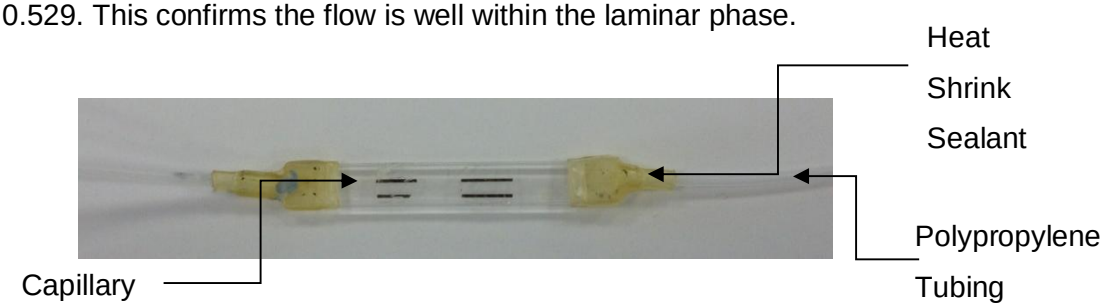

Figure 5-2 Image of a sealed and marked capillary. The capillary is 50 mm long and 6 mm wide. Lines were drawn on the capillary to ensure the same area of the capillary was imaged.

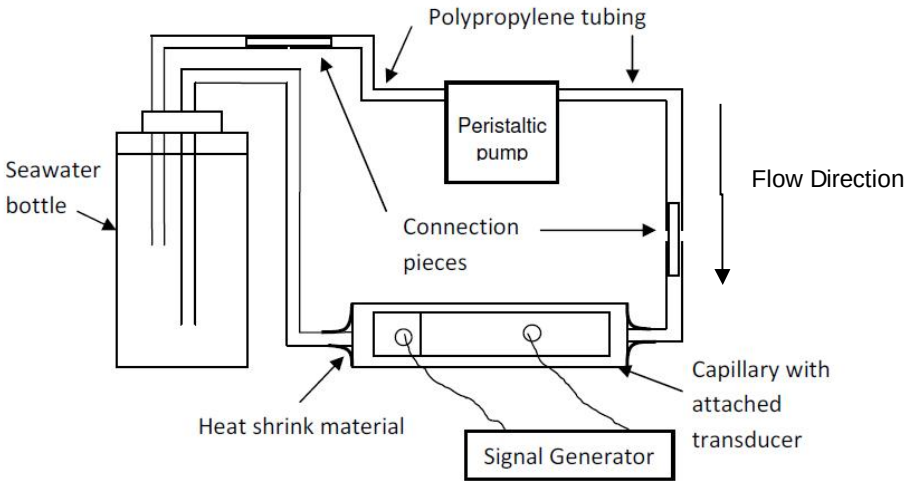

Figure 5-3 Experimental setup of the initial experiment, in reality several capillaries were connected in parallel to the bottle. Residence time in the capillary was 54 s.

Machined PZT transducers (30 x 8 x 1 mm) were glued to two of the capillaries using epoxy resin and the devices were excited at half wave resonance. The resonant frequency was classed as the point of minimum electrical impedance, as measured using a cyphergraph C60, see Figure 5-4. One of the capillaries was powered continuously at 5 V_{pp} whilst the second capillary was excited for 30 minutes a day at 10 V_{pp}. The excitation frequency was altered throughout the course of the experiment to ensure optimal resonance. The frequency was adjusted to the impedance minimum daily. A third control capillary was connected to the seawater but was not excited ultrasonically.

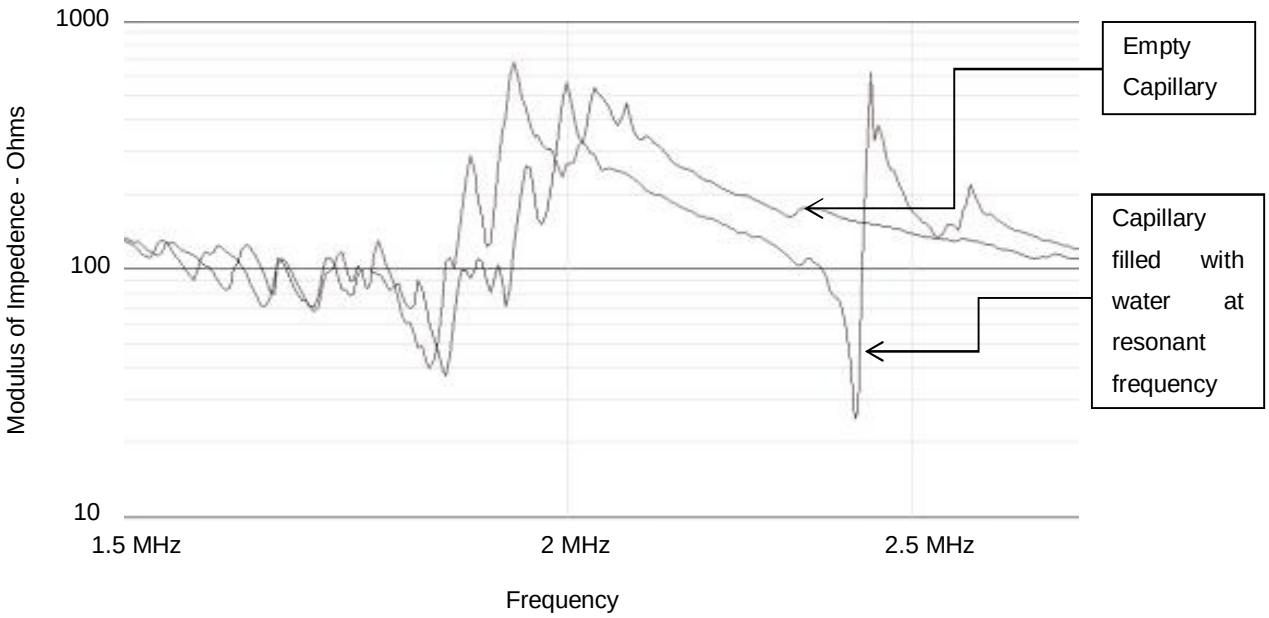

Figure 5-4 Impedance plot of a capillary with and without water in the channel. A distinct resonance can be seen at approximately 2.4 MHz.

The experiment ran for 5 days and images were taken daily using an Olympus IX71 microscope. Reflected light microscopy was used to view the area over the transducer. The quality of the images was poor but the following observations were made.

1) The excitation frequencies were consistent over the course of the week, not migrating more than 0.85% from the average, see Table 5-1. This was checked by monitoring the impedance minimum using an oscilloscope.

Table 5-1 Resonant frequency over the course of the experiment.

Day	Capillary 1 (5 V_{pp} Continuous) MHz	Capillary 2 (10 V_{pp}, 30 Mins Daily) MHz
1	2.3945	2.46
2	2.391	2.465
3	2.3885	2.445
4	2.3865	2.445
5	2.384	2.485

2) Reflected light microscopy is not suitable for this work. It was not possible to take images of a high enough quality for a rigorous analysis. This was because the surface of the transducer and the glue layer distort the image too much. Observations indicated that there was less biofilm formation in the ultrasonically powered capillaries but no clear conclusions can be drawn.

5.2.1.1 Discussion

This initial trial identified key areas for improvements in the experimental setup and analysis. It also highlighted some positives in that the ultrasonic characteristics were consistent not only between different devices but also over a substantial time period of 5 days. Whilst the variation in resonant frequency is small, an improvement to experimental setup would be to apply a frequency sweep to the transducers, which will ensure the optimal resonance of the capillary is always covered. A second advantage of this is that any manufacturing variations along the length and width of the capillary, PZT or glue layer will have less of an effect on the final acoustic field generated. Figure 5-5 shows the variation in capillary dimensions across its width. This will have a detrimental effect on the acoustic forces generated across the device. Measurements are shown in Table 5-2.

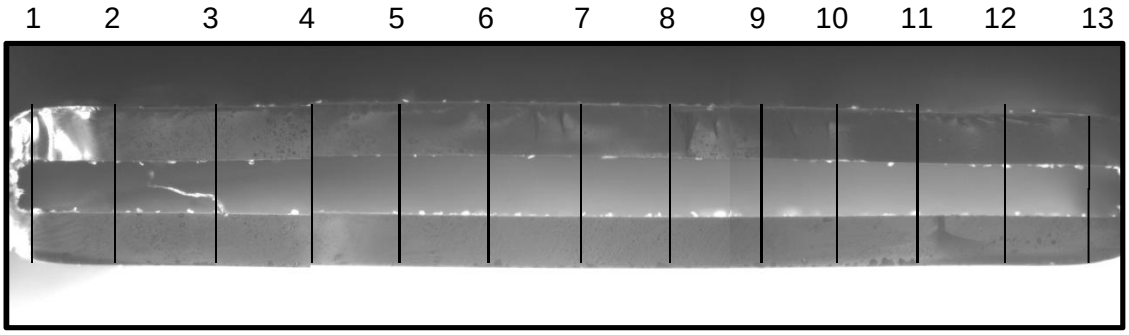

Figure 5-5 a series of images along the face of a capillary showing how the dimensions differ from the expected 300 µm high rectangle. Black lines represent where measurements were taken across the face of the capillary, they are numbered and the results are shown below in Table 5-2.

Table 5-2 Measurements of the above capillary, Figure 5-5. Variation in glass thickness was low (±3 %) but variation in the fluid chamber was significant (±8 %). This will have a detrimental effect on the strength of the acoustic field across the device.

Position	1	2	3	4	5	6	7	8	9	10	11	12	13
Top µm	292	295	295	295	298	301	295	292	288	288	285	288	285
Cavity µm	288	298	314	311	334	337	337	331	324	311	298	288	282
Bottom µm	292	295	292	295	285	285	285	285	285	282	279	275	266

A weakness of the current experimental setup is the poor quality of the images taken over the transducer; this limits the availability of quantitative and qualitative data attainable from each experiment. As a solution to this, a clamp was designed to hold the transducer against the capillary whilst using a coupling fluid such as glycerol. This allows the transducers to be removed for imaging; the experiment was repeated using the removable transducers.

5.2.2 Experiment 2

To increase the quantity of data generated from each experiment, a 2nd continuously powered capillary was added to the experiment, also at 5 V_{pp}. The daily powered capillary was again powered at 10 V_{pp}. The transducers were only clamped to the capillaries rather than glued and the experiment ran for 7 days, Figure 5-6. The resonant frequency of the capillaries was consistently within the range of 2.2 and 2.45 MHz. A frequency sweep was applied with a range of 50 kHz centered on the impedance minimum of each transducer. This will produce a more consistent and stable acoustic field, as discussed in Section 2.3.1 Bulk Acoustic Devices. Daily impedance measurements were taken and it was observed that the resonant frequency varied over a range of 40 kHz which corresponds to impedance variations of 50 Ohms. This was attributed to the glycerol coupling layer drying out over the course of the experiment and was counteracted by the fresh addition of glycerol midway through the experiment. When the experiment was finished the capillaries were rinsed with Milli-Q water, 18.2 MΩ cm @ 25°C.

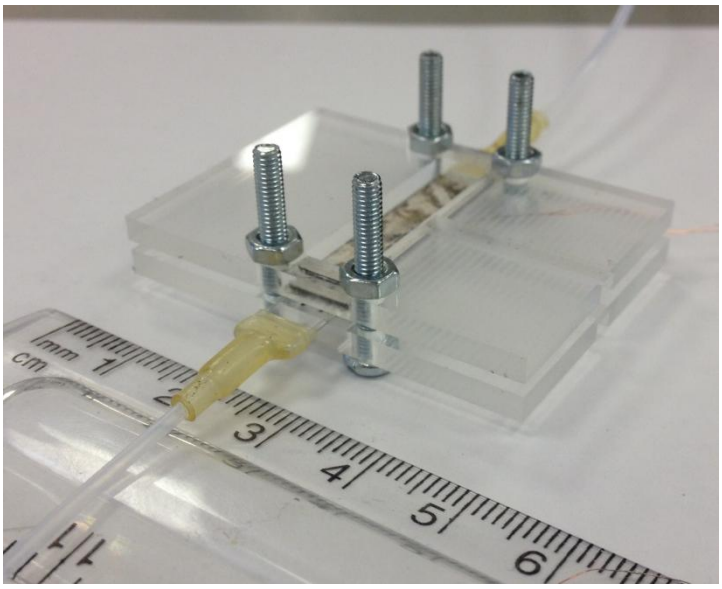

Figure 5-6 Photograph of the capillary in the clamp allowing removal of the transducer for imaging.

The quantity of biofilm growth was significantly higher in this experiment than the first experiment as it was visible to the naked eye. This could potentially be due to the two extra days the experiment was running for. Biofilm growth was so significant that it could be seen in the control capillary that there were areas in which the formation could be identified without the aid of a microscope, Figure 5-7. In different parts of the same capillary, biofouling was only identifiable under a microscope, Figure 5-8.

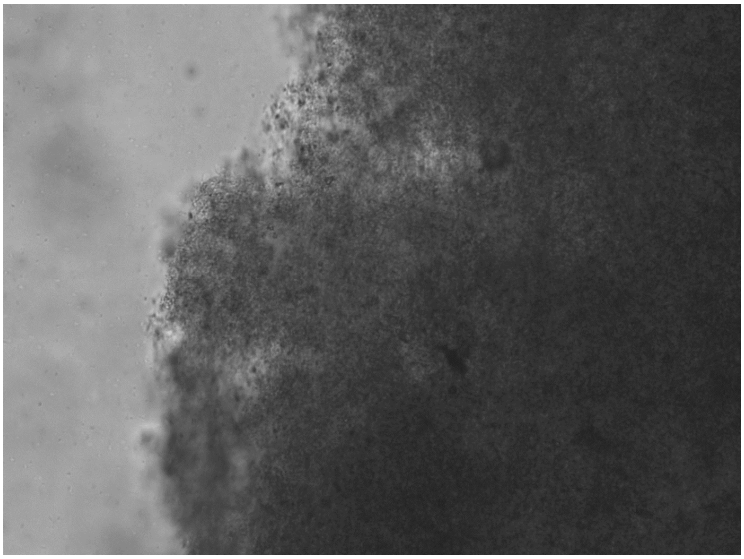

Figure 5-7 Image take at 10x magnification of biofilm growth in the control capillary, the film was very well developed and it was possible to identify it without the aid of a microscope.

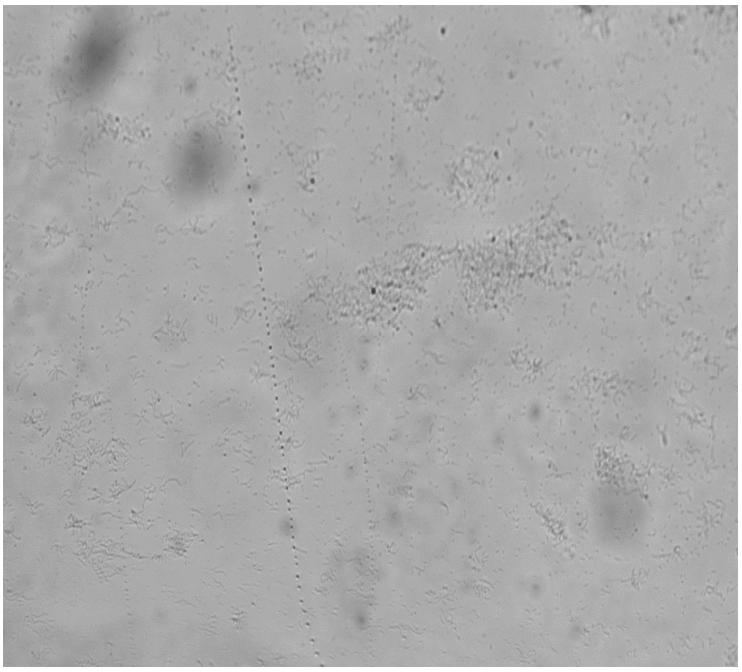

Figure 5-8 Image taken at 10x magnification of colonies of bacteria inside the control capillary. An unexplained strand can be seen across the fluid channel, the formation is perpendicular to the flow and no explanation has been found as to what it was. Later experiments did not see this patterning.

Whilst the quantity of biofilm observed in the ultrasonically powered capillaries was noticeably lower, there was still significant biofilm formation within the ultrasonically powered capillaries, Figure 5-9. These observations are based on general observations and lack analytical rigour.

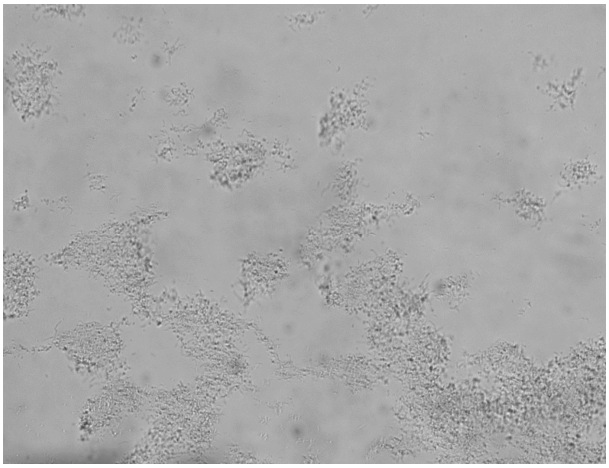

Figure 5-9 Image taken at 10x magnification of colonies of bacteria inside the capillary powered continuously at 5 Vpp.

5.2.2.1 Discussion

Being able to take images of bacteria growth over areas of the capillary directly in line with the transducer was a significant improvement. Whilst bacteria were seen in these areas, growth was significantly lower than in the control capillary. This can be seen from the images above which are good representations of the results of the experiment. Observations suggest that the continuously powered capillaries are more effective at reducing biofilm formation than powering the capillary for 30 minutes per day. To investigate this further a higher power will be used on the daily powered capillary. Applying the frequency sweep to the transducers worked well, as the observed impedance minimum was always within the range of the frequency sweep. The resonant frequency was also very similar between the 3 ultrasonically powered devices which implies good repeatability of the experiment. One of the current limitations of the experimental set up is the ability to generate clear quantitative evidence.

5.2.3 Experiment 3

To check the repeatability of the experiment, it was repeated with some minor changes. The ultrasonic excitation strategies were adapted; one of the continuously powered capillaries had its excitation voltage doubled. This allowed the two experiments to be compared with each other but should also provide a clearer result. By having two continuously powered capillaries at different voltages, it will be possible to verify the effects of ultrasonic excitation and compare it with theory. The theory suggests that the higher powered capillary will have a greater affect on the formation of biofilms. The capillary that was powered daily also had its excitation voltage doubled, as little reduction in biofilm formation was observed in experiment 2. The excitation strategies are defined in Table 5-3 below. The experiment was run for 10 days in total.

Table 5-3 Excitation strategies for Experiment 3

Capillary	A	B	C	D
Excitation Voltage (V_{pp})	10	20 (30 minutes daily)	5	0
Frequency (MHz)	2.250-2.350	2.230-2.330	2.235-2.335	-

As an addition to this experiment, thermocouples were also used to monitor the temperature of the control capillary and the continuously powered capillary, to identify if heating would be having a significant effect of the growth of biofilms. The results from

the thermocouples are shown below, Table 5-4. Measurements were taken as close to the transducer as possible.

Table 5-4 Readings from the thermocouples over the course of the experiment.

	Capillary A (°C)	Control B (°C)
Day 1	14.0	12.1
Day 2	13.5	12.0
Day 3	14.1	12.7
Day 4	15.9	14.5
Day 5	15.0	14.1
Day 6	16.6	16.0
Day 7	16.7	15.2
Day 8	17.2	16.4
Day 9	15.2	14.7
Day 10	15.0	14.5
Average Difference	+1.1°C	-

The findings showed the capillary powered at 10 V_{pp} was on average 1.1 ˚C warmer than the control capillary, which was less than the natural temperature fluctuations in the laboratory. The temperature never exceeded 17.2 ˚C, so it did not reach the temperatures deemed to be detrimental to bacteria growth (Eagon, 1962). If anything the temperature increase would be beneficial to the growth of Vibrio Natriegens, (Mullenger, 1973).

5.2.3.1 Discussion

Significant biofilm growth was observed in the control capillary compared to the continuously powered capillaries and the capillary powered for 30 minutes daily. The initial experiments showed that ultrasonic excitation was capable of reducing biofilm growth within microfluidic devices. These conclusions are based on qualitative observations of images taken along the length of the capillaries. Continuously powering the capillaries was deemed the most effective at reducing biofilm growth. This implies

that once the bacteria have adhered to the walls of a device acoustic radiation forces alone are insufficient to remove them. This matches well with experiments that utilise acoustic streaming to remove biofilms, see Section 2.3.1.2 Flow Free Standing Wave Devices.

5.2.4 Conclusions

The qualitative results from the initial experiments show that ultrasonic standing wave techniques are able to limit the growth of biofilms within microfluidic devices. The work also showed that the long term use of ultrasonic excitation over 10 days is possible with a robust excitation strategy such as frequency sweeping about the nominal resonant frequency. The experiment showed that continuous excitation was better at reducing biofilm formation than higher powered excitation for small timescales. This implies that the acoustic radiation forces generated are sufficient to manipulate bacteria within a fluid, but unable to remove bacteria that have adhered to a surface. Whilst it has been proven that acoustic streaming is capable of removing biofilms from a surface, this tends to have high power requirements, (Sankaranarayanan et al., 2008, Delauney et al., 2010). On the understanding that once bacteria have adhered to a surface acoustic radiation forces will not be sufficient to remove them, further experiments will not image the devices during the experiment so that there is no break in the ultrasonic excitation. For a method of biofilm reduction to be suitable for oceanographic sensing, it will need to be proven in polymer devices as this is the preferred material for *in-situ* microfluidic oceanographic sensors. The biggest limitation in the experimental method so far is the ability to generate qualitative data.

5.3 Initial experiments – Polymer Chips

The new generation of sensors being developed for remote *in-situ* oceanography are primarily made from polymers for their ease of production. One of the main drawbacks of using ultrasonic standing wave technology in polymer chips is the relatively low Q factor compared to glass and silicon devices, requiring higher power consumption for the same level of acoustic focusing.

5.3.1 Methods

A one-dimensional Matlab model was used to design an effective ultrasonic microfluidic capillary in PMMA. Details of this modelling can be found in Chapter 4.

A polymer chip was designed and manufactured from two sheets of 1 mm thick PMMA. A fluid channel 300 µm deep and 350 µm wide was milled into one sheet. The other sheet had a 350 µm window milled into it as a reflector layer. The chips were 6 mm wide and 38 mm long. Holes were drilled through the base piece to allow fluidic access. The pieces were then sealed using the acetone/ethanol process developed by Harris et al (Harris et al., 2010). Steel tubes were glued into the fluid access points using Epotek 320. It was not possible to autoclave the chips due to the glass transition temperature of PMMA being below the autoclave temperature. Instead ethanol was syringed into the fluid channels and left for 15 minutes to sterilise the chips.

Three chips were connected in parallel to a 5 L batch of 3MN seeded with Vibrio natriegens. One chip was used as a control and the other two were clamped to PZT transducers powered at 2 and 4 V_{pp} with a frequency sweep of 50 kHz centered over the initial measured impedance minimum. The resonant frequency for these chips was between 2.1 and 2.15 MHz and this was consistent over the course of the experiment. The impedance of all 3 chips to be used in the experiment was measured and they had very similar impedance plots implying good repeatability, Figure 5-10. The flow rate through each chip was 0.036 mL min^{-1}, corresponding to a Reynolds number of 1.845, well within the bounds of laminar flow.

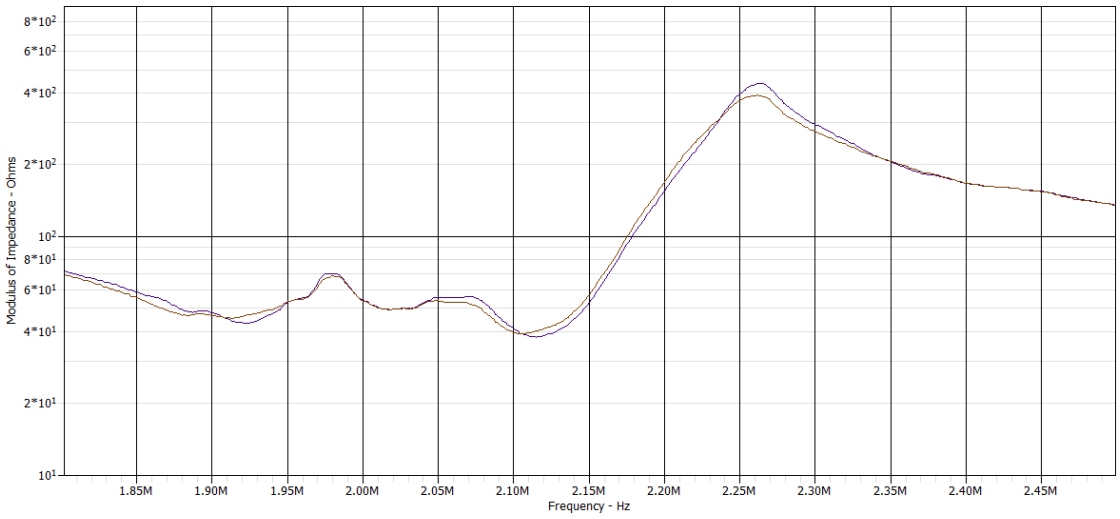

Figure 5-10 Impedance plot of the two continuously powered chips. The impedance characteristics are very close and can therefore be considered comparable devices.

Figure 5-11 shows how the force required for total cell levitation changes with density. The red and blue lines show the calculated forces exerted on bacteria and how they change with the acoustic contrast factor.

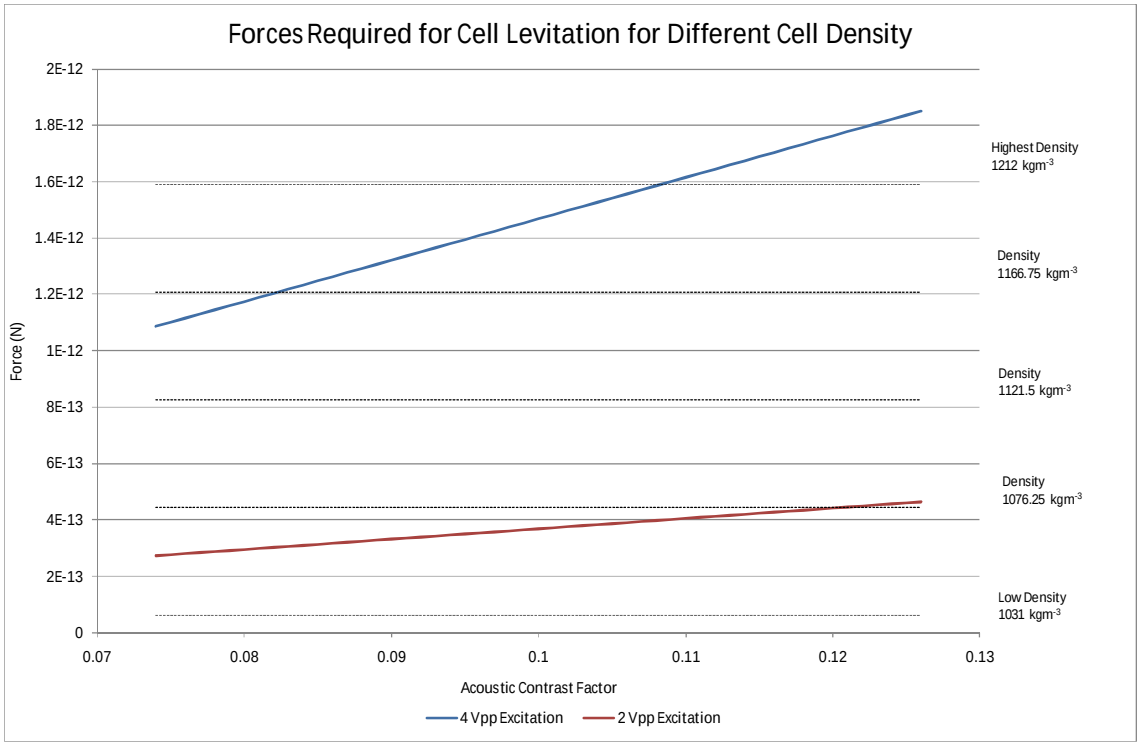

Figure 5-11 Whilst the exact density of bacteria cells are not known, it is possible to show that excitation at 4 V_{pp} (Blue) is likely to be strong enough for complete cell levitation and 2 V_{pp} (Red) will be sufficient to have an impact on biofilm formation but may not be strong enough for total cell levitation. The force required for total cell levitation depends on the density of the bacteria cells. Dotted lines show the required force for total cell levitation at different cell densities.

After 14 days the experiment was stopped, the channels were rinsed with Milli-Q water and images were taken along the length of the channel, an example image is shown below, Figure 5-12. It was not possible to count individual bacteria so estimates were made based on the area of each colony. The position of each colony was noted as left boundary, left, centre, right or right boundary, see Figure 5-13. Measurements were taken along the length of all 3 chips over which the transducer was present, see Table 5-5, Table 5-6.

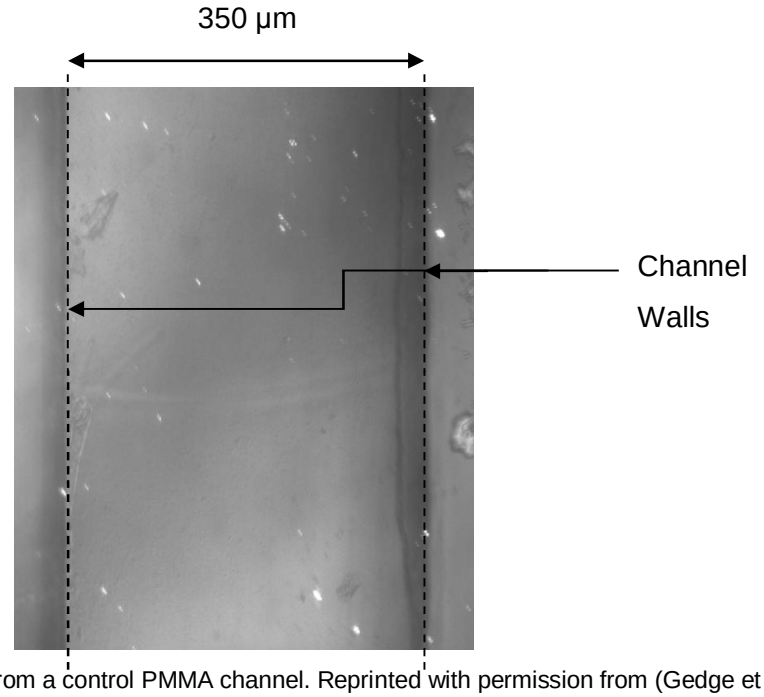

Figure 5-12 Example image from a control PMMA channel. Reprinted with permission from (Gedge et al., 2012). Copyright 2012, AIP Publishing LLC.

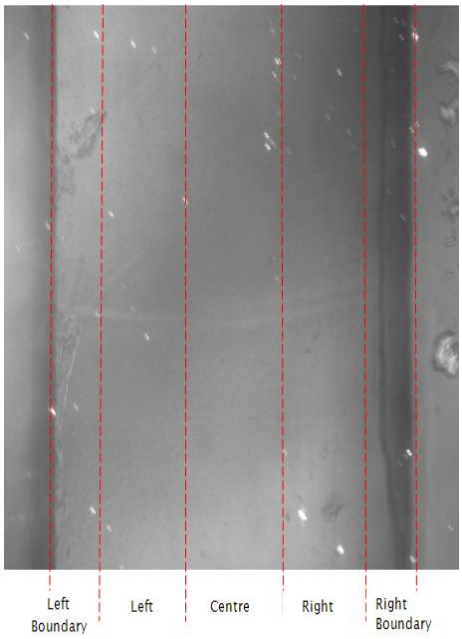

Figure 5-13 Example image showing how position of colonies was recorded along the length of the PMMA channel. Reprinted with permission from (Gedge et al., 2012). Copyright 2012, AIP Publishing LLC.

5.3.2 Results

In general, bacteria tended to be concentrated in the middle of the chip, this fits with the idea that the bacteria have less time in the presence of the acoustic field as they will be travelling faster in the middle of the capillary than at the edges. The majority of bacteria adhered on the lower surface of the chips, implying the cells are denser than the surrounding medium and therefore sink.

Table 5-5 Estimate of the number of bacteria on the floor of the PMMA Chips. Reprinted with permission from (Gedge et al., 2012). Copyright 2012, AIP Publishing LLC.

Position	PMMA chip at 4 V_{pp}	PMMA chip at 2 V_{pp}	Control
Left Boundary	105	80	310
Left	175	185	415
Centre	155	220	450
Right	85	110	310
Right Boundary	60	150	340
Total	**580**	**745**	**1825**

Table 5-6 Estimate of the number of bacteria on the roof of the PMMA Chips. Reprinted with permission from (Gedge et al., 2012). Copyright 2012, AIP Publishing LLC.

Position	PMMA chip at $4V_{pp}$	PMMA chip at 2 V_{pp}	Control
Left Boundary	0	45	0
Left	10	25	10
Centre	20	15	0
Right	10	10	15
Right Boundary	80	0	35
Total	**120**	**95**	**60**

The results show a reduction in the quantity of biofilm growth in the continuously powered PMMA chips. The control chip had approximately 2.7 and 2.2 times the total bacteria growth than the 4 and 2 V_{pp} powered chips respectively. The fact that the higher powered chip was more effective at reducing biofouling than the lower powered chip agrees with the hypothesis that the reduction was due to the ultrasonic excitation, as any heating effects are likely to encourage bacteria growth rather than stop it, (Eagon, 1962). Significantly more bacteria growth was seen on the floor of the chip than the roof of the chip; this can be attributed to gravity as the chips were laid flat whilst the experiment was running.

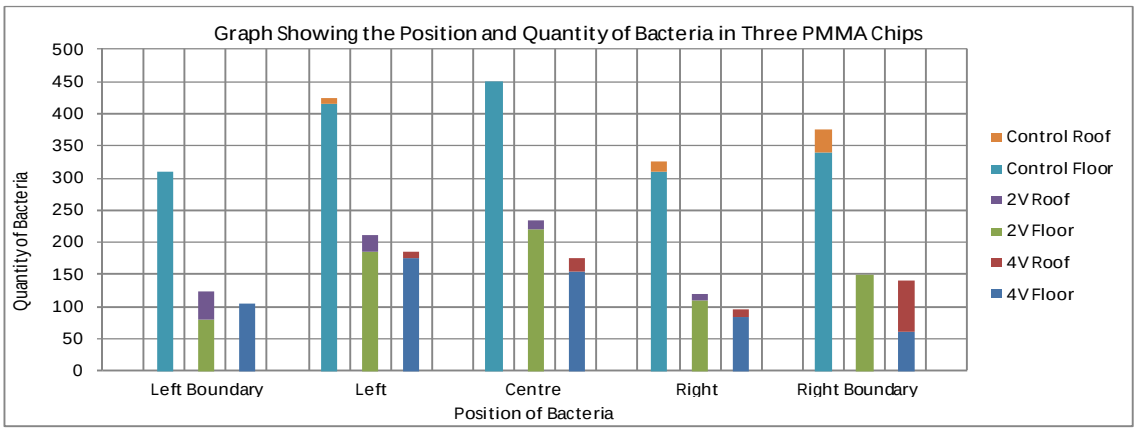

Figure 5-14 Graph showing position and quantity of bacteria found in the PMMA chips. It should be noted that values for quantity of bacteria are based on colony surface area, more precise methods are needed to produce more statistically relevant values. Reprinted with permission from (Gedge et al., 2012). Copyright 2012, AIP Publishing LLC.

The bacteria in the powered capillaries tended to be more focused towards the middle of the channel floor, with 26.7 % and 29.5 % of the bacteria found in the centre section for the 4 V_{pp} and 2 V_{pp} chips respectively, compared to 24.6 % in the control chip, see Figure 5-14. This difference is even more apparent when the middle three sections are compared, with 71.6 % and 69.1 % of the bacteria found in the middle three sections of the channel for the 4 V_{pp} and 2 V_{pp} chips respectively, compared to 64.4 % in the control chip. On the roof of the channel the positioning of the bacteria tends to be more skewed towards one side of the channel or the other, though it is difficult to draw conclusions as the quantity of bacteria involved is significantly lower. The power consumption of the PMMA devices is estimated at 0.1 W and 0.025 W for the 4 V_{pp} and 2 V_{pp} chips respectively.

The powered chips did experience more bacteria growth on the roof of the channels than the control chip. This is due to the positioning of an antinode just below the roof of the channel which led to a small section of the channel having a positive force into the roof. This was later shown using simulation when the actual measured dimensions of the chip were loaded into the Matlab model, see Figure 5-15. This error was due to manufacturing tolerances. This is congruent with the fact that the higher powered chip experienced more bacteria growth on its roof than the lower powered chip. This implies that the chips powered at 4 V_{pp} had sufficient ultrasonic excitation to completely levitate cells and push them into the roof of the channel.

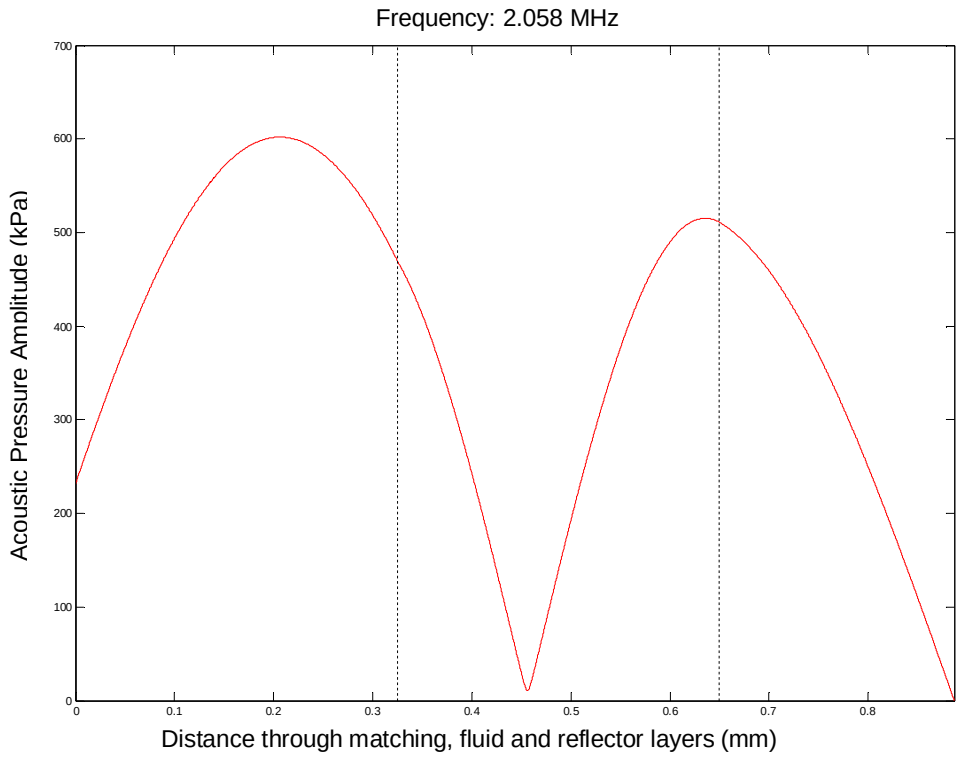

Figure 5-15 Showing the pressure variations through the device when the actual measured dimensions were loaded into Matlab. They show the presence of an antinode close to the roof of the device.

5.3.3 Conclusions

In conclusion ultrasonic standing waves have been shown to reduce biofilm growth in polymer microfluidic devices. Continuous low power excitation has been shown to be most effective and excitation methods have been used that would be suitable for continuous *in-situ* use. Effects due to heating are minimal and the devices have been shown to work over relatively long periods of time. The limitations of these experiments are the quantity of data being generated per experiment and the manufacturing tolerances in producing the chips. Staining methods should be used in future so that more accurate quantitative results can be obtained and so that viability studies can be carried out. To overcome the issue of manufacturing tolerances, a new method of manufacturing devices will be used involving ready-made sheets of PMMA so that variations in the thickness are subdued. As a final change, chips will be held with the fluid channel vertical so that sedimentation effects are removed.

5.4 Polymer Slide Experiments

Due to the unrepeatability of micromilled PMMA channels, a new method of manufacturing PMMA chips was developed. PMMA sheets were obtained from Cadillac plastics in thicknesses of 250 and 375 µm. The sheets were milled into 25 x 75 mm slides, matching in size to standard microscope slides. The 250 µm thick slides had a fluid channel 3.8 mm wide and 50 mm long cut into the centre of each slide. The width of the channel was increased for two main reasons.

1) Increase the area that biofilms could potentially form to get more statistically relevant results.
2) Decouple the width of the channel from the height of the channel to get a more robust 1 dimensional resonance.

Half the 375 µm slides had holes 1 mm diameter holes drilled through them for fluidic access so as to line up with the ends of the fluid channel in the 250 µm slide. The 2:1 ethanol:acetone method was used to bond the slides together in a 375, 250, 375 µm sandwich. Fluid connectors were glued in place using Epotek 320. The slides were annealed at 85°C for four hours to relieve internal stress. A clamp was designed such that a PZT transducer could be held against the polymer slide. PZT was milled to 4 x 30 x 1 mm. More information on the computational modelling of this device can be found in Chapter 4.

The expected forces can be plotted along with the gravitational forces for a range of densities and excitation voltages, Figure 5-16. At the highest excitation voltage, the forces generated are expected to be strong enough for total cell levitation. At the lower voltages the forces generated would not be sufficient for total cell levitation, but would limit bacteria adhesion over the transducer. As the polymer slides being used in this experiment will be orientated vertically, the low forces should still be sufficient to move bacteria away from the surfaces of the slides.

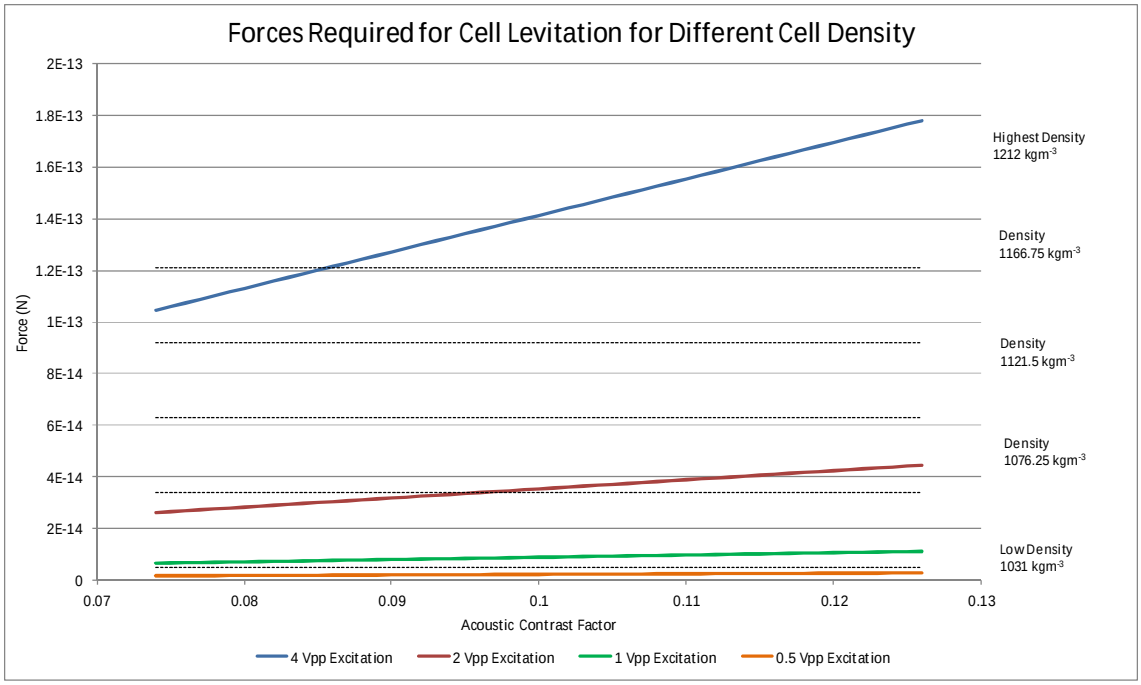

Figure 5-16 The expected forces generated on bacteria cells within the fluid chamber for a range of different excitation voltages. The chart shows the effect of different cell densities and acoustic contrast factors.

5.4.1 Experimental Methods

For these experiments, 1 L bottles of 3MN solution were prepared and autoclaved along with steel connectors and polypropylene tubing for the peristaltic pump. Each bottle had 4 polymer slides connected via a peristaltic pump to form a closed system. The polymer slides were sterilised using ethanol for 15 minutes before being air dried. Three experiments were ran in series, each with two powered slides and two control slides. Details of the experiment are summarised below, see Table 5-7.

Table 5-7 Summary of the experiments undertaken with the polymer slides.

Experiment	Slide Number	Voltage Vpp
1	1	4
1	2	2
1	3	0
1	4	0
2	5	1
2	6	2
2	7	0
2	8	0
3	9	1
3	10	0.5
3	11	0
3	12	0

For consistency between experiments, each batch of seawater was left on a heated stirring plate at 25 °C at 60 rpm. At the beginning of each experiment the 3MN solution was seeded with *Vibrio natriegens*. Each experiment ran for 1 week, when the slides were flushed with milli-Q water. Each slide was then treated with 5-cyano-2,3-ditolyl tetrazolium chloride (CTC) stain for actively respiring cells and 4',6-diamidino-2-phenylindole (DAPI) dye for the total number of cells, (Rodriguez et al., 1992, Cappelier et al., 1997, Sieracki et al., 1999, Pyle et al., 1995). Full instructions on the staining process can be found in Appendix B. These dyes were chosen for the following reasons. Knowing the total cell quantity is important as every cell will have an effect on physical readings in an oceanographic sensor, this can be achieved through the use of DAPI. Knowing what proportion of the cells are actively respiring is important as this would affect chemical readings through the uptake and release of chemicals, this is achieved through the use of CTC. Other dyes are available that would determine if the cells are alive but would not distinguish if they were respiring. For instance, even if the quantity of cells are the same in each experiment, if the ultrasonic standing waves inhibit metabolism this would be beneficial in chemical sensors but less applicable in physical sensors.

5.4.2 Image Analysis

Images were taken along the length of the internal surfaces, the reflector side and the matching layer side. Three series of images were taken along each surface, one at each edge and one along the centre of the channel, all at a magnification of 10x. A diagram of the imaging method is shown below, Figure 5-17. Images were taken using fluorescence microscopy using the appropriate filters for each of the stains used.

Figure 5-17 A figure describing the method used to image the surface of the polymer slides.

Cellprofiler software was used to analyse the images and was calibrated in the following way, (Carpenter et al., 2006).

5.4.2.1 Crop Images

Within the software there are several prebuilt “modules” for image analysis which can be selected and added to the workflow in the desired order. The first such module applied to the images was a crop. 200 pixels were discarded from the outer edge of each image for the following reasons.

1) Variations in lighting towards the outer edge of the image caused by the illumination of the microscope. This can be seen by the darker background in images in the outer corners of the image, see Figure 5-19.
2) Lack of focus around the outside of the image. This can again be seen in the example image below, see Figure 5-19.
3) Evanescent illumination at edges of the image if it was close to the boundary of the fluid channel. This can be seen along the bottom edge of the image below, Figure 5-19.
4) Avoid overlapping of images when later modules are applied to the images. Images were taken in succession along the length of the fluid channel and it is likely the edges of each image overlap with the next.

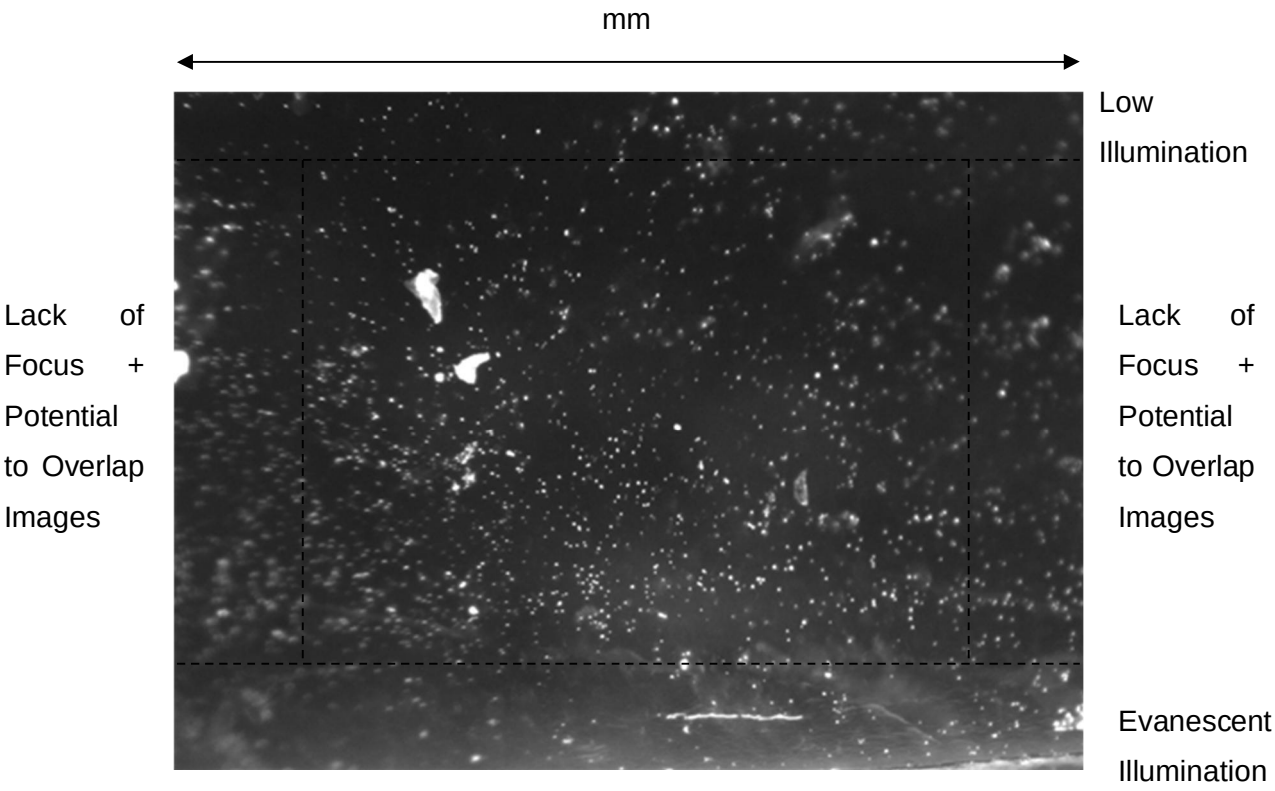

Figure 5-18 Example DAPI image before cropping is applied.

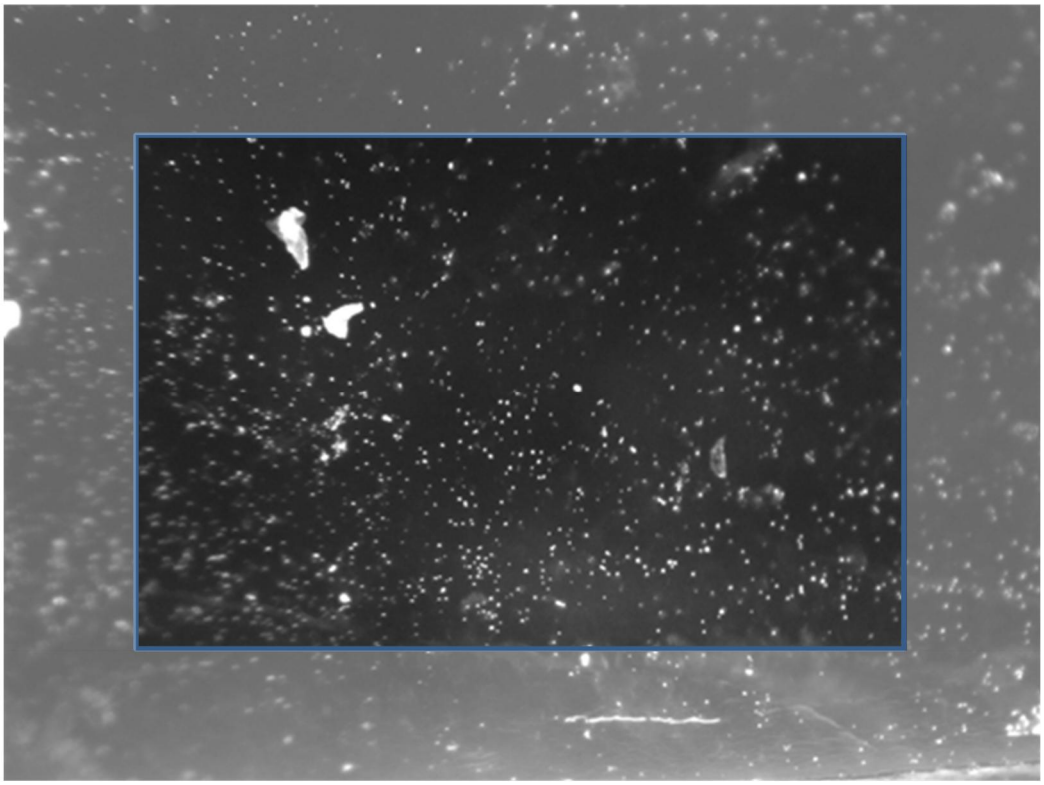

Figure 5-19 Example DAPI image after cropping.

Applying the crop to the image had a positive effect on the correlation of the images in terms of the total image intensity against the number of bacteria identified in the image, Figure 5-20, Figure 5-21.

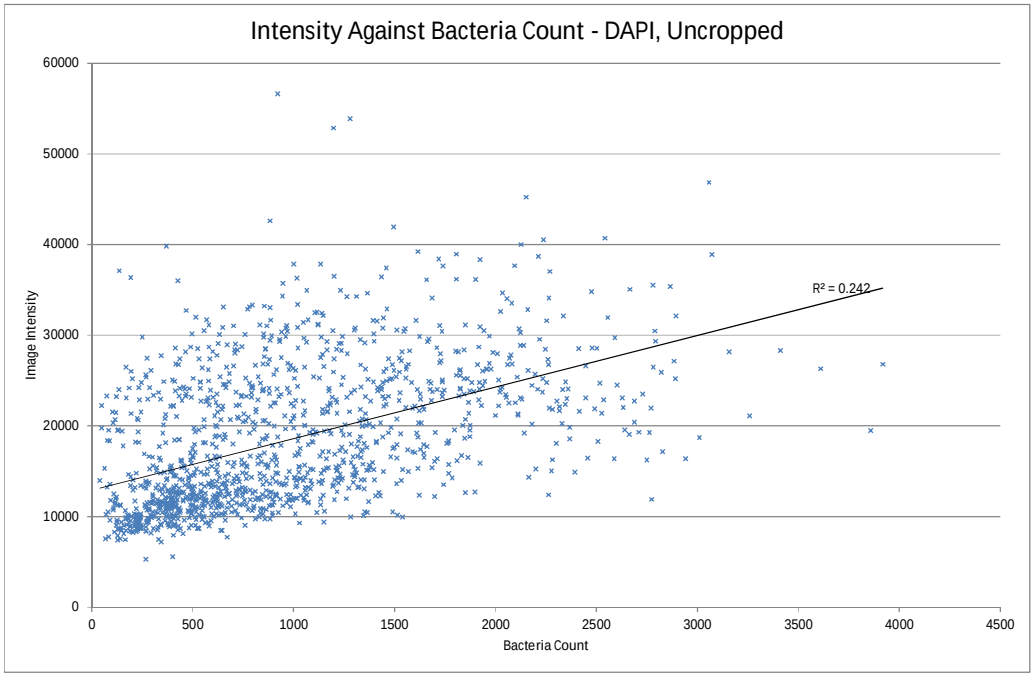

Figure 5-20 A plot of image intensity against bacteria counted for the uncropped images. The R^2 value is low at 0.242 implying poor correlation.

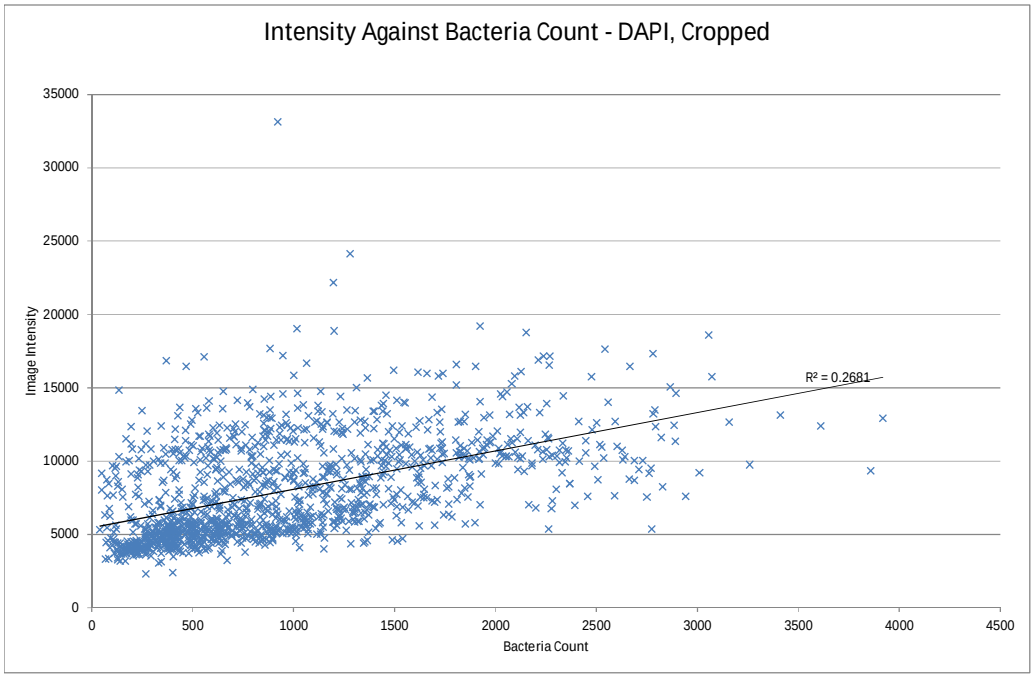

Figure 5-21 A plot of image intensity against bacteria counted for the cropped series of images. The R^2 value has increased slightly to 0.2681, which still implies poor correlation.

5.4.2.2 Enhance and Suppress Features

The second module applied to the images was used to enhance individual bacteria against the background image and to remove large contaminants from the image. The module loaded the cropped image and sharpened areas of pixels less than 10 pixels across. The module also removed objects consisting of 10 or more saturated pixels. Filtering for larger objects had no effect on the final quantity of bacteria identified, but increased dramatically the computational time required. Dropping below 10 pixels reduced dramatically the number of bacteria identified and visual inspection confirmed that bacteria were not being counted, see Figure 5-22. An example image is shown below in the pre and post enhanced and suppressed stage, Figure 5-23.

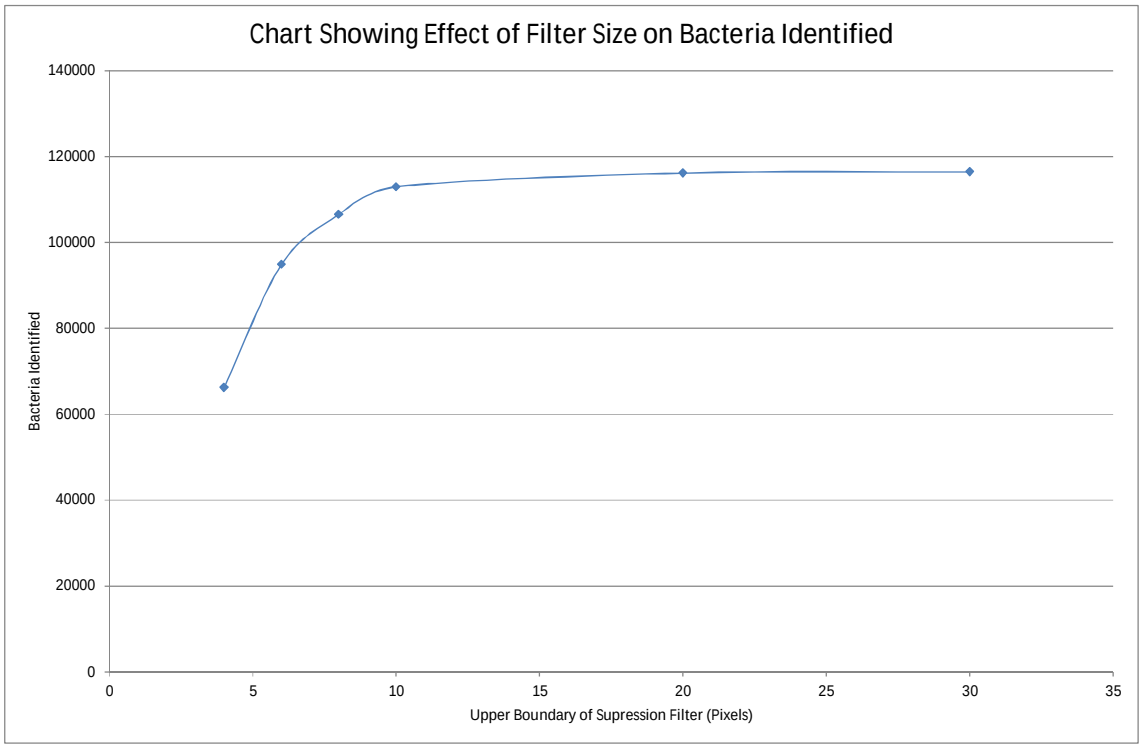

Figure 5-22 Chart showing the effects of the upper limit of the suppression filter on the total number of bacteria identified. Down to approximately 10 pixels there is negligible change. Above this computational time increases dramatically. Below this bacteria are being removed from the image and therefore not counted. A sample of 87 DAPI images was used to produce this graph.

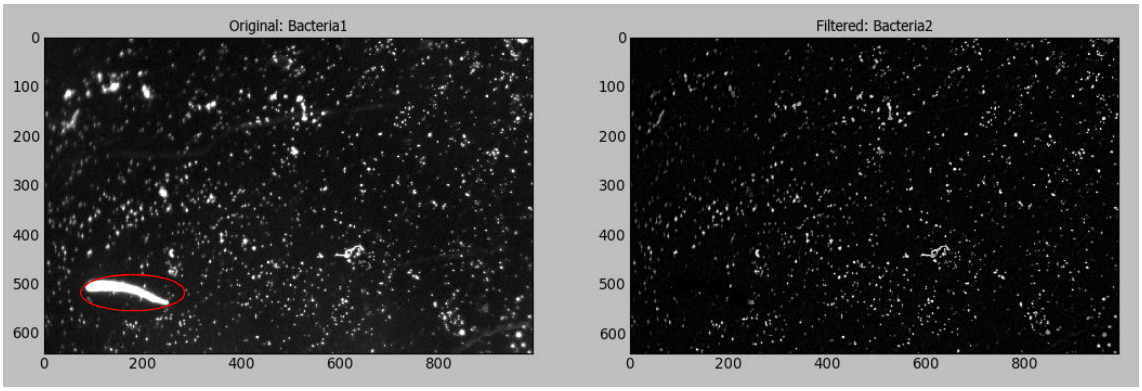

Figure 5-23 Example image showing the original image on the left, including a contaminant circled in red. After applying the suppression filter the contaminant is removed from the image and individual bacteria have been enhanced relative to the background.

Applying the enhancement module to the series of images had a strong positive effect on the correlation between the intensity and number of bacteria counted. This can be seen below in Figure 5-24.

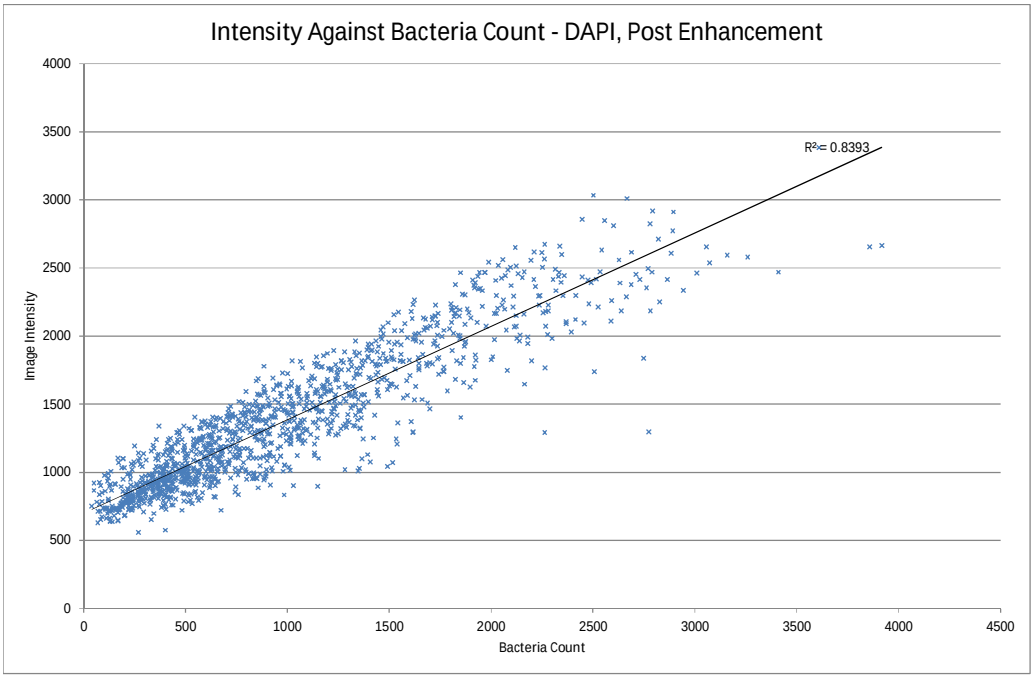

Figure 5-24 A plot showing strong correlation between image intensity and the number of bacteria identified. An improved R^2 value of 0.8393 was achieved.

5.4.2.3 Identify Primary Objects

The next module applied to the images was used to count the number of bacteria cells in each image. The module was set to identify objects between 2 and 10 pixels across using intensity peaks. The upper limit of 10 pixels was chosen as the previous

module suppressed features larger than this. There is also very little change to the total cells counted when it is set higher than 10 but increases the computational time required, see Table 5-8 for results.

Using a minimum object size of 1 resulted in an increase in the number of cells counted, see Table 5-8. By inspecting a selection of images it became clear that this increase in cell count was due to the module over counting the number of bacteria in an image, this can be seen in, Figure 5-25. When zoomed in it is possible to identify individual bacteria. It also shows that some bacteria are being counted multiple times, these are highlighted in red. Increasing the minimum bacteria size to 3 pixels causes a drop in the number of bacteria being identified, see Table 5-8. Visual inspection shows that it fails to identify bacteria that are clearly present, Figure 5-26 . Highlighted in red are two bacteria that are present in input image but are not identified as individual bacteria.

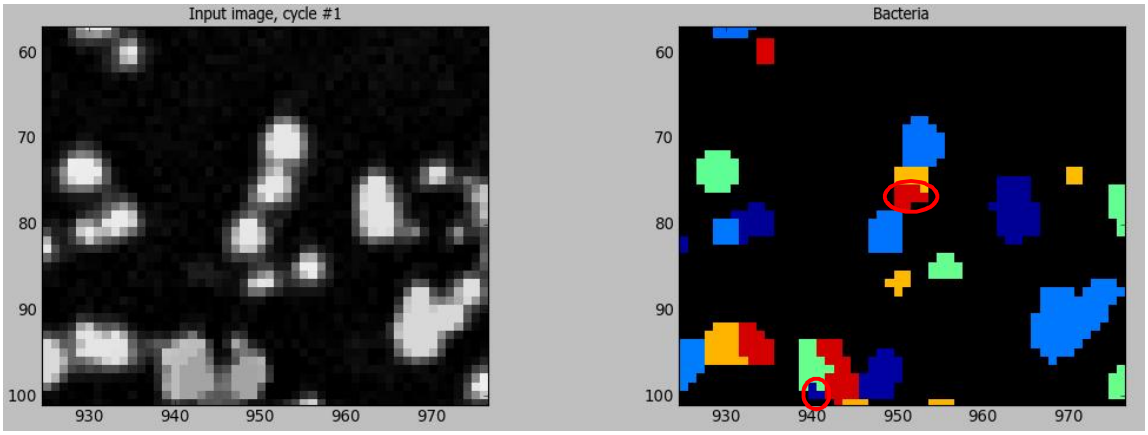

Figure 5-25 Close up image of a series of bacteria cells that have been miscounted due to the minimum threshold filter being set to 1 pixel. Highlighted in red are two objects that have been classified as bacteria but in reality each are variations within a larger bacteria.

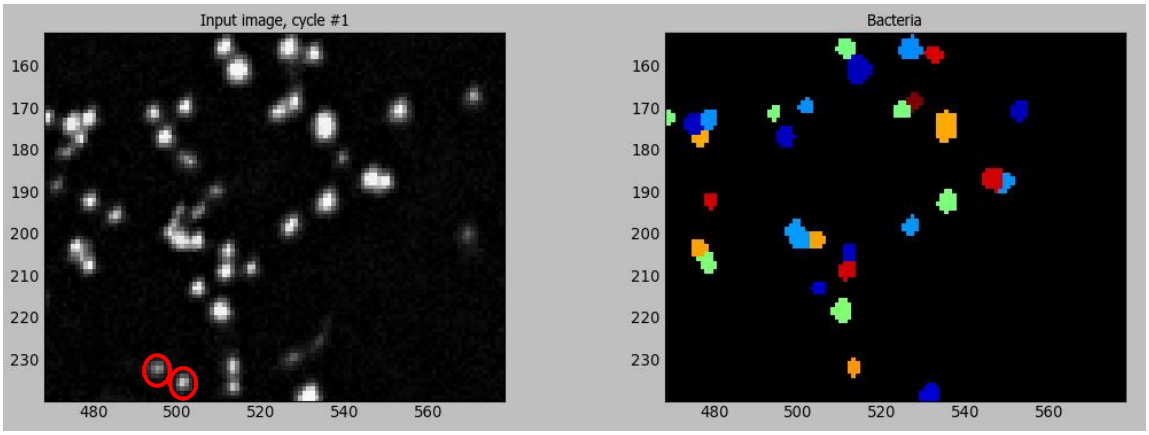

Figure 5-26 Close up image of a series of bacteria cells that have been undercounted due to the minimum threshold for bacteria being too high at 3 pixels. The left image shows the original and the right image shows what has been identified as bacteria. Significant quantities of bacteria have not been identified. Highlighted in red are two bacteria that were not identified despite clearly being stained bacteria cells.

The upper bound for identifying objects is significantly less critical down to 10 pixels. Below this large bacteria are not counted and thus the count is artificially low. The table below shows how changing the expected object size affects the number of bacteria identified in a sample of 87 DAPI images, Table 5-8.

Table 5-8 The effect of changing the expected object size on the quantity of bacteria identified. Changing the minimum object size causes significant variation in the quantity of bacteria identified. Changing the maximum object size causes little variation down to 10 pixels, below which the number of bacteria identified drops drastically.

Minimum Object Size	1	2	3	2	2	2	2
Maximum Object Size	10	10	10	20	15	8	6
Sum of Bacteria	137302	112945	84910	113423	113421	110316	99095

The number of pixels in an image is 1040 x 1392 and corresponds to approximately 0.7 x 0.52 mm, which is approximately 0.5 µm/pixel. The module was set to identify objects between 2-10 pixels which is approximately 1-5 µm. This corresponds well with the measured size of 0.606 x 3.334 µm, (Cheng et al., 2010). It would also have been possible to measure surface coverage however the volume of *Vibrio natriegens* is known to vary significantly. This could mask characteristics of the biofilm. For instance, if the film was populated with a lot of small actively respiring bacteria this would be a small reading using the surface coverage method. Under more optimal conditions these small cells could form substantial colonies greatly effecting

chemical readings. The method used in this work gives insight into the abilities of the biofilms to carry on respiring and growing over a longer time scale.

5.4.2.4 Anomalous Results

The analysis preformed on the images worked well for the vast majority of the images and a strong correlation was seen between the number of bacteria and the intensity of the image, see Figure 5-24. For both dye sets there were some erroneous results caused by extremely low bacteria counts in the images. This caused the programme to identify any minor variations in the images as bacteria resulting in an incredibly high count of bacteria. The images are identifiable by an incredibly high bacteria count coupled with a low overall image intensity, see Figure 5-28. An example image is shown below, where it can be seen that the input image has a low bacteria count, but the software identifies a high surface coverage, which is mistaken for a high quantity of bacteria cells, Figure 5-27.

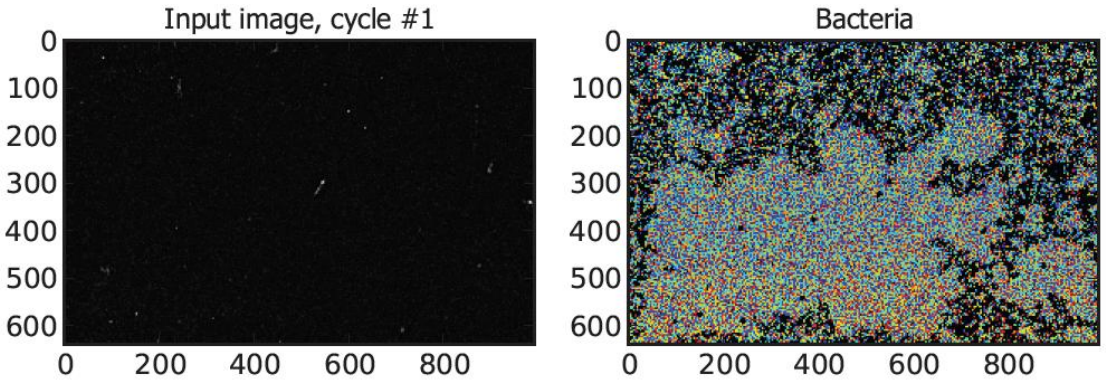

Figure 5-27 The input image (left) has a particularly low bacteria count but the software identifies bacteria based on intensity peaks. Because of this any minor variation in the image is considered a bacteria leading to an artificially high count which can be seen in the output image (right).

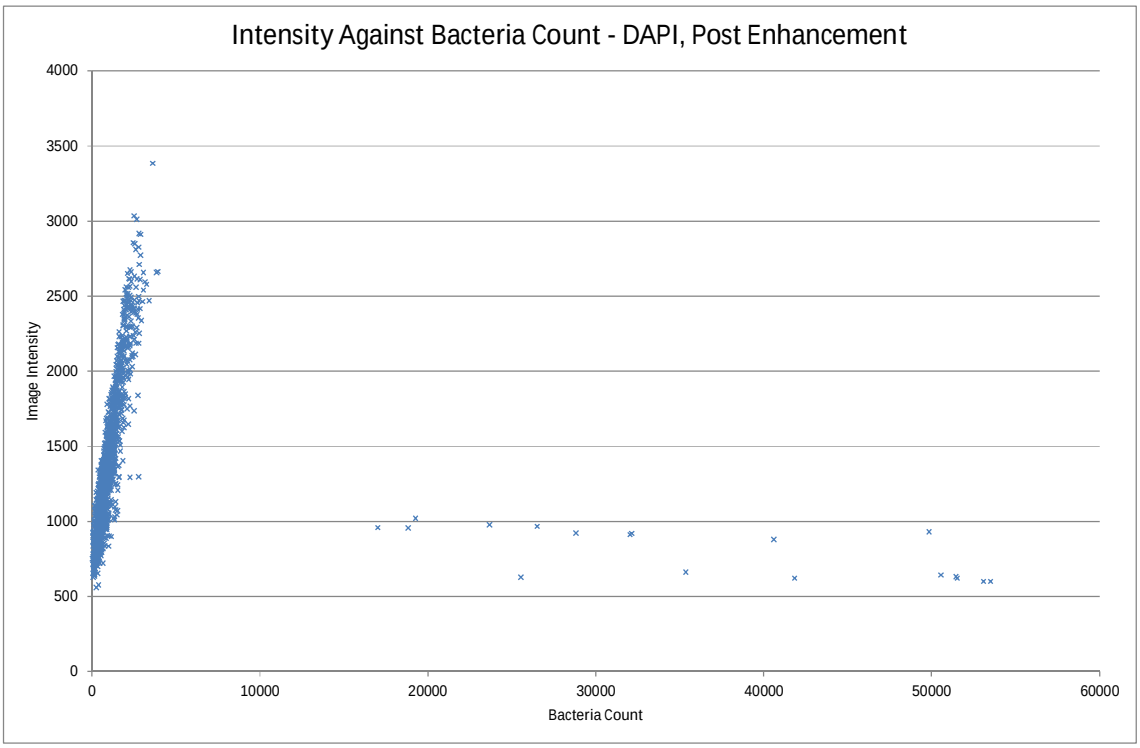

Figure 5-28 Plot showing erroneous results, charecterised by incredibly high bacteria counts with low overall image intensity.

Due to the relative scarcity of these results it was possible to view each image individually, confirming a low bacteria count in each image. Using the line of best fit from Figure 5-24 it was possible to assign an appropriate value to these results. For images where the calculated bacteria count was negative, the result was set to 0.

5.4.2.5 Discussion

In total 3532 images were analysed and the same settings were used for the DAPI images as the CTC images. This is a large number of images for the 12 chips analysed, meaning the results will be statistically significant and it will be possible to see the effects of ultrasonic excitation. It will also be possible to compare bacteria growth on the different surfaces as well as cell viability with and without ultrasonic excitation.

5.4.3 Results

The aim of the experiment was to reduce biofilm formation in polymer microfluidic channels and show the effects in a quantitative way. The following sections will show the effects of ultrasonic excitation on biofilm formation, cell viability and positioning.

5.4.3.1 Total quantity of bacteria (DAPI Images)

The effect of ultrasonic excitation reduced the total quantity of bacteria adhered to the surface of the polymer slides. This can be seen below in Figure 5-29. Interestingly, the quantity of bacteria identified in the control slides varies noticeably between experiments but the variation between control slides in the same experiment is within the ±1 standard error of its' sister reading. Each individual experiment showed a reduction in the total quantity of bacteria adhered to the surface of the polymer slide.

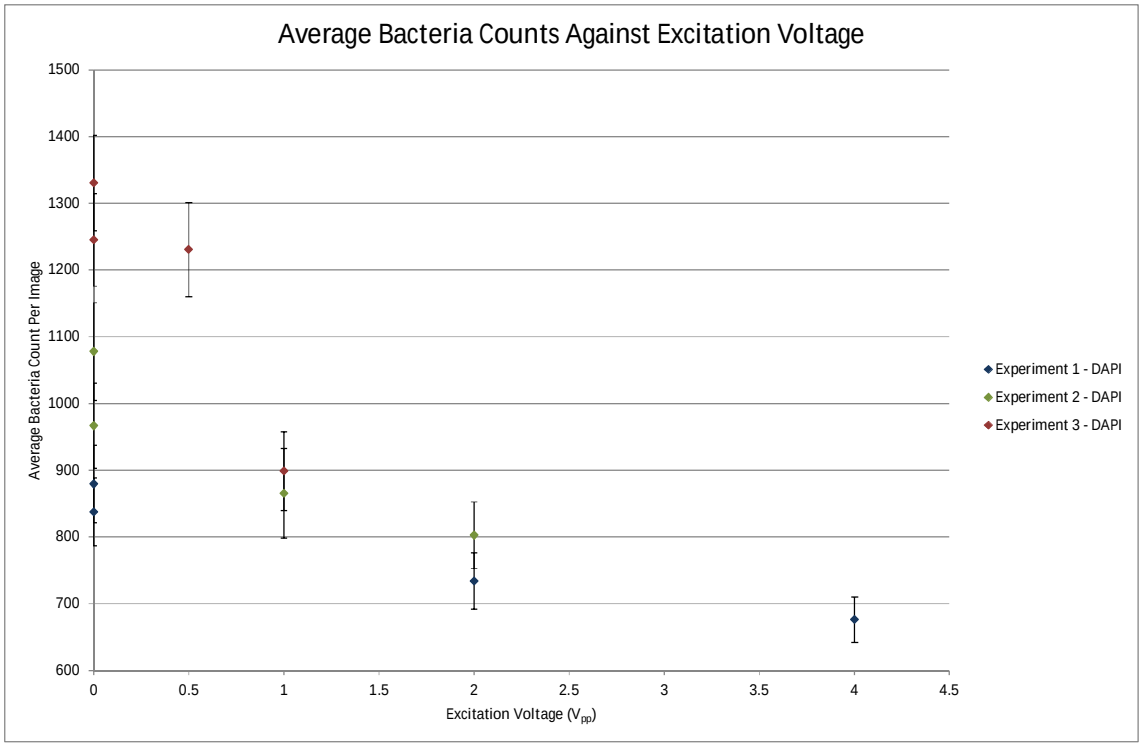

Figure 5-29 Excitation voltage is plotted on the abscissa and the ordinate refers to the average number of DAPI stained bacteria identified in each chip. Error bars are defined as ± the standard error. Readings from the same experiment share colour. DAPI readings indicate total cell count. Every experiment showed a reduction in total biofilm formation from ultrasonic excitation.

Whilst the control slides vary between experiments, the slides that received the same level of ultrasonic excitation but were in different experiments gave similar average readings. This implies that had more bacteria been present in the control slides of experiments 2 and 3, a similar drop in the quantity in the ultrasonically powered slides would have been seen.

Whilst steps were taken to minimise variations between the experiments, there are still ways in which small differences between the experiments could cause these variations.

1) Temperature – This has been shown to have a significant effect on the growth rate of V*ibrio natriegens*, whilst all 3 experiments were placed on a heat plate at 25°C, temperature variations within the lab could have had a bigger effect. As an example, an increase in the temperature of 5°C would have increased the growth rate by 37%, (Eagon, 1962).
2) Variations in the composition of the 3MN solution. To limit variation, the three batches of 3MN solution were prepared at the same time and the same pre-mixed solutions were used. Some variations may still have occurred due to the relatively small volumes of ingredients being used. This could have been improved by monitoring/adjusting the pH of the solution before inoculation.
3) Differences in the initial inoculum. It has been shown that the initial quantity of inoculum deposited into a solution can have an effect on the initial growth rate of the bacteria, (Eagon, 1962). Whilst the final quantity of bacteria in the solution should be the same, a significant difference might occur in the early stages of the experiment. This could have a large effect when the experiment is first being set up if different quantities of bacteria make contact with the inside surfaces of the slides.
4) The timescale over which the experiments took place. Each experiment lasted 1 week but the solutions for all 3 experiments were prepared at the start and then autoclaved. By preparing them all at the same time the initial errors should be minimised but changes over time will cause differences between the solutions.
5) Dissolved oxygen levels were not monitored in these experiments. It is known that dissolved oxygen levels are an important factor in the development and characteristics of *Vibrio natriegens* biofilms, (Casey et al., 1999).

Despite the variations in the quantity of bacteria in the control slides between experiments, a reduction in the total quantity of bacteria in the slides has been observed by the addition of ultrasonic standing wave techniques.

5.4.3.2 Actively Respiring Bacteria (CTC Images)

A similar but less pronounced drop in bacteria numbers can be seen in the actively respiring bacteria, see Figure 5-30. Experiment 1 shows a significant drop in the quantity of actively respiring bacteria in the ultrasonically active slides. Experiment 2 shows a marginal drop in actively respiring bacteria. Experiment 3 shows contradicting results for the slides when powered at 0.5 V_{pp} and 1 V_{pp}. The lower

powered slide led to a significant increase in the number of actively respiring cells, whilst the higher powered slide led to a significant drop. Variation between control slides of the same experiment is greater than in the total cell count. This can also be seen by the significant differences between slides with the same ultrasonic excitation but in different experiments. Whilst in the total cell count they were similar, in the actively respiring bacteria they are vastly different.

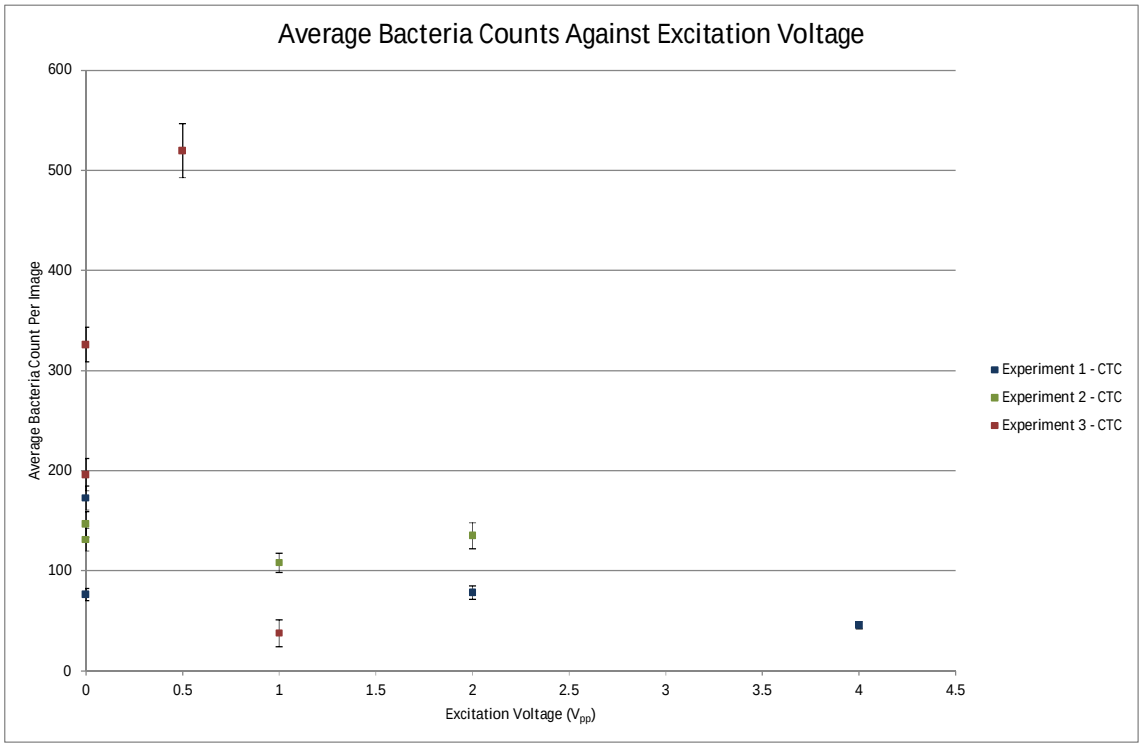

Figure 5-30 Excitation voltage is plotted on the abscissa and the ordinate refers to the average number of CTC stained bacteria identified in each chip. Error bars are defined as ± the standard error. Readings from the same experiment share colour. CTC readings indicate actively respiring cells.

Ultrasonic excitation in a polymer microfluidic channel can lead to a reduction in the quantity of bacteria adhering to a surface. Even at particularly low voltages, a reduction in biofilm formation was seen. Whilst the forces generated at 0.5 V_{pp} would not be sufficient to levitate cells even if they had favourable properties (density, acoustic contrast factor), the slides were orientated vertically. This means that the forces only need to overcome any attractive forces between the cells and the surface of the slide, Figure 5-31.

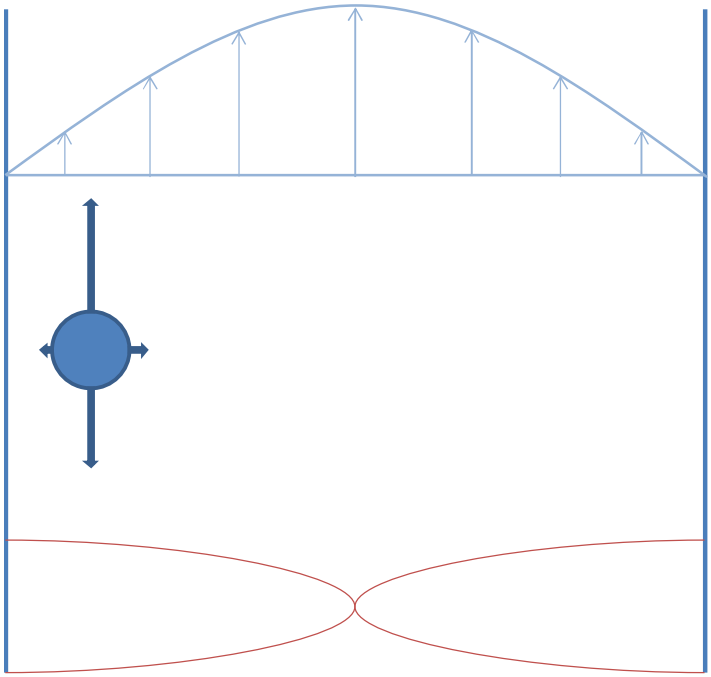

Figure 5-31 Diagram depicting the forces acting on a bacteria cell in the microfluidic slide. In the vertical orientation the weight of the cell is overcome by the drag of the fluid. The acoustic forces can be much smaller than the weight of the cell but still lead to a reduction in biofilm formation. This is because the forces need only overcome attractive forces between the bacteria and the surface of the device.

Assuming a parabolic fluid flow was set up across the channel, any bacteria cell within the flow would lag behind the flow due to sedimentation. This would produce a force on a bacteria cell towards the centre of the channel, (Kim and Yoo, 2009).

5.4.3.3 Discussion - Effects on Cells

It is important to understand any effects that ultrasonic excitation has on the behavior of bacteria cells. By plotting total bacteria counts and actively respiring bacteria counts it can be seen there is no real variation in how a colony of cells behave with and without ultrasonic excitation, Figure 5-32. Experiments 1 and 2 show a decrease in the total number of bacteria and the number of actively respiring bacteria. This is consistent with the idea that ultrasonic excitation only affects the quantity of bacteria that adheres to a surface and does not affect the growth or death of the bacteria once it has adhered. Experiment 3 follows this trend excluding the slide that was powered at 0.5 V_{pp}, this slide shows a significant increase in the ratio of respiring bacteria to non-active bacteria. When plotted as a %, it is clear that ultrasonic excitation does not have a noticeable effect on the ratio of active to total cells. A slight reduction in the proportion of actively respiring cells can be seen excluding the slide

powered at 0.5 V_{pp} which shows a significant increase in actively respiring bacteria, see Figure 5-33.

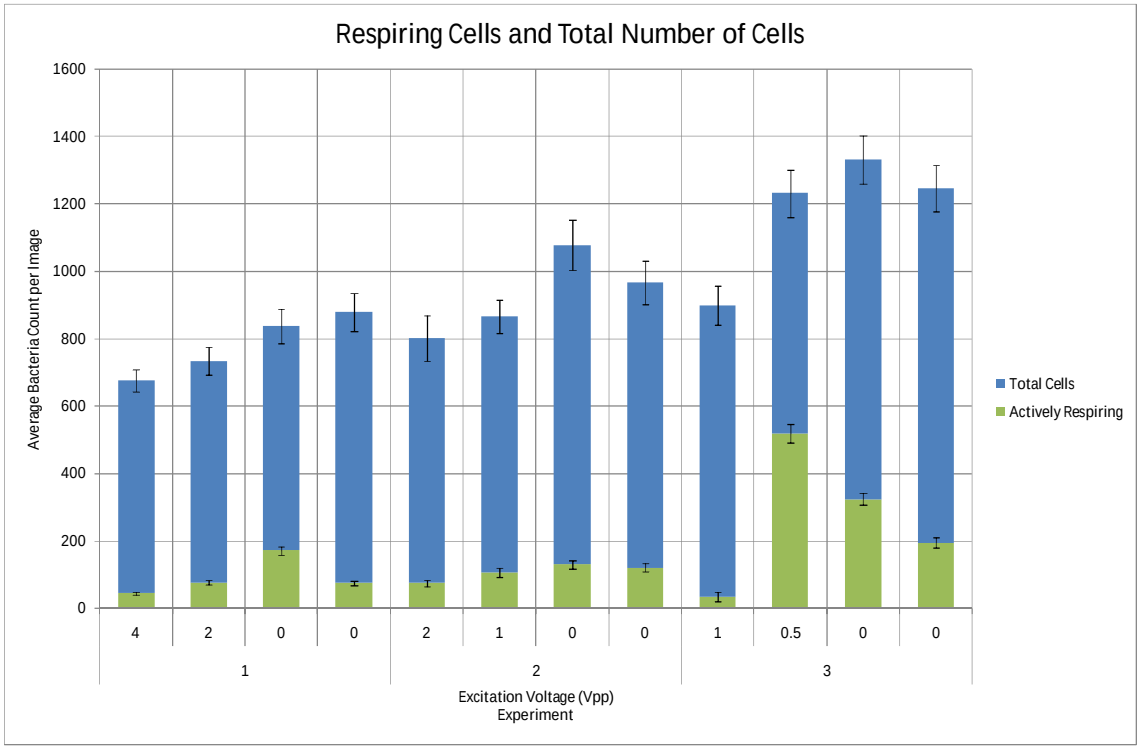

Figure 5-32 A graph showing the effects of ultrasonic excitation on the ratio of actively respiring cells to total cells. Each experiment is grouped together and shown in descending order of ultrasonic excitation. There is no noticeable difference in the ratio of actively respiring to non active cells excluding the slide powered at 0.5 V_{pp}. Error bars are equal to plus or minus 1 standard error.

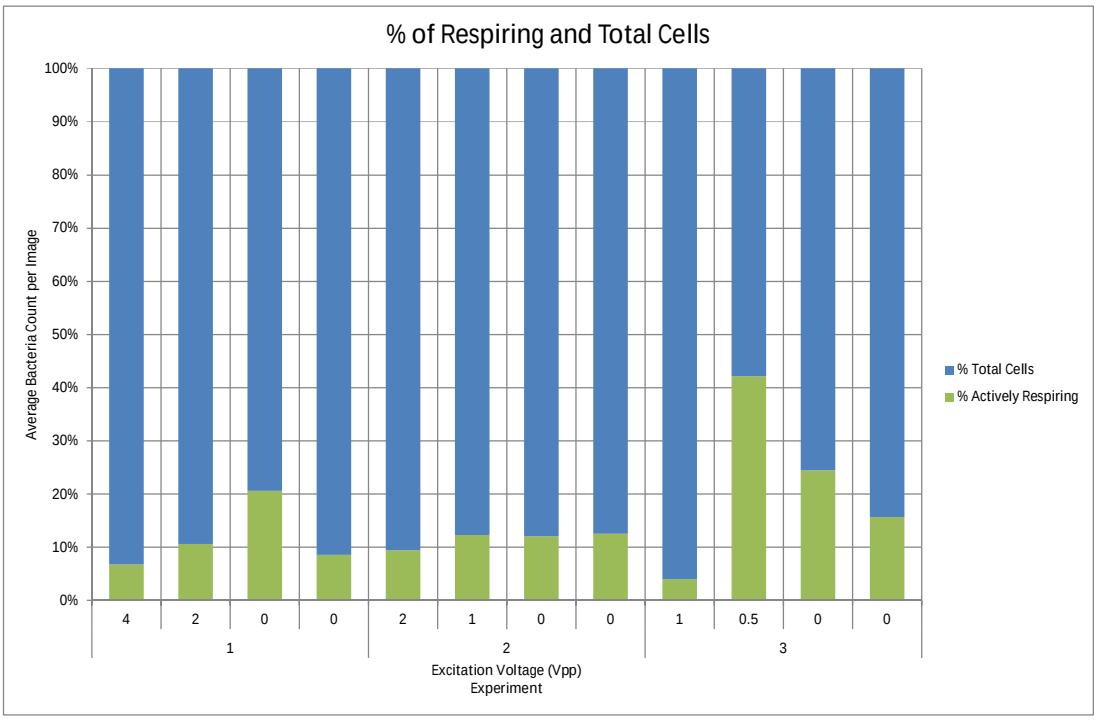

Figure 5-33 When the data is plotted as a % it shows that ultrasonic excitation has does not have a noticeable impact on the proportion of cells actively respiring and the total number of cells. If anything, a slight decrease in % of actively respiring cells can be seen.

The presence of ultrasonic excitation not only reduces the adherence of bacteria to a surface, but also appears to inhibit metabolic activity within the cells. In every experiment, the chip with the highest level of ultrasonic excitation had the lowest percentage of metabolising cells. The total cell density is vastly different in every experiment, it can be expected that this would lead to variations in the % of actively respiring cells, as competition for nutrients and concentrations of waste metabolites differs. This could explain why there is significant variation in the % of metabolising cells between slides that were powered at the same excitation voltage but in different experiments.

The obvious exception to this idea is the slide powered at 0.5 V_{pp} in experiment 3. The quantity of bacteria that is actively respiring is significantly higher than in any other chip. One potential reason for this could be that at such low levels of ultrasonic excitation, variations within the cell population in terms of size, density and acoustic contrast factor could cause a bias in the bacteria that do attach to the surface. For instance, the forces acting on the bacteria that have a low acoustic contrast factor will be less than the forces on bacteria with a high acoustic contrast factor. If the bacteria that are less likely to metabolise have a high acoustic contrast factor then this would lead to a % increase in metabolising bacteria on the surface of the slide but an overall

reduction in bacteria numbers. As the excitation voltage increases the acoustic forces would be sufficient to act on all the bacteria cells and the % discrepancy would stop.

Whilst no firm conclusions can be drawn about the effect of ultrasonic excitation on the metabolism of bacteria cells, if true it would be an additional benefit. The metabolites produced by bacteria will have a negative impact on the accuracy of readings taken within a microfluidic oceanographic sensor. Therefore reducing the quantity of metabolising cells will lead to more accurate and repeatable readings.

One potential mechanism for the reduction in the percentage of metabolising cells could be that cells adhere to the surface but still experience the acoustic radiation force. This could be exerting a stress on the cell which reduces the ability of the cell to metabolise. The idea fits with the fact that in each experiment the slide with the higher level of ultrasonic excitation had the lower percentage of metabolising bacteria.

5.4.3.4 Discussion - Bacteria Positioning

It is conceivable that there are hydrodynamic forces acting on the particles as they enter the microfluidic device, this could give the cells momentum towards one surface of the chip over the other, which matches well with the fact that more bacteria were found on the matching layer than the reflector.

It is possible to compare biofilm formation between the two different surfaces of the slides. In the control slides of experiments 1 and 3, bacteria formation was approximately equal between the reflector and the matching layer. In experiment 2 there was a tendency for more bacteria to be found on the matching layer. This could be due to an unidentified difference in the experimental setup, causing more bacteria to be present near the matching layer than the reflector layer.

Modelling suggested that the forces acting on bacteria at the matching layer would be stronger than the forces acting on bacteria at the reflector layer, implying that more bacteria would be found on the reflector layer than the matching layer for ultrasonically powered chips. In general, the reduction in bacteria numbers is seen at the reflector which is inconsistent with the modelling results, Figure 5-34. At the higher excitation voltage of 4 V_{pp} bacteria formation is approximately equal on both sides of the slide.

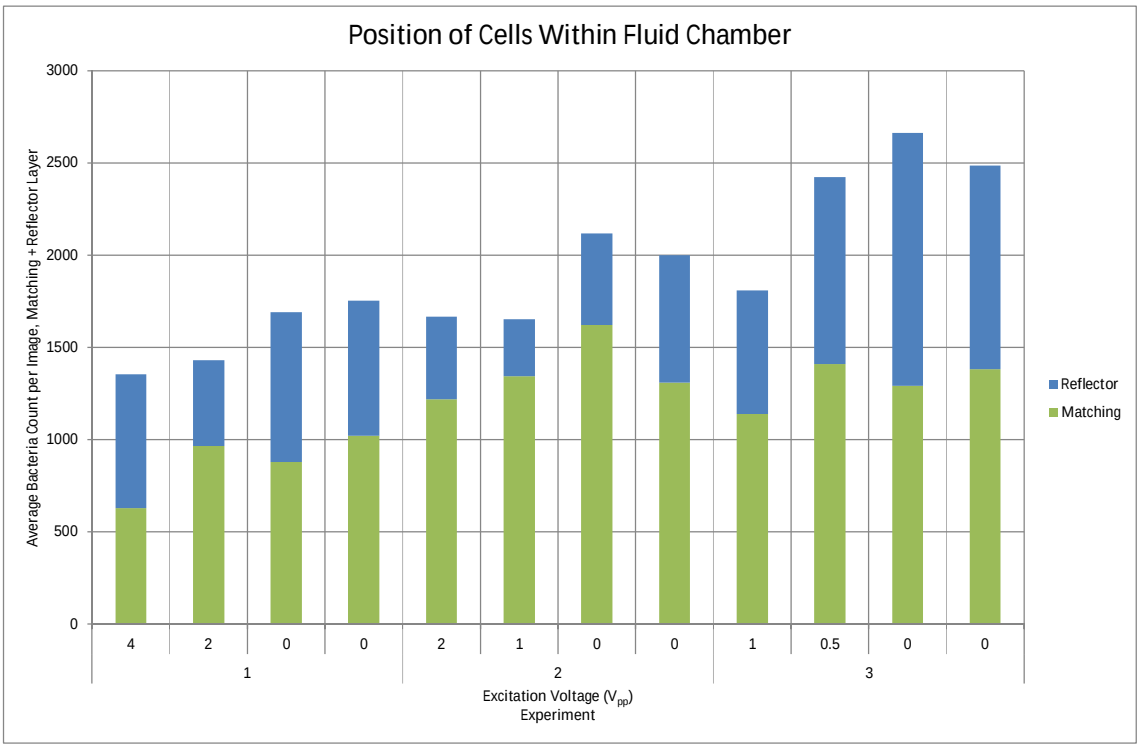

Figure 5-34 A plot showing differences in biofilm formation between the two inner surfaces of the polymer slides. Ultrasonic excitation has a greater effect on the reflector which is inconsistent with computational modelling. At 4 V_{pp} there is approximately equal biofilm formation on both surfaces, implying that as ultrasonic power increases the forces at both the reflector and matching layer are sufficient to stop bacteria adhering to either surface.

It was observed that bacteria cells tended to collect on the matching layer more than the reflector layer, this was seen in all of the control slides and a possible reason for this has been given. In terms of the effects of ultrasonic excitation, it appears to have a greater effect on the reflector layer than the matching layer for voltages below 4 V_{pp}. The modelling predicts a stronger force away from the matching layer than the reflector layer, which is in contrast to the experimental results, Figure 5-35. One potential reason for this is if the bacteria cells had momentum towards the matching layer as they entered the fluid chamber. This would make it possible for acoustic forces to reduce biofilm formation at the reflector at low voltages but the reduction would be less obvious at the matching layer. As the voltage increases, the forces generated would be sufficient to overcome any momentum bacteria cells had towards the matching layer.

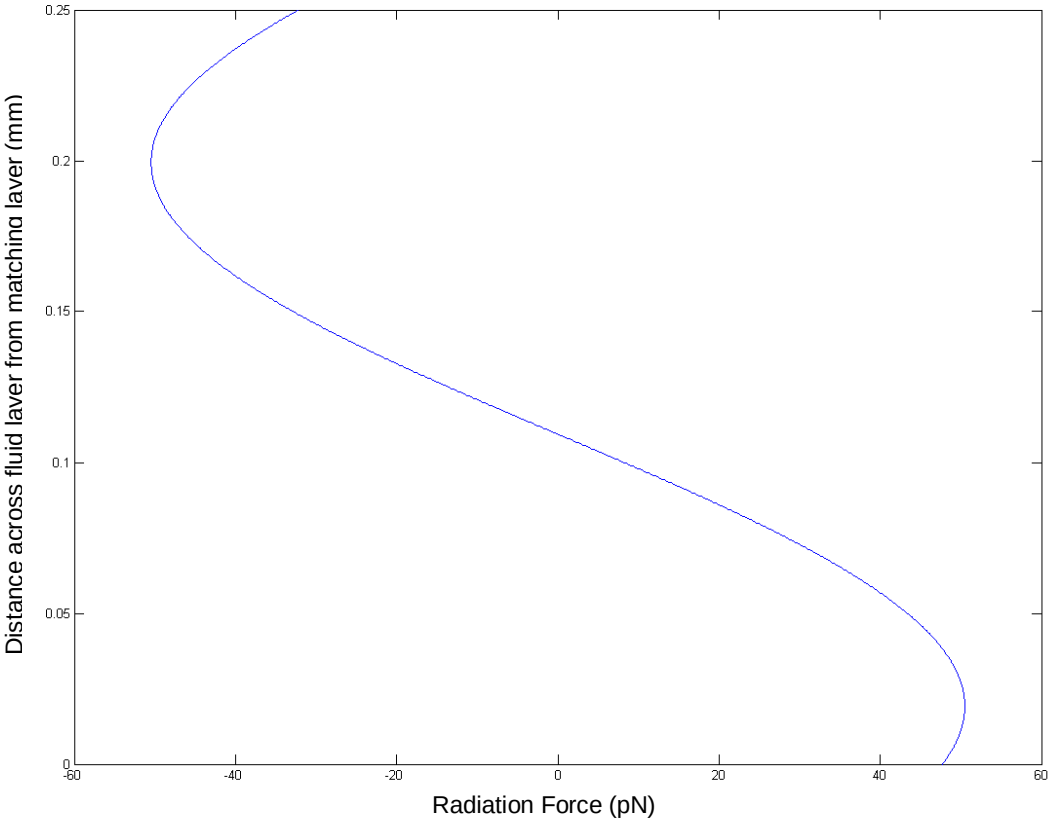

Figure 5-35 A force plot for the fluid chamber in the polymer slides. At 10 V_{pp} excitation and with 10 µm beads a force of over 45 pN is seen acting on particles at the matching layer. At the reflector layer a force of just under 35 pN is seen acting towards the middle of the channel.

5.4.4 Conclusions

In this section it has been shown that it is possible to reduce the formation of biofilms within PMMA devices using ultrasonic standing wave technology. A robust and repeatable manufacturing method has been used to run a series of experiments that proved effects on biofilm reduction. A thorough experimental setup has been used to limit variations between experiments. An in depth quantitative analysis was performed which matched well with theoretical predictions. This method for the reduction of biofilm formation is a novel use of ultrasonic standing wave technology and is a new low power solution for *in-situ* remote oceanographic sensing.

Chapter 6 Surface Acoustic Wave Devices

Shi et al (Shi et al., 2008) demonstrated the possibility of using SAWs to manipulate particles into a tightly focussed beam in a microfluidic device. The device uses interdigitated electrodes to generate a surface acoustic wave on lithium niobate, a transparent piezoelectric substrate, see Section 2.1.2.7 Generation of Surface Waves for further information. The device is described in more detail in Section 2.3.1.3 Flowing Standing Wave Devices. A device like this would be of significant use in an oceanographic sensing application, in particular for a µ-flow cytometer. For this to happen, the device would need to be adapted for the size of particles and fluid channels used. The following chapter investigates the mechanism involved in this two dimensional focussing and factors affecting the robustness of such a device. The work also looks to develop a device for oceanographic sensing and looks at novel manufacturing techniques.

6.1 Modelling

The following section models a free lithium niobate transducer with a standing wave. ANSYS software (ANSYS, U.S.A.) is an FEA package and example code is given Appendix D. A thin (0.01 mm) slice is generated from a series of coordinates, which are used to define areas and volumes. The model is constrained to only allow movement in the x and z direction, see Figure 2-1. Material properties are loaded into the volumes and orientated appropriately for the Y+128° lithium niobate, see 2.3.1 Surface Acoustic Devices for further information. The model was produced by Dr P.Glynne-Jones and was adapted for surface acoustic wave devices. The model assumes the surface is unbound which is sufficient as attenuation caused by loading from a gas is negligible, see Table 2-1. The work investigates how the transducer will work and compares it with theory explained in Section 2.1 Ultrasonics. The work goes on to investigate the mechanism by which particles are focussed within a fluidic chamber. The aim of this work is to generate a model of the SAW device presented by Shi et al. Initially a simplified model of a lithium niobate transducer will be produced and compared with theory. A PDMS layer will be added to the model and observations made regarding the effects on the SAW. Finally, a fluid channel will be added to the model and the mechanism presented by Shi et al will be investigated. The model will

be scaled up to confirm the feasibility of designing a µ-flow cytometer for use as an oceanographic sensor.

6.1.1.1 Substrate Thickness

The work by Shi et al used a square fluid channel 50 µm wide and spaced the electrode fingers with a period of 100 µm. A computational study was conducted investigating the required thickness of lithium niobate for surface wave generation. As shown in Figure 2-2, the displacement of a surface wave is considerable up to a depth of approximately 1.5 wavelengths. If the substrate is less than this thickness the wave generated will not be a pure surface wave, though in reality, there is no distinct cut off depth, but a gradual transition from surface wave to plate wave as the thickness of the substrate decreases. At 0.5 mm a distinct asymmetric plate wave can be seen when the excitation electrodes have a period of 400 µm, Figure 6-1. This corresponds to a plate thickness 1.25 times the excitation wavelength.

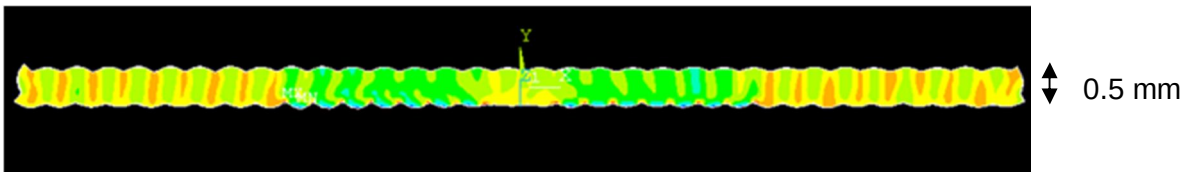

Figure 6-1 An ANSYS plot showing the displacement on a 0.5 mm lithium niobate plate when interdigitated electrodes are used to generate a “surface wave” on the lower surface of the substrate. The thickness of the substrate is equal to 1.25 wavelengths.

As the thickness of the substrate increases further, the wave generated becomes less plate like and transforms into a surface wave. When the thickness of the substrate is equal to five times the wavelength the wave appears to be a pure surface wave, Figure 6-2. The work by Shi et al used a substrate that was five times thicker than the period of the surface acoustic wave. The modelling confirms that a surface wave was generated in the Shi device.

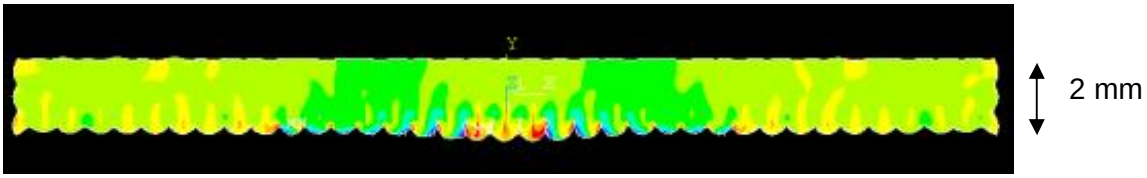

Figure 6-2 The displacement generated by 400 µm wavelength interdigitated electrodes on a 2 mm thick piece of Lithium Niobate. Displacement is confined to the side of the substrate on which the electrodes are positioned.

Differences were also seen in the impedance plots when different thickness substrates were modelled. When the thickness of the substrate is the same as the period of the electrodes on the surface of the substrate, the impedance plot produces several resonances, all relating to plate type modes, Figure 6-3.

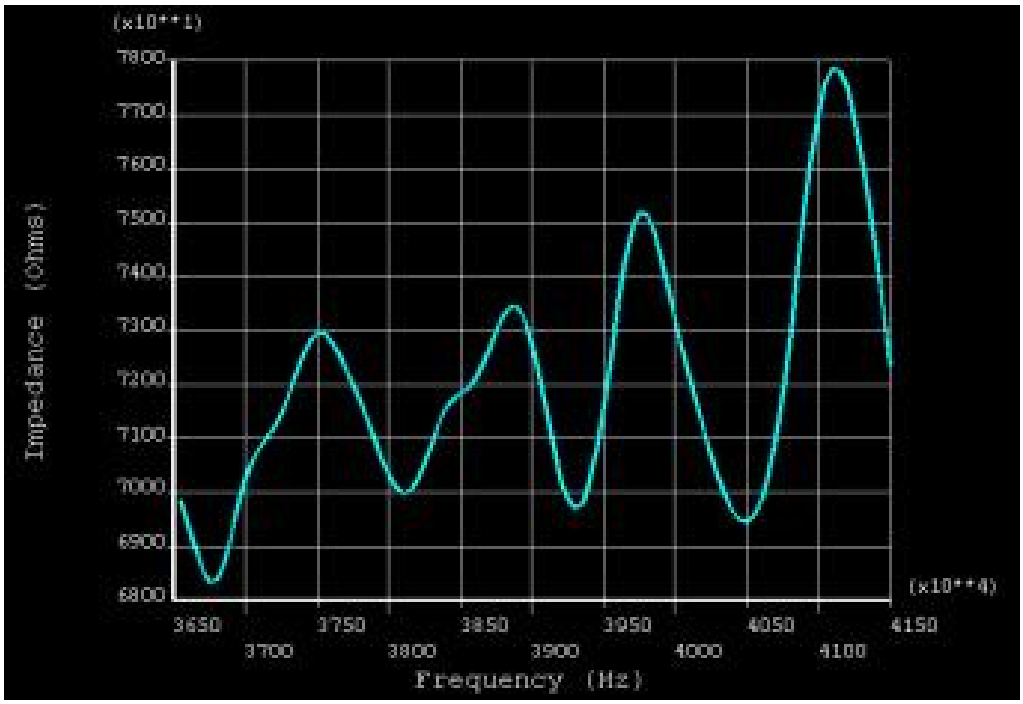

Figure 6-3 The predicted impedance plot for a surface wave device when the thickness of the substrate is 100 μm and the period of the electrodes generating the wave is also 100 μm. When the thickness of the substrate is the same the wavelength, several plate type resonances are seen.

As the thickness of the lithium niobate exceeds 2 wavelengths a single distinct resonance is seen at approximately 39 MHz. The impedance plot is consistent as the thickness of the substrate increases further, which matches well with the theory of a pure surface wave being generated once the thickness of the substrate is sufficient.

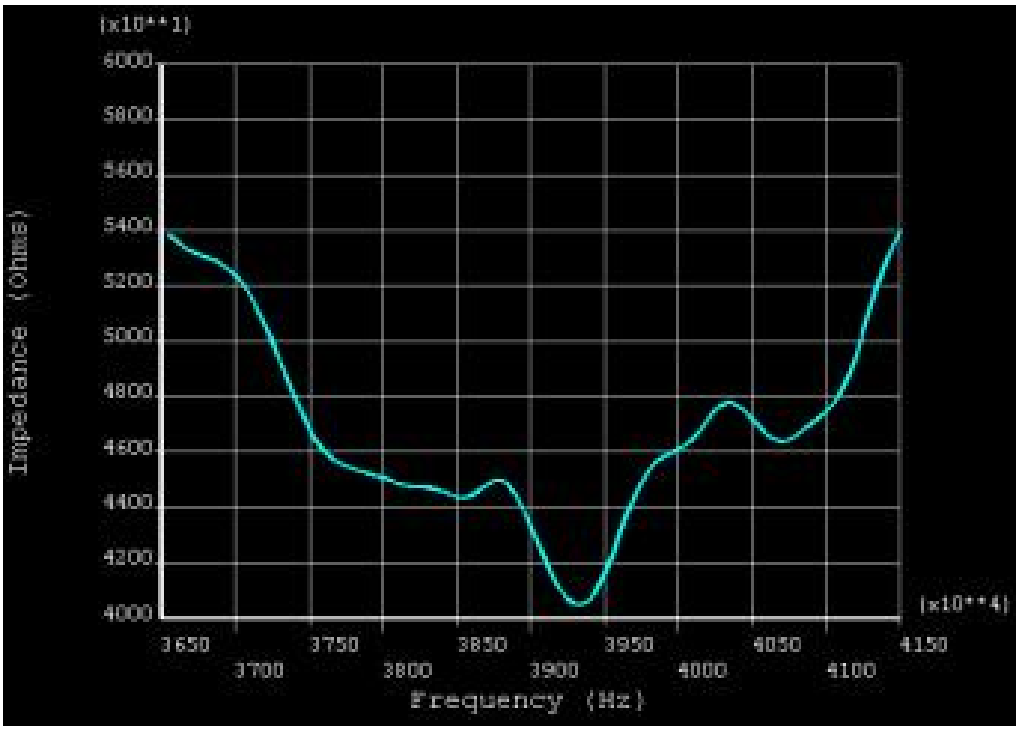

Figure 6-4 The predicted impedance plot for a surface wave device when the thickness of the substrate is large compared to the generated wavelength. When the thickness of the substrate is sufficiently thick, a surface wave is generated and the plate wave type resonance is no longer seen.

6.1.1.2 Multiple Wavelength Changes In Transducer Width

The next stage of the study looked at how the width of the lithium niobate affected the resonance. This was carried out to investigate if reflections of waves would be an issue. Initially, a 2 mm wide and 500 µm thick piece of lithium niobate was modelled, before increasing the width in 1 mm jumps. This corresponds to 10 λ steps, whilst this is quite high; this investigation was into macro changes of scale. The electrical impedance of the device was modelled and compared for a series of different device widths.

When the width of the lithium niobate is small, reflections from the boundaries affect the resonance of the substrate causing a narrow and more pronounced resonance, see Figure 6-5. This is because the wave must culminate in a velocity anti-node at the edge of the substrate. As the width of the transducer increases a more broadband response is seen as the wavelength has the opportunity to expand or contract whilst staying within the confines of the excitation fingers and producing a velocity anti-node at the edge of the substrate. This eventually leads to more than one resonance being present on the impedance plot, see Figure 6-6. This is the expected response and helps verify that the model is working correctly.

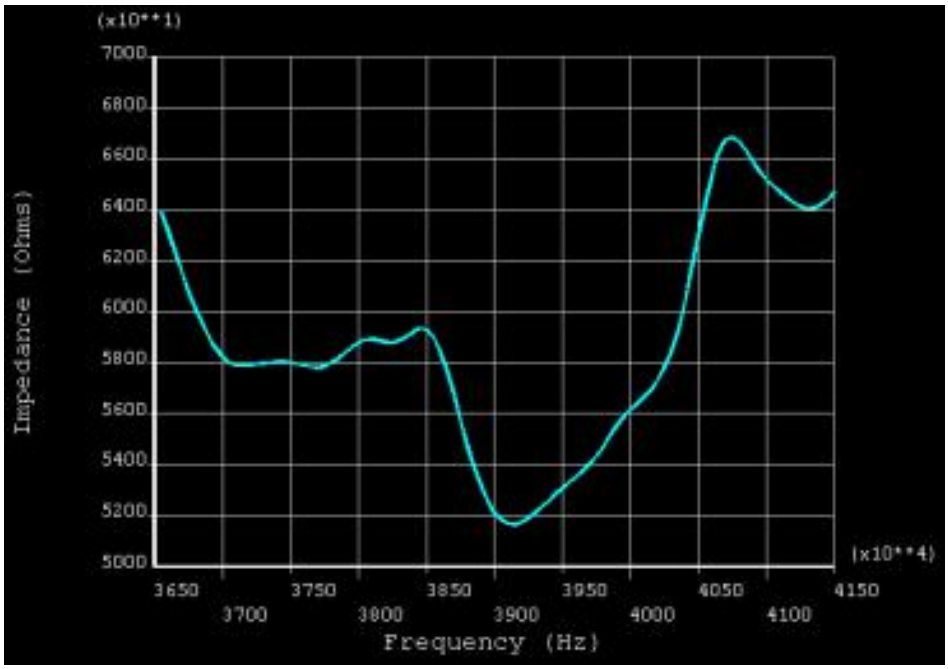

Figure 6-5 The predicted impedance plot for a surface wave device when the width of the substrate is only 5 times larger than the generated wavelength. A single distinct resonance is predicted.

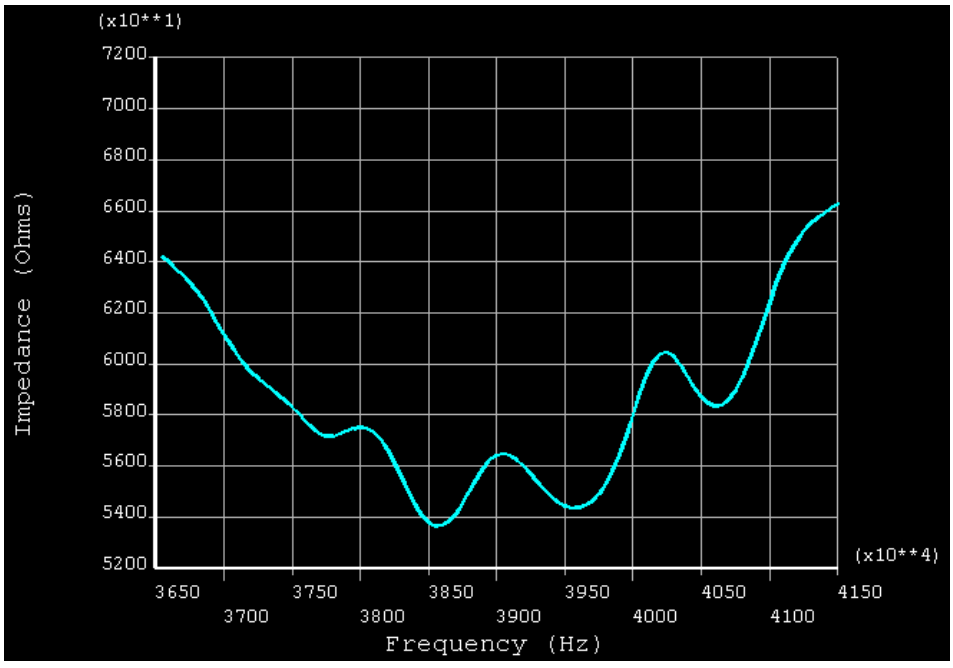

Figure 6-6 The predicted impedance plot for a surface wave device when the width of the substrate is more than 10 times larger than the generated wavelength. Multiple resonances can be seen and a more broadband response. This is because the wavelength has space to expand or contract whilst still keeping a velocity node at the end of the substrate.

6.1.1.3 Sub Wavelength Transducer Width

The models assumed that a perfect number of wavelengths would fit onto the surface of the lithium niobate. In reality, when the lithium niobate chips are cut they will not be a width equal to an integer number of the designed wavelength. To model this, the width of the transducer was increased in 0.1 λ steps and the electrical impedance plots compared. A 4 mm wide, 500 µm thick piece of lithium niobate was modelled. The width of the lithium niobate was increased in 10 µm steps, corresponding to 10% of the intended wavelength. The initial 4 mm was chosen so that the electrical impedance plots would show distinct resonances. The impedance plots showed small variations in the impedance minimum, Figure 6-7. This implies that the device will be robust to slight variations in its width due to manufacturing tolerances. More interestingly, each impedance plot showed 2 or 3 resonances between 37.5 MHz and 41.5 MHz, which is again down to the contracting and expanding of the wavelength within the confines of the substrate and electrodes.

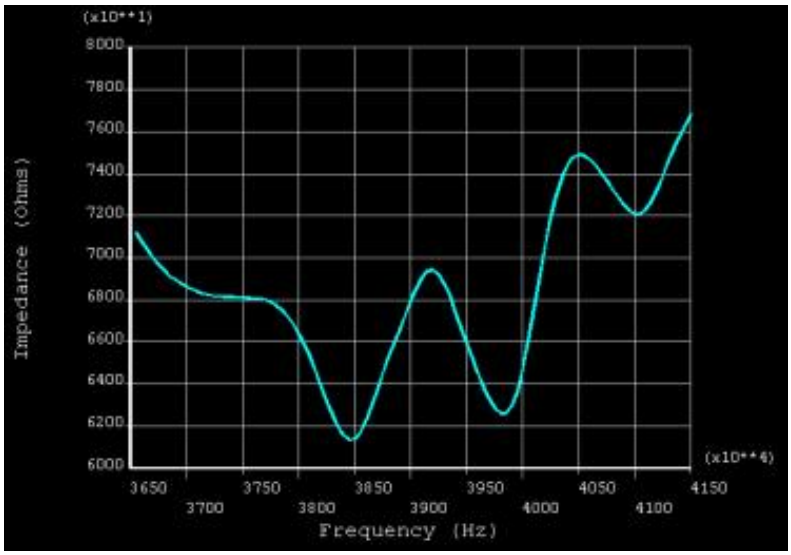

Figure 6-7 The impedance plot for a 4.02 mm wide lithium niobate transducer, multiple resonances are seen corresponding to small changes in the wavelength that still results in a velocity node at the edge of the substrate.

This means that the standing wave on the surface of the substrate is able to contract or expand, enabling a complete number of half wavelengths to fit. The resonances appear when a displacement maximum occurs at the edge of the substrate. The resonances from each width were plotted on a single graph; a general resonance trough can be seen, showing small variations in the width of the lithium niobate will not affect the ability to find a resonance, Figure 6-8. This plot illustrates the robustness of the device in terms of sub wavelength variations in its width.

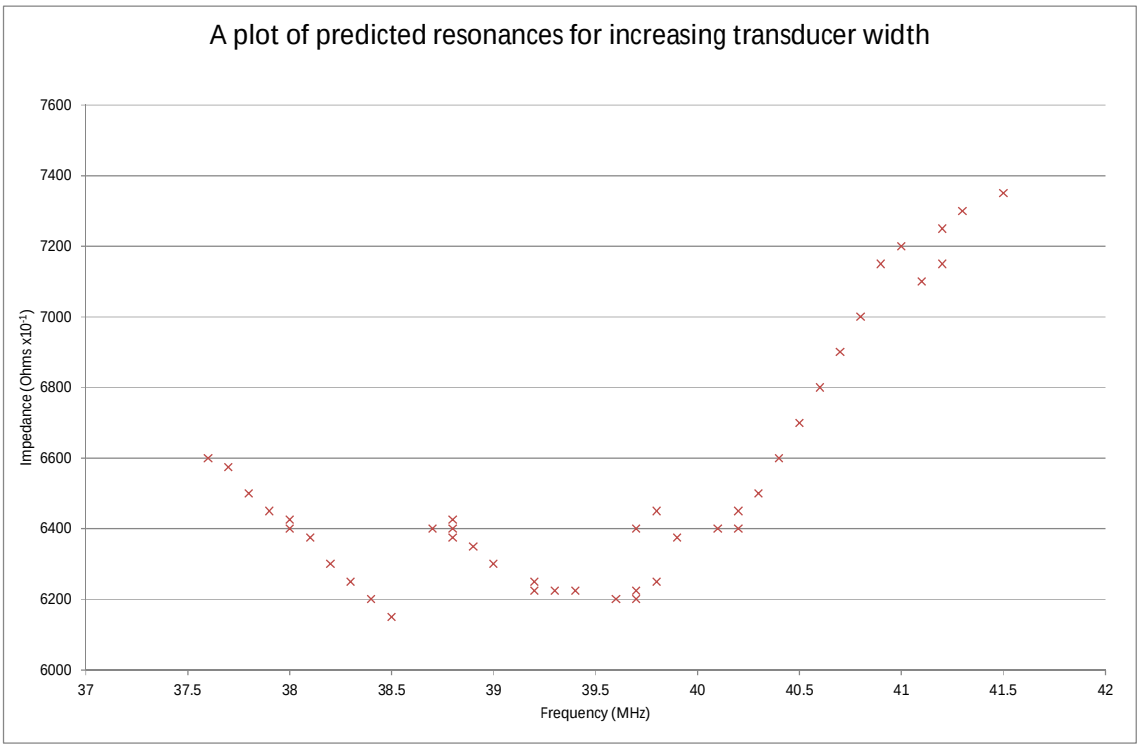

Figure 6-8 A graph showing all of the impedance minima predicted by varying the width of the lithium niobate by 1/10 λ.

As the resonant frequency of the device shifts to allow complete half waves to form, the wavelength must expand or contract. As the interdigitated electrode spacing is pre-determined, this means that wavelengths do not always fit perfectly into the fingers. This causes an overall impedance minimum at 38.5 MHz, and all the points either side are moving away from the perfectly fitting wavelength/electrode spacing combination. This matches well with the 38.2 MHz resonant frequency given by Shi et al, (Shi et al., 2008). The position of maximum displacement must shift slightly from the centre of the electrode finger towards its edge. The direction it moves will be dependent on whether the wavelength is contracting or expanding. This model shows that the wave must end at a velocity maximum at edge of the substrate.

Reflections of SAW waves can be reduced in several ways. By cutting the lithium niobate at an angle reflections can be directed away from the area of interest. The addition of an acoustically absorbent material at the edge of the lithium niobate will also help (Soluch, 1998). It is also possible to add passive electrodes to the device, which will convert mechanical energy back into electrical energy.

If a higher Q factor is required, more fingers can be added to the IDT. This would make it more difficult for the wavelength to expand or contract whilst keeping all displacement maxima within the bounds of the electrode fingers. Conversely, reducing the number of electrode fingers will give a more broadband response. Fewer fingers

allow the wavelength to expand or contract more whilst remaining in the constraints of the electrodes.

6.1.1.4 PDMS Layers

The modelling so far has investigated the behaviour of a free lithium niobate transducer with interdigitated electrodes producing a standing surface wave. For particle manipulation to take place, the energy of the surface wave needs to be directed into a fluid channel or chamber. For many microfluidic applications this is PDMS, and is the material most commonly associated with SAW particle manipulation devices. Further information on PDMS can be found in section 3.2 Polydimethylsiloxane (PDMS).

The presence of a block of PDMS between the electrodes was modelled and the effect on the behaviour of the device is investigated. The PDMS will load the lithium niobate due to the very low sound speed of PDMS, (Tsou et al.). The first part of this study changed the height of the PDMS from 1 mm to 2 mm, Figure 6-9 and Figure 6-10. There should be little difference in the response as the height of the PDMS is large compared to the SAW wavelength, see section 2.1.2.4 Interface Waves for further information. Initially, the PDMS was positioned between the 2 sets of electrodes without overlapping them. As expected, doubling the height of the PDMS had little effect on the resonant frequency or impedance. This was the case for several widths of PDMS, including cases where the PDMS overlaps the electrodes. Making the PDMS thicker had little effect on the magnitude of the displacement of the surface of the transducer.

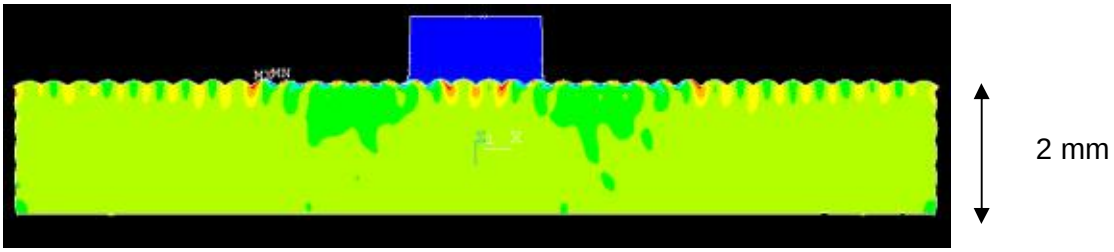

Figure 6-9 An ANSYS plot showing predicted displacements when a 1 mm thick PDMS layer is coupled with a lithium niobate transducer.

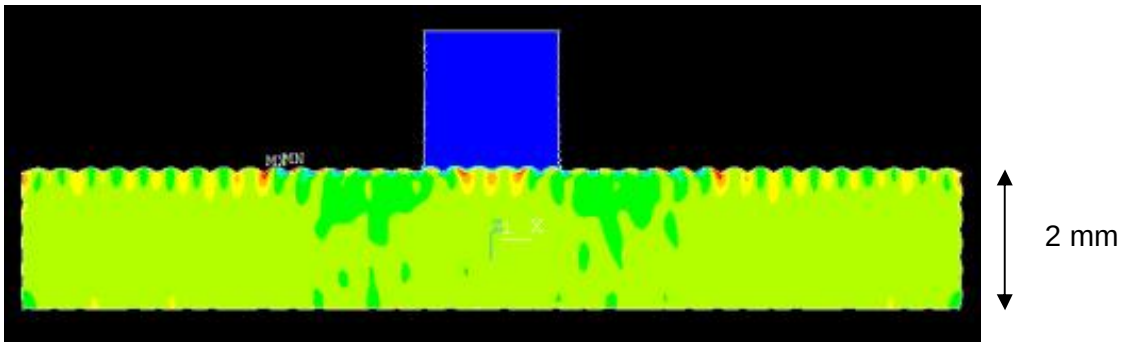

Figure 6-10 An ANSYS plot showing predicted displacements when a 2 mm thick PDMS layer is coupled with a lithium niobate transducer.

The next part of the study looked at how the width of the PDMS affects the SAWs. To do this, a 1 mm thick piece of PDMS was modelled on a 2 mm thick piece of lithium niobate. The width of the PDMS was increased in the following step size; 0.8, 1, 2, 3, 5, 9, and 13 mm. Theory suggests that increasing the width of the PDMS will have a damping effect on the SAW, see Section 2.1.2.4 Interface Waves. This damping effect was seen in the modelling as the width of the PDMS increased, Figure 6-11.

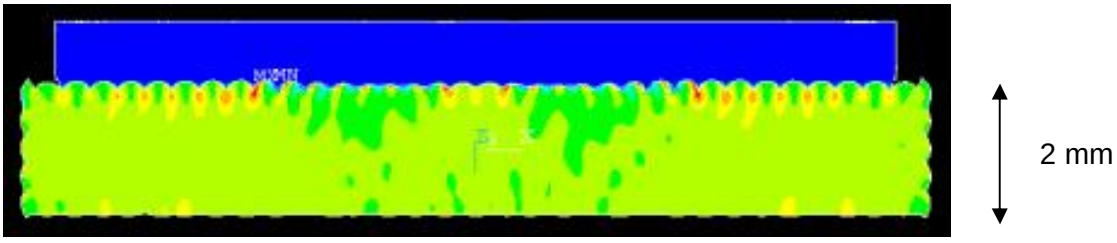

Figure 6-11 An ANSYS plot showing predicted displacements when a 1 mm thick PDMS layer is coupled with a lithium niobate transducer. Once the wave front leaves the interdigitated electrodes they begin to attenuate. This is shown by the maximum displacement depicted by MX.

The modelling so far has verified the presence of a surface like wave on a 2 mm thick lithium niobate transducer with behavior that matches well with what would be expected from theory. The addition of a PDMS layer causes a reduction in the magnitude of displacement but has little effect on the frequency response as the behaviour is dominated by the lithium niobate. Increasing the height of the PDMS has little effect, which is expected as the modelling only investigated multiple wavelength heights of PDMS, as it will be difficult to manufacture PDMS layers thinner than this. As expected, increasing the width of the PDMS increased the damping of the SAW. The work so far has matched well with theory and has shown that the device will be robust to small changes in the width of components. It is now of interest to investigate the mechanism behind the device shown by Shi et al.

6.1.1.5 Mechanism

The work by Shi et al puts forward the idea of diagonally propagating waves from the corners of the fluid channel at the PDMS/transducer boundaries. There are two main reasons why this cannot be the mechanism behind the particle focussing seen in the device. Using Equation 2-73 from Section 2.1.2.2 Leakey Rayleigh Waves it is possible to calculate the angle at which the acoustic wave would be projected into the fluid.

$$sin\theta = \frac{C_F}{C_R}$$

Repetition of Equation 2-73

where C_R and C_F are the Rayleigh wave speed of the lithium niobate and the speed of sound in water. These are equal to approximately 3980 and 1500 m s^{-1} respectively. This gives a propagation angle of 22 ° from perpendicular to the surface in the direction of the travelling wave. If this were the case, the waves would not interfere with each other within the fluid chamber.

The other reason that the focussing is not caused by a diagonal propagation of waves is that this would not lead to a single beam of particles forming in the channel as more than one pressure node would be present in the channel. The frequency of excitation in the Shi device is 38.2 MHz, equalling a wavelength in un-damped lithium niobate of approximately 100 µm. If the wave was coupling diagonally across the fluid chamber, the wavelength would be equal to 40 µm, meaning several pressure nodes would form across the device at 20 µm intervals. If the wavelength of the diagonally coupled wave was equal to that of the lithium niobate rather than the water, there would still be four pressure nodes found in the cross section of the fluid channel.

For one beam of particles to form within the channel, the mechanism must be dominated by the lithium niobate with the PDMS being compliant to the surface wave. To investigate this disparity the model was adapted to include a 200 µm square fluid channel, Figure 6-12.

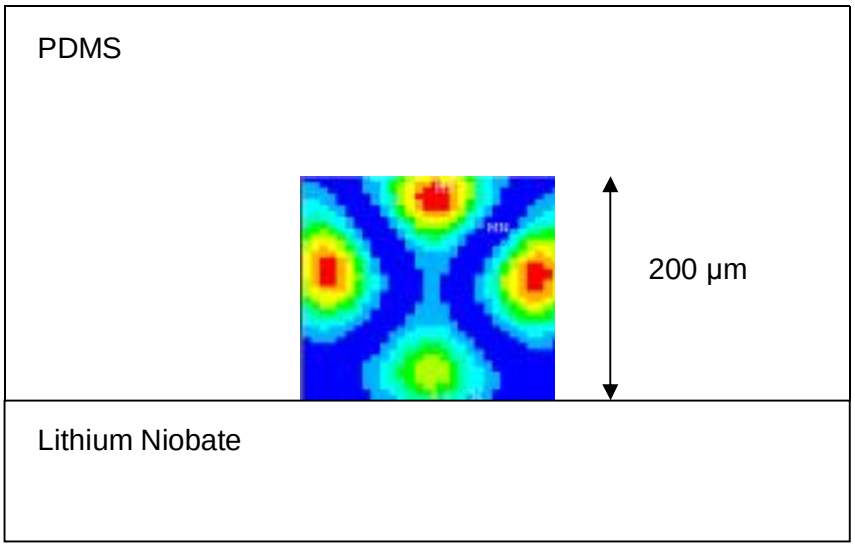

Figure 6-12 An ANSYS plot showing the predicted force profile for a 200 µm square PDMS fluid channel coupled with a lithium niobate SAW device operating at approximately 9.5 MHz. Red areas indicate areas of high pressure and dark blue areas indicate areas of low pressure. There are nodes coupled from top to bottom and side to side of the fluid channel. This would cause particles to move away from the channel walls into the middle of the channel.

The modelling shows that a half-wavelength type mode is generated between the top and bottom of the channel and between the two sides of the channel. Animations show that the top and bottom of the fluid channel deform into the fluid channel in unison. The sides of the channel are also synchronised but are out of phase with the top/bottom deformations, Figure 6-13.

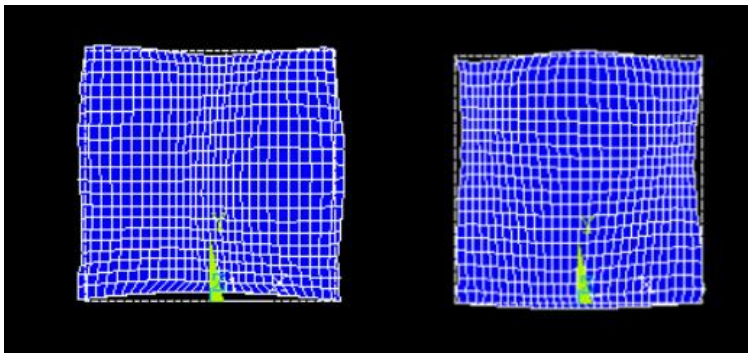

Figure 6-13 Screenshots of an Ansys animation of the fluid channel deforming under the presence of a standing surface wave.

The fluid is able to deform more than the PDMS, which causes an effective velocity anti-node in the centre of the channel. Because the PDMS is able to deform so much, a proper standing wave is not set up across the width and height of the device.

Whilst the PDMS is not an efficient material to be coupled to a surface wave, its ability to deform allows a focusing mode to be generated.

To investigate this further, a stiff plastic, COC was modelled, but no such particle focusing mechanism could be found. As the resonance is based strongly on the properties of the lithium niobate, the polymer channel must be compliant for any type of particle focussing to occur. Because the resonance is based on the transducer, differences in the speed of sound of the fluid should have less of an effect than in a bulk acoustic device. This is highly desirable for an ultrasonic particle manipulator intended to be used in a wide range of oceanographic environments.

6.1.1.6 Conclusions

Modelling has matched well with what theory predicts in terms of how the wave behaves as the dimensions of the lithium niobate changes. The effect of adding PDMS to the lithium niobate acts to damp the amplitude of the deformations but doesn't have significant effects on the frequency of excitation, as the PDMS is a very compliant material. Further modelling gave insight into how particles can be focussed in the centre of a fluid channel. It showed that the mechanism is dominated by the properties of the lithium niobate and that the fluid channel deforms in such a way to create a pseudo half wave from top to bottom and from side to side. This means that the properties of the fluid will not have a significant effect on the resonant frequency.

6.2 Manufacturing

A standard cut of lithium niobate, Y+128˚ was used for the initial SAW devices. The initial 2 mm wafers were patterned with 20 nm Cr, 200 nm Au and then 20 nm Cr. Square PDMS fluid channels were cast in micromilled PMMA molds. The following sections will present different manufacturing techniques trialled in the production of a SAW device.

6.2.1 Chemical Bonding

The chemical bonding method suggested by Sofla et al was attempted as this would be the easiest method for aligned bonding (Sofla and Martin, 2010), see Section 3.2.2.3 Chemical Bonding. Drops of tridecafluoro-1,1,2,2-tetrahydrooctyl were placed in an air tight container along with a lithium niobate chip with an aligned PDMS fluid channel. Several attempts were made but no bonding was seen. The following steps were carried out to establish why the technique was unsuccessful.

- *Thinner PDMS*. The bonding mechanism requires the diffusion of the chemical through the PDMS to the interface. Diffusion will occur quicker in thinner PDMS. 250 µm pieces of PDMS were tested.
- *Bond the PDMS to Glass*. The method described bonds PDMS to glass so this was carried out to try to verify the paper.
- *Reduce the surface roughness of the PDMS*. The PDMS was cast in a micromilled PMMA mold. The surface roughness was visible by eye. PDMS was cast on smooth glass slides before attempting the vapour bonding technique.

Even with these changes, no bonding was seen between PDMS and ceramic substrates. The only other difference was the type of PDMS being used. For these experiments, Sylgard 184 from Dow Corning was used but in the paper pre-fabricated strips of BISCO HT-6240 silicone were used. As the chemical bonding method was unsuccessful, the oxygen plasma technique will be used to bond the PDMS fluid channels to the lithium niobate chips.

6.2.2 Oxygen Plasma Bonding

See Section 3.2.2.1Oxygen Plasma Bonding for information on the theory of oxygen plasma bonding. Initial attempts at oxygen plasma technique were unsuccessful. Bonding was attempted under vacuum and a variety of different times were trialled from 15 s to 60 s however it was not possible to completely bond the PDMS to the lithium niobate. It was thought this was partly due to the surface roughness of the PDMS. This surface roughness comes from the micromilled PMMA mold. To reduce the surface roughness of the cast PDMS, the PMMA mold was treated with chloroform vapours in a technique shown by Ogilvie et al (Ogilvie et al., 2010). The chloroform causes the surface of the PMMA to reflow, smoothing out the effects of micromilling (Ogilvie et al., 2010). Smoothing the PMMA molds did help to improve the bonding of PDMS to lithium niobate, however complete bonding did not occur.

To understand why complete bonding did not occur, a series of trials were carried out. To begin with, a study was carried out comparing bonding of PDMS to lithium niobate and to glass. The substrates were rinsed with acetone, isopropanol alcohol then methanol. The PMMA mold was also rinsed in the same solvents. The substrates and molds were dried using an air gun. PDMS pieces were prepared according to the manufacturer's instructions. Each substrate PDMS pair was subjected to 30 s of oxygen plasma before being brought into contact. The pieces were placed on a hot plate at 80 °C for 5 minutes. Qualitative observations showed that bonding between the PDMS and borosilicate glass was more successful than between PDMS and lithium

niobate. Complete bonding was attainable between the PDMS and glass but this was not achieved with the PDMS and lithium niobate.

One potential reason for this could be the availability of hydroxyl (OH) pairs in the borosilicate glass being greater than that of the lithium niobate. It is known that OH pairs play an important part in oxygen plasma bonding and that OH pairs are found on the surface of borosilicate glass, (Schott, 2014, IMSLab, 2010). Little information is available on the availability of OH pairs on the surface of lithium niobate which implies that they are either not present, or less prevalent. If this is the case then the understood mechanism for oxygen plasma bonding would not be as effective.

The process was repeated, but with a 30 s delay between removing the pieces from the chamber and contact being made between the PDMS and the substrate. This was to simulate the time taken to align the PDMS on the lithium niobate. This reduced the area of the PDMS that was able to make a complete bond with each substrate. This matches well with theory, which suggests that over time the OH groups on each surface have time to recover hydrophobicity, (Owen, 2005).

Various other parameters were investigated; one limiting factor identified was over curing of the PDMS. The longer PDMS is allowed to cure, the more interlocked and stiff the piece becomes. This means the piece is less able to flow to ensure full contact with the substrate. There will also be fewer Si-CH_3 pairs available to convert into Si-OH pairs. Several tests were carried out and it was possible to reduce the curing time to 60 minutes at 65 ˚C. The PDMS forms a solid elastomeric mass but is slightly tacky to the touch. The PDMS continues to cure even when removed from the oven, it is important to perform the oxygen plasma technique as soon as possible once removed from the oven.

The amount of time the PDMS is exposed to the plasma was also investigated. Samples were treated for 15, 20, 25, and 30 s. Each test was carried out on glass and lithium niobate. Bonding was improved with shorter exposure times, and complete bonding of PDMS to lithium niobate was possible with an exposure of 20 s.

Aligning the PDMS channels proved difficult, several attempts at using a solvent to prolong the hydrophilic nature of the PDMS were made. Methanol acted to prolong the hydrophilic nature of PDMS and lithium niobate that had undergone oxygen plasma technique and it was possible to produce a SAW device.

6.2.3 Spin Coating

Because of the difficulties in aligning a fluid channel on a lithium niobate transducer, novel ideas for the construction of such a device were investigated. One

method investigated adapted the method described by Unger et al, (Unger et al., 2000). The group used partially cured PDMS pieces of very different compositions, 30:1 and 3:1, to be brought into contact. The excess components found in each piece diffuse across the interface forming permanent bonds.

To adapt this for use in SAW devices, the least viscous part (3:1) was spin coated onto the SAW devices, see Section 3.3.2 Spin Coating for further information. Partially cured PDMS (30:1) was brought into contact and aligned. The entire piece was then cured for several hours. Channel alignment is not difficult to achieve. The final bond was stronger than just placing PDMS on a cleaned SAW device. The bond was comparable with the oxygen plasma technique, consistent across the entire substrate and the process was easily repeatable.

Earlier computational modelling predicted that the effect of PDMS over the IDT's would not have a substantial effect on the behaviour of the free transducer. This was based on PDMS layers of over 1 mm thick. The predicted thickness of the PDMS is less than 20 µm and will therefore have less of a loading effect on the SAW.

6.2.4 Conclusions

Several methods for the bonding of PDMS channels to lithium niobate have been investigated, two of which were successful; oxygen plasma and spin coating PDMS. Oxygen plasma bonding is more difficult to achieve and is likely to result in areas without complete bonding. In many cases this does not affect fluid flow through the device. The spin coating technique allows for the easy alignment of fluid channels and complete bonding is easier to achieve. The bond strength is lower than the oxygen plasma technique and the presence of a thin layer of PDMS within the fluid channel may affect the behaviour of the device.

6.3 Experiments

Experiments were carried out on the finished devices, with the aim of verifying the modelling and replicating the work by Shi et al, (Shi et al., 2008). From here it was hoped that the design could be optimised for use in an oceanographic environment and that the mechanism proposed by the modelling could be investigated.

6.3.1 First Generation Devices

The first generation of devices had IDT's deposited onto 15 x 15 mm lithium niobate chips. Two different designs were made, with long and short finger lengths of 2

and 3 mm respectively. Figure 6-14 shows the two different devices. Two sets of IDT's can be seen either side of the fluid channel, each IDT consisting of 7 electrode pairs. Each electrode finger is a quarter of a wavelength wide along with the spacing between electrodes.

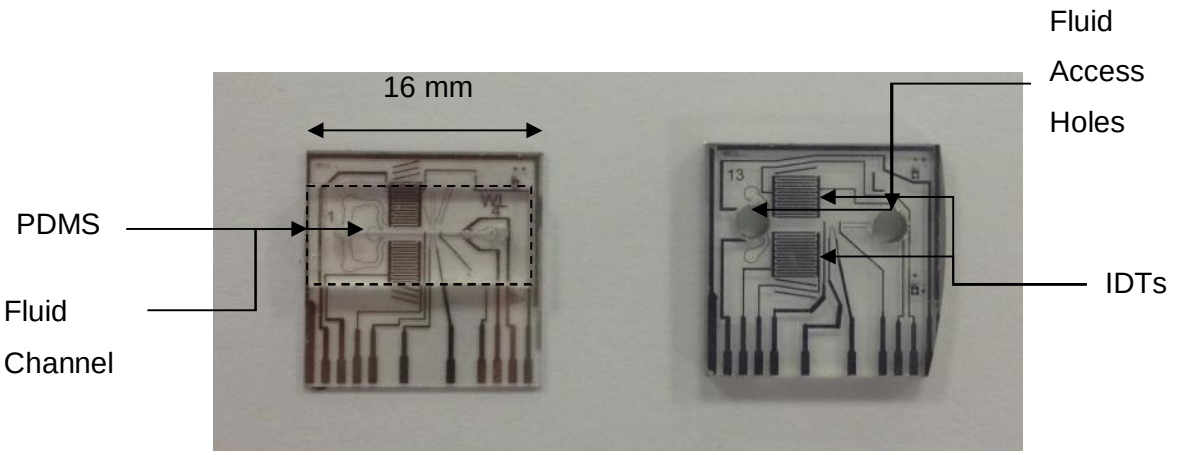

Figure 6-14 An image of the two different first generation devices. The device on the left shows the PDMS fluid channel positioned between the two sets of IDTs.

Fluid connectors were glued in place and the devices were wired to a signal generator and oscilloscope. The devices exhibited a relatively broadband response, with 10 impedance troughs between 9.4 and 9.95 MHz. This is the response expected given the relatively low number of electrode fingers.

A solution of 10 µm fluorosphere beads was passed through the device and the IDT's were excited at the impedance minimum of the device, found using an oscilloscope. The excitation voltage was increased from 2 to 40 V_{pp} but no particle focusing was seen in the fluid channel. At higher voltages, acoustic streaming was observed in the fluid channel.

The device shown by Shi et al had one major difference in that the PDMS channel did not overlap the IDT's. Whilst the modelling predicted that the presence of PDMS over the IDT's would not adversely affect generation of a SAW, it was thought this could be reducing the amplitude of the generated SAW. A second PDMS mold was designed that reduced the width of the PDMS over the IDTs. Further experiments were unable to generate particle focusing within the fluid chamber.

6.3.2 Second Generation Devices

Due to the difficulties in generating a particle focussing mode in the SAW device, a simplified 2nd generation device was designed. The new device was designed to have parallel pairs of electrodes for each electrode finger rather than one solid finger. This is

to reduce the effect of reflections and was discussed in Section 2.1.2.7 Generation of Surface Waves. The devices also had 10 mm long electrode fingers and a series of parallel electrodes specifically to absorb travelling waves heading away from the fluid channel. An image of the device is shown in Figure 6-15. Each set of IDTs had 18 electrode pairs so a narrow band response is expected. The design also removed all ancillary µ-flow cytometer circuitry.

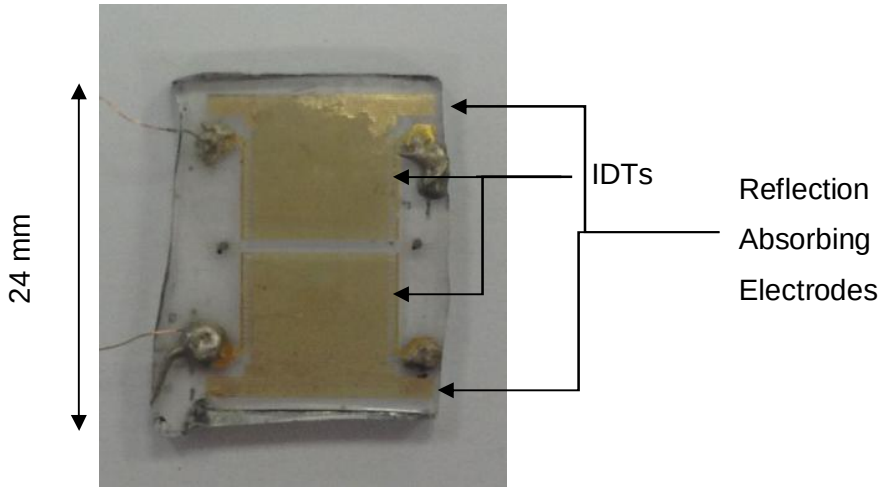

Figure 6-15 An image of the second generation SAW device.

Devices were created using the oxygen plasma technique and the spin coating technique. The devices were connected to a signal generator and impedance analyser as before, this time only 6 impedance troughs were identified, between 9.505 and 9.754 MHz. A solution of 10 µm fluorosphere beads was flowed through the device and the chips were excited at minimum impedance. No lateral particle motion was seen as the voltage was increased from 2 to 40 V_{pp}. Again, acoustic streaming was observed at higher voltages and was seen in both the oxygen plasma device and the spin coated device.

6.3.3 Conclusions

Experiments were unable to generate a particle focussing mode using surface acoustic waves. Two different devices were tested but only acoustic streaming was observed. Acoustic streaming was seen in the devices made using the oxygen plasma technique and the spin coating technique. This suggests that the addition of a thin PDMS layer at the bottom of the fluid channel does not drastically alter the characteristics of the surface wave. This would mean that the spin coating method for

attaching the fluid channel is a novel and easy technique for the construction of particle focussing SAW devices.

Chapter 7 Conclusions

This chapter presents a summary of the experimental work discussed in Chapters 4, 5 and 6. The novel aspects of the work will be discussed along with any potential advantages. The chapter concludes by identifying potential areas for further development and highlights other challenges this would present.

7.1 Bulk Acoustic Wave Devices

This work on bulk acoustic wave devices has proven two novel ideas in ultrasonic particle manipulation. This work is the first time that planar polymer particle focussing devices have been developed. This work has developed the capabilities of ultrasonic particle manipulation devices to be integrated with lab-on-a-chip style devices, which are almost always produced in polymers. The work has also developed a novel transparent particle focussing device that uses lithium niobate in a bulk acoustic wave set up.

Conventional ceramic bulk acoustic devices tend to require expensive and time consuming manufacturing techniques. Producing repeatable devices is difficult to achieve meaning each device has unique characteristics. They can also be sensitive to small changes in the setup, causing erroneous results. For ultrasonic particle manipulation devices to be used more widely in laboratories they need to be repeatable, robust, easy to use and ultimately they need to be cheap.

7.1.1 Polymer Devices

Polymer devices are not generally used as ultrasonic particle manipulation devices due to the higher associated losses. The work presented in this thesis shows that it is possible to design effective devices in polymers. The work has shown that by designing devices that operate at a frequency close to that of the free transducer, it is possible to generate forces within a fluid channel comparable to a typical ceramic device.

The work identified the possibility of designing sub half wavelength fluid channels. The acoustic impedance of PMMA and water are similar which allows any portion of a standing wave to be set up across a fluid channel. This differs from traditional ceramic devices where an exact half wavelength is designed for across the fluid channel. There are several advantages to producing sub half wavelength devices:

- Robustness to changes in the fluid properties
- Significant forces at the fluid/solid interface
- Robustness to variations in the layer thickness

As the resonance is dominated by the entire device, rather than the fluid channel, changes in the fluid properties have a smaller proportional effect. The properties of the fluid can change substantially without adversely affecting the forces generated in the fluid channel. When an exact half wavelength is set up across the fluid channel, small changes to the operating frequency are likely to cause a pressure anti-node to form in the fluid channel, which would be detrimental to the performance of the device. In these polymer devices less than a half wavelength is set up in the fluid channel. As a result, changes to the operating frequency, caused by changes in the fluid properties, will not be enough to generate a pressure anti-node in the fluid channel.

When an exact half wavelength is set up in the fluid channel, the forces at the solid/fluid interfaces are zero. Close to the solid/fluid interfaces the acoustic forces on a particle are small. Some particles may not experience enough force to move to the pressure node in the middle of the channel. In the polymer devices where less than a half wavelength is set up, the forces generated at the fluid/solid interface are non-zero. In an optimal design, a quarter wavelength is set up across the fluid channel with a centralised pressure node. In this configuration, the forces generated at the fluid/solid interfaces are maximised.

Designing sub half wavelength PMMA devices brings advantages in repeatability. In more common ceramic devices the manufacturing techniques used lead to significant variations between devices. This leads to significant variations in the forces generated in different devices and the operating frequency. There is also the possibility of anti-nodes forming within the fluid channel. By designing a sub half wavelength device, the chances of an anti-node forming in the fluid channel are reduced.

Designing sub half wavelength devices in polymers is a novel approach in ultrasonic standing wave devices. The devices are low cost, quick to make and bring advantages in terms of the forces exerted on particles at the solid/fluid interface. Previous work by Harris et al (Harris et al., 2010) generated a sub half wavelength planar resonance, however, this was a side effect of the design of an exact half wavelength lateral mode. Glynne-Jones et al (Glynne-Jones et al., 2009) used a similar technique to produce a device capable of moving particles to the reflector. This work differs in that a centralised planar pressure node in the fluid channel was generated. The force exerted on particles was maximised by matching the resonance of the device

to that of the free transducer. The device was also designed to be robust by deliberately moving away from a perfect half wavelength mode.

Another important aspect of designing devices in PMMA is the high level of repeatability. In traditional ceramic devices each device tends to have unique characteristics. In recent years this has been improved through the use of off the shelf components such as glass capillaries. However, such components may not always be suitable for the applications required by the user. By using ready-made PMMA films, it would be possible to incorporate planar particle focussing with complex channel geometries. Due to the repeatability in the thickness of the PMMA films it would also be possible to make significant numbers of these devices, each with the same characteristics.

Another advantage of using PMMA films is the ease with which they can be produced. It is possible to build a batch of devices and have them working in a lab on the same day. Trying various similar designs is possible as the most basic designs can be hand made using a scalpel. The use of PMMA sheets also lends itself to laser cutting, which allows complex channel geometries to be made. All of these techniques are quicker and, perhaps more importantly, cheaper than the techniques required for traditional ceramic devices.

7.1.2 Lithium Niobate Devices

The use of lithium niobate as a bulk acoustic wave transducer is a new idea in ultrasonic particle manipulation. In general, PZT transducers are used for bulk acoustic wave devices and lithium niobate for surface acoustic wave devices. Lithium niobate brings advantages for the user because of its transparency. Some biological applications may require transmission microscopy which is not always possible when a PZT transducer is used. It is possible in wedge transducer designs but this style of device tends to have narrow fluid channels.

This work has coupled the transparency of lithium niobate with an ITO film to produce a device that is compatible with transmission microscopy and multiple wavelength fluid channel widths. The novel transducer/electrode combination was used with the PMMA particle focussing devices and was able to generate comparable forces on a 10 μm diameter polystyrene bead. The thickness of the ITO film could be increased to reduce the resistance at the expense of a lower optical transmittance. This is a novel piece of work that increases the number of applications for which ultrasonic standing wave technology could be used.

7.2 Biofouling

Biofouling is one of the main constraints on the working life of oceanographic sensors for two main reasons:

- The physical presence of the film will reduce fluid flow and could potentially cover sensing surfaces.
- The biological presence of the film will affect the readings taken through the uptake and release of chemicals.

This work has presented a novel and low power method to reduce the formation of biofilms in microfluidic channels. Several aspects of this work have improved the capabilities of ultrasonic particle manipulation techniques. Before this work, attempts to use ultrasonic techniques to reduce biofouling relied on high power acoustic streaming used over short timescales to actively lift adhered bacteria. Using continuous low power excitation is a novel approach.

The initial biofouling experiments showed a qualitative reduction in the formation of biofilms in traditional ceramic devices. The experiments ran for a long time compared to the type of experiments usually undertaken using ultrasonic particle manipulation. This was made possible by using a frequency sweep centred over the minimum measured impedance. This ensured that the device was always excited at its optimal frequency regardless of external temperature variations, heating or other factors that could change the acoustic impedance.

The use of ultrasonic standing wave technology was tested in specially designed polymer chips. This proves that it is feasible for ultrasonic techniques to be used to reduce biofilm formation in an oceanographic sensor. A simple quantitative method was used to confirm a significant reduction in biofilm formation and calculations showed that it was a low power technique with noticeable reductions achieved using only 0.025 W. The work also matched well with the modelling, including the presence of an anti-node close to the roof of the fluid chamber. This was shown by higher concentrations of bacteria in the higher powered chip.

Finally, a series of experiments were carried out using polymer slide devices. These devices were proven to focus particles at comparable input powers to traditional ceramic devices. They also had advantages in terms of robustness which has already been discussed. The use of these slides in this series of experiments also proved another characteristic of these devices: their repeatability. Throughout these experiments, twelve devices were created that showed very similar acoustic properties. To manufacture twelve comparable devices using traditional ceramic methods would

be difficult to achieve, as minor variations in dimensions causes large differences in the frequency response.

This series of experiments used a thorough image analysis technique to show a reduction in the total number of bacteria and in the actively respiring bacteria. The results showed a general decline as the voltage applied increased which is consistent with theory. The percentage of actively respiring bacteria appeared to reduce as the strength of the acoustic field increased. It was not possible to confirm if this was due to the acoustic forces or natural variations.

The position of the bacteria cells within the fluid channel was biased towards the matching layer which is inconsistent with the modelling. This is probably due to the momentum of the cells as they enter the fluid chamber or small differences in the properties of the PMMA used in the modelling. The methods and analysis used throughout these experiments was robust, detailed and provided significant quantitative evidence that ultrasonic particle manipulation techniques can reduce the formation of biofilms over a relatively long period of time.

7.3 Surface Acoustic Wave Devices

The development of surface acoustic wave devices in recent years is an exciting prospect for ultrasonic particle manipulation techniques. The ability to manipulate particles in two dimensions on such a small scale opens up numerous applications for which ultrasonic techniques could be used. Another advantage of SAW devices is that they primarily use PDMS fluid channels which is the material of choice in microfluidic devices.

The mechanism behind the focussing of particles is not fully understood. To better understand the mechanism computational modelling was carried out in Ansys. Initially, the model investigated how the substrate thickness affected the type of wave being generated; a plate wave or a surface wave. The results matched well with theory and showed the substrate must be at least two wavelengths thick for a surface wave type mode to exist.

The modelling went on to show general characteristics of surface acoustic wave devices, such as how increasing the total width of the substrate results in a more broadband response. It also showed that minor variations in the width of the substrate would not greatly affect the characteristics of the device; this implies that SAW devices are relatively robust against manufacturing variations. The model went on to show the damping effect of a PDMS layer on top of the substrate.

The model matched closely with the expected behaviour of a loaded surface acoustic wave and so was modified to investigate the mechanism that causes particles to focus in a fluid channel. The modelling identified a mode in which the horizontal surfaces of the fluid channel oscillate towards the centre of the channel and then away in unison. This causes the vertical walls of the channel to oscillate away from the centre of the channel and then towards it, also in unison. The compliant nature of the PDMS allows this fluid channel resonance to occur. This creates a half wave type resonance horizontally and vertically.

The work also developed a novel manufacturing technique which allows for the relatively easy production of SAW devices. By spin coating PDMS on to the substrate it is possible to align the fluid channel before curing. If the spin coated PDMS has a low base to curing agent ratio (3:1) and the fluid channel has a high ratio (30:1), the excess agents in each piece will diffuse across the boundary forming a permanent bond. The bond strength was comparable to the oxygen plasma technique and was significantly more repeatable. It was not possible to say if the presence of a thin PDMS layer in the fluid channel affected the performance of the device as none of the devices produced were able to focus particles.

Whilst it was not possible to focus particles in a SAW device there were several aspects that matched well with the modelling. The devices showed impedance minima close to what was predicted in ANSYS. The reason why the devices did not work is not known. One potential explanation could be that the devices had too low a Q factor, in which case more electrodes could be added to make a single distinct resonance. Another reason could be that the overall size of the chip was too narrow and there was too much interference from reflections. The devices shown by Shi et al tend to have a lot more free surface. One other suggestion is the presence of the PDMS over the electrodes damps the wave to such an extent that very little acoustic energy is radiated into the fluid channel.

7.4 Final Remarks

The work undertaken in this thesis has made improvements in the robustness and repeatability of bulk acoustic wave devices by using polymers combined with novel manufacturing techniques. A novel use of lithium niobate as a bulk acoustic transducer was shown which is compatible with transmission microscopy. The mechanism behind particle focussing in SAW devices was investigated and a new manufacturing technique was developed, however, it was not possible to verify the modelling

experimentally. The main aspect of this work is the reduction in biofouling seen in the PMMA devices that were operational for a week.

The biofouling work offers the most opportunity for further development. The reduction in biofouling was impressive but it is expected that further improvements could be made by combining ultrasonic techniques with surface treatments. The efficiency of the devices could also potentially be improved by using different thickness layers such that the force applied to particles is at a maximum at the fluid/solid boundaries. Another area that could be developed is in applying the technique to more complex fluidic systems. The work used straight channels that were well suited to bulk acoustic waves. The addition of reservoirs, bends and contractions in the fluid channel will all add complexity. It would also be of interest to develop the work in other polymers, such as COC and COP, as they are better suited to oceanographic sensing.

For the SAW work to be developed further, a working device is needed. From there it would be possible to verify if the novel manufacturing technique affects the device. It would also allow for the verification of the model. Long exposure images would allow the vertical position of the particle to be calculated and the horizontal position could be directly measured. It would also be possible to alter the properties of the PDMS channel to show that the compliance of the material is one of the reasons that particle focussing is observed in the channel. This could be achieved by altering the ingredient ratios and curing time to produce stiffer PDMS.

In conclusion, several novel ideas have been presented with the aim of creating robust ultrasonic particle devices tailored towards oceanographic sensing. The use of ultrasonic standing wave techniques in polymer devices is a new area and the devices developed are comparable to ceramic devices. The biofouling work is a substantial step towards ultrasonic techniques being used outside of the laboratory environment.

Appendix A

Calculation for the speed of sound in seawater.

Variables are shown in yellow.

Constants are shown in blue.

Formulas are shown in green.

1/A	B	C	D	E	F	G
2	Depth (m)	Latitude (Degrees)			Temperature(C)	Salinity(%)
3	0	0			20	40
4						
5	k1	k2	k3	k4	k5	k6
6	5.01132	-1.27E-02	2.06E-08	-1.05E-08	-5.51E-02	9.54E-05
7						
8	k7	k8	k9	k10	k11	k12
9	2.22E-04	1.332947	1.61E-02	2.12E-07	2.18E-13	-2.25E-13
10						
11	Latitude (Radians)				Pressure(decibars)	
12	"C3*3.141592/180"				"1.0052405*(1+(0.00528)*((SIN(B12))^2))*B3+((0.00000236)*(B3^2))"	
13						
14	Speed of Sound(m/s)					
15	"1402.394+(C9*G3)+(E12*(D9+E12*(E9+((F9*F3+G9*G3)*E12))))+F3*(B6+E6*E12*E12+G3*(C6+D6*G3*E12)+F3*((F6+G6*G3)+B9*F3))"					

Appendix B

Method and Recipe for 3MN Solution

Method

1. Add 920 mL Nine Salt Solution (NSS) to a sterile 1 litre bottle.
2. Add 40 mL 1 M 3-(N-morpholino)propanesulfonic acid **(**MOPS) solution.
3. Add 10 mL 0.4 M Tricine & $FeSO_4$ solution.
4. Slowly add 10 mL 132 mM K_2HPO_4 solution while stirring.
5. Add 10 mL 952 mM NH_4Cl solution.
6. Add 33.3 µL of nutrient solution.
7. Add 9.9667 mL of water.
8. Autoclave

Recipe

Component	Stock Concentration	Unit	Final Concentration	Volume of Stock (mL)
NSS	1.1		1.012	920
MOPS	1	M	0.04	40
Tricine + $FeSO_4$	0.4	M	0.004	10
K_2HPO_4	132	mM	1.32	10
NH_4Cl	952	mM	9.52	10
Nutrients	33333		0.01	0.0333
MilliQ Water				9.9667

Component Recipe

NSS 1.1x	**Major salts (combined)**		23.49	G
	Minor salts		5.50	mL
	MilliQ water		994.50	mL
	Adjust to pH7			
		Major salts		
		NaCl	19.36	G
		Na_2SO_4	1.62	G
		$MgCl_2$	2.06	G
		$CaCl_2$	0.45	G
		Minor salts		
		$NaHCO_3$	8.00	G
		KCl	25.00	G
		KBr	4.00	G
		$SrCl_2$	0.80	G
		H_2BO_3	0.80	G
		MilliQ water	500.00	mL
MOPS 1M	**MOPS**		209.26	G
	MilliQ water		1000.00	Ml
Tricine + $FeSO_4$ 0.4M	**Tricine**		71.67	G
	$FeSO_4$ $7H_2O$		0.28	G
	MilliQ water		1000.00	mL
K_2HPO_4 132mM	**K_2HPO_4**		22.99	G
	MilliQ water		1000.00	mL
NH_4Cl 952mM	**NH_4Cl**		50.92	G
	MilliQ water		1000.00	mL
	Adjust to pH 7.8			
Nutrients 33333x	**Peptone**		50.00	G
	Yeast extract		10.00	G
	MilliQ water		1000.00	mL
	Autoclave			

Appendix C

Method for Staining Cells

1. Add enough 3 mM CTC to fill each channel and incubate at 25 º C for 2 hours.
2. Remove CTC by carefully syringing out of the fluid channel.
3. The channels are washed with sterile MilliQ water slowly so as not to disturb the biofilm.
4. Add enough formaldehyde to fill each channel and incubate at RT for 10 minutes in order to fix cells.
5. Remove formaldehyde by carefully syringing out of the fluid channel.
6. The channels are washed with sterile MilliQ water slowly so as not to disturb the biofilm.
7. Allow the fluid channels to dry out. 30 minutes at room temperature.
8. Add enough 1 µg mL^{-1} DAPI in each channel and incubate at RT for 20 minutes.
9. Remove CTC by carefully syringing out of the fluid channel.
10. The channels are washed with sterile MilliQ water slowly so as not to disturb the biofilm.
11. Allow the fluid channels to dry out. 30 minutes at room temperature.
12. Store fluid channels at 4º C until microscopy is performed.

Appendix D

Example ANSYS code, modelling a piece PDMS on a 2 mm thick wafer of lithium niobate.

```
finish
/clear
/title, Lithium Niobate impedance test
/filnam,lithium1
/UNITS,SI

/PREP7 !define the coordinate system for the lithium niobate
rotate=90+128  !rotate so the z axis is aligned along ANSYS y axis
LOCAL,11,CART,0,0,0,0,90,0  !angle to rotate coordinate system.
csys,0  !come back to the global scheme

voltage=30 !voltage to be applied to electrodes

w=7.00e-3 ! values used to define corners of model
l=0.01e-3
h=1.0e-3
W2=0.50e-3
H2=2.00e-3

numsteps=50 !the number of load substeps
F1=8.0e6 !starting frequency
F2=10.5e6 !end frequency

k1,-w,-h,-l !define the corners of the model, repeat as required
k,2,-w,-h,l
k,19,W2,h+H2,l
k,20,W2,h+H2,-l

a,1,2,3,4 !define areas, repeat as required
a,9,10,11,12
```

```
elec1=-450e-6 !define values for interdigitated electrodes (+ve), repeat as required
elec2=-550e-6

elec1b=-650e-6 !define –ve electrodes, repeat as required
elec2b=-750e-6

DMPRAT,0.01 !damping

ET,1,80,,0 !define element types
ET,8,5,3      !LiNbO3 element type
ET,7,45

VA,1,2,3,4,5,6 !define volumes using areas
VA,2,7,8,9,10,11
VA,9,12,13,14,15,16
VA,10,17,18,19,20,21

MP,EX,7,0.360e9 !material properties, elastic moduli, mass density, Possions ratio
MP,DENS,7,1020
MP,PRXY,7,0.499

mat,8 !lithium niobate material properties
type,8
TB,ANEL,8,1,,0,, !table for anisotropic elastic matrix
TBDATA,1,2.0300E+11,5.7300E+10,7.5200E+10,8.5000E+09,0.0000,0.0000  !define  data  for
table
TBDATA,7,2.0300E+11,7.5200E+10,-8.5000E+09,0.0000E+00,0.0000,
TBDATA,12,2.4240E+11,0.0000E+00,0.0000,0.0000,
TBDATA,16,5.9500E+10,0.0000,0.0000,
TBDATA,19,5.9500E+10,1.7000E+10
TBDATA,21,7.2850E+10
TB,PIEZ,8, !piezoelectric matrix data
TBDATA,1,0.0000,-2.3000,0.1400
TBDATA,4,0.0000,2.3000,0.1400
TBDATA,7,0.0000,0.0000,1.3600
TBDATA,13,0.0000,3.7000,0.0000
```

```
TBDATA,16,3.7000,0.0000,0.0000
TBDATA,10,-4.6000,0.0000,0.0000

EMUNIT,EPZRO,8.85E-12 !specifies the system of units for magnetic field problems
MP,PERX,8,26.700 !material parameters, electrical permitivities
MP,PERY,8,26.700
MP,PERZ,8,44.900
MP,DENS,8,4640.000

vsel,s,,,1, !volume select, repeat for all transducer volumes
VATT,8,8,8,11  !attach material 8 to volume

vsel,s,,,4, !plastic volume above transducer
VATT,7,7,7,0

mshsize=(10e-6)/1.6        !mesh spacing

lsel,all !select all lines

lsel,u,loc,x,w !unselect specific lines
lsel,u,loc,x,-w
lsel,u,loc,x,W2
lsel,u,loc,x,-W2
lsel,u,loc,y,h+H2
lsel,u,loc,x,0
lesize,all,,,675        !meshing across end sections

lsel,s,loc,x,0
lesize,all,,,50         !meshing across middle section

lsel,s,loc,x,W2
lsel,a,loc,x,-W2
lsel,u,loc,y,h+H2
lsel,u,loc,y,h
lsel,u,loc,y,-h
lesize,all,,,40                !meshing from top to bottom
```

```
lsel,s,loc,y,h+H2
lsel,a,loc,y,h
lsel,a,loc,y,-h
lesize,all,,,1          !meshing from front to back

vsel, all

mshkey,1
MSHAPE,0,3D
vmesh,all               !mesh it

nsel,s,loc,z,l,-l !set up plain strain condition
D,all,uz,0
!nsel,s,loc,z,-l
!D,all,uz,0

!add voltages electrodes (+ve), repeat as required for interdigitated electrodes
vsel,s,MAT,,8   !select lithium niobate vol
aslv,s   !get its areas
nsla,s,1  !get nodes on the areas including end points
nsel,r,loc,y,h   !keep only those on top of lithium niobate
nsel,r,loc,x,elec1,elec2
cp,next,volt,all   !couple all these together for voltage
cm,te,node
d,All,volt,voltage

!add voltages electrodes (-ve), repeat as required for interdigitated electrodes
vsel,s,MAT,,8   !select lithium niobate vol
aslv,s   !get its areas
nsla,s,1  !get nodes on the areas including end points
nsel,r,loc,y,h  !keep only those on top of lithium niobate
nsel,r,loc,x,elec1b,elec2b
cp,next,volt,all   !couple all these together for voltage
cm,be,node
d,All,volt,0 !set voltage to 0
```

```
FINISH
/SOLU
ANTYPE,HARMIC !harmonic analysis
nsteps=numsteps    !the number of load substeps
NSUBST,nsteps   !number of frequency steps
HARFRQ,F1,F2 !solve between these frequencies
KBC,1    !Stepped load ie the voltage is applied evenly to all steps
HROPT,FULL !full harmonic analysis
HROUT,ON    !output options
eqslv,sparse
SOLVE
save
FINISH

!Energy density in liquid layer calcs vs freq
/post1
*dim,liq_energy,ARRAY,nsteps  !create array for energy results

*do,loop_a,1,nsteps,1      !loop this variable 1 to nsteps in inc. 1
        vsel,s,MAT,,1   !select fluid
        eslv,s !get elements on selected areas
        stepnum=loop_a     !the macro wants the load sub step number
        *USE,79acoustic.txt    !My macro calculates energies and acoustic quantities
        liq_energy(loop_a)=liq_energy_dens            !average energy density stored
*enddo
/dscale,all,off
vsel,s,mat,,1
eslv

finish    !****the data will be displayed in post26 following

!*****************************************************************

/post26 !calculate electrical impedance and plots it and the energy density
rforce,2,botelec,amps,,Charge_unitwidth !get charge store in #2
area_fac=1      !ratio electrode area to modelled area
```

```
prod,2,2,,,Charge,,,area_fac   !multiply charge per unit width by width for actual charge
prod,3,1,2,,Current,,,2*3.14,1    !store current in #3
FILLDATA,4,,,,1          !#4: just an array of 1's to let allow use of qout
quot,5,4,3,,Z_pzt,,,voltage                ! #5 =  (#4)* voltage/ #3

ABS,6,5              !#6 takes on the complex magnitude of #5, the impedance
/axlab,x,Frequency (Hz)
/axlab,y,Impedance (Ohms)
plvar,6              !plots the impedance
VPUT,liq_energy(1),7,,,Energy          !transfer variable liq_energy into #7
/axlab,x,Frequency (Hz)
/axlab,y,Energy
plvar,7              !plots the energy stored in liquid layer
EXTREM,7
*get,fmax,VARI,7,EXTREM,TMAX  !freq of max energy
stepmax=(fmax-F1)/((F2-F1)/(NUMSTEPS))  !step number of the maximum

!************WRITE DATA*******************
*DIM,freqarray,ARRAY,nsteps
VGET,freqarray,1              !get freq data
*CFOPEN,Li_en,txt       !write data to txt document
*VWRITE,freqarray(1),liq_energy(1)
(E15.8,E15.8)
*CFCLOS

!************WRITE DATA*******************
*DIM,imparray,ARRAY,nsteps
VGET,imparray,6
*CFOPEN,Li_imp,txt      !write data to txt document
*VWRITE,freqarray(1),imparray(1)
(E15.8,E15.8)
*CFCLOS
!*****************************************************************

/POST1     !plot radiation force potential
ALLSEL
```

```
stepnum=stepmax
vsel,s,MAT,,1   !select fluid layer
eslv,s !get elements on selected vol
*USE,79acoustic.txt     !macro to calculate stuff
bead_dens=1055
bead_speed=1962
*use,Gorkov.txt    !macro calculates force potential

/yrange
path,vert,2,8,1000          !new path 2 defined points, 8 data items, 20 divisions
ppath,1,,0,0,0
ppath,2,,0,Tfluid,0
pdef,myforce_pot,etab,force_pot
pdef,myEpot,etab,E_POT
PCALC,DERI,vert,myforce_pot,S   !force is calculated as derivate d(force_pot)/d(distance)
plpath,vert

/yrange
path,latmid,2,8,1000                !new path  defined points, 8 data items, 20 divisions
ppath,1,,-W2,Tfluid/2,0
ppath,2,,W2,Tfluid/2,0
pdef,myforce_pot,etab,force_pot
pdef,myEpot,etab,E_POT
pdef,myPRESA,etab,PRESA
PCALC,DERI,latmid,myforce_pot,S   !force is calculated as derivate d(force_pot)/d(distance)
plpath,latmid
!prpath,latmid !prints it

pletab,force_pot
/dscale,all,1   !do not scale the displacements

/post1   !plot the voltage ditribution
!set,1,stepnum
!esel,s,mat,,8
!plnsol,volt
save
```

A print of 79acoustic file.

```
!*************************************************************************
!79ACOUSTIC  macro
!Peter Glynne-Jones 2008
!*************************************************************************
!When using fluid799 in acoustic simulation, this calculates the acoustic
!parameters and energy terms after a harmonic analysis.
!includes energy density for radiation forces
!INPUTS:
!  On entry you must have all the fluid79 elements selected.
!  stepnum    must hold the load substep:  it uses set,1,stepnum
!  rho_water          must hold the fluid density
!OUTPUTS:
!E_KIN, E_POT    Time averaged energy densities, kinetic and potential (etable)
!liq_energy_dens   The average energy density of the liquid layer
!REALPRES, IMAGPRES        acoustic pressure
!RVelX,RVelY,IVelX,IVelY     Real and Imaginary acoustic velocity

        LCSUM,ALL    !forces ansys to allow summing (allow amplitude to be found) for non-summable components (NMISC). This needed for HRCPLX macro
        HRCPLX,1,stepnum,1000    !Get amplitude (not Real/Imag)  results  of loop_a load step [1000>360 so amplitude]
        etab,PRESA,SMISC,1     !get pressure amplitude
set,1,stepnum   !Real
        *GET,freq,ACTIVE,0,SET,FREQ   !get the frequency of current load step
        omega=2*3.14159*freq   !angular frequency
        etab,elem_vol,VOLU              !get element volumes
        etab,RUX,U,X       !Real x displacement
        etab,RUY,U,Y       !Real y displacement

set,1,stepnum,,1  !Imaginary
        etab,IUX,U,X       !IMAG x displacement
        etab,IUY,U,Y       !IMAG y displacement

        SMULT,RvelY,IUY,,-omega    !the velocity is dU/dt = j*omega*U
```

```
SMULT,IvelY,RUY,,omega     !find the real and imag parts of both x and y components
SMULT,RvelX,IUX,,-omega
SMULT,IvelX,RUX,,omega

!get magnitudes of X and Y velocities
SMULT,RY2,RvelY,RvelY    !squared
SMULT,RX2,RvelX,RvelX    !squared
SMULT,IY2,IvelY,IvelY    !squared
SMULT,IX2,IvelX,IvelX    !squared
sadd,sumy,RY2,IY2   !sum of squares
sadd,sumx,RX2,IX2   !sum of squares
sexp,velXamp,sumx,,0.5 !sqrt:  this is now the amplitude of the x component of the velocity
sexp,VelYamp,sumy,,0.5          !sqrt
smult,E_KINX,velXamp,velXamp,0.25*rho_water  !the time averaged kinetic energy density from X component
smult,E_KINY,VelYamp,VelYamp,0.25*rho_water  !the time averaged kinetic energy density from Y component
sadd,E_KIN,E_KINX,E_KINY     !add them for total time averaged kinetic energy density.

smult,E_POT,PRESA,PRESA,0.25/(rho_water*c_water**2)     !the time averaged potential energy density
sadd,E_dens,E_POT,E_KIN              !total energy density is sum E_POT+E_KIN
etab,elem_vol,VOLU              !get element volumes
smult,elem_energy,elem_vol,E_dens !the energy for the element (of unit width)
SSUM                          !sum all columns

*GET,Etot,SSUM,elem_energy          !get the sum of E_dens.  This is total energy in fluid for unit width
*GET,Voltot,SSUM,elem_vol     !get the total volume (for unit width)

*get,myfreq,ACTIVE,,SET,FREQ
liq_energy_dens=Etot/Voltot       !This is the average energy density in the fluid layer
```

A print of the Gorkov file

```
!Calculate force potential from acoustic parameters
```

```
!E_KIN,POT have kinetic/potential time averaged energy density

!NEEDED: bead_rad, bead_dens, bead_speed, rho_water, c_water

mr=bead_dens/rho_water !mass ratio: lambda in groschl
vr=bead_speed/c_water  !velocity ratio: sigma in groschl
bead_rad=5e-6
bead_volume=(4/3)*3.141592*(bead_rad**3)
KIN_mult=-bead_volume*3*(mr-1)/(2*mr+1)      !from Gorkov, what we need to multiply
E_POT by: Note the initial MINUS sign
POT_mult=bead_volume*(1-1/(mr*vr*vr))        !from Gorkov.

sadd,force_pot,E_POT,E_KIN,POT_mult,KIN_mult      !Gorkovs force potential
```

References

ADAMSON, A. W. 1960. *Physical Chemistry of Surfaces,* New York, Interscience.

AUGUSTSSON, P., PERSSON, J., EKSTROM, S., OHLIN, M. & LAURELL, T. 2009. Decomplexing biofluids using microchip based acoustophoresis. *Lab on a Chip,* 9**,** 810-818.

AWAJA, F., GILBERT, M., KELLY, G., FOX, B. & PIGRAM, P. J. 2009. Adhesion of polymers. *Progress in Polymer Science,* 34**,** 948-968.

BECKER, H. & LOCASCIO, L. E. 2002. Polymer microfluidic devices. *Talanta,* 56**,** 267-287.

BELL, A. T., HOLLAHAN, J. R., HUDIS, M., KIRK, R. W., MILLARD, M., PAVLATH, A. E., SUHR, H., THOMAS, R. S. & WYDEVEN, T. 1974. *Techniques and Applications of Plasma Chemistry*.

BEYSSEN, D., LE BRIZOUAL, L., ELMAZRIA, O. & ALNOT, P. 2006. Microfluidic device based on surface acoustic waves. *Sensors and Actuators B - Chemical,* 118**,** 380-385.

BHATTACHARYA, S., DATTA, A., BERG, J. M. & GANGOPADHYAY, S. 2005. Studies on surface wettability of poly(dimethyl) siloxane (PDMS) and glass under oxygen-plasma treatment and correlation with bond strength. *Microelectromechanical Systems, Journal of,* 14**,** 590-597.

BORRIELLO, G., WERNER, E., ROE, F., KIM, A. M., EHRLICH, G. D. & STEWART, P. S. 2004. Oxygen Limitation Contributes to Antibiotic Tolerance of Pseudomonas aeruginosa in Biofilms. *Antimicrobial Agents and Chemotherapy,* 48**,** 2659-2664.

BOTT, T. R. & TIANQING, L. 2004. Ultrasound enhancement of biocide efficiency. *Ultrasonics Sonochemistry,* 11**,** 323-326.

BREKHOVSKIKH, L. M. 1957. *Waves in Layered Media,* Moscow, Izdatelstvo "Nauka".

BREWERSCIENCE. 2011. *http://www.brewerscience.com/products/cee/equipment-200mm/spin-coater* [Online]. [Accessed 17th January 2011.

BRUUS, H. 2008. *Theoretical Microfluidics*, Oxford University Press.

BRUUS, H. 2012. Acoustofluidics 7: The acoustic radiation force on small particles. *Lab on a Chip,* 12**,** 1014-1021.

CAI, D. & NEYER, A. 2010. Cost-effective and reliable sealing method for PDMS (PolyDiMethylSiloxane)-based microfluidic devices with various substrates. *Microfluidics and Nanofluidics,* 9**,** 855-864.

CAPPELIER, J. M., LAZARO, B., ROSSERO, A., FERNANDEZ-ASTORGA, A. & FEDERIGHI, M. 1997. Double staining (CTC-DAPI) for detection and enumeration of viable but non-culturable Campylobacter jejuni cells. *Vet Res,* 28**,** 547-55.

CARPENTER, A., JONES, T., LAMPRECHT, M., CLARKE, C., KANG, I., FRIMAN, O., GUERTIN, D., CHANG, J., LINDQUIST, R., MOFFAT, J., GOLLAND, P. & SABATINI, D. 2006. CellProfiler: image analysis software for identifying and quantifying cell phenotypes. *Genome Biology,* 7**,** R100.

CARUGO, D., ANKRETT, D. N., GLYNNE-JONES, P., CAPRETTO, L., BOLTRYK, R. J., ZHANG, X., TOWNSEND, P. A. & HILL, M. 2011. Contrast agent-free sonoporation: The use of an ultrasonic standing wave microfluidic system for the delivery of pharmaceutical agents. *Biomicrofluidics,* 5**,** -.

CARUGO, D., OCTON, T., MESSAOUDI, W., FISHER, A. L., CARBONI, M., HARRIS, N. R., HILL, M. & GLYNNE-JONES, P. 2014. A thin-reflector microfluidic resonator for continuous-flow concentration of microorganisms: a new approach to water quality analysis using acoustofluidics. *Lab on a Chip,* 14**,** 3830-3842.

CASEY, E., GLENNON, B. & HAMER, G. 1999. Oxygen mass transfer characteristics in a membrane-aerated biofilm reactor. *Biotechnology and Bioengineering,* 62**,** 183-192.
CHAMP, M. A. 2003. Economic and environmental impacts on ports and harbors from the convention to ban harmful marine anti-fouling systems. *Marine Pollution Bulletin,* 46**,** 935-940.
CHANG, W.-J., AKIN, D., SEDLAK, M., LADISCH, M. R. & BASHIR, R. 2003. Poly(dimethylsiloxane) (PDMS) and Silicon Hybrid Biochip for Bacterial Culture. *Biomedical Microdevices,* 5**,** 281-290.
CHARCOSSET, C. 2012. 3 - Microfiltration. *In:* CHARCOSSET, C. (ed.) *Membrane Processes in Biotechnologies and Pharmaceutics.* Amsterdam: Elsevier.
CHAUDHURY, M. K. & WHITESIDES, G. M. 1991. Direct measurement of interfacial interactions between semispherical lenses and flat sheets of poly(dimethylsiloxane) and their chemical derivatives. *Langmuir,* 7**,** 1013-1025.
CHEEKE, J. D. N. 2002. *Fundamentals and Applications of Ultrasonic Waves*, CRC Press.
CHENG, S., LAU, K.-T., CHEN, S., CHANG, X., LIU, T. & YIN, Y. 2010. Microscopical Observation of the Marine Bacterium Vibrio Natriegeus Growth on Metallic Corrosion. *Materials and Manufacturing Processes,* 25**,** 293-297.
CHIEN, A.-C., HILL, NORBERT S. & LEVIN, PETRA A. 2012. Cell Size Control in Bacteria. *Current Biology,* 22**,** R340-R349.
CHOI, A., KIM, J. Y., LEE, J. E. & JUNG, H.-I. 2009. Effects of PDMS curing ratio and 3D micro-pyramid structure on the formation of an in vitro neural network. *Current Applied Physics,* 9**,** e294-e297.
CHOU, H. P., SPENCE, C., SCHERER, A. & QUAKE, S. 1999. A microfabricated device for sizing and sorting DNA molecules. *Proceedings of the National Academy of Sciences of the United States of America,* 96**,** 11-3.
CHOU, N. J., TANG, C. H., PARASZCZAK, J. & BABICH, E. 1985. Mechanism of oxygen plasma etching of polydimethyl siloxane films. *Applied Physics Letters,* 46**,** 31-33.
COATES, R. F. W. 1989. *Underwater Acoustic Systems*, Macmillan New Electronics.
CONSCIOUSALLIANCE. 2011. *http://www.consciousalliance.org/pr/Phytoplankton_Ultimate-Nutrogenomic-Superfood.pdf* [Online]. [Accessed 1st February 2011.
COSTANZA, R., D'ARGE, R., GROOT, R. D., FARBER, S., GRASSO, M., HANNON, B., LIMBURG, K., NAEEM, S., O'NEILL, R. V., PARUELO, J., RASKIN, R. G., SUTTON, P. & BELT, M. V. D. 1998. The value of the world's ecosystem services and natural capital. *Ecological Economics,* 25**,** 3-15.
DAUGHTON, W. J. & GIVENS, F. L. 1982. An Investigation of the Thickness Variation of Spun-on Thin Films Commonly Associated with the Semiconductor Industry. *Journal of The Electrochemical Society,* 129**,** 173-179.
DAVID, B. 2011. *http://xnet.rrc.mb.ca/davidb/biofilms.htm* [Online]. [Accessed 28th January 2011.
DELAMARCHE, E., BERNARD, A., SCHMID, H., BIETSCH, A., MICHEL, B. & BIEBUYCK, H. 1998. Microfluidic Networks for Chemical Patterning of Substrates:â€‰ Design and Application to Bioassays. *Journal of the American Chemical Society,* 120**,** 500-508.
DELAMARCHE, E., BERNARD, A., SCHMID, H., MICHEL, B. & BIEBUYCK, H. 1997. Patterned Delivery of Immunoglobulins to Surfaces Using Microfluidic Networks. *Science,* 276**,** 779-781.
DELAUNEY, L., COMPERE, C. & LEHAITRE, M. 2010. Biofouling protection for marine environmental sensors. *Ocean Science* 6**,** 503-5011.

DENKIN, S. M. & NELSON, D. R. 1999. Induction of Protease Activity in Vibrio anguillarum by Gastrointestinal Mucus. *Applied and Environmental Microbiology,* 65**,** 3555-3560.

DES MARAIS, D. J. 2013. Carbon Exchange Between the Mantle and the Crust, and its Effect Upon the Atmosphere: Today Compared to Archean Time. *The Carbon Cycle and Atmospheric CO2: Natural Variations Archean to Present.* American Geophysical Union.

DI CARLO, D., IRIMIA, D., TOMPKINS, R. G. & TONER, M. 2007. Continuous inertial focusing, ordering, and separation of particles in microchannels. *Proceedings of the National Academy of Sciences,* 104**,** 18892-18897.

DOINIKOV, A. A. 1994. Acoustic radiation pressure on a compressible sphere in a viscous fluid. *Journal of Fluid Mechanics,* 267**,** 1-22.

DOUGHERTY, G. M. & PISANO, A. P. 2003. Ultrasonic particle manipulation in microchannels using phased co planar transduers. *Transuders 03***,** 670-673.

DRANSFIELD, K. & SALZMANN, E. 1970. Excitation, Detection and attenuation of High Frequency elastic Surface Waves. *In:* W.P.MASON AND R.N.THURSTON (ed.) *Physical Acoustics 7.* New York: Academic Press.

DUFFY, D. C., MCDONALD, J. C., SCHUELLER, O. J. A. & WHITESIDES, G. M. 1998. Rapid Prototyping of Microfluidic Systems in Poly(dimethylsiloxane). *Analytical Chemistry,* 70**,** 4974-4984.

E.P.A. 2014. *http://www.epa.gov/region9/waste/features/safe-paint/san-diego.html* [Online]. [Accessed 7th October 2014.

EAGON, R. G. 1962. Pseudomonas Natriegens, A marine bacterium with a generation time of less than 10 minutes. *J. Bacteriology.,* 83**,** 736-737.

EFFENHAUSER, C. S., BRUIN, G. J. M., PAULUS, A. & EHRAT, M. 1997. Integrated Capillary Electrophoresis on Flexible Silicone Microdevices: Analysis of DNA Restriction Fragments and Detection of Single DNA Molecules on Microchips. *Analytical Chemistry,* 69**,** 3451-3457.

EGITTO, F. D. & MATIENZO, L. J. 1994. Plasma Modification of polymer surfaces for adhesion improvement. *IBM journal of Research and Development,* 38**,** 423-439.

EIJKEL, J. C. T., PRAK, A., COWEN, S., CRASTON, D. H. & MANZ, A. 1998. Micromachined heated chemical reactor for pre-column derivatisation. *Journal of Chromatography A,* 815**,** 265-271.

EMSLIE, A. G., BONNER, F. T. & PECK, L. G. 1958. Flow of a Viscous Liquid on a Rotating Disk. *Journal of Applied Physics,* 29**,** 858-862.

ENGEN, W. V. 2011. *http://willem.engen.nl/uni/intern-mbx/material/Sylgard-184-spincoat.php* [Online]. [Accessed 17th January 2011.

EWING, W. M. 1957. *Elastic Waves in Layered Media,* New York, McGraw-Hill.

FAGERBAKKE, K., HELDAL, M. & NORLAND, S. 1996. Content of carbon, nitrogen, oxygen, sulfur and phosphorus in native aquatic and cultured bacteria. *Aquatic Microbial Ecology,* 10**,** 15-27.

FALLAH, H. R., GHASEMI, M., HASSANZADEH, A. & STEKI, H. 2007. The effect of annealing on structural, electrical and optical properties of nanostructured ITO films prepared by e-beam evaporation. *Materials Research Bulletin,* 42**,** 487-496.

FAN, Z. H. & HARRISON, D. J. 1994. Micromachining of capillary electrophoresis injectors and separators on glass chips and evaluation of flow at capillary intersections. *Analytical Chemistry,* 66**,** 177-184.

FARNELL, G. W. 1970. Properties of Elastic Surface Waves. *In:* W.P.MASON AND R.N.THURSTON (ed.) *Physical Acoustics 6.* New York: Academic Press.

FARNELL, G. W. & ADLER, E. L. 1972. Elastic Wave Propagation in Thin Layers. *In:* W.P.MASON AND R.N.THURSTON (ed.) *Physical Acoustics 9.* New York: Academic Press.

FERROTEC. 2012. http://www.ferrotec.com/technology/electronbeam/ [Online]. [Accessed 23rd May 2012.
FIORINI, G. S. & CHIU, T. 2005. Disposable microfluidic devices: fabrication, function, and application. *Biotechniques,* 38**,** 429-446.
FITTS, C. R. 2013. 2 - Physical Properties. *In:* FITTS, C. R. (ed.) *Groundwater Science (Second Edition).* Boston: Academic Press.
FOLCH, A., MEZZOUR, S., DU¨RING, M., HURTADO, O., TONER, M. & MU¨LLER, R. 2000. Stacks of Microfabricated Structures as Scaffolds for Cell Culture and Tissue Engineering. *Biomedical Microdevices,* 2**,** 207-214.
FRANKE, T., BRAUNMULLER, S., SCHMID, L., WIXFORTH, A. & WEITZ, D. A. 2010. Surface acoustic wave actuated cell sorting (SAWACS). *Lab on a Chip,* 10**,** 789-794.
FROMMELT, T., KOSTUR, M., WENZEL-SCHÃ¤FER, M., TALKNER, P., HÃ¤NGGI, P. & WIXFORTH, A. 2008. Microfluidic Mixing via Acoustically Driven Chaotic Advection. *Physical Review Letters,* 100**,** 034502.
FU, A. Y., SPENCE, C., SCHERER, A., ARNOLD, F. H. & QUAKE, S. R. 1999. A microfabricated fluorescence-activated cell sorter. *Nat Biotech,* 17**,** 1109-1111.
GEDGE, M. & HILL, M. 2012. Acoustofluidics 17: Theory and applications of surface acoustic wave devices for particle manipulation. *Lab on a Chip,* 12**,** 2998-3007.
GEDGE, M., VOON, L., GLYNNE-JONES, P., MOWLEM, M., MORGAN, H. & HILL, M. 2012. The use of ultrasonic waves to minimise biofouling in oceanographic microsensors. *AIP Conference Proceedings,* 1433**,** 765-768.
GEORGE, J. & MENON, C. S. 2000. Electrical and optical properties of electron beam evaporated ITO thin films. *Surface and Coatings Technology,* 132**,** 45-48.
GIRAUDET, L., FAUVEAUX, S., SIMONETTI, O., PETIT, C., BLARY, K., MAUREL, T. & BELKHIR, A. 2006. Spin-coated conductive polymer film resistivity measurement using the TLM method. *Synthetic Metals,* 156**,** 838-842.
GLORIEUX, C., VAN DE ROSTYNE, K., NELSON, K., GAO, W., LAURIKS, W. & THOEN, J. 2001. On the character of acoustic waves at the interface between hard and soft solids and liquids. *The Journal of the Acoustical Society of America,* 110**,** 1299-1306.
GLYNNE-JONES, P., BOLTRYK, R. J., HILL, M., HARRIS, N. R. & BACLET, P. 2009. Robust acoustic particle manipulation: A thin-reflector design for moving particles to a surface. *The Journal of the Acoustical Society of America,* 126**,** EL75-EL79.
GLYNNE-JONES, P., DEMORE, C. E. M., CONGWEI, Y., YONGQIANG, Q., COCHRAN, S. & HILL, M. 2012. Array-controlled ultrasonic manipulation of particles in planar acoustic resonator. *Ultrasonics, Ferroelectrics and Frequency Control, IEEE Transactions on,* 59**,** 1258-1266.
GOGOLADZE, V. G. 1948. Rayleigh waves on the interface between a compressible fluid medium and a solid elastic half-space. *Trudy Seismolo. Inst. Acad. Nauk. USSR,* 127**,** 27–32.
GOR'KOV, L. P. 1962. On the forces acting on a small particle in an acoustic field in an ideal fluid. *Soviet Physics,* 6**,** 773-775.
GROENENDAAL, L., JONAS, F., FREITAG, D., PIELARTZIK, H. & REYNOLDS, J. R. 2000. Poly(3,4-ethylenedioxythiophene) and Its Derivatives: Past, Present, and Future. *Advanced Materials,* 12**,** 481-494.
GRÖSCHL, M. 1998. Ultrasonic Separation of Suspended Particles - Part I: Fundamentals. *Acta Acustica united with Acustica,* 84**,** 15.
GROUPSRV. 2011. http://www.groupsrv.com/science/about143348.html [Online]. [Accessed 17th January 2011.
GUTTENBERG, Z., MULLER, H., HABERMULLER, H., GEISBAUER, A., PIPPER, J., FELBEL, J., KIELPINSKI, M., SCRIBA, J. & WIXFORTH, A. 2005. Planar chip

device for PCR and hybridization with surface acoustic wave pump. *Lab on a Chip,* 5**,** 308-317.

HA, Y. H., NIKOLOV, N., POLLACK, S. K., MASTRANGELO, J., MARTIN, B. D. & SHASHIDHAR, R. 2004. Towards a Transparent, Highly Conductive Poly(3,4-ethylenedioxythiophene). *Advanced Functional Materials,* 14**,** 615-622.

HAMMARSTROM, B., EVANDER, M., BARBEAU, H., BRUZELIUS, M., LARSSON, J., LAURELL, T. & NILSSON, J. Non-contact acoustic cell trapping in disposable glass capillaries. *Lab on a Chip,* 10**,** 2251-2257.

HARRIS, N., HILL, M., SHEN, Y., TOWNSEND, R. J., BEEBY, S. & WHITE, N. 2004. A dual frequency, ultrasonic, microengineered particle manipulator. *Ultrasonics,* 42**,** 139-144.

HARRIS, N. R., HILL, M., BEEBY, S., SHEN, Y., WHITE, N. M., HAWKES, J. J. & COAKLEY, W. T. 2003. A silicon microfluidic ultrasonic separator. *Sensors and Actuators B - Chemical,* 95**,** 425-434.

HARRIS, N. R., HILL, M., TORAH, R., TOWNSEND, R. J., SEEBY, B., WHITE, N. M. & DING, J. 2006. A multilayer thick-film PZT actuator for MEMs applications. *Sensors and Actuators A - Physical,* 132**,** 311-316.

HARRIS, N. R., KEATING, A. & HILL, M. 2010. A Lateral Mode Flow-through PMMA Ultrasonic Separator. *APCOT2010.* Perth, Western Australia.

HARRISON, D. J., MANZ, A. & GLAVINA, P. G. Electroosmotic pumping within a chemical sensor system integrated on silicon. Solid-State Sensors and Actuators, 1991. Digest of Technical Papers, TRANSDUCERS '91., 1991 International Conference on, 24-27 Jun 1991 1991. 792-795.

HAWKES, J. J. & COAKLEY, T. W. 2001. Force field particle filter, combining ultrasound standing waves and laminar flow. *Sensors and Actuators B - Chemical,* 75**,** 213-222.

HILL, M., SHEN, Y. & HAWKES, J. J. 2002. Modelling of layered resonators for ultrasonic separation. *Ultrasonics,* 40**,** 385-392.

HILL, M., TOWNSEND, R. J. & HARRIS, N. R. 2008. Modelling for the robust design of layered resonators for ultrasonic particle manipulation. *Ultrasonics,* 48**,** 521-528.

HILLBORG, H. & GEDDE, U. W. 1998. Hydrophobicity recovery of polydimethylsiloxane after exposure to corona discharges. *Polymer,* 39**,** 1991-1998.

HILLBORG, H. & GEDDE, U. W. 1999. Hydrophobicity changes in silicone rubbers. *Dielectrics and Electrical Insulation, IEEE Transactions on,* 6**,** 703-717.

HIRANO, M., HOSHIDA, T., SAKAUE-SAWANO, A. & MIYAWAKI, A. 2010. A poly(dimethylsiloxane)-based device enabling time-lapse imaging with high spatial resolution. *Biochemical and Biophysical Research Communications,* 392**,** 307-310.

HOLLAHAN, J. R. & CARLSON, G. L. 1970. Hydroxylation of Polymethylsiloxane surfaces by Oxidizing Plasmas. *Journal of Applied Polymer Sciences,* 14**,** 2499-2508.

HONG, J. W., FUJII, T., SEKI, M., YAMAMOTO, T. & ENDO, I. 2001. Integration of gene amplification and capillary gel electrophoresis on a polydimethylsiloxane-glass hybrid microchip. *ELECTROPHORESIS,* 22**,** 328-333.

HSIEH, S., CHENG, Y. A., HSIEH, C. W. & LIU, Y. 2009. Plasma induced patterning of polydimethylsiloxane surfaces. *Materials Science and Engineering: B,* 156**,** 18-23.

HSU, C. H., DI CARLO, D., CHEN, C., IRIMIA, D. & TONER, M. 2008. Microvortex for focusing, guiding and sorting of particles. *Lab on a Chip,* 8**,** 2128-2134.

HU, X., BESSETTE, P. H., QIAN, J., MEINHART, C. D., DAUGHERTY, P. S. & SOH, H. T. 2005. Marker-specific sorting of rare cells using dielectrophoresis.

Proceedings of the National Academy of Sciences of the United States of America, 102**,** 15757-15761.
HULTSTROM, J., MANNEBERG, O., DOPF, K., HERTZ, H. M., BRISMAR, H. & WIKLUND, M. 2007. Proliferation and viability of adherent cells manipulated by standing-wave ultrasound in a microfluidic chip. *Ultrasound in Medicine and Biology,* 33**,** 145-151.
IMSLAB. 2010. *http://www.ims.ut.ee/~alar/microtech/Ch1_5/* [Online]. [Accessed 21st December 2010.
ISMAGILOV, R. F., NG, J. M. K., KENIS, P. J. A. & WHIESIDES, G. M. 2001a. Microfluidic Arrays of Fluidâ^'Fluid Diffusional Contacts as Detection Elements and Combinatorial Tools. *Analytical Chemistry,* 73**,** 5207-5213.
ISMAGILOV, R. F., ROSMARIN, D., KENIS, P. J. A., CHIU, D. T., ZHANG, W., STONE, H. A. & WHITESIDES, G. M. 2001b. Pressure-Driven Laminar Flow in Tangential Microchannels: an Elastomeric Microfluidic Switch. *Analytical Chemistry,* 73**,** 4682-4687.
JO, B. H., VAN LERBERGHE, L. M., MOTSEGOOD, K. M. & BEEBE, D. J. 2000. Three-dimensional micro-channel fabrication in polydimethylsiloxane (PDMS) elastomer. *Microelectromechanical Systems, Journal of,* 9**,** 76-81.
KARASAWA, T. & MIYATA, Y. 1993. Electrical and optical properties of indium tin oxide thin films deposited on unheated substrates by d.c. reactive sputtering. *Thin Solid Films,* 223**,** 135-139.
KIM, Y. W. & YOO, J. Y. 2009. Axisymmetric flow focusing of particles in a single microchannel. *Lab on a Chip,* 9**,** 1043-1045.
KING, L. V. 1934. On the Acoustic Radiation Pressure on Spheres. *Proceedings of the Royal Society of London. Series A, Mathematical and Physical Sciences,* 147**,** 212-240.
KIRBY, B. 2011. *http://www.kirbyresearch.com/index.cfm/wrap/textbook/microfluidicsnanofluidics.html* [Online]. [Accessed 2nd October 2011].
KNIGHT, J. B., VISHWANATH, A., BRODY, J. P. & AUSTIN, R. H. 1998. Hydrodynamic Focusing on a Silicon Chip: Mixing Nanoliters in Microseconds. *Physical Review Letters,* 80**,** 3863-3866.
KNOL. 2011. *http://knol.google.com/k/mems-fabrication-process#* [Online]. [Accessed 24th January 2011.
KOBAYASHI, H., ISHIDA, T., NAKAMURA, K., NAKATO, Y. & TSUBOMURA, H. 1992. Properties of indium tin oxide films prepared by the electron beam evaporation method in relation to characteristics of indium tin oxide/silicon oxide/silicon junction solar cells. *Journal of Applied Physics,* 72**,** 5288-5293.
KOLSKY, H. 1953. *Stress Waves in Solids,* Oxford, Clarendon Press.
KUMAR, M., FEKE, D. L. & BELOVICH, J. M. 2005. Fractionation of cell mixtures using acoustic and laminar flow fields. *Biotechnology and Bioengineering,* 89**,** 129-137.
KUNDT, L. 1894. Longitudinal vibrations and acoustic figures in cylindrical columns of liquid. *Annal Physik,* 153**,** 11.
LEE, J. N., PARK, C. & WHITESIDES, G. M. 2003. Solvent Compatibility of Poly(dimethylsiloxane)-Based Microfluidic Devices. *Analytical Chemistry,* 75**,** 6544-6554.
LEE, N. Y. & CHUNG, B. H. 2009. Novel Poly(dimethylsiloxane) Bonding Strategy via Room Temperature Chemical Gluing. *Langmuir,* 25**,** 3861-3866.
LEHAITRE, M., DELAUNEY, L. & COMPERE, C. 2008. Real-time Coastal Observing Systems for Marine Ecosystem Dynamics and Harmful Algal Blooms. *Biofouling and underwater measurements.* UNESCO.
LEWANDOWSKI, Z. 2007. *Fundamentals of Biofilm Research*, CRC Press.

LINDER, V., VERPOORTE, E., THORMANN, W., DE ROOIJ, N. F. & SIGRIST, H. 2001. Surface Biopassivation of Replicated Poly(dimethylsiloxane) Microfluidic Channels and Application to Heterogeneous Immunoreaction with On-Chip Fluorescence Detection. *Analytical Chemistry,* 73**,** 4181-4189.

LISENSKY, G. C., CAMPBELL, D. J., BECKMAN, K. J., CALDERON, C. E., DOOLAN, P. W., REBECCA, M. O. & ELLIS, A. B. 1999. Replication and Compression of Surface Structures with Polydimethylsiloxane Elastomer. *Journal of Chemical Education,* 76**,** 537.

LUONG, T. D., PHAN, V. N. & NGUYEN, N. T. 2010. High-throughput micromixers based on acoustic streaming induced by surface acoustic wave. *Microfluidics and Nanofluidics,* 10**,** 619-625.

MADOU, M. J. 2002. *Fundamentals of Microfabrication: The Science of Miniturization*, CRC Press; 2 edition.

MALIKA, T., MOHAMED, A., EDOUARD, R. & BERTRAND, N. 1999. Acoustic measurement of compressibility and thermal expansion coefficient of erythrocytes. *Physics in Medicine and Biology,* 44**,** 1277.

MANNEBERG, O., HAGSATER, S. M., SVENNEBRING, J., HERTZ, H. M., KUTTER, J. P., BRUUS, H. & WIKLUND, M. 2009a. Spatial confinement of ultrasonic force fields in microfluidic channels. *Ultrasonics,* 49**,** 112-119.

MANNEBERG, O., SVENNEBRING, J., HERTZ, H. M. & WIKLUND, M. 2008. Wedge transducer design for ultrasonic manipulation in a microfluidic chip. *Journal of micromechanics and microengineering,* 18.

MANNEBERG, O., VANHERBERGHEN, B., ONFELT, B. & WIKLUND, M. 2009b. Flow-free transport of cells in microchannels by frequency-modulated ultrasound. *Lab on a Chip,* 9.

MANZ, A., HARRISON, D. J., VERPOORTE, E. M. J., FETTINGER, J. C., PAULUS, A., LÜDI, H. & WIDMER, H. M. 1992. Planar chips technology for miniaturization and integration of separation techniques into monitoring systems: Capillary electrophoresis on a chip. *Journal of Chromatography A,* 593**,** 253-258.

MARK, J. E. 2009. *Polymer Data Handbook*, OUP USA; 2nd edition.

MARTIN, S. P., TOWNSEND, R. J., KUZNETSOVA, L. A., BORTHWICK, K. A. J., HILL, M., MCDONNELL, M. B. & COAKLEY, W. T. 2005. Spore and micro-particle capture on an immunosensor surface in an ultrasound standing wave system. *Biosensors and Bioelectronics,* 21**,** 758-767.

MARTYNOVA, L., LOCASCIO, L. E., GAITAN, M., KRAMER, G. W., CHRISTENSEN, R. G. & MACCREHAN, W. A. 1997. Fabrication of Plastic Microfluid Channels by Imprinting Methods. *Analytical Chemistry,* 69**,** 4783-4789.

MCCREEDY, T. & WILSON, N. G. 2001. Microfabricated reactors for on-chip heterogeneous catalysis. *Analyst,* 126**,** 21-23.

MCDONALD, J. C., CHABINYC, M. L., METALLO, S. J., ANDERSON, J. R., STROOCK, A. D. & WHITESIDES, G. M. 2002. Prototyping of Microfluidic Devices in Poly(dimethylsiloxane) Using Solid-Object Printing. *Analytical Chemistry,* 74**,** 1537-1545.

MCDONALD, J. C., DUFFY, D. C., ANDERSON, J. R., CHIU, D. T., WU, H., SCHUELLER, O. J. A. & WHITESIDES, G. M. 2000. Fabrication of microfluidic systems in poly(dimethylsiloxane). *ELECTROPHORESIS,* 21**,** 27-40.

MCDONALD, J. C. & WHITESIDES, G. M. 2002. Poly(dimethylsiloxane) as a Material for Fabricating Microfluidic Devices. *Accounts of Chemical Research,* 35**,** 491-499.

MICRONIT. 2009. *http://www.micronit.com/en/technologies/etching/drie_etching.php*. [Online]. [Accessed 24th June 2009.

MITCHELL, R. F. & READ, E. 1975. Suppression of Bulk Wave Radiation from Surface Acoustic Wave Devices. *Sonics and Ultrasonics, IEEE Transactions on,* 22**,** 264-269.
MONTANASTATEUNIVERSITY. 2011. *http://www.biofilm.montana.edu/biofilm-basics.html* [Online]. [Accessed 28th January 2011.
MORRA, M., OCCHIELLO, E., MAROLA, R., GARBASSI, F., HUMPHREY, P. & JOHNSON, D. 1990. On the aging of oxygen plasma-treated polydimethylsiloxane surfaces. *Journal of Colloid and Interface Science,* 137**,** 11-24.
MOTT, I. E. C., STICKLER, D. J., COAKLEY, W. T. & BOTT, T. R. 1998. The removal of bacterial biofilm from water-filled tubes using axially propagated ultrasound. *Journal of Applied Microbiology,* 84**,** 509-514.
MULLENGER, L. G., NIJOLE R. 1973. Vibrio natriegens: A Rapidly Growing Micro-Organism Ideally Suited for Class Experiments. *Journal of Biological Education,* 7**,** 33-39.
NOAA. 2009. *http://www.osdpd.noaa.gov/PSB/EPS/SST/contour.html* [Online]. [Accessed 10th June 2009.
OFFICEOFNAVALRESEARCH. 2009. *http://www.onr.navy.mil/Focus/ocean/water/salinity1.htm* [Online]. [Accessed 10th June 2009.
OGILVIE, I. R. G., SIEBEN, V. J., FLOQUET, C. F. A., ZMIJAN, R., MOWLEM, M. C. & MORGAN, H. 2010. Reduction of surface roughness for optical quality microfluidic devices in PMMA and COC. *Journal of Micromechanics and Microengineering,* 20**,** 065016.
OLINER, A. A., FARNELL, G. W., GERARD, H. M., ASH, E. A., SLOBODNIK, A. J. & SMITH, H. I. 1978. *Acoustic Surface Waves*, Springer-Verlag Berlin Heidelberg.
OWEN, M. J. 2005. Plasma/Corona Treatment of Silicones. *Australian Journal of Chemistry,* 58**,** 433-436.
OWEN, M. J. & SMITH, P. J. 1994. Plasma treatment of polydimethylsiloxane. *Journal of Adhesion Science and Technology,* 8**,** 1063-1075.
PAUL, C. H. L. 2010. *Fundamentals of microfluidics and lab on a chip for biological analysis and discovery*, CRC Press.
PETERSON, R. V. & PITT, W. G. 2000. The effect of frequency and power density on the ultrasonically-enhanced killing of biofilm-sequestered Escherichia coli. *Colloids and Surfaces B: Biointerfaces,* 17**,** 219-227.
PETERSSON, F., ÅBERG, L., SWÄRD-NILSSON, A.-M. & LAURELL, T. 2007. Free Flow Acoustophoresis: Microfluidic-Based Mode of Particle and Cell Separation. *Analytical Chemistry,* 79**,** 5117-5123.
PETERSSON, F., NILSSON, A., JÖNSSON, H. & LAURELL, T. 2005. Carrier Medium Exchange through Ultrasonic Particle Switching in Microfluidic Channels. *Analytical Chemistry,* 77**,** 1216-1221.
PIEDRAHITA, R. H. & WONG, K. B. H. 1999. Method and apparatus for preventing biofouling of aquatic sensors. Google Patents.
PITT, W. G. & ROSS, S. A. 2003. Ultrasound Increases the Rate of Bacterial Cell Growth. *Biotechnology Progress,* 19**,** 1038-1044.
POKAIPISIT, A., HORPRATHUM, M. & LIMSUWAN, P. 2007. Effect of Films Thickness on the properties of ITO Thin Films Prepared by Electron Beam Evaporation. *The Kasetsart Journal: Natural Science,* 41**,** 255-261.
POLLARD, H. F. 1977. *Sound Waves in Solids,* London, Pion Limited.
PYLE, B. H., BROADAWAY, S. C. & MCFETERS, G. A. 1995. Factors affecting the determination of respiratory activity on the basis of cyanoditolyl tetrazolium chloride reduction with membrane filtration. *Appl Environ Microbiol,* 61**,** 4304-9.
RAYLEIGH, L. 1885. On Waves Propagated along the Plane Surface of an Elastic Solid. *Proc. London Math. Soc.,* 17**,** 4-11.

RISTIC, V. M. 1983. *Principles of Acoustic Devices,* New York, John Wiley & Sons.
ROBERTS, D., RITTSCHOF, D., HOLM, E. & SCHMIDT, A. R. 1991. Factors influencing initial larval settlement: temporal, spatial and surface molecular components. *Journal of Experimental Marine Biology and Ecology,* 150**,** 203-221.
RODRIGUEZ, G. G., PHIPPS, D., ISHIGURO, K. & RIDGWAY, H. F. 1992. Use of a fluorescent redox probe for direct visualization of actively respiring bacteria. *Applied and Environmental Microbiology,* 58**,** 1801-1808.
ROSE, J. L. 1999. *Ultrasonic Waves in Solid Media,* Cambridge, Cambridge University Press.
SANKARANARAYANAN, S. K. R. S., CULAR, S., BHETHANABOTLA, V. R. & JOSEPH, B. 2008. Flow induced by acoustic streaming on surface-acoustic-wave devices and its application in biofouling removal: A computational study and comparisons to experiment. *Physical Review E,* 77**,** 066308.
SCHOTT. 2014. *http://www.schott.com/tubing/india/pharma-infoletter/2014-01/article-5.html* [Online]. [Accessed 17th July 2014.
SÉGUIN, C., MCLACHLAN, J. M., NORTON, P. R. & LAGUGNÉ-LABARTHET, F. Surface modification of poly(dimethylsiloxane) for microfluidic assay applications. *Applied Surface Science,* 256**,** 2524-2531.
SHARMA, R. V., EDWARDS, R. T. & BECKETT, R. 1998. Analysis of bacteria in aquatic environments using sedimentation field-flow fractionation: (II) physical characterization of cells. *Water Research,* 32**,** 1508-1514.
SHI, J., MAO, X., AHMED, D., COLLETTI, A. & HUANG, T. J. 2008. Focusing microparticles in a microfluidic channel with standing surface acoustic waves (SSAW). *Lab on a Chip,* 8**,** 221-223.
SIERACKI, M. E., CUCCI, T. L. & NICINSKI, J. 1999. Flow cytometric analysis of 5-cyano-2,3-ditolyl tetrazolium chloride activity of marine bacterioplankton in dilution cultures. *Appl Environ Microbiol,* 65**,** 2409-17.
SILICONFAREAST. 2009. *http://www.siliconfareast.com/wetetch.htm* [Online]. [Accessed 24th June 2009.
SIMMONS, S., SHAH, M., MACKEVICH, J. & CHANG, R. J. 1997. Polymer outdoor insulating materials. Part III-Silicone elastomer considerations. *Electrical Insulation Magazine, IEEE,* 13**,** 25-32.
SIVAKUMAR, P. M., PRABHAWATHI, V. & DOBLE, M. 2010. Antibacterial activity and QSAR of chalcones against biofilm-producing bacteria isolated from marine waters. *SAR and QSAR in Environmental Research,* 21**,** 247-263.
SOFLA, A. Y. N. & MARTIN, C. 2010. A vapor-assisted method for adhering polydimethylsiloxane and glass. *Lab on a Chip,* 10**,** 250-253.
SOLUCH, W. 1998. Design of SAW delay lines for sensors. *Sensors and Actuators A: Physical,* 67**,** 60-64.
SOPER, S. A., FORD, S. M., QI, S., MCCARLEY, R. L., KELLY, K. & MURPHY, M. C. 2000. Peer Reviewed: Polymeric Microelectromechanical Systems. *Analytical Chemistry,* 72**,** 642 A-651 A.
SRIVASTAVA, S. S. P. S. 2003. *Understanding bacteria,* Dordrecht; Boston; London, Kluwer academic publ.
STAUDT, C., HORN, H., HEMPEL, D. C. & NEU, T. R. 2004. Volumetric measurements of bacterial cells and extracellular polymeric substance glycoconjugates in biofilms. *Biotechnology and Bioengineering,* 88**,** 585-592.
STOICA, T. F., STOICA, T. A., ZAHARESCU, M., POPESCU, M., SAVA, F., POPESCU-POGRION, N. & FRUNZA, L. 2000. Characterization of ITO thin films prepared by spinning deposition starting from a sol-gel process. . *Journal of Optoelectronics and Advanced Materials,* 2**,** 684-688.
TABELING, P. 2003. *Introduction to Microfluidics*, Oxford University Press.

TERRY, S. C., JERMAN, J. H. & ANGELL, J. B. 1979. A gas chromatographic air analyzer fabricated on a silicon wafer. *Electron Devices, IEEE Transactions on,* 26**,** 1880-1886.
THIBAULT, C., SEVERAC, C., TRÉVISIOL, E. & VIEU, C. 2006. Microtransfer molding of hydrophobic dendrimer. *Microelectronic Engineering,* 83**,** 1513-1516.
TIERSTEN, H. F. 1969. Elastic Surface Waves guided by Thin Films. *Journal of Applied Physics,* 40**,** 770-789.
TOWNSEND, R. J., HILL, M., HARRIS, N. R. & MCDONNELL, M. B. 2008. Performance of a quarter-wavelength particle concentrator. *Ultrasonics,* 48**,** 515-520.
TOWNSEND, R. J., HILL, M., HARRIS, N. R. & WHITE, N. M. 2004. Modelling of particle paths passing through an ultrasonic standing wave. *Ultrasonics,* 42**,** 319-324.
TOWNSEND, R. J., HILL, M., HARRIS, N. R. & WHITE, N. M. 2006. Investigation of two-dimensional acoustic resonant modes in a particle separator. *Ultrasonics,* 44, Supplement**,** e467-e471.
TSOU, J. K., LIU, J., BARAKAT, A. I. & INSANA, M. F. Role of Ultrasonic Shear Rate Estimation Errors in Assessing Inflammatory Response and Vascular Risk. *Ultrasound in Medicine and Biology,* 34**,** 963-972.
TURNBAUGH, P. J. 2007. The Human Microbiome Project. *Nature,* 449.
TURNER, J. D. & PRETLOVE, A. J. 1991. *Acoustics for Engineers,* London, Macmillan Education.
ÜBERALL, H. 1973. Surface Waves in Acoustics. *In:* W.P.MASON AND R.N.THURSTON (ed.) *Physical Acoustics 10.* New York: Academic Press.
UNGER, M. A., CHOU, H.-P., THORSEN, T., SCHERER, A. & QUAKE, S. R. 2000. Monolithic Microfabricated Valves and Pumps by Multilayer Soft Lithography. *Science,* 288**,** 113-116.
UNIVERSITYOFSOUTHAMPTON. 2011. *http://www.southampton.ac.uk/cmm/* [Online]. [Accessed 31st January 2011.
VANNESTE, J. & BÜHLER, O. 2010. Streaming by leaky surface acoustic waves. *Proceedings of the Royal Society A: Mathematical, Physical and Engineering Science,* 467**,** 1779-1800.
VIKTOROV, I. A. 1967. *Rayleigh and Lamb Waves,* New York, Plenum Press.
VIRGINIASEMICONDUCTORINC. 2011. *http://www.virginiasemi.com/pdf/siliconetchingandcleaning.pdf* [Online]. [Accessed 31st January 2011.
WALTERS, M. C., ROE, F., BUGNICOURT, A., FRANKLIN, M. J. & STEWART, P. S. 2003. Contributions of Antibiotic Penetration, Oxygen Limitation, and Low Metabolic Activity to Tolerance of Pseudomonas aeruginosa Biofilms to Ciprofloxacin and Tobramycin. *Antimicrobial Agents and Chemotherapy,* 47**,** 317-323.
WANG, M. M., TU, E., RAYMOND, D. E., YANG, J. M., ZHANG, H., HAGEN, N., DEES, B., MERCER, E. M., FORSTER, A. H., KARIV, I., MARCHAND, P. J. & BUTLER, W. F. 2005. Microfluidic sorting of mammalian cells by optical force switching. *Nature biotechnology,* 23**,** 83-87.
WANG, T. G. & LEE, C. 1998. *Radiation pressure and acoustic levitation.* , Academic press, New York.
WEIGL, B. H. & YAGER, P. 1999. Microfluidic Diffusion-Based Separation and Detection. *Science,* 283**,** 346-347.
WHELAN, A. & REGAN, F. 2006. Antifouling strategies for marine and riverine sensors. *Journal of Environmental Monitoring,* 8**,** 880-886.
WILDING, P., KRICKA, L. J., CHENG, J., HVICHIA, G., SHOFFNER, M. A. & FORTINA, P. 1998. Integrated Cell Isolation and Polymerase Chain Reaction

Analysis Using Silicon Microfilter Chambers. *Analytical Biochemistry,* 257**,** 95-100.

WIXFORTH, A. 2003. Acoustically driven planar microfluidics. *Superlattices and Microstructures,* 33**,** 389-396.

WOOD, C., CUNNINGHAM, J., O'RORKE, R., WALTI, C., LINFIELD, E., DAVIES, A. & EVANS, S. 2009. Formation and manipulation of two-dimensional arrays of micron-scale particles in microfluidic systems by surface acoustic waves. *American Institute of Physics,* 94.

WORLDOCEANREVIEW. 2011. *http://worldoceanreview.com/en/fisheries/state-of-affairs/* [Online]. [Accessed 1st February 2011.

WU, Z., WILLING, B., BJERKETORP, J., JANSSON, J. K. & HJORT, K. 2009. Soft inertial microfluidics for high throughput separation of bacteria from human blood cells. *Lab on a Chip,* 9**,** 1193-1199.

YOSIOKA, K. & KAWASIMA, Y. 1955. Acoustic radiation pressure on a compressible sphere. *Acustica,* 5**,** 167-173.

ZHANG, W. Y., FERGUSON, G. S. & TATIC-LUCIC, S. Elastomer-supported cold welding for room temperature wafer-level bonding. Micro Electro Mechanical Systems, 2004. 17th IEEE International Conference on. (MEMS), 2004 2004. 741-744.

ZHANG, X., MACDIARMID, A. G. & MANOHAR, S. K. 2005. Chemical synthesis of PEDOT nanofibers. *Chemical Communications***,** 5328-5330.

ZHAO, D. S., ROY, B., MCCORMICK, M. T., KUHR, W. G. & BRAZILL, S. A. 2003. Rapid fabrication of a poly(dimethylsiloxane) microfluidic capillary gel electrophoresis system utilizing high precision machining. *Lab on a Chip,* 3**,** 93-99.